

INFORMATION TO USERS

This manuscript has been reproduced from the microfilm master. UMI films the text directly from the original or copy submitted. Thus, some thesis and dissertation copies are in typewriter face, while others may be from any type of computer printer.

The quality of this reproduction is dependent upon the quality of the copy submitted. Broken or indistinct print, colored or poor quality illustrations and photographs, print bleedthrough, substandard margins, and improper alignment can adversely affect reproduction.

In the unlikely event that the author did not send UMI a complete manuscript and there are missing pages, these will be noted. Also, if unauthorized copyright material had to be removed, a note will indicate the deletion.

Oversize materials (e.g., maps, drawings, charts) are reproduced by sectioning the original, beginning at the upper left-hand corner and continuing from left to right in equal sections with small overlaps. Each original is also photographed in one exposure and is included in reduced form at the back of the book.

Photographs included in the original manuscript have been reproduced xerographically in this copy. Higher quality 6" x 9" black and white photographic prints are available for any photographs or illustrations appearing in this copy for an additional charge. Contact UMI directly to order.

U·M·I

University Microfilms International
A Bell & Howell Information Company
300 North Zeeb Road, Ann Arbor, MI 48106-1346 USA
313/761-4700 800/521-0600

Order Number 9408663

**A study of the HII region populations of M101, M51 and NGC
4449**

Scowen, Paul Andrew, Ph.D.

Rice University, 1992

U·M·I

300 N. Zeeb Rd.
Ann Arbor, MI 48106

RICE UNIVERSITY

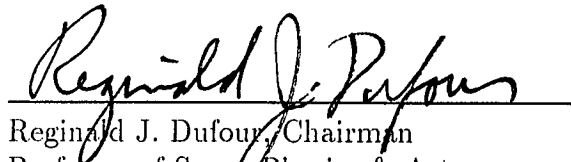
**A Study of the HII Region Populations of M101,
M51 and NGC 4449**

by

Paul A. Scowen

A THESIS SUBMITTED
IN PARTIAL FULFILLMENT OF THE
REQUIREMENTS FOR THE DEGREE
Doctor of Philosophy

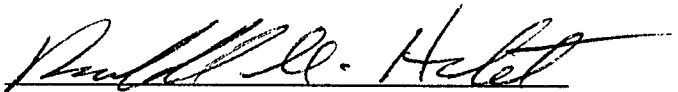
APPROVED, THESIS COMMITTEE:



Reginald J. Dufour, Chairman
Professor of Space Physics & Astronomy
Rice University



Jon C. Weisheit
Professor of Space Physics & Astronomy
Rice University



Randall G. Hulet
Assistant Professor of Physics
Rice University



J. Jeff Hester
Assistant Professor of Physics &
Astronomy
Arizona State University

Houston, Texas

June, 1992

Abstract

A Study of the HII Region Populations of M101, M51 and NGC 4449

by

Paul A. Scowen

An optical study of the HII region populations evident in three galaxies, M101, M51 and NGC 4449, has been made. Using narrow-band filters, emission line imagery has been taken using a CCD focal-reducing camera, at wavelengths covering the emission from H α , H β , [O III] λ 5007 and [S II] $\lambda\lambda$ 6716+6731. Using several identification techniques to spatially select the HII regions, emission line properties have been derived for 625 HII regions in M101, 465 in M51 and 163 in NGC 4449, making this the most complete study of its kind to date. Several trends have been discovered concerning the properties of the HII regions with radial position within their galaxy. M101 exhibits a large gradient in excitation, and oxygen abundance, as well as a gradient in the line-of-sight reddening. No positional variation in the derived ionization parameter for each HII region was found. Local variations in the effective collapse density for neutral gas have been detected for both M101 and M51. No such analysis was possible for NGC 4449 due to a lack of available data. M51 shows systematic emission variations only in the brightest cores of its largest HII regions, an effect attributed to a larger influence of the local ISM on the properties of the fainter, and more obscured, HII regions. M51 exhibits a spiral pattern that does not follow a single mathematical description, departing most dramatically at the corotation radius. A variation in the evolutionary time from peak local compression to peak star formation with radius has been detected for one of the arms in the galaxy, but not the other. NGC 4449 displays no systematic variations in the derived emission properties of its HII region population. This is attributed to a star formation mechanism that is independent of the radial ordinate, contrasting with the spiral density wave mechanism dominant in spiral galaxies. Unprecedented deep CCD imagery of this galaxy is presented, revealing the complicated structure of ionized filaments between the HII regions. The emission properties of these filaments are studied.

Acknowledgments

Over the past five years I have met and worked with many good people who deserve what small appreciation this passage may give. I would like to thank my advisor Reggie Dufour for all his guidance and advice, for giving me the opportunity to work with him after my Masters project, and for his often aggressive encouragement. I would also like to thank Donald Clayton and Kurt Liffman for introducing me to the wonders of computer coding. Appreciation is made to Bob Parker, for funding my initial term under Dufour. Great thanks also goes to my future co-worker Jeff Hester, who kindly introduced me to the world of astronomical observing, and who, with Reggie, made most of the imagery used in this project available to me.

Thanks, too, go to Bryan Bales and Patrick Shopbell with whom it has been often a joy and a pleasure to learn and develop new tricks and techniques involved with the operation of UNIX based computers on most levels. Their great expertise and friendly manner have always served to encourage me in my endeavours.

Other individuals who have, over the years, rendered aid and given sage advice to me have been: Don Walter (my partner in crime, so to speak), Steve and Ann Sturner, Frank Toffoletto, Rob Schmunk, David Oro, Paul Geis, Jim Sokolowski, and numerous others who cannot be listed here.

My greatest thanks is reserved for my family. In the course of my secondary education my parents always gave me the support and encouragement that took me this far, without any predefined agenda based on their hopes, but based purely on what I felt was best for myself. For this I will be eternally grateful. Finally, I would like to thank my dear wife, Linda, for her love and support especially during the last year of my graduate study. Without her presence and her constant encouragement and interest with my work, the outcome would probably have been very different.

Contents

Abstract	ii
Acknowledgments	iii
List of Illustrations	vii
List of Tables	xiii
1 Introduction	1
1.1 Preamble to the Study	1
1.2 The Main Conclusions of the Study	7
1.2.1 M101	7
1.2.2 M51	8
1.2.3 NGC 4449	8
2 The HII Regions of the Galaxy M101	10
2.1 Introduction	10
2.2 Data Reduction	13
2.2.1 Observations	13
2.2.2 Processing and Calibration	13
2.2.3 Region Identification	17
2.3 Results	19
2.3.1 Generation of datasets	19
2.3.2 Reddening as a function of radius	24
2.3.3 Excitation and Oxygen Abundance as a Function of Radius	26
2.3.4 Dependence of Excitation on Threshold	30
2.3.5 Behavior of the [S II]/H α ratio	33
2.4 Discussion	36
2.4.1 The H II Region Luminosity Function	36
2.4.2 The Ionization Parameter, U	39
2.4.3 Star Formation	42
2.5 Summary and Conclusions	52

3	The H II Region Population of the Galaxy M51	54
3.1	Introduction	54
3.2	Data reduction and calibration	56
3.2.1	Derivation of the H II Region population	57
3.3	Results	61
3.3.1	Emission Properties of the Brightest Regions	65
3.3.2	The H II Region Luminosity Function	67
3.3.3	Velocity Dispersion	69
3.4	Discussion	70
3.4.1	The Brightest H II Regions	70
3.4.2	Equivalent Widths at H β	71
3.4.3	Spiral Structure	76
3.4.4	Star Formation Efficiency	87
3.5	Summary and Conclusions	93
4	Line Emission from the Irregular Galaxy NGC 4449	95
4.1	Introduction	95
4.2	Data Reduction and Calibration	97
4.2.1	Selection of the H II regions	98
4.2.2	Line ratio imagery	99
4.3	Results	100
4.3.1	The H II Regions	105
4.3.2	Objects of interest within the galaxy	108
4.4	Discussion	115
4.4.1	Imagery of the Filaments	115
4.4.2	The Supernova Remnant SB 187	119
4.4.3	Star Formation	120
4.5	Summary and Conclusions	124
	Bibliography	126
	Appendices	134
A	The automatic registration of HII regions in CCD im-	
	agery	134

A.1	Introduction	134
A.2	Specification	135
A.3	Application	135
A.3.1	Initial Registration of the HII regions	136
A.3.2	Determining the physical extent of an HII region	137
A.3.3	Calculating the physical properties	141
A.4	Subsequent developments	144
A.5	Scientific Application	144
A.6	Summary	145
A.7	Details of calculations used	146
B	Emission Properties and Positional Information of the HII regions in M51	148
C	Emission Properties and Positional Information of the HII regions in NGC 4449	156
D	Glossary	159

Illustrations

1.1	The three galaxies studied in this thesis reprojected to the same distance, allowing better comparison between the objects.	5
2.1	The grey-scaled logarithmic H α line emission image of M101, the angular extent of the image is approximately 18' by 30'. The regions previously identified by Hodge 1969 are labelled by the prefix 'H', and those by Searle 1971 by 'S'. The display range used is from -16.7 to -14.0 dex (ergs cm ⁻² sec ⁻¹).	16
2.2	Full field gray-scaled image of the logarithm of the direct ratio of [O III] λ 5007 to H β with the identification mask applied. The threshold used to produce this mask was the lower of the two, set at 2×10^{-16} ergs cm ⁻² sec ⁻¹ in H α . The image is displayed between the limits -1.0 and 1.2 dex.	21
2.3	The logarithm of the direct ratio of [O III] λ 5007 to H β for each region, displayed using the overall deduced value from the integrated fluxes in each line over the entire area of each region. This highlights the gradients evident in the galaxy. The higher threshold (defined at 1×10^{-15} ergs cm ² sec ⁻¹ in H α) has been used. The display range is slightly different: -1.1 to 0.9 dex.	22
2.4	The logarithm of the direct ratio of [O III] λ 5007 to H β for each region, replacing the entire region with the calculated value, created using the lower threshold. The display range used is -1.1 to 0.9 dex. .	23

2.5	(a) Region reddening as a function of radial position. The higher threshold has been used to assemble this data. The equivalent reddening in magnitudes (A_V) is also represented on the right hand axis. A clear increase in reddening towards the galactic center is illustrated. (b) A similar plot except that the lower threshold has been used. Again, a rise in reddening towards the center of the galaxy is observed. The increase in errorbar size is a direct result of the lower fluxes (and lower numbers of photons) sampled by this threshold.	25
2.6	(a) The measured excitation of each H II region as a function of its galactocentric radius. The higher threshold has been used. (b) The galactic excitation gradient, calculated using the lower threshold. The increase in the population of H II regions between the two thresholds is well illustrated by these two figures.	27
2.7	(a) Calculation of the corresponding oxygen abundances for each H II region, derived from the correlation presented by Edmunds & Pagel 1984. The higher threshold has been used. (b) Calculation of the oxygen abundance as a function of position, using the lower threshold. The dominant source of error is the spread in the correlation used, about ± 0.2 dex.	29
2.8	(a) Calculated [S II]/H α ratio for each H II region as a function of position, using the high threshold. (b) The variation in the [S II]/H α ratio, calculated using the lower threshold.	34
2.9	Derived differential luminosity functions for the H II region population resulting from application of the the two thresholds. The derived inner and outer LF's are also represented; the boundary being at a radius of 8.6 kpc (the radius at which the excitation gradient appears to suddenly increase).	37
2.10	In all calculations the higher threshold has been used. (a) Plot of the ionization parameter, log U, against oxygen abundance. (b) Plot of log U versus radial position. (c) Plot of Q_{LyC} against the logarithm of the apparent size of each region in square pixels (1 pixel = 43 pc). (d) Plot of Q_{LyC} against radial position.	41

2.11	Contours of constant atomic hydrogen mass surface density overlaid onto our H α imagery. Note that the H I ridges coincide with those arms where areas of active star formation are visible, indicating that the two phenomena could have a common origin. The H α image is linear and displayed between 0 and 10^{-15} ergs cm $^{-2}$ sec $^{-1}$; the H I image is contoured at 10 equally spaced levels between 7 and 12 M $_{\odot}$ pc $^{-2}$	46
2.12	Logarithmic qualitative star formation efficiency image, displayed from -16.5 to -15.5. Radial markers at 5, 10 and 15 kpc have been added. The central region of the galaxy has a remarkably flat distribution of efficiencies, out to greater than 10 kpc to the west of the nucleus, and out to 5 kpc to the east.	49
2.13	Variation in the effective star formation law as a function of radial position. This is observational confirmation that the effective collapse criterion changes as a function of radius.	50
3.1	The disk of the galaxy M51 in the light of H α . The continuum contribution to the emission has been subtracted. Indicated on the image are the bright regions that exhibit systematic variations in their emission properties. The inset illustrates the bright ambient H α emission component.	59
3.2	Derived emission properties of the H II region population of M51 as a function of galactocentric radius. Two thresholds are presented: the highest used for the upper panels, the lowest for the lower set. (a) and (b) depict the Balmer decrement. (c) and (d) depict the ratio of [S II]/H α	62
3.3	Derived emission properties of the H II region population of M51 as a function of galactocentric radius. Two thresholds are presented: the highest used for the upper panels, the lowest for the lower set. (a) and (b) show the region excitation as a function of radius. (c) and (d) depict the corresponding oxygen abundance, using a correlation between region excitation and oxygen abundance.	63
3.4	Derived emission properties of the Carranza set of H II regions as a function of radius. Numerical analysis of the linearity of the distributions in Figures 3.2 and 3.3 are presented in Table 3.3.	64

3.5	The H II region luminosity function, as derived from our imagery using an adopted distance of 9.6 Mpc, and a calibration coefficient calculated as part of the Galactic H II region survey mentioned in the text.	68
3.6	Emission properties of the full set of H II regions plotted as a function of line-of-sight reddening. (a) the integrated H α emission plotted against reddening. (b) the region excitation versus C(H β). (c) the value of the ratio of [O III]/H β compared to the surface brightness of each H II region.	73
3.7	Results of the mathematical description of the spiral arms in M51. (a) assumes a logarithmic description, a break in the arms appears at a radius of around 6 kpc. (b) uses the material arm description to apply a hyperbolic solution, again exhibiting the break at 6 kpc. . . .	79
3.8	The mathematical solutions for each arm, as represented in Figure 3.7, reprojected onto the plane of the sky. The logarithmic description appears better in the inner disk, while the hyperbolic solution appears to more successfully model the shape of the arms in the outer disk. . .	80
3.9	A plot of the logarithmic solution to the dust arms in M51 compared to the inner disk solutions represented on Figure 3.7(a). The two components of Arm 1 diverge with increasing radius, while the two components of Arm 2 appear parallel indicating a constant timescale with radius.	85
3.10	A cartoon representing the physical situation being used to calculate the timescale for the density wave to pass from the observed peak in local compression to the observed local peak in star formation.	86
3.11	Spatial representation of the star formation efficiency (SFE) across the disk of M51. The contrast between the efficiency on-arm to that off-arm is very evident, in complete contrast to the much more uniform distribution seen in Figure 10 of SDH. The display range used is logarithmic from 10^{-19} to 10^{-16} ergs cm $^{-2}$ sec $^{-1}$ M $_{\odot}^{-1}$ pc 2	90
3.12	Analysis of the star formation law exhibited by the galactic disk of M51. A marked drop in the median gas surface density, a measure of the local collapse density for star formation, is seen with increasing radius.	91

4.1	Continuum subtracted H α line emission image of NGC 4449 displayed logarithmically between the limits of 10^{-16} and 3×10^{-14} ergs cm $^{-2}$ sec $^{-1}$	101
4.2	The line-of-sight reddening displayed two-dimensionally using the Balmer decrement, C(H β). The image is displayed between the limits of 0.0 and 1.5.	102
4.3	The excitation of the ionized gas, as measured using the ratio of [O III]/H β , displayed logarithmically from -0.2 to 0.8. Note the bright signature of the supernova remnant SB 187 in the north of the galaxy.	103
4.4	The value of the ratio of [S II]/H α , displayed logarithmically between -1.0 and 0.0. Note the two filaments wrapped around the superassociation in the south of the galaxy.	104
4.5	The derived emission properties of the H II region population, as a function of radial position (in parsecs). (a) The reddening as a function of radius. (b) The value of the ratio of [S II]/H α , exhibiting a large scatter with essentially no systematic variations. (c) Excitation as a function of position, again no systematic variation. (d) Inferred oxygen abundance as a function of radial position.	106
4.6	Plots of the derived emission properties of the H II regions as a function of their reddening values. No systematic variations are observed between the H II region reddening and (a) surface brightness, (b) the region excitation, and (c) the value of the ratio of [S II]/H α	109
4.7	H II region luminosity function. The peak in the distribution occurs at 10^{38} ergs sec $^{-1}$, with a low luminosity cut-off at $10^{36.8}$ ergs sec $^{-1}$	110
4.8	Line ratio image for [O III]/H α . The image is displayed logarithmically between the limits of -0.7 and -0.1. Note the large volume of emission from the host H II region associated with the SNR SB 187, as well as numerous arcs of emission.	112
4.9	The ratio of [O III]/[S II] displayed logarithmically between -0.5 and 0.7. Note again the large signature from the H II region 107 in the north.	113
4.10	The result of applying an “unsharp mask” to the H α image to enhance the filamentary structure that runs throughout the galaxy.	116

4.11	Schematic of the main features in Figure 4.10. The size and scale of this figure has been purposely made identical to all the other images included in this paper to allow an overlay to be made for each cross-reference and comparison.	117
A.1	Diagram showing hierarchy of the search protocol used by the algorithm upon encountering a candidate pixel. The coordinate scheme, together with its origin, is also included.	138
A.2	Flow chart of the subroutine that explores and registers a previously unknown region upon encountering the first pixel in its structure. The eight level hierarchy represented in Figure 1 is explicitly detailed here.	139
A.3	An example of the passage of the identification algorithm across a simple geometric form. Step (a) indicates the first pixel encountered. At (d), the fourth pixel is identified. The top edge of the shape is followed back to the original pixel using positions 7 and 8 in the grid.	140
A.4	A pictorial representation of four examples of typical morphological types of HII region encountered in real imagery: (a) well separated HII regions, (b) an extended structure with a single local maximum, (c) an extended source with many local maxima, and (d) a point like HII region (magnified x2 over the other images).	142

Tables

2.1	Observation Log for M101 Imagery	14
2.2	Calibration Factors for the Two Fields	15
2.3	Derived Oxygen Abundance Gradients as a Function of Threshold . .	28
2.4	Comparison of Derived [O/H] Values for Specific Regions	32
3.1	Details of Observations made of M51	57
3.2	Basic Physical and Geometric Information for M51	60
3.3	Results of χ^2 Analysis of H II Region Emission Properties	65
3.4	Comparison of Emission Properties with Velocity Data	70
3.5	Equivalent Width of H β as a Function of Spectral Type	75
3.6	Results of Theoretical Fits to the Apparent Spiral Structure in M51 .	82
4.1	Details of Observations made of NGC 4449	97
4.2	Basic Physical and Geometric Information for NGC 4449	100
4.3	Comparison of Emission Properties of H II Region 107	120
A.1	Examples of Information Required at Initiation	141
A.2	Examples of Information Produced	141
A.3	Example of Resulting Entries for Each Region	143

Chapter 1

Introduction

1.1 Preamble to the Study

The study of H II regions in other galaxies may be used as a diagnostic tool to study the very nature of the interstellar medium (ISM) local to that part of a galaxy as well as mapping global changes in physical parameters across the full extent of the galaxy. In this thesis, three different galaxies have been selected for study based on their morphological differences, two spirals and an irregular, and their kinematical properties. It is the aim of this research to study the differences and similarities between the systems in an attempt to better understand the processes most important to the evolution of galaxies as a whole, as well as the creation of H II regions themselves.

An H II region is defined as being an ionized volume of predominantly hydrogen gas, centrally excited by at least one star, of sufficient temperature and ultraviolet luminosity to achieve the ionization of a large enough volume of the local ISM to make the region visible. The name is derived from the dominance of ionized hydrogen, H II, in the ionization balance within the system. The analysis of these regions may be carried out by studying the line emission from the ionized hydrogen atoms. In this study the two Balmer lines, named after Johannes Balmer who first discovered them, have been primarily used to study the emission characteristics of the nebulae. The transition from the third orbital to the second ($H\alpha$ $\lambda 6563$), and from the fourth to the second ($H\beta$ $\lambda 4861$), have been used since they are among the strongest of emission lines observed in such objects, allowing the taking of sufficiently deep imagery to detect as many of the H II regions as possible.

Specific emission lines can be used to make some statements about the physical conditions within any particular H II region. The ratio of $H\alpha/H\beta$ can be used as a direct measure of the interstellar extinction between the observer and the source of emission. This extinction is a function of the wavelength of radiation passing through the absorbing medium (Osterbrock 1989, Figure 7.1), such that $H\beta$ is extinguished more than $H\alpha$. Using assumptions about the stellar type ionizing the H II region, and

about the temperature and density of the region as a whole, it is possible to derive the quantity $C(H\ \beta)$ which is a direct measure of the amount of line-of-sight extinction experienced by the radiation we receive. A value of zero for $C(H\ \beta)$ represents essentially no interstellar extinction.

The mean temperature of the electrons in the ionized volume of an H II region is an interesting quantity, and can be used to study the relative importances of radiative cooling mechanisms, ionizing radiation fields, and so on. A gauge of this temperature is the ratio of the forbidden transition [O III] $\lambda 5007$ to H β . The physical basis for this correlation comes from the theory of nebular astrophysics. The [O III] line is termed forbidden because under normal terrestrial conditions this radiative transition is not seen, but in the very low densities of interstellar gas excited atoms of oxygen do not collisionally de-excite allowing enough time for the spontaneous emission of the $\lambda 5007$ photon. The electron temperature it measures is largely set by the oxygen abundance in the nebula, or the metallicity, therefore this ratio a good measure of the temperature when the dominant factor is abundance related. The temperature dependence of this line is very sensitive, and is given by Osterbrock 1989 as:

$$I_{\lambda}(T) \propto \frac{1}{\lambda} T^{-0.5} e^{\frac{-\chi}{kT}} \quad (1.1)$$

for a forbidden transition. In this equation λ is the wavelength of the transition, T is the electron temperature of the ionized gas, and χ is the ionization energy of the atom from which the transition is being emitted. The temperature dependence of the H β transition is given as:

$$I_{\lambda}(T) \propto T^{-0.90} \quad (1.2)$$

and is therefore less sensitive to a temperature variation than the [O III] line. Other advantages of this transition include the fact that the wavelengths of the two transitions are quite close (5007 Å for [O III], 4861 Å for H β) making the possible effects of extinction a minimum. In addition, the ratio of [O III] $\lambda 5007$ /H β is also a function of the ionization fraction $N(O^{++})/N(H^{+})$, and will be affected if this ratio varies from region to region. In this study we ignore these possible variations, and assume a constant fraction.

In many cases, however, the extinction of H β is so severe that there simply are not enough photons to produce an image, which then makes necessary the use of the H α line for the ratio, whose temperature dependence is given as:

$$I_{\lambda}(T) \propto T^{-1}. \quad (1.3)$$

Another line ratio that is of interest is the ratio of the forbidden transitions from [S II] at $\lambda 6716$ and $\lambda 6731$. If we could split these two lines then estimates of electron density would be possible. These two emission lines possess the same lower level, and nearly the same upper state energetically. Therefore the relative excitation rates are purely a function of the relative collision strengths and since they have different transition probabilities, the relative populations of the two upper levels will depend on the density. However, the filter used in this study is wide enough to encompass the emission from both lines, so it will purely serve as a temperature diagnostic. Since it is another forbidden line, the same temperature dependence as oxygen is followed, allowing another gauge of the electron temperatures, but with a different set of considerations concerning the physical nature of H II regions.

The first ionization potential of oxygen compared to hydrogen is very similar (13.60 eV for hydrogen, 13.62 eV for oxygen). Accordingly the extent of the physical nebula in singly ionized oxygen will be essentially the same as the ionized hydrogen volume when ionized by the intense ultraviolet flux from OB stars. The energy typically emitted by these stars so well matches the ionization energies of these atoms that they are preferentially populated. The ionization potential of O III is 35.1 eV resulting in the extent of the zone containing this species to be much smaller than the larger hydrogen volume. At the boundary to the larger radiative volume, there is a “recombination edge” beyond which those atoms with ionization potentials less than 13.6 eV become populated by the lower energy photons that escape the nebula. The first ionization potential of sulphur is 10.4 eV making it an ideal sink for these photons. Of course, the actual levels of emission seen will be a function of the temperature of the radiation field as well as the local density of sulphur atoms, usually highest along the boundary between H II regions and the molecular cloud in which the region formed. The reason that S II is seen brightest along the edge of the nebula is that interior to the ionized volume most, if not all, sulphur is in the higher ionized states of S III and S IV (potentials 23.3 eV and 31.8 eV respectively). It is only outside the boundary to this volume that S II is seen in any great quantity.

The sulphur lines are also diagnostics for shock excited gas, since the equivalent temperature in thermal equilibrium for an energy of 10.4 eV is around 120,000 K which can be achieved locally in a post shock medium, after the passage of a strong shock. Accordingly the ratio of [S II]/H α can be used for more than one purpose.

Such ionized volumes are usually found in regions of star formation and therefore serve as probes of the local conditions on the ISM when stars are formed. The typical

size of an H II region varies depending on the strength of the ionizing source and the density and composition of the local ISM. Sizes can vary from as little as a few parsecs (such as the Orion Nebula in our own Galaxy), to more than a kiloparsec (NGC 5461 in M101, ionized by a superassociation of O stars).

The study of these H II regions in CCD images of other galaxies is a complex and challenging task. There are several pitfalls involved with the procedure, and a number of different options available to the researcher, two of which are used in this study. The reader is referred to Appendix A for a discussion of the first and more complex approach used for M101. In that chapter, the problems associated with the successful extraction of meaningful results are dealt with in a terse fashion.

In this study we will concentrate on H II regions that are observable in the structures of other galaxies. Of course, the study of the H II regions in our own Galaxy provides much detailed information concerning the more microscopic structure of each region, but due to the fact that we are resident within the disk of our Galaxy, and the zone of avoidance (the part of the sky obscured by the disk of our own Galaxy) prevents our study of H II regions more than 1-2 kpc away, we suffer from an incompleteness problem. This hinders the successful study of global variations in the H II regions since our range of observations is limited by a dependence on the position of the solar system relative to the local arms of our spiral host.

The three galaxies selected are illustrated in Figure 1.1, where the images have been rescaled to the same equivalent distance. These galaxies have been chosen using several selection criteria. M101 is a large face-on spiral, with a flocculent spiral pattern that defies the best methods of description. It is an isolated object in the optical, with no visible companions. Studies in the radio have revealed it to be part of a much larger system of objects that occupy a common halo of neutral gas. This group is large enough that it bears the name of its largest member: the M101 group. The class of galaxy is described as being late-type, in that its structure is characterized by a small and compact nucleus with large well-separated arms. Since H II regions are usually located along the spiral arms in such a system, this makes M101 ideal for a study of this type.

M51 is a galactic system interacting with a companion galaxy, and is famous for its well described spiral pattern. It has a high surface brightness of emission that has made it one of the most studied galaxies. It is again a late-type galaxy, with well defined arms, although they are more obscured by local dust, and a large population of H II regions. The interaction is clearly affecting the star formation throughout the

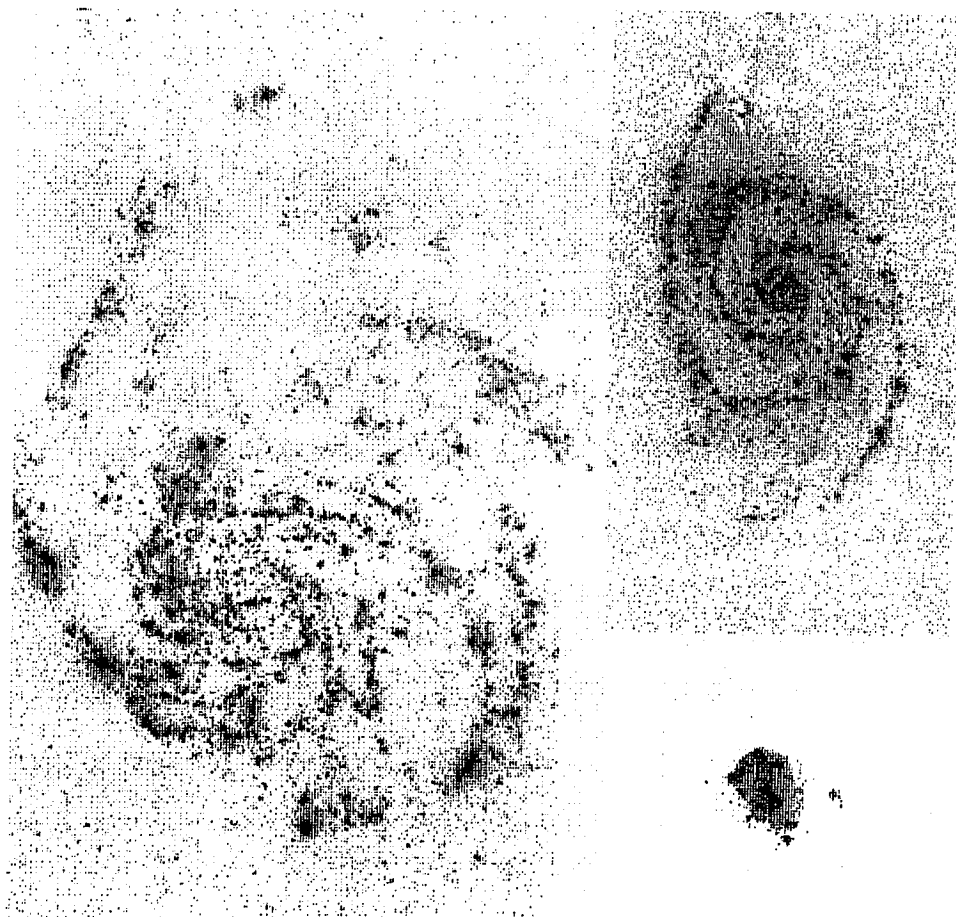


Figure 1.1 The three galaxies studied in this thesis reprojected to the same distance, allowing better comparison between the objects.

galaxy, and it is by comparison with M101 that we hope to study the nature of these changes.

Lastly, NGC 4449 has been selected as a “control” case in our study, although it may be better described as an “odd-man”. This galaxy is an Irregular, in that it displays little or no organized structure of the kind apparent in spiral systems. NGC 4449 is also very low in metallicity, with its star formation not being driven by density waves or having much to do with the local molecular gas density. In that regard the distribution of the H II regions, as well as the nature of the star formation process, will be very different since the source driving such formation in spirals (the spiral density wave) will be absent, providing a valuable contrast to the other two objects.

In studying the star formation processes active within each galaxy we will study the relative surface densities of neutral gas in both atomic and molecular forms. Current ideas for star formation involve large dense clouds of molecular gas that spontaneously collapse to produce a local density at the core high enough to trigger the initiation of nuclear fusion. After this, the “wind” of intense radiation from the new star will dissipate the remains of the molecular cloud to leave the hot, young stars set in a large volume of ionized gas - an H II region. Later, the ionized hydrogen will recombine into clouds of neutral atomic hydrogen, and these clouds will eventually begin to coalesce into larger groups, finally producing the molecular clouds that started the lifecycle.

The distributions of these three phases of hydrogen may be measured using three different bands of radiation. The ionized phase we have already discussed. The atomic phase is traced using the 21cm ground state hyperfine transition that is emitted in the radio bandpass. The molecular phase is mapped through a more indirect method, using the millimeter vibrational transitions from the CO molecule. An assumption is implicit in this approach that the local density of CO is proportional to the local density of molecular hydrogen, ie. that the two are associated.

In most spirals the expected distribution of this material, from spiral density wave theory, is as follows. The molecular clouds are arranged along the arms of the galaxy where the underlying spiral density wave has triggered their formation by inducing further collapse of the HI clouds. This is also expected to coincide with the dust arms seen in the optical. Just outside these distributions another arm will be defined by the newly-formed H II regions, easily visible in the optical in the light of H α . Throughout both sets of arms, there is expected to be a pervasive HI component with local enhancements in the densities close to the arms themselves. The molecular

material is also seen to be more dense towards the center of a spiral galaxy, exceeding the local density of the atomic material by as much as two orders of magnitude.

Each of the chapters in this piece have been assembled into papers for separate publication in professional journals. The second chapter, dealing with M101, has already been accepted for publication at the time of this writing, and will be published as Scowen, Dufour and Hester 1992a. The following two chapters will be submitted in a similar manner following the presentation of this thesis, as Scowen, Dufour and Hester 1992b, and Scowen, Dufour and Hester 1992c.

1.2 The Main Conclusions of the Study

Since each of the following chapters is an independent piece of work, and has been included as such, it was felt valuable to have a summary of the main points of this thesis in the introduction. These points will be addressed galaxy by galaxy.

1.2.1 M101

In studying M101 we have identified gradients in the derived line ratios for each H II region in a set numbering 625. The quantity $C(H\ \beta)$ that measures line-of-sight reddening increases towards the center of the galaxy; also, the ratio of $[O\ III]/H\ \beta$ increases considerably with radius. This latter ratio has been re-expressed in terms of a radial decrease in the abundance of oxygen in each H II region studied. A break in the gradient has been observed and may be correlated with the corotation radius.

The numbers of ionizing photons present within each H II region, as derived from the surface brightness of $H\ \beta$, has revealed a powerlaw between the number of photons and the size of the region itself. A luminosity function of the H II region population reveals that our sample of regions is complete to luminosities comparable to the Orion Nebula.

The apparent star formation efficiency is seen to vary across the face of the galaxy, with the star formation process being most efficient in the outer disk, where the neutral gas is dominated by atomic hydrogen. A change in the local critical collapse density for the creation of star formation sites has been detected with radius.

No correlations are found between the size of an H II region and its position within the galaxy, or between the derived ionization parameter for each region and position.

1.2.2 M51

Again, we derive emission properties for a suite of H II regions within the galaxy, for a sample of 465 H II regions. Systematic variations in these properties are seen only in the brightest H II regions. This is apparently due to large amounts of intervening dust as well as an appreciable underlying absorption problem from the stars in the H II regions themselves.

Comparison is made between the magnitude of the gradients observed and those seen in M101; most are quite comparable with the excitation gradient being much flatter and therefore similar to the outer gradient observed in M101.

A luminosity function has been assembled, and compared with existing versions in the literature, to confirm that our sample is as good as the best examples previously published.

Mathematical description of the spiral pattern in M51 has yielded interesting results concerning the dynamical nature of the inner and outer disk of the galaxy. The inner disk is rotating with a pattern speed faster than the outer disk, which rotates with the companion. The interface between the two speeds occurs at the corotation radius.

Estimates of the timescale between the compression of the molecular clouds and the star formation exhibited by the H II regions have been made for both of the arms in the galaxy. One arm indicates a constant timescale between the compression phase and the star formation phase, while the other arm indicates a linear function of this timescale with radius. This latter arm is the arm that most closely approaches the interacting companion over the range in radius studied.

Estimates of the star formation processes active in M51 have confirmed the high contrast between the arms and the interarm regions. The change in local collapse density with radius is again observed, although the absolute densities are an order of magnitude lower in M51 than in M101.

1.2.3 NGC 4449

Successful calibration of the CCD imagery of NGC 4449 has yielded emission line information on 160 H II regions. All of the line ratios calculated exhibit completely flat distributions with radius, indicative of the fact that the star formation process in this galaxy is essentially independent of position. The galaxy appears very metal-poor.

Identification of several interesting objects, based on emission line characteristics and morphology, have been made due both the good resolution and proximity of the galaxy. Among these is the supernova remnant SB 187, which is seen to be interacting with a nearby H II complex. Another arc-like object, previously unmentioned has been imaged and emission-line fluxes measured. This will be the subject of future work.

A study has been made of the many filaments that are seen in emission across the face of the galaxy. A finding chart to allow study of these objects has been included. Although imagery in the radio and millimeter bands was unavailable, a review of the theories concerning star formation in NGC 4449 has been made. There are believed to be very low levels of molecular gas, although such estimates are based on the CO emission, and due to the low abundances in the galaxy, the use of this tracer has been questioned. Star formation appears to be driven by a chain-reaction process that stochastically fills the galaxy with H II regions, rather than being triggered by a position dependent process as appears typical in spiral galaxies.

Chapter 2

The HII Regions of the Galaxy M101

2.1 Introduction

Among spiral galaxies, M101 (NGC 5457) is the nearest of the giant high luminosity “grand design” spirals. In the RC2 (de Vaucouleurs, de Vaucouleurs, & Corwin 1976) it is classified as a SAB(rs)cdI system with an isophotal diameter of 26.9 arcminutes. It is one of the foundation systems used in studies of the extragalactic distance scale; for example, Sandage & Tammann 1974 give a distance of 7.2 ± 1 Mpc, while Buta & de Vaucouleurs 1983 gives 4.7 ± 1.8 Mpc. In this paper, we adopt a distance of 7.4 Mpc based on the 21cm measurements of Sandage and Tammann 1976, since we believe the six methods they used to be a better independent verification of the true distance than any individual cepheid analysis. Its large apparent size, high galactic latitude, nearly face-on orientation (17° , Zaritsky et al. 1990), and declination ($+54$ degrees) makes M101 a prototype for studies of the stellar and gaseous components of spiral galaxies.

H II regions provide much information on the properties of gaseous material distributed within galaxies, as well as estimates of abundance gradients and changes in the stellar populations associated with them (Shields 1990). M101 contains a rich population of H II regions that has attracted many investigations. The distribution and morphology of the H II region population have been studied by Hodge 1969, Searle 1971, Sandage & Tammann 1974, Talbot and Arnett 1975, Shields & Searle 1978, Hodge & Kennicutt 1983, Kennicutt and Kent 1983, Hill et al. 1984, McCall 1985, Keel et al. 1985, Kennicutt et al. 1987, Kennicutt et al. 1989. Detailed spectrophotometry of various M101 H II regions have been published by Searle 1971, Smith 1975, Shields & Searle 1978, McCall 1985, Torres-Peimbert et al. 1989, Zaritsky et al. 1990. The results indicated that, among all spiral galaxies, M101 shows an exceptionally steep gradient in O/H; for example, Evans 1986 finds a gradient of -0.074 ± 0.006 dex kpc $^{-1}$ and notes that the varied results of previous studies are likely to be affected by bias towards the brighter cores, slit sizes, orientations, etc.

More recently, Zaritsky et al. 1990 presented spectrophotometry of some 80-odd H II regions in M101 using a multi-fiber-optic spectrograph, whereupon they identified a steepening of the excitation (and possibly abundance) gradient near the galactic center compared to the outer parts.

The H II regions and neutral gaseous components of M101 have attracted numerous radio studies as well. H I 21cm studies have been made by Allen et al. 1973, Israel et al. 1975, Allen & Goss 1979, Bosma et al. 1981, Viallefond et al. 1981, Viallefond et al. 1982, van der Hulst & Sancisi 1988. These studies found a great asymmetry in the galactic radio emission (Israel et al. 1975), identified the association between NGC 5477 and the M101 group (Allen et al. 1978), detected the large variation in the ratio of H I/H II gas mass across the galaxy (Viallefond et al. 1981), measured a well behaved rotation curve out to 7' (Bosma et al 1981), and showed that the various H I clouds appear to be tidally stable (Blitz & Glassgold 1982). Additionally, CO studies have been made by Kenney et al 1991 which indicate the presence of a gaseous bar in the center of the galaxy. Finally, we note the radio line and continuum observations of H II regions in M101 by Israel et al 1975, who found that the H II region cores account for the majority of their optical luminosities. In addition, they found that local dust obstructs part or all of the emission from many regions in the optical, making their overall extinction in the radio larger by up to 0.5 mag in A_v compared to the optical studies.

The rich population of H II regions in M101, the detailed (though nonetheless limited in number) spectrophotometric studies of the brighter H II regions, coupled with available radio data on the H I and CO distribution, makes this galaxy an excellent object for detailed studies of the morphology and spectral characteristics of the H II region population in a giant spiral galaxy. The pioneering study of this type was by Talbot & Arnett 1975 who used very limited (then) optical H II region spectrophotometry and imagery with low resolution radio 21 cm data to investigate qualitatively the radial distribution of star formation rates and gaseous properties of several spirals for comparison with theoretical model expectations of the structure and evolution of disk systems. Most recently, Kennicutt 1989 studied the nature of the "star formation law" in several spirals using azimuthally averaged emission line profiles in an attempt to characterize the relationship between the star formation rate (SFR) and the observed gas surface density. He found that the interstellar gas instability criterion acts as a delimiter between regions where a Schmidt Law appears

to describe the local SFR, and lower density regions where the “law” breaks down, a behavior that was well modelled by a simple Toomre model (Toomre 1964).

The present paper attempts to improve on the previous studies of the physical properties and composition of the H II region population of M101 (with other systems to follow in succeeding papers) using techniques based on spatially resolved “imaging spectroscopy” of the H II region population of nearby spiral and irregular galaxies. Herein we concentrate on M101 and present the observational and calibration techniques in Section 2; the basic results of the datasets of several hundred H II regions in Section 3; and finally a discussion of the physical properties of the H II region population with the distribution of neutral gas, galaxy dynamics and star formation processes in Section 4.

2.2 Data Reduction

2.2.1 Observations

Observations were made by two of us (R.J.D. and J.J.H.) of two fields in M101 using the Wide Field PFUEI on the Palomar 1.5m telescope. See Hester & Kulkarni 1989 for a description of the instrument. This re-imaging system images a 16 arcminute field onto a TI 800x800 CCD at an effective focal ratio of f/1.66 at a plate scale of 1.2 arcseconds/pixel. Three-inch square filters were used in the f/8.75 telescope beam to avoid field dependent bandpass and other complications common to the use of interference filters in a collimated beam.

Observations included images taken at narrow band wavelengths of 6574/20 Å (peak wavelength/ FWHM) (H α), 4869/31 Å (H β), 5014/32 Å ([O III]), 6730/36 Å ([S II]), and at nearly line-free continuum bandpasses centered at 6450/104 Å (RC1), 4805/75 Å (GC1), 5103/98 Å (GC2). A log of the observation details may be found in Table 2.1. Observations were timed to catch the object near the meridian on both nights. The quoted recessional velocity of M101 is +372 km sec⁻¹ (Sandage & Bedke 1988), so the corresponding redshifts of the nebular lines (6 - 8 Å) within the filter bandpasses is not significant. In addition, any spiral galaxy with a non-zero inclination angle will have a line-of-sight velocity shift due to galactic rotation that will vary with position in the field. M101 has an inclination angle of 17° (Zaritsky et al. 1990) producing a corresponding shift of at most 2Å for H α , a small effect that will have no significant impact on our bandpass.

2.2.2 Processing and Calibration

Routine flattening and registration were carried out using IRAF *. Subsequent data analysis was performed using code developed at Rice. The images were aligned to better than 0.1 pixel using coordinates from a large sample of stars (>50). All continuum contributions to the narrow band images were subtracted using the continuum images, scaled accordingly in intensity using the same sample of stars. The scaling was calculated using a linear least squares fit to the photometry of the sample stars, thus any effects due to differences in continuum and line variations in the stellar spectra were effectively minimized.

*IRAF is distributed by the National Optical Astronomy Observatories, which is operated by the Association of Universities for Research in Astronomy, Inc., under cooperative agreement with the National Science Foundation.

Table 2.1 Observation Log for M101 Imagery

Name: Date (UT)	Filter Å (λ /FWHM)	Filter Name	Exposure (seconds)	Field Center RA (h m s)	(1950.0) Dec ($^{\circ}$ ' ")
North: 28 Feb 1987				14 01 15.1	+54 47 06
	6574/20	H α +500	1500		
	6450/104	RC1	500		
	6730/36	S II	3000		
	5014/32	O III	3000		
	5703/98	GC2	500		
	4869/32	H β	2000		
	4805/75	GC1	500		
Central: 1 Mar 1987				14 01 19.7	+54 33 00
	6574/20	H α +500	1500		
	6450/104	RC1	500		
	6450/104	RC1	50		
	6574/20	H α +500	100		
	6730/36	S II	3000		
	6730/36	S II	100		
	5014/32	O III	100		
	5014/32	O III	3600		
	4869/32	H β	2000		
	4869/32	H β	100		
	4805/75	GC1	2x500		
	5703/98	GC2	2x500		

Figure 2.1 shows the location of several major H II regions in the M101 system and their assigned names. The ‘S’ regions originate from the notation in Searle 1971, and the ‘H’ regions from Hodge 1969. Simulation of the large apertures used in the spectrophotometric observations by Searle 1971 allowed us to calibrate the Central Field (CF) narrow band images. Using four of the regions from Searle’s sample: S2, S5, S6 and S10 (NGC 5455) - regions whose aperture positions and sizes could easily be simulated, we arrived at the calibration constants for the line images shown in Table 2.2. Since Searle had no [S II] data, we followed the same procedure using published spectrophotometry for various regions in M101 by Torres-Peimbert et al. 1989 to allow calibration of the CF [S II] image. The regions used were S2, H40, S5, H47 and S10.

The dominant source of error in the calibration factors is the difference in the derived factors from region to region. We attribute these differences to relative positioning errors between our reconstructions and the reported positions for the spectrophotometry, as well as seeing variations between the two sets of results. Contributions from photon statistics to the variance for each region are very small, while errors in the original spectrophotometric work would be systematic and would not affect the consistency of results between individual regions.

The lack of documented H II regions in the Northern Field (NF) required us to use regions that appeared in both fields as the references for the calibration of the NF. Four nebulae were identified and sampled in the same manner to give the calibration factors shown for the NF in Table 2.2.

Thus for the case of the NF the sources of variance differ. The contribution from photon statistics is greater because we are comparing two sets of exposures that had slightly different signal to noise characteristics. We also had a pixelation problem due

Table 2.2 Calibration Factors for the Two Fields

Line (CF)	Calibration Factor (ergs cm ⁻² sec ⁻¹ dn ⁻¹)	
	Central Field	Northern Field
H α	$(1.42 \pm 0.15) \times 10^{-18}$	$(1.05 \pm 0.03) \times 10^{-18}$
H β	$(1.85 \pm 0.31) \times 10^{-18}$	$(1.93 \pm 0.14) \times 10^{-18}$
[O III]	$(1.43 \pm 0.23) \times 10^{-18}$	$(1.41 \pm 0.05) \times 10^{-18}$
[S II]	$(2.99 \pm 0.67) \times 10^{-19}$	$(2.50 \pm 0.16) \times 10^{-19}$

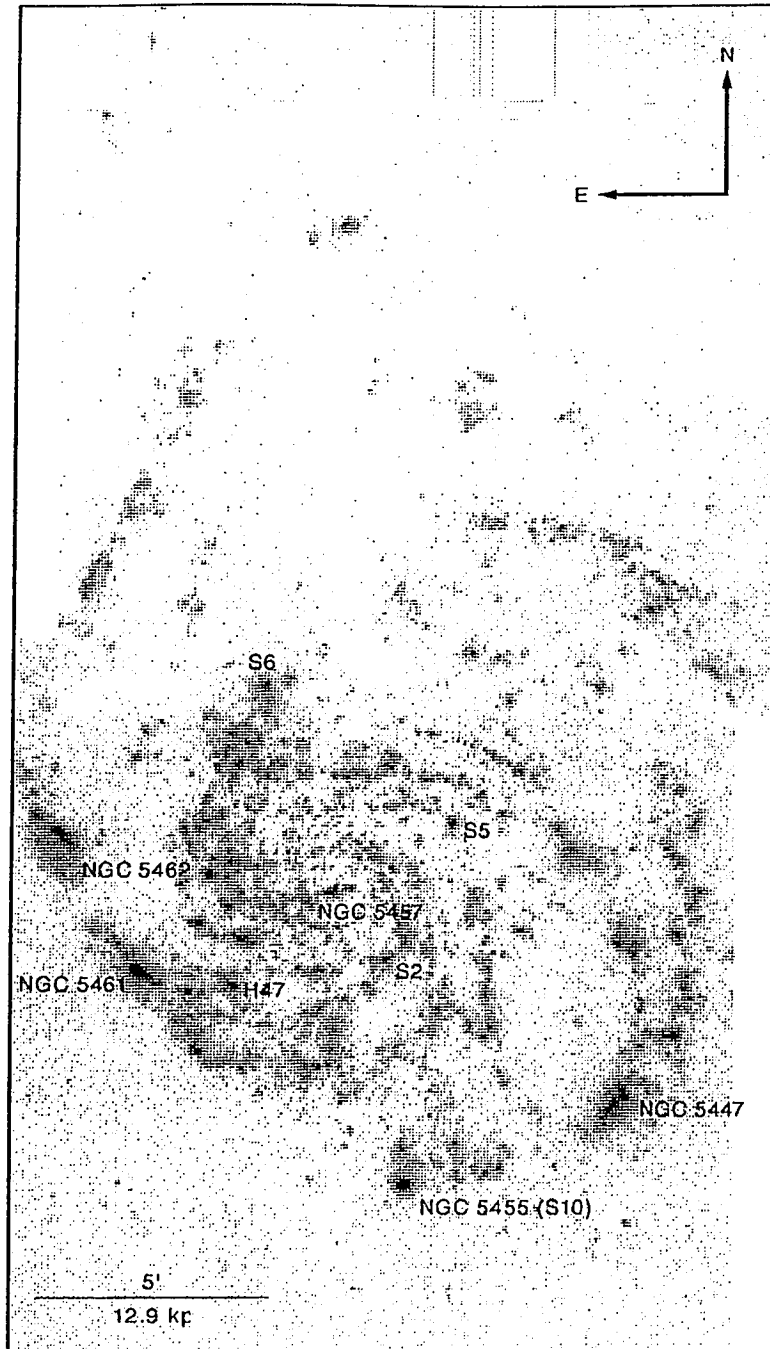


Figure 2.1 The grey-scaled logarithmic $H\alpha$ line emission image of M101, the angular extent of the image is approximately $18'$ by $30'$. The regions previously identified by Hodge 1969 are labelled by the prefix 'H', and those by Searle 1971 by 'S'. The display range used is from -16.7 to -14.0 dex ($\text{ergs cm}^{-2} \text{ sec}^{-1}$).

to the fact that the overlap region is only a thin strip near the edge of both fields. The instrument itself corrects for the change in passed wavelength as a function of position in the field, a problem with interference filters in converging beams, but the quality of the images at the edge of the field varies. This is demonstrated by the typically non-circular appearance of stellar images near the field edge. This exacerbates the pixelation problem since the region images appear to be slightly different shapes and sizes in the two sets of pictures.

Ultimately, the two sets of images were mosaicked together to give a combined field of the galaxy that measured 18×30 arcminutes. Although the region intensities match well between the two sets of data, there was a noticeable difference in the level of the sky background, attributable to some high cirrus on the second night, during the CF imagery.

2.2.3 Region Identification

The $H\alpha$ images were used, together with a predefined threshold, to identify $H\ II$ regions and establish a template for extracting fluxes for these regions in other emission lines. Each region of emission seen in the $H\alpha$ image is taken to be an individual region or complex, ignoring any line-of-sight coincidences, since the scale height for these objects is typically 50 pc making it extremely unlikely that this could occur in an image of a face-on spiral. The choice of the threshold level is critical. It must be high enough to avoid background contributions to the emission in order to identify the regions as separate entities, while being low enough to allow detection of a large number of regions.

Pixel identification, as being part of an $H\ II$ region, is based on the intensity of the subject pixel relative to its neighbors. If the pixel is a member of a contiguous group of pixels, all of which are also above the threshold, then it is successfully identified. Upon encountering the first pixel in such a group the algorithm will identify all members of that group before moving on.

The final product produced by this method of analysis consists of several parts. For each emission line image studied, a table of calculated physical quantities is assembled with an entry for each region identified. These quantities include the integrated surface brightness, the physical area, the deprojected galactocentric radius, and the accurate position of the brightest pixel in $H\alpha$ in right ascension and declination.

Together with these datasets, two auxiliary products are also calculated. Each product is an image that is the same size as the original, and that resembles that original morphologically, except that it includes additional information. One image contains a sequence of identification flags, each one unique for each region, allowing subsequent analysis of each region after the identification procedure has been applied. The second image is a binary mask that is opaque at all positions except those identified as being part of a legitimate HII region.

The success of this technique is excellent. Location and registration of isolated HII regions, no matter their morphology, has been checked many times. However, the identification of regions that are members of a set that occupy a continuous luminous halo has proven less easy. Since the technique employs a threshold to define the luminosity of acceptable pixels, in a superassociation it is all too easy to have all the member regions be identified as one. This was the reason multiple thresholds were used, one to study the fainter, more isolated regions, another to study the individual bright cores in associations of regions.

The technique was very successful compared to visual identification of the same regions, but in recent work flaws of the process have become apparent. M101 is a simple system to study in this manner since the majority of the regions are well separated, and are set against a uniform background. Recent application of the same technique to images of more tightly wound spirals and irregular galaxies have revealed that the code cannot deal very well with a large variation in background emission from diffuse $H\alpha$. This problem will clearly require a modification of the code for further use, but for the purposes of studying this galaxy it is sufficient.

Further specifics of the identification algorithm, and the suite of routines developed around it, are detailed in Appendix A.

2.3 Results

2.3.1 Generation of datasets

The identification of H II regions can be a rather subjective matter. To the naked eye it seems a simple matter to determine those regions that are distinct from others, and those that are not. However, in developing an automatic process to identify regions, one is faced with the question of what defines the physical boundary of an H II region. Setting a threshold as a boundary identifier is the most obvious manner to do this, but the technique involves elaborating on what the physical extent of a region is defined to be. Indeed, many of the regions that are identified by our work are listed as assemblies of separate regions by other authors (eg. Hodge et al. 1990).

This raises the issue of whether regions that have distinctly separate bright cores but a common diffuse halo should be considered to be physically independent. This would make a difference if the integrated flux from each sub-region were to be plotted as separate data points on, say, a radial plot of region flux, since those points would represent changes within the H II region complex and could not be interpreted alongside global data. There would be a danger for misleading information to be drawn from such a graph, since many (outer) large H II complexes which should only be represented by one point, would be fragmented into many points.

Our method also has certain limitations. The identification procedure is limited by the effective resolution of the system, and since our pixel size is 1.2 arcseconds seeing effects could affect how well the identification procedure extracts the extent of each region. However, the process is not affected by changes in seeing between different line emission images. The secondary procedure (used to calculate the emission properties of the regions in the other line images) uses the H α mask as the template for further region identification, so the definition of each region is fixed after the first step removing any influence of the seeing on the extent of each region. It is possible for flux to be scattered out of the mask “apertures” by changes in seeing, but in general this will have little effect, since on average as much light scattered out of the aperture will be scattered in.

As noted earlier, Evans 1986 pointed out the problem of non-equal apparent integration areas presented by the same region in different emission line images. If the other lines are used as the source of their own templates, it would result in a variation in the calculated H II region areas from line to line, not to mention that only those regions bright in that emission line would be detected. An additional problem is that

radial gradients are seen in the surface brightness of H II regions in certain emission lines such as [O III] and [S II], causing a radial bias to be introduced in the selection procedure. However, no such gradient is seen in the emission in the lines of H α and H β .

Line emission from H α is a good tracer to use for identification purposes since, (i) it represents all of the ionized gas (while [O III] and [S II] represent only part), (ii) it is a strong line compared to H β , and (iii) it is relatively unaffected by reddening compared to H β since the interstellar extinction curve is a function of wavelength and affects lines with shorter wavelengths. The identification technique, though, can be applied to the other line images to select those H II regions much brighter in either [O III] or [S II]; something which would be useful, for instance, for searches for supernova remnants.

Two suites of data were generated from the four line emission images. The first set used a rather high intensity threshold (set at 1×10^{-15} ergs cm $^{-2}$ sec $^{-1}$) to isolate the bright cores from the more diffuse emission in the regions. This sample predictably consists of well separated regions, but has a much smaller population since many fainter regions have simply been lost. The second set has a much lower threshold (set at 2×10^{-16} ergs cm $^{-2}$ sec $^{-1}$), set at the point where the emission from the regions begins to approach the level of the background noise in the images (a threshold which was equivalent to a S/N of 6). However, the calculations of the properties of the fainter regions suffer more uncertainty due to both the lower flux levels (Poissonian statistics) and their smaller areas, since in general the fainter regions are apparently smaller.

Figures 2.2, 2.3 and 2.4 highlight the power of the approach. Figure 2.2 depicts the pixel-by-pixel ratio map after the region identification has been applied. The resolution of the excitation structure within the structures of the giant extragalactic H II regions is particularly apparent. The next two figures use another approach to represent the data. Here each region has been replaced by a single value equal to the ratio of the integrated flux of each emission line over the entire area of the region. This serves to highlight the gradients evident in later figures in a more visually instructive manner. Both the higher (Figure 2.3) and the lower threshold (Figure 2.4) have been used.

In all subsequent analysis, the integrated surface brightnesses for each H II region in each emission line observed have been used for the line ratio calculations, since this allows direct comparison with most existing spectrophotometric studies. It should be noted that area-averaged quantities were studied, with the general result that

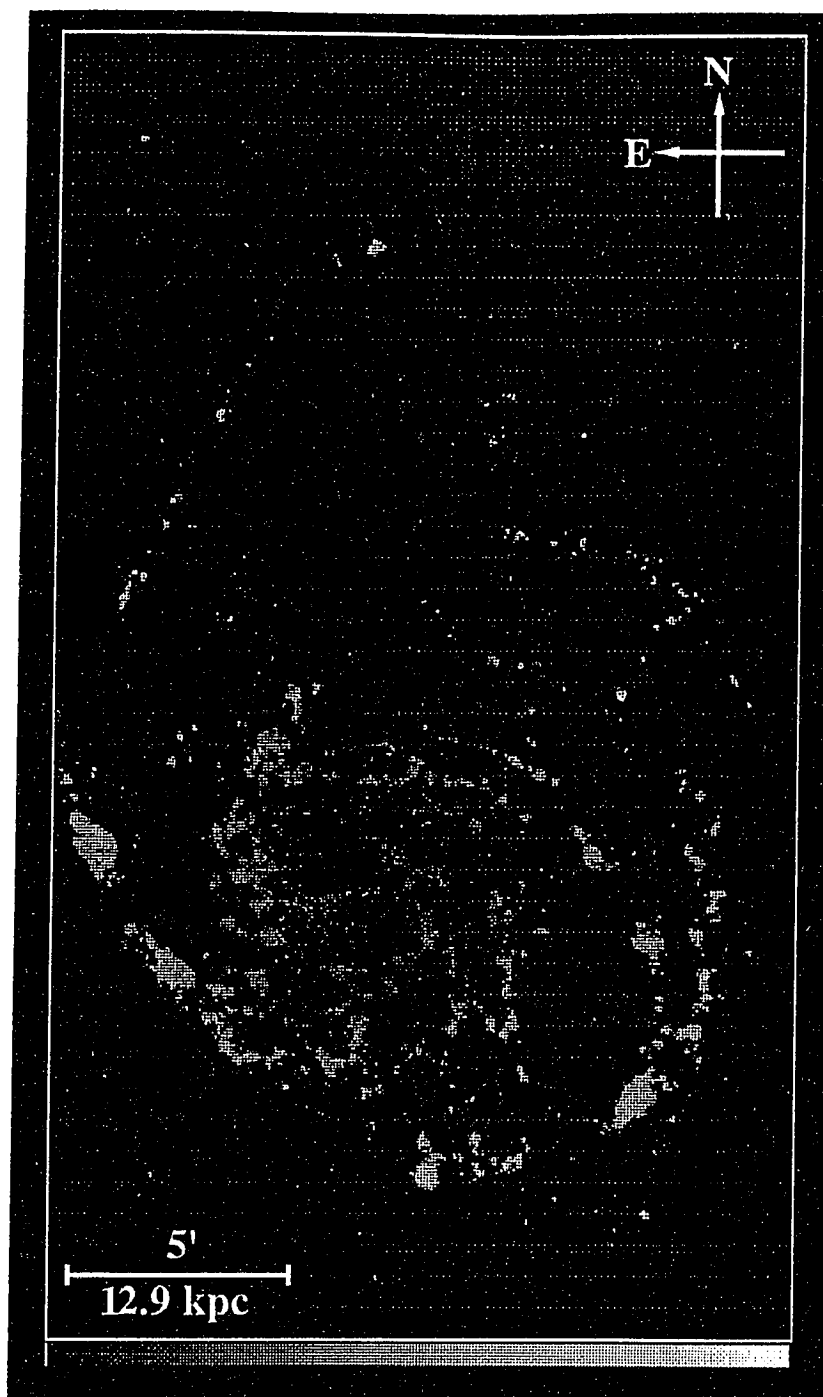


Figure 2.2 Full field gray-scaled image of the logarithm of the direct ratio of [O III] $\lambda 5007$ to H β with the identification mask applied. The threshold used to produce this mask was the lower of the two, set at 2×10^{-16} ergs cm $^{-2}$ sec $^{-1}$ in H α . The image is displayed between the limits -1.0 and 1.2 dex.

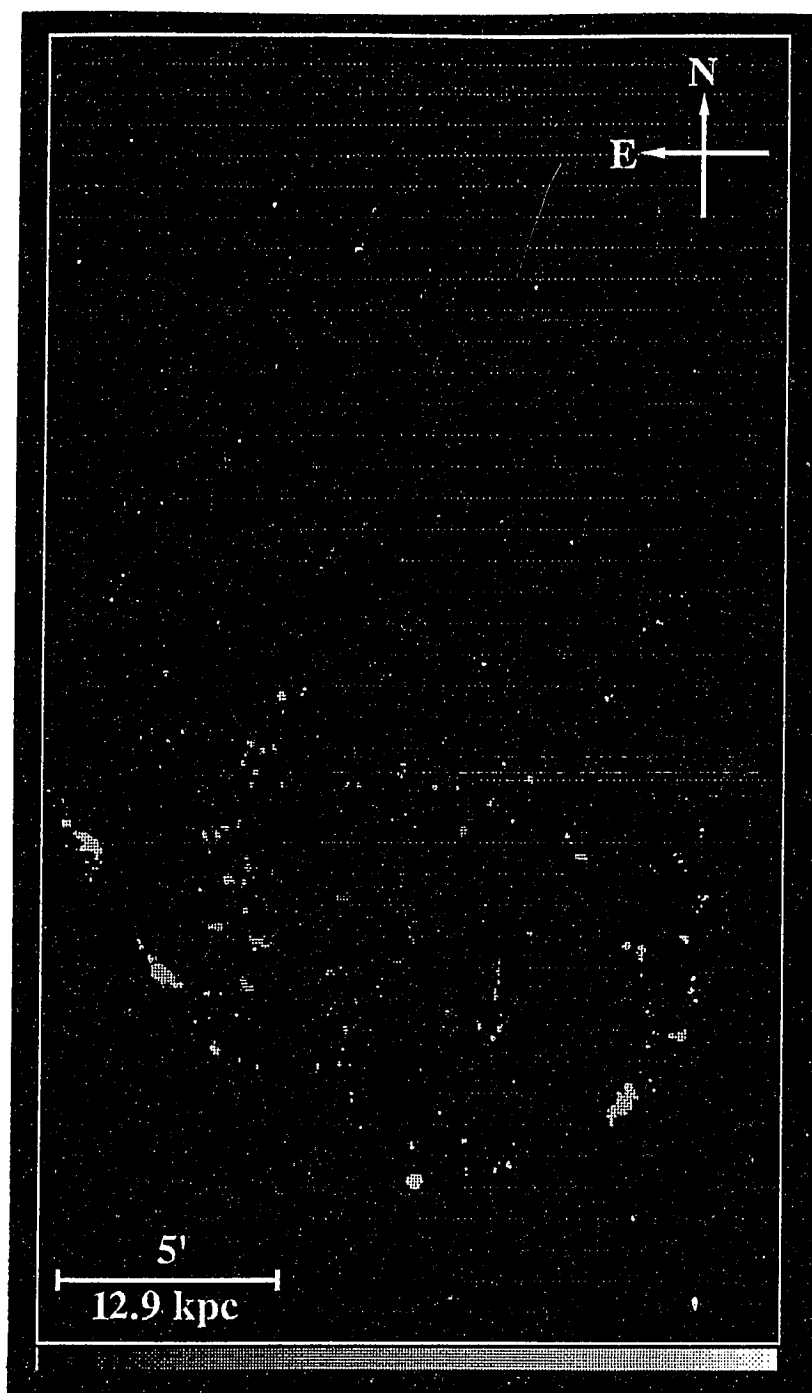


Figure 2.3 The logarithm of the direct ratio of [O III] $\lambda 5007$ to $H \beta$ for each region, displayed using the overall deduced value from the integrated fluxes in each line over the entire area of each region. This highlights the gradients evident in the galaxy. The higher threshold (defined at 1×10^{-15} ergs $\text{cm}^2 \text{sec}^{-1}$ in $H \alpha$) has been used. The display range is slightly different: -1.1 to 0.9 dex.

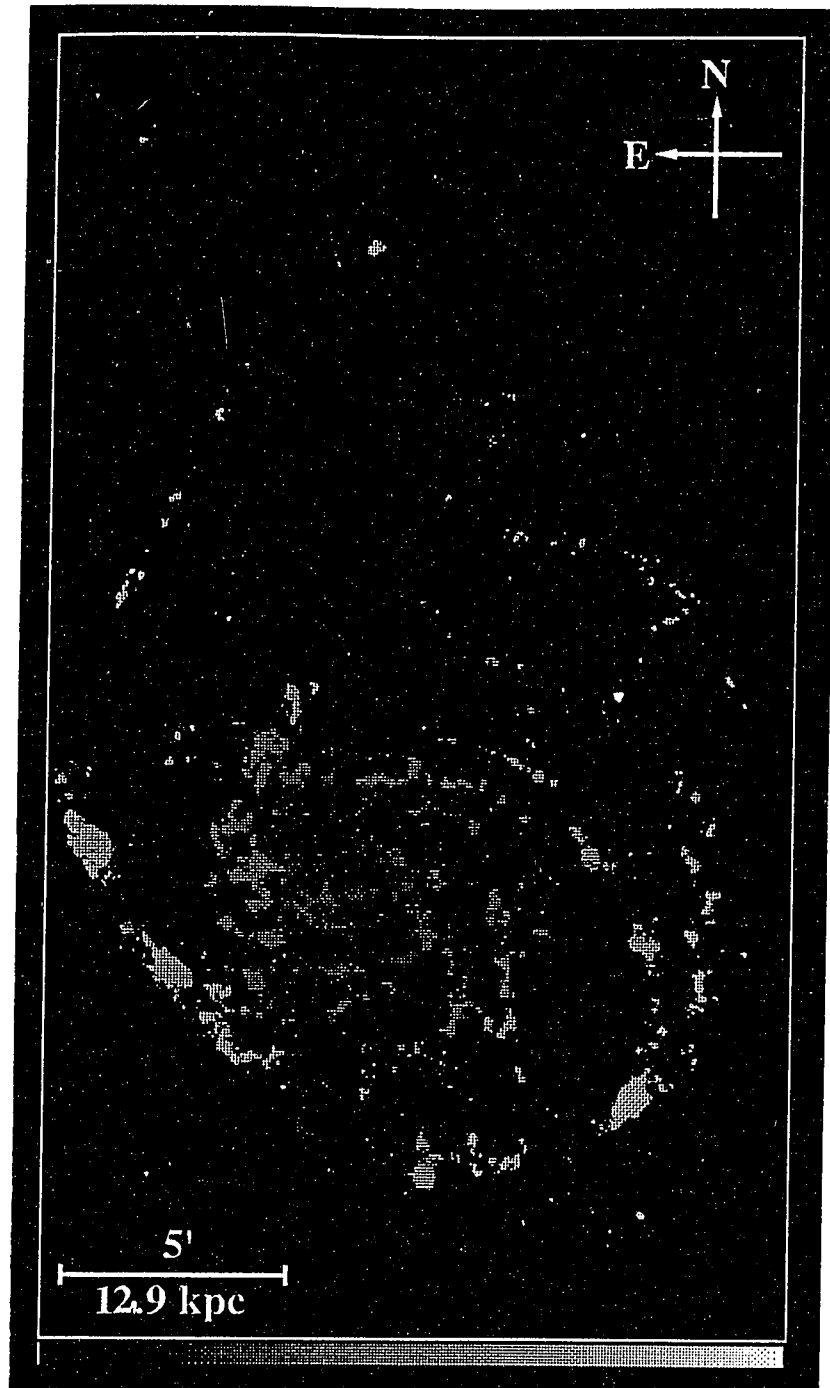


Figure 2.4 The logarithm of the direct ratio of $[\text{O III}] \lambda 5007$ to $\text{H } \beta$ for each region, replacing the entire region with the calculated value, created using the lower threshold. The display range used is -1.1 to 0.9 dex.

similar conclusions were drawn but that the numerical value of many gradients were somewhat smaller than the integrated values.

2.3.2 Reddening as a function of radius

An estimate of the amount of reddening effective along the line of sight to an object may be made using the Balmer decrement. From Osterbrock 1989 (AGN²),

$$\frac{I_\lambda}{I_{H\beta}} = \frac{F_\lambda}{F_{H\beta}} 10^{C_{H\beta} f(\lambda)} \quad (2.1)$$

where we have taken $f(\lambda 4861)=0$. $f(\lambda)$ is related to both the interstellar extinction at wavelength λ , and to the type of star emitting the radiation. $I(\lambda)$ denotes the unreddened intensity, while $F(\lambda)$ denotes the measured intensity. Using the newer values for the extinction curve from Seaton 1979, we get for H α that $f(H \alpha)$ is -0.323, for a typical HII region. Inverting the equation yields:

$$C_{H\beta} = (3.096) \log \frac{F_{H\alpha}}{F_{H\beta}} - (1.413) \quad (2.2)$$

where we have used a value of 2.86 for $I_{H\alpha}/I_{H\beta}$ (assuming case B, $N_e \sim 100$, $T \sim 10000$ K, AGN² Table 4.4). It should be noted here that any gradient in the electron temperature of a region would flatten the derived gradient by this method, overestimating the extinction at small radii and underestimating the reddening in the outer parts of the galaxy. Figure 2.5 is a plot of the region $C(H \beta)$ value as a function of galactocentric radius: (a) for a higher threshold to show the trend for the cores of the regions and (b) with a lower threshold to include the outer full extent of the H II regions.

Belley & Roy 1992 studied two spirals galaxies: NGC 628 and NGC 6946, and reported no evidence for a change in region reddening with radius. However, re-evaluation of their errors suggest to us that trends comparable to what we found in M101 would be lost in their relatively higher noise.

From Figure 2.5(a), a slight trend in reddening is evident with radius for the core data from the H II regions; upon lowering the threshold (and raising the number of identified regions from 248 to 625) a global trend does become apparent, as shown in Figure 2.5(b). In lowering the threshold, the increase in scatter in the values of the ratio cause some non-physical results (ie. $C(H \beta) < 0$). However, such values could be produced by dust scattering blue light preferentially into the line-of-sight. This was discovered by Garnett and Shields 1987, where very low values of $C(H \beta)$ were

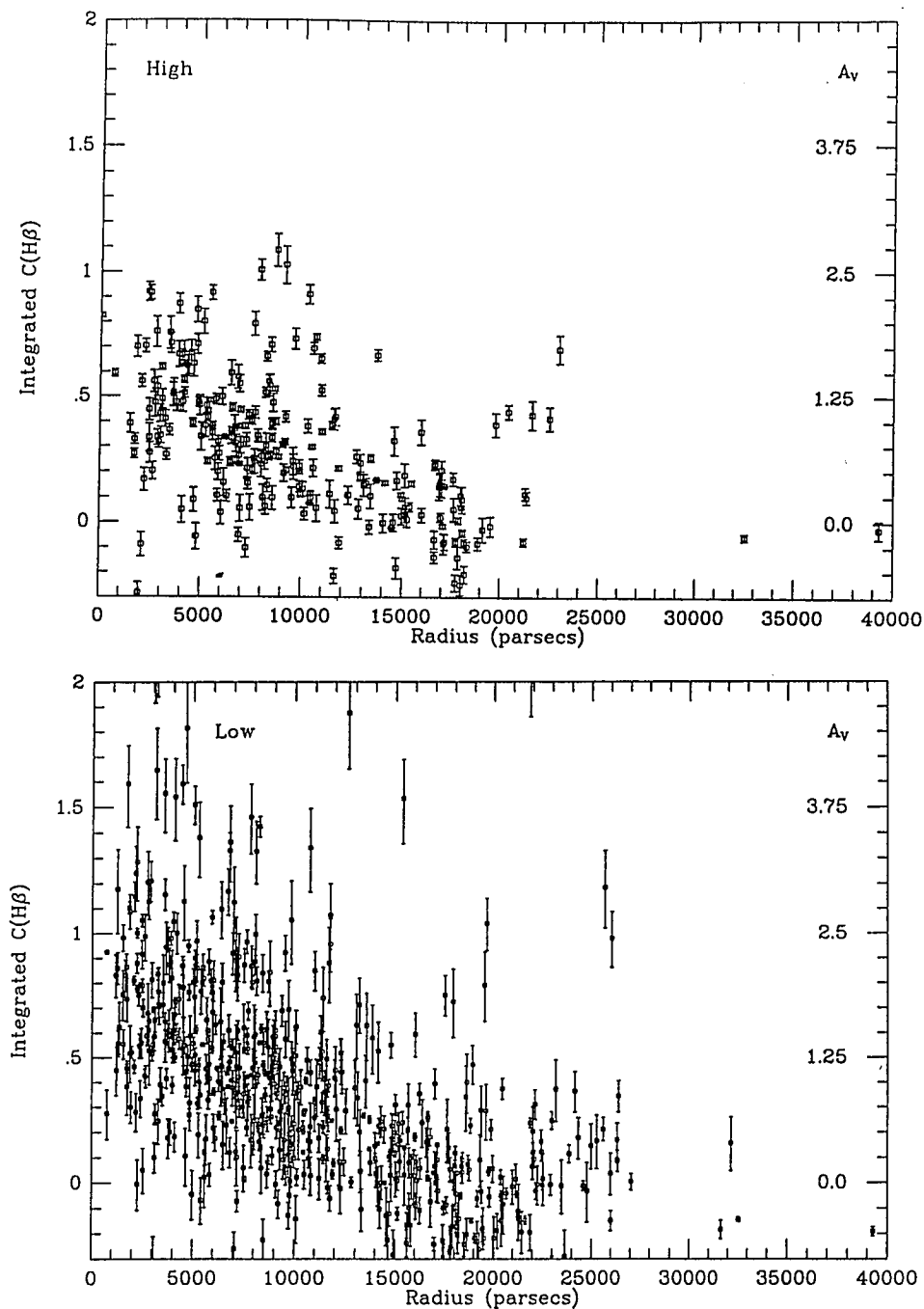


Figure 2.5 (a) Region reddening as a function of radial position. The higher threshold has been used to assemble this data. The equivalent reddening in magnitudes (A_V) is also represented on the right hand axis. A clear increase in reddening towards the galactic center is illustrated. (b) A similar plot except that the lower threshold has been used. Again, a rise in reddening towards the center of the galaxy is observed. The increase in errorbar size is a direct result of the lower fluxes (and lower numbers of photons) sampled by this threshold.

found for several regions in their sample, especially region 7. Our estimates of the line-of-sight reddening are flux weighted, introducing a bias towards the cores of the regions, causing the derivation of typical reddening values about 0.5 magnitude lower than those estimates made by direct radio measurements (Israel et al 1975).

There are notably six or so regions at a radius of 20-25 kpc, in Figure 2.5(a), that have anomalously large values of $C(H\ \beta)$. These regions have been identified through the imagery of the galaxy, and cluster along an arm to the northwest of the nucleus. The higher level of reddening in the regions could indicate a general region of dust between the observer and source. The region locations fall on a ridge of H I emission which is not associated with the dominant spiral pattern of the galaxy at all. Only one region falls on another ridge to the east. Looking at the respective ratios of $[O\ III]/H\ \beta$ and $[S\ II]/H\ \alpha$, we find that these regions appear to match well with the global trend exhibited in that neighborhood of the galaxy. Only the reddening appears anomalous.

This introduces a caveat with any measurement of $C(H\ \beta)$ in extragalactic objects. If there are major environmental variations as a function of position, as implied by our general result, then any statement about azimuthally averaged radial variations in the average level of region reddening may prove impossible and physically unjustifiable.

2.3.3 Excitation and Oxygen Abundance as a Function of Radius

Estimates of the excitation of an H II region may be made using $F([O\ III]\ \lambda 5007)/F(H\ \beta)$. We observe a radial increase in the value of the logarithm of this ratio for each H II region, as shown in Figure 2.6 for both thresholds. The ratio exhibits a large variation across the face of the galaxy: up to three orders of magnitude. As noted earlier, there is no variation in the observed integrated H β emission across the face of the galaxy, but it is the observed brightening of the [O III] emission that causes the ratio to rise.

To be able to make comparisons with most published spectrophotometry and subsequently about the observed variations in the oxygen abundance, it is useful to study the $[O\ III]\ (\lambda 5007 + \lambda 4959)$ ratio with H β . Since we observed only the $\lambda 5007$ line of [O III] it is necessary to include the numerical ratio of 0.35 for the two [O III] lines $[I(\lambda 4959)/I(\lambda\ 5007)]$ resulting from the corresponding atomic transition probabilities (Mendoza 1983); thus our plots of $[O\ III]/H\ \beta$ are $(1.35)F(\lambda 5007)/F(\lambda 4861)$.

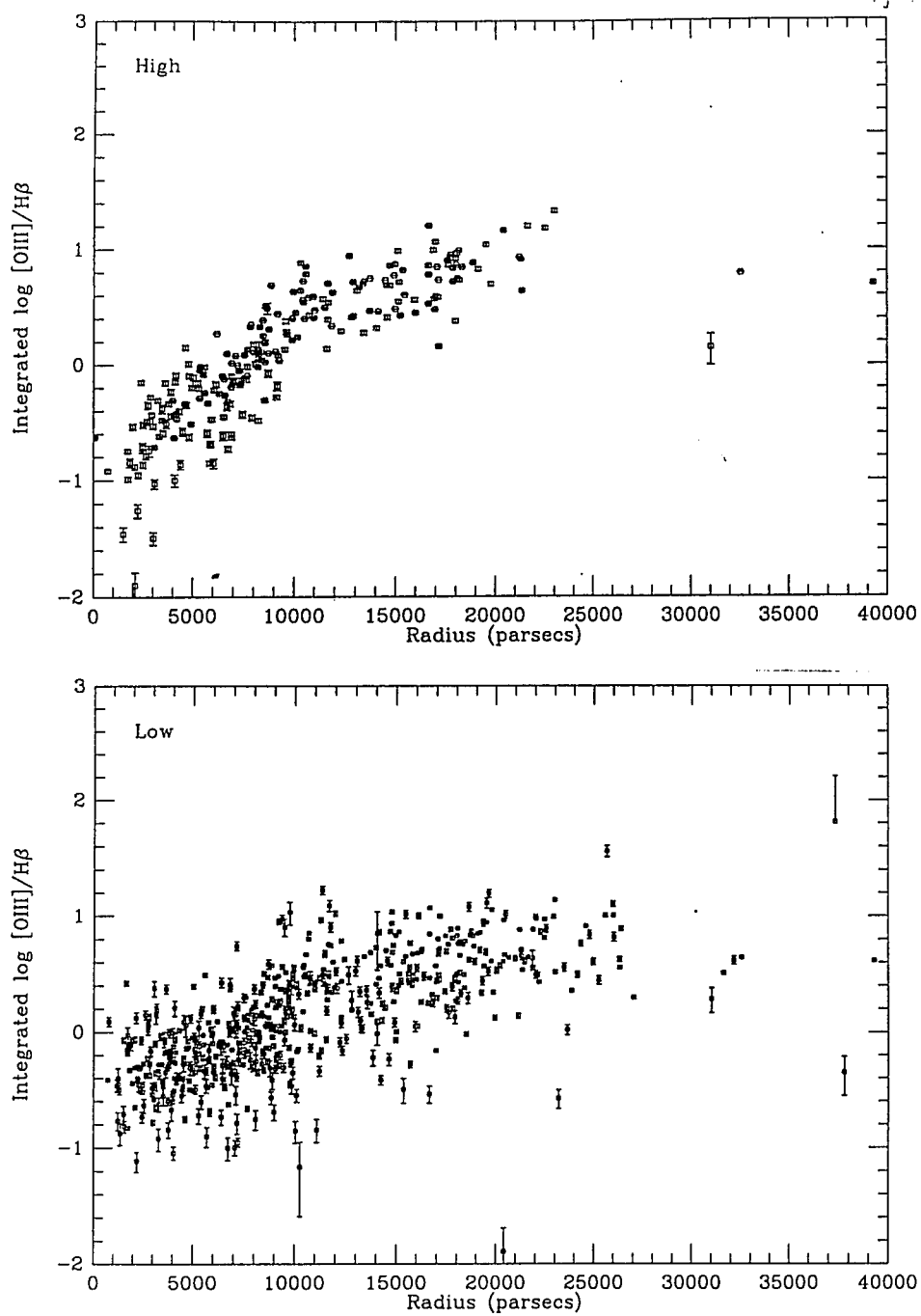


Figure 2.6 (a) The measured excitation of each H II region as a function of its galactocentric radius. The higher threshold has been used. (b) The galactic excitation gradient, calculated using the lower threshold. The increase in the population of H II regions between the two thresholds is well illustrated by these two figures.

Using the empirical calibration between $\log [[\text{O III}]/\text{H } \beta]$ and $(12 + \log \text{O}/\text{H})$ derived by Edmunds & Pagel 1984, it is possible to convert the region excitation values into estimates of the oxygen abundance as a function of radius. This is detailed in Figure 2.7 (a) and (b) for the high and low thresholds respectively. Both show a clear trend, with a definite change in the abundance gradient: becoming steeper at smaller radii; with a transition at $R \sim 11$ kpc (or 5.1 arcminutes) from the nucleus. Caution should be employed using this correlation, since it is non-unique for excitation values greater than 0.5 in the log, with a second lower population of regions that have much lower abundances for a given value of $[\text{O III}]/\text{H } \beta$. A sizeable portion of our population appears to satisfy this condition, but since the population is usually rather small we take the trend to be good for the majority of our sample.

It is possible to fit a linear function to the entire set of data (yielding a value of $\chi^2 \sim 0.049$), but a better fit is achieved by fitting two linear segments to the data (the inner fit giving $\chi^2 \sim 0.030$, and the outer fit giving $\chi^2 \sim 0.182$ where the larger value is partly due to the much lower number of data points), and estimating some interim radius where the two segments meet. When different thresholds are used, the result of the fits change. This is shown in Table 2.3, where we include results for two additional thresholds.

Table 2.3 Derived Oxygen Abundance
Gradients as a Function of Threshold

Threshold*	Intercept [†]	Inner Gradient ^{‡ §}	Outer Gradient [‡]	# Regions
[¶] 1×10^{-14}	9.57 ± 0.28	-0.121 ± 0.035	$+0.012 \pm 0.007$	18
3×10^{-15}	9.48 ± 0.04	-0.106 ± 0.006	-0.025 ± 0.006	64
1×10^{-15}	9.45 ± 0.03	-0.093 ± 0.005	-0.037 ± 0.005	248
2×10^{-16}	9.15 ± 0.03	-0.049 ± 0.003	-0.020 ± 0.003	625

*Thresholds are in units of ($\text{ergs cm}^{-2} \text{ sec}^{-1}$).

[†]Intercepts are units of dex of $[12 + \log(\text{O}/\text{H})]$.

[‡]Gradients are in units of (dex kpc^{-1}).

[§]The inner region is defined as ($r < 11 \text{ kpc}$), visually estimated.

[¶]The numbers of regions identified is a strong function of the threshold used. As a result, only a low number of regions are identified from this threshold providing for a certain amount of caution when considering the derived gradients, but the continuation of the trend is evident.

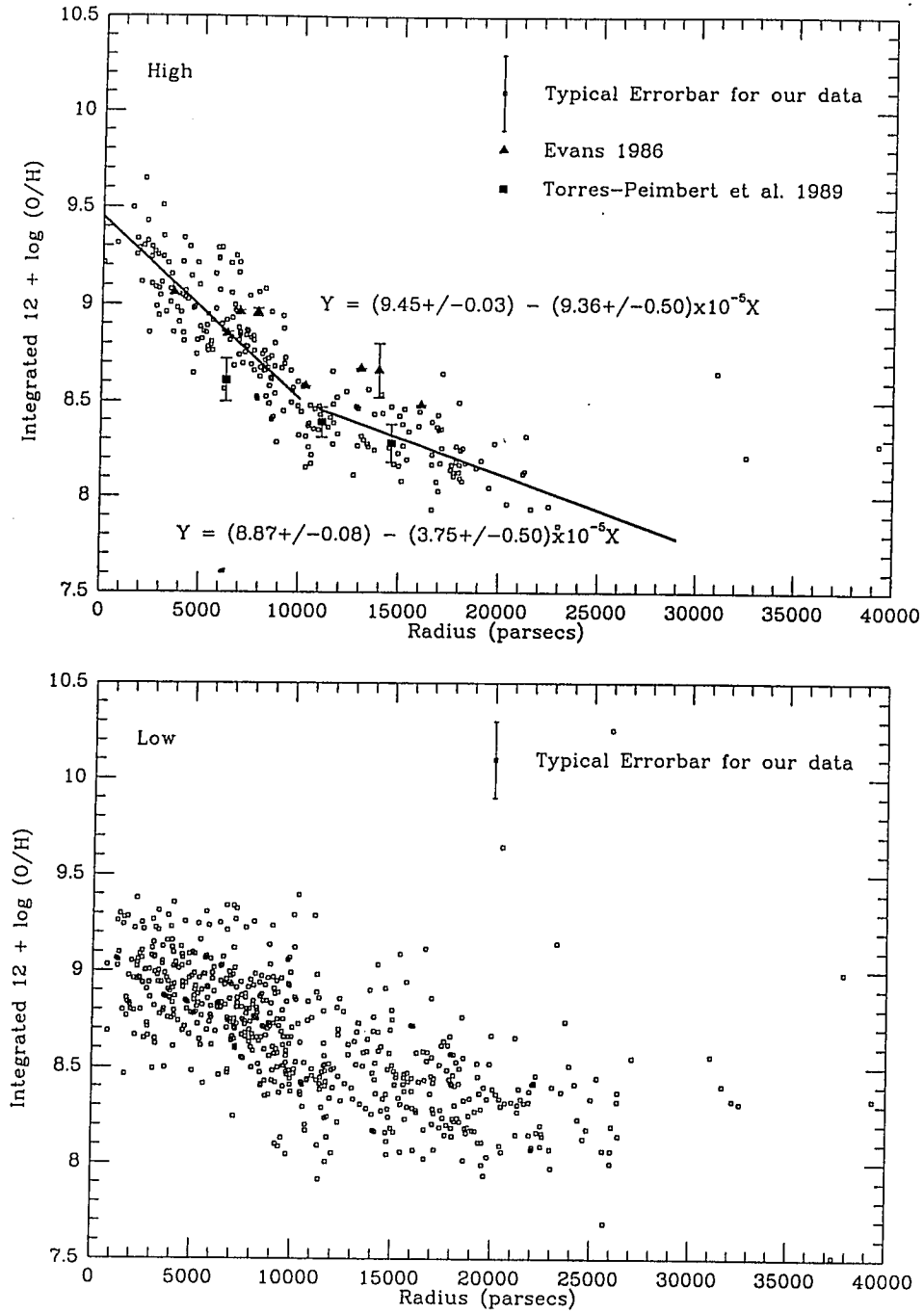


Figure 2.7 (a) Calculation of the corresponding oxygen abundances for each H II region, derived from the correlation presented by Edmunds & Pagel 1984. The higher threshold has been used. (b) Calculation of the oxygen abundance as a function of position, using the lower threshold. The dominant source of error is the spread in the correlation used, about ± 0.2 dex.

2.3.4 Dependence of Excitation on Threshold

The derived inner abundance gradient and central abundance appear to be functions of the threshold used in the calculation, however, caution should be employed in interpreting this result. The high threshold H II regions, in many cases, are the central cores and thus may be expected to be of higher excitation, while the lower threshold would produce regions of lower excitation since this includes their ionization boundaries. Since we do not measure $[\text{OII}]\lambda 3727$ we cannot make a definitive statement about the detailed ionization structure of each region, though most have $[\text{O III}]$ concentrated in their centers, and $[\text{S II}]$ more so around their perimeters, in ratio maps. However, if true, this effect would explain the wide variations in the reported abundance gradients given by many observers.

An interesting result, however, came from simulating standard circular apertures to measure the line emission from each region. Using the coordinates derived from the first analysis, 1", 2" and 4" apertures were centered on each region to derive the line ratio quantities. This is the same method that researchers using devices such as the MX spectrograph might employ to derive their values. The same radial gradients were derived, except that for each calculation a slightly different value was produced due to the loss of a small amount of flux from the aperture for each integration. When calculating abundances from these results, the individual values differed by no more than 0.1 dex from ours. Thus the use of well-centered, circular apertures could reproduce our results, if enough regions were observed. However, the increase in observing time required to do this, even using the MX spectrograph, might be considered prohibitive.

Comparison of the gradients in Table 2.3 with others derived by other workers (eg. Dufour et al. 1980, derived from Shields & Searle 1978), show values that fall between our inner and outer values. Estimates of abundance gradients are not common, and it has been pointed out that the results presented by Dufour et al are now invalid since they were based on H II region models that omitted charge transfer. However, their values serve as an adequate comparison for this purpose.

The earlier gradients were derived by fitting a linear relation to the entire dataset since the available data would not have allowed the detection of a change in gradient. If such an intermediate gradient is taken between our inner and outer values, the result is in the range of $-(0.05-0.06)$ (dex kpc^{-1}), which compares well with the value quoted

for M101 in Table 4 of Dufour et al. 1980 of $-(0.04 \pm 0.01)$ (dex kpc^{-1}) (correcting for the difference in assumed distances to M101).

Consulting another source, Zaritsky et al. 1990 derived a value of (-0.072 ± 0.006) (dex kpc^{-1}) using an assumed distance to M101 of 4.1 Mpc; (-0.040 ± 0.003) (dex kpc^{-1}) when corrected for distance. The latter agreement is comforting since the Zaritsky value was also derived using more modern instrumentation and a larger dataset.

Comparison of our central value of $(12 + \log(\text{O}/\text{H}))$ with Dufour et al. shows good agreement since our values range from 9.2-9.4, and their value was 9.4 ± 0.2 . Further comparison with Zaritsky et al. (although they quote no central abundance) reveals their extrapolated value to be 10.0 ± 0.3 , using only those regions featured in their Table III. This value appears very high, and is probably a result of not including their entire population in the estimate. Furthering our comparisons, we compared the $[\text{O}/\text{H}]$ results for individual regions using data from Evans 1986 and Torres-Peimbert et al. 1989. Only certain regions in Evans' dataset were used due to difficulties locating certain regions in our field. The results of the comparisons are shown in Figure 2.7(a) as well as being detailed in Table 2.4.

We see that our values differ quite markedly from the Evans values, most of ours being below those referenced in his paper. This is to be expected since Evans used a different calibration between the observed $\log [[\text{O III}]/\text{H } \beta]$ and the oxygen abundance (Figure 10 of his Paper II, Dopita & Evans 1986). The two relations merge at excitation ratio values approaching 10, but differ by up to 0.6 dex in $\log(\text{O}/\text{H})$ at levels closer to unity. Despite this, comparison of our Figure 2.7(a) with Figure 1 of Torres-Peimbert et al shows similar results: that their relatively newer calculations of the abundances are lower than Evans. If Evans' abundances are systematically reduced by 0.1 or 0.2 dex then a better match with our data is achieved.

We conclude that a change in the radial abundance gradient is evident in M101, but that *the exact determination of the value of the $[\text{O}/\text{H}]$ gradient is a function of the limiting surface brightness of the study.* By varying the thresholds used, we see that a variation of nearly two orders of magnitude in the threshold will cause an order of magnitude difference in the derived central abundance gradient and a difference of more than 0.4 dex in the estimated central oxygen abundance. This has implications for several recent discussions about the expected nature of any variation in the abundance gradient (Vilchez et al. 1989, Diaz 1989, Zaritsky et al. 1990), since to date most studies of this kind have been based on spectrophotometry that is

Table 2.4 Comparison of Derived [O/H] Values for Specific Regions

Region	This paper	Torres-Peimbert	Evans
NGC 5455 (S10)	8.34 ± 0.20	8.28 ± 0.10	8.66 ± 0.14
NGC 5447	8.34 ± 0.20		8.48
H 47	8.97 ± 0.20		8.96 ± 0.02
NGC 5461	8.46 ± 0.20	8.39 ± 0.08	8.58
S2 (H108+111)	9.26 ± 0.20		9.06 ± 0.01
H 40	8.78 ± 0.20	8.61 ± 0.11	8.85 ± 0.01
NGC 5462	8.33 ± 0.20		8.67
S5	9.06 ± 0.20		8.96 ± 0.01

weighted towards the bright cores of H II regions rather than their entire areas (the latter of which may be more appropriate for both physical reasons and for comparisons with models). Another possibility is that the observed differences in the derived gradients, calculated by this method, may result from a systematic change in the corresponding observed ionization parameter for each region. This type of study will be made in the near future using differing relations between the observed ratio of [O III]/H β and the oxygen abundance, derived theoretically by McGaugh 1991.

The three regions in Figure 2.7(a) that appear at very large radii seem to depart from the global trend. The relation derived between abundance and excitation by Edmunds & Pagel has a duality in the values of $(12 + \log \text{O/H})$ predicted from certain values of [O III]/H β , for $(12 + \log \text{O/H}) \leq 8.0$, or $\log [[\text{O III}]/\text{H } \beta] \geq 0.5$. Comparison of Figure 2.7 with Figures 2.6(a) and (b) shows that two of these outer regions have values of $\log [[\text{O III}]/\text{H } \beta]$ of 0.6-0.8. These regions could be members of the lower “turn around” population evident in Edmund & Pagel’s Figure A1, and that the true value of their abundances are probably closer to 7.7 - 7.8, which agrees with the global trend.

Nonetheless, extrapolation of these results indicate that at very large radii the abundance of the oxygen in M101 is very low, with $(12 + \log (\text{O/H})) \sim 8.0$. However, in the inner regions the abundances are much higher and the gradient is steeper: and this coupled with the overall low ionization levels and the efficient cooling by the heavier ions produce lower [O III]/H β values. The level of excitation in each region is seen to fall off dramatically towards the center of the galaxy, implying a

softening in the mean stellar radiation field. This could result from an increase in the metallicity of the stellar population, since this would cause higher opacities in the stellar atmospheres.

2.3.5 Behavior of the $[\text{S II}]/\text{H } \alpha$ ratio

It is well known that the ratio of $[\text{S II}]/\text{H } \alpha$ is high in areas of shocked gas, and should allow tracing of highly energetic processes across the galaxy. The change in this ratio as a function of radius is illustrated in Figure 2.8(a). At larger radii the ratio is seen to fall off, consistent with the idea that general metal abundance levels are dropping with corresponding increases in overall ionization level. Another interesting trend is that evident at smaller radii, where a clear decrease in the mean $[\text{S II}]/\text{H } \alpha$ ratio occurs at radii interior to about 7kpc. The higher threshold samples purely the region cores and so very little information about the ionization boundaries, where the ratio is the strongest, is included.

The derived ratios from the lower threshold dataset are depicted in Figure 2.8(b). Here, no radial correlation is apparent, although the average level of the ratio is much higher with values ranging up to 1-2 dex. This is consistent with the idea that this lower boundary includes the ionization boundaries and thus raises the region integrated ratios. The lack of correlation is consistent with later results that show that similarly no radial correlation exists between the ionization parameter, the number of ionizing photons or the mean H II region electron density with position.

This ratio can also be used as a possible indicator of the existence and location of supernova remnants (SNR's). In general young SNR's will be small in size but have very large excitations, derivable from the $[\text{O III}]/\text{H } \beta$ ratio. Older SNR's will be large in size, exhibiting arclike or filamentary structure as the bow shock from the explosion encounters obstacles like giant molecular clouds or smaller dense pockets of material. These older regions will exhibit both strong $[\text{O III}]$ and $[\text{S II}]$ emission. However, when considering the distance to M101 we are faced with one immediate difficulty, a SNR the size of the Cygnus Loop (about 100pc) will only occupy 2 pixels on the image. Thus the morphological separation becomes a moot point.

Analysis of the two dimensional variation in the $[\text{S II}]/\text{H } \alpha$ ratio reveals certain correlations which may be of interest. The ratio is apparently highest along the more well defined arms in the outer parts of the optical disk. This area is identified radially by the peak in the ratio seen at around 10 kpc.

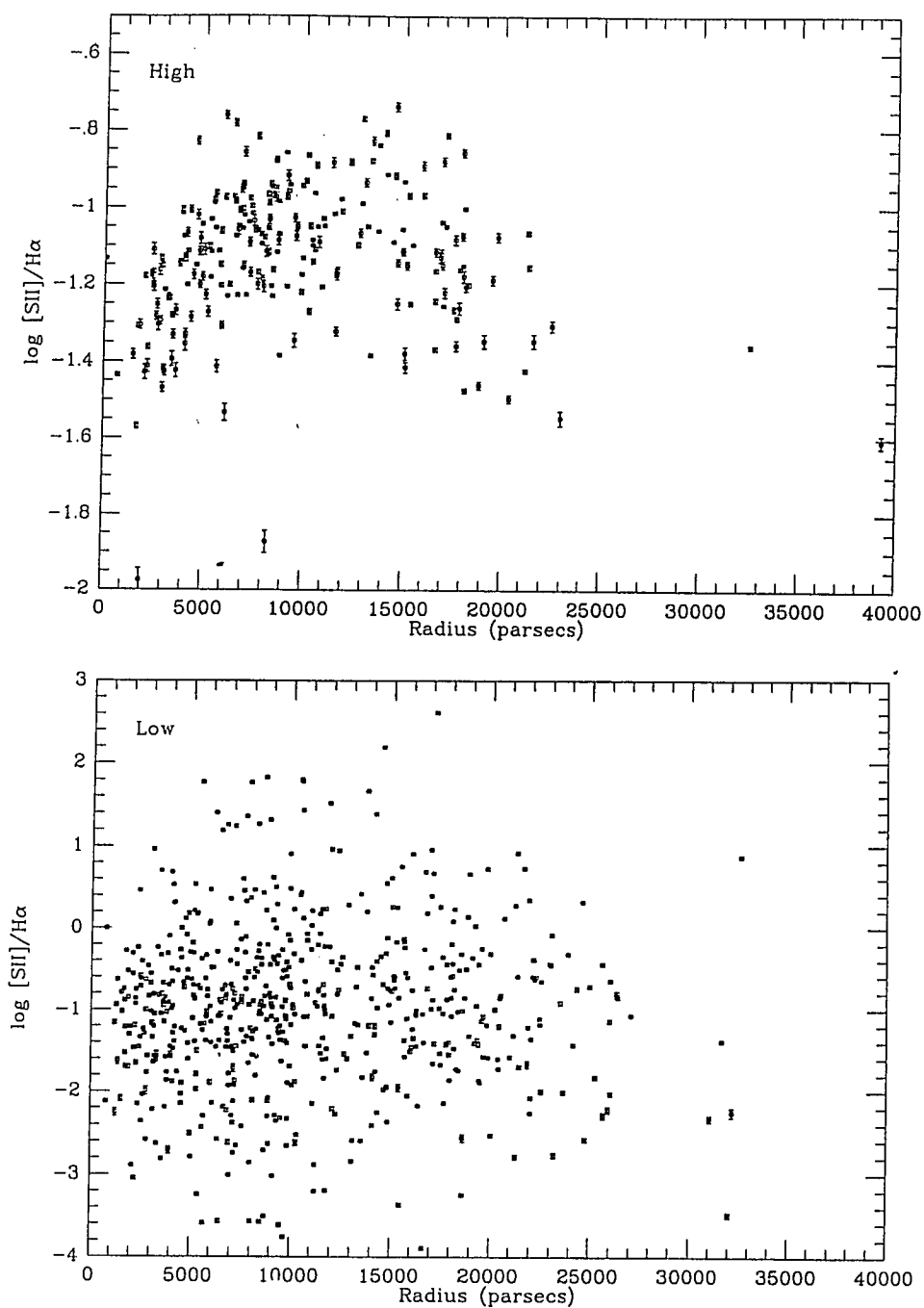


Figure 2.8 (a) Calculated $[S II]/H\alpha$ ratio for each $H II$ region as a function of position, using the high threshold. (b) The variation in the $[S II]/H\alpha$ ratio, calculated using the lower threshold.

The largest superassociations possess the highest ratios indicating the extremely energetic processes at work in those environments. Since, in H II region models, the ratio is maximized near ionization fronts, the ratio is seen to peak within the regions themselves, along the borders. In the inner sections of the galaxy, the overall ratio is much lower, especially along the inner arms that appear to connect the nucleus with the more “grand” arms further out.

There are a few regions which, although not immediately apparent as superassociations like NGC 5447, NGC 5461 and NGC 5462, have similarly high values of the ratio. These regions exist to the northeast of the nucleus, on the outer edge of the most major arm; and almost directly west of the nucleus and directly north of NGC 5447. The exact nature of these, and other, potentially anomalous regions will be the subject of future work.

2.4 Discussion

In this section we will discuss the global variations of physical properties of the H II regions in M101 compared to model expectations derived from other galaxies. After that we will discuss the evident star formation in the galaxy in a broad sense, with respect to current ideas on star formation processes, and in comparison with results from studies of other galaxies.

2.4.1 The H II Region Luminosity Function

Due to the large number of H II regions measured by our study, it is possible to assemble a detailed Luminosity Function (LF) for the H II region population in M101. By calculating a differential LF, it is possible to study any selection effects that may be present in our sample. The LF's derived for both the high and low thresholds used in this paper are shown in Figure 2.9.

A more general treatment of this method of analysis for spiral galaxies was presented by Kennicutt et al. 1989. Direct comparison of our LF for M101 with theirs (their Figure 3) reveals very similar results.

For our higher threshold, the slope of the LF monotonically decreases with luminosity, exhibiting a low-luminosity cut-off at a luminosity of 2.5×10^{37} ergs s^{-1} . For reference, the integrated luminosity of the Orion Nebula may be estimated to be 1×10^{37} ergs s^{-1} . The upper threshold, however, begins to flatten out at a luminosity of 1×10^{38} ergs s^{-1} , and then turns over at 1×10^{37} ergs s^{-1} . At lower luminosities a drop in population is evident. The ultimate cut-off occurs at 4×10^{36} ergs s^{-1} , which is more than a factor of two below the Orion luminosity.

This type of study normally suffers from two major sources of incompleteness; (i) the non-detection of the faintest H II regions, and (ii) the failure to separate individual H II regions from their nearest neighbors. The first effect should result in a turnover in the observed LF, while the second problem (which should also produce a turnover in the LF, and which was specifically investigated by Kennicutt et al.) is only important when the limiting spatial resolution of the study approaches 200-300 pc.

At the distance used for our study (7.4 Mpc), the second effect may be safely ignored (1 pixel = 1.2 arcseconds = 43 pc). However, by virtue of our low detectivity levels, the first effect could have an appreciable impact on our sample. Clearly, by setting an upper threshold we deliberately circumvent the problem for that sample,

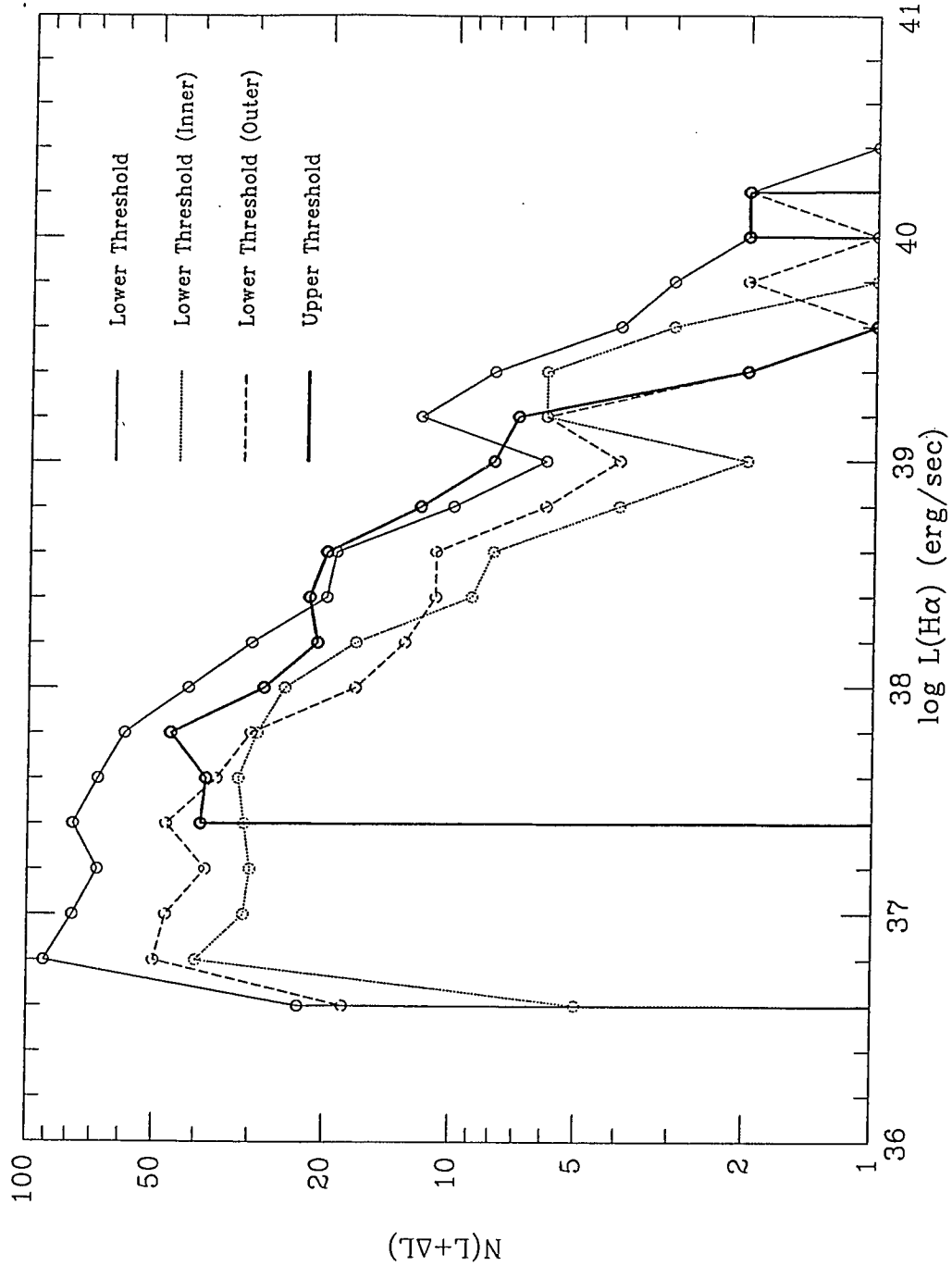


Figure 2.9 Derived differential luminosity functions for the H II region population resulting from application of the the two thresholds. The derived inner and outer LF's are also represented; the boundary being at a radius of 8.6 kpc (the radius at which the excitation gradient appears to suddenly increase).

as evident by the lack of turnover for that curve in Figure 2.9. However, at the lower threshold, the effects of the incompleteness in the sample due to our limiting luminosity become evident.

It is interesting to note, though, the magnitude of the limiting luminosity for the lower threshold. In their study, Kennicutt et al. stated that for galaxies closer than 15 Mpc it was statistically prudent to limit the population under study to those regions whose integrated luminosity was greater than 10^{37} ergs s⁻¹. Taking the pessimistic view that all regions whose luminosities are below this limit are subject to incompleteness, and applying this criterion, we find that better than 80% of our sample may be taken to be free of selection effects arising from any limiting luminosity problem.

However, at such low luminosity levels, a turnover of some form is to be expected due to the change in the specific physical nature of such H II regions. The physical size of such regions also has to be considered here. The Orion Nebula (if taken to be typical of that luminosity class of H II region) is only 5-6 pc across. Clearly our study will not be able to resolve such objects in M101. Thus the turnover evident at low luminosities in Figure 2.9 could be viewed as incompleteness due not to a limiting luminosity, but to a limiting spatial resolution. (Our selection criterion required at least 4 contiguous pixels).

The LF for the lower threshold apparently reproduces an enhancement in the H II region population at luminosities greater than 1.5×10^{39} ergs s⁻¹, originally shown in Figure 3 of Kennicutt et al. The source of this enhancement may be argued to be both the presence of the giant H II regions that are very evident towards the outer edge of the optical disk, and those regions that have a low surface brightness but large surface areas. If this additive population is removed, the underlying population may be fit to the common solution of a powerlaw of the form:

$$N(L) = AL^a dL \quad (2.3)$$

with an index a of (-1.85 ± 0.05) . The additional population appears to obey the same powerlaw, but with a slightly different normalization. This number compares to that derived by Kennicutt of (-2.1 ± 0.2) , using all of the data in a single fit, without removing the additional population.

2.4.2 The Ionization Parameter, U

In the recent past (Evans 1986, Campbell 1988, and Diaz et al. 1991) it has been reported that the ionization parameter U exhibits a systematic variation with H II region metallicity. These results have been primarily based on results from photoionization modelling. As a verification of this result, it is possible to make observational estimates of the U parameter from the H β luminosity displayed by each H II region, and then to compare this with the known metallicity for each region.

An estimate of U is best made from counting the Lyman Continuum photons from the Balmer Lines (either H α or H β), and from estimating the rms electron density from the H β surface brightness by way of an emission measure.

The number of ionizing photons contained within any given H II region may be calculated from (Osterbrock 1989 (AGN²), p.146):

$$Q_{\text{LyC}} = \int_{\nu_0}^{\infty} \left(\frac{L_{\nu}}{h\nu} \right) d\nu = \left[\frac{\alpha_{H\beta}^{\text{eff}}}{\alpha_B} \right] \frac{L_{H\beta}}{h\nu_{H\beta}} \quad (2.4)$$

where $L_{H\beta}$ is the observed luminosity of H β photons integrated over the entire apparent surface of the region (in units of ergs sec⁻¹). A typical effective temperature for an H II region would be 10000 K, and if case B conditions are assumed, then the following recombination coefficients are applicable:

$$\begin{aligned} \alpha_B &= 2.59 \times 10^{-13} \text{ cm}^3 \text{ sec}^{-1} \\ \alpha_{H\beta}^{\text{eff}} &= 3.03 \times 10^{-14} \text{ cm}^3 \text{ sec}^{-1} \\ \alpha_{H\alpha}^{\text{eff}} &= 8.64 \times 10^{-14} \text{ cm}^3 \text{ sec}^{-1} \end{aligned}$$

Defining R to be the value of the ratio of the effective recombination coefficient of a given line to the total recombination coefficient for the atom, this implies that:

$$R(\text{H } \beta) = 0.117$$

$$R(\text{H } \alpha) = 0.333$$

An estimate of the rms electron density in an H II region may be made using the emission measure, which may be derived from the observed integrated H β surface brightness $I_{H\beta}$ (in units of ergs sec⁻¹ cm⁻² Sr⁻¹). AGN² lists simple formulae for the surface brightness of either H α or H β (p.153). Applying the simplifying assumption of a pure hydrogen nebula, charge neutrality ($N_i = N_e$), a filling factor of unity and by assuming a spherical nebula we can reduce the path integral to the physical extent of the nebula along the line of sight, D , to give:

$$N_e^2 = \left[\frac{4\pi I_{H\beta}}{h\nu_{H\beta} \alpha_{H\beta}^{\text{eff}}} \right] \left(\frac{1}{D} \right) \quad (2.5)$$

Combining these two results allows calculation of the value of U for any of the regions observed:

$$U = \frac{Q_{LyC}}{4\pi R_s^2 N_e c} \quad (2.6)$$

where Q_{LyC} is the number of Lyman Continuum photons calculated above, R_s is the Strömgren Radius, N_e is the rms electron density, c is the speed of light. The Strömgren Radius is given by:

$$R_s = \left(\frac{3Q_{LyC}}{4\pi} \frac{1}{N_e^2 \alpha_B} \right)^{\frac{1}{3}} \quad (2.7)$$

In Figure 2.10(a) we plot the results of comparing $\log U$ versus O/H , no variation is evident. This result contradicts earlier claims that U is a function of metallicity. Reasons for the discrepancy might originate from the complex reality of H II regions compared to the simplified representation of models.

The use of a filling factor of close to unity is a major assumption. The ionization parameter derived is roughly proportional to the filling factor used in the calculation, when introduced by way of the equations on p.166 of AGN² ($\epsilon^{1.17}$). Thus any strong functional dependence of U on position or another quantity may be somewhat hidden by a random variation of filling factor from region to region. Since we had no way to measure this value directly the assumption of a constant filling factor had to be made.

It might also be argued that a temperature of 10000 K is rather high for typical H II regions. Taking the extreme case of 5000 K from AGN², a temperature difference of this size would cause little or no change in either Q_{LyC} or R_s , a reduction in N_e of 25%, and an increase in U of at most 40%. These are upper limits on the possible effect of a variation in temperature, which would not cause enough of a change in the graphs of Figure 2.10 to recover any gradient.

This observational determination of U for an ensemble of H II regions for a given galactic system is the first of its kind. Indeed it is apparent that a mean value of U will hold for the majority of the H II region population, indicating that the nature of the predicted variations from the modelling may have been exaggerated. Since we have demonstrated that measurable estimates of U are possible, they should be used as input variables rather than results calculated by the models.

In the course of the calculation, we made estimates of the numbers of ionizing photons in each region. This quantity is compared to other physical characteristics

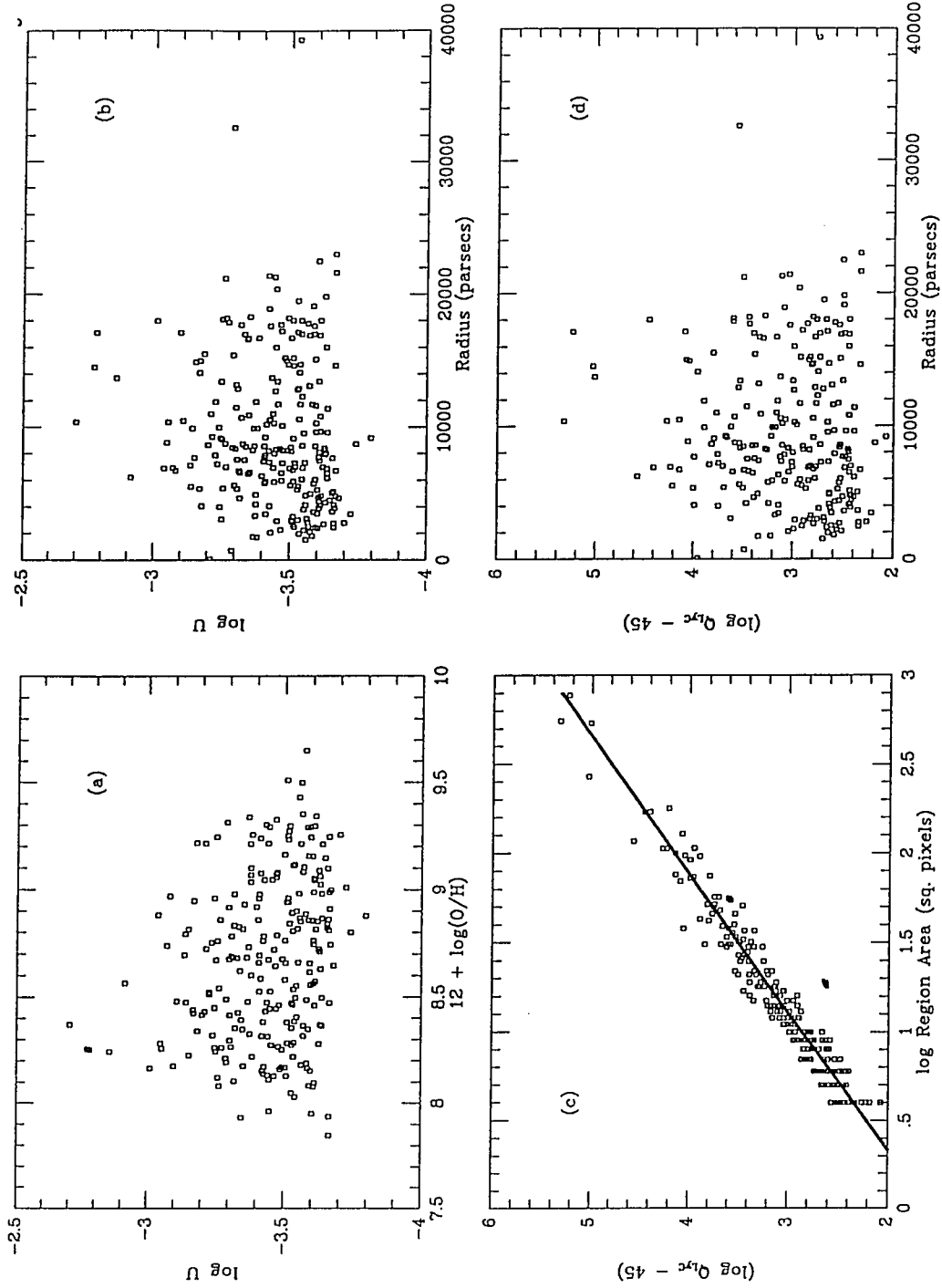


Figure 2.10 In all calculations the higher threshold has been used. (a) Plot of the ionization parameter, $\log U$, against oxygen abundance. (b) Plot of $\log U$ versus radial position. (c) Plot of Q_{LyC} against the logarithm of the apparent size of each region in square pixels (1 pixel = 43 pc). (d) Plot of Q_{LyC} against radial position.

of the H II regions, along with U, in Figures 2.10(b), (c) and (d). It is apparent from these figures that most regions have similar levels of ionizing radiation. A few exceptions exist, and it may be safely assumed that these are the superassociations that dominate the appearance of the galaxy. The mean level of the ionizing radiation is 10^{48} photons s^{-1} , which is equivalent to an ensemble of late O or early B stars numbering between 1 and 15 (AGN² Table 2.3 p.22). Only very few regions have radiation levels high enough for a population of early O stars to be responsible for the emission observed.

We see that no correlation exists between the value of U for a region and the position of that region in the galaxy. Similarly, no positional correlation exists for the number of ionizing photons integrated over the surface area of any given region. However, a very well defined correlation does exist between Q_{LyC} and the apparent region area A, since Q_{LyC} is proportional to the integrated luminosity. The correlation evident in Figure 2.10(c) may be fit as,

$$\log Q_{LyC} = (1.29 \pm 0.03)\log A + (1.57 \pm 0.03), \quad (2.8)$$

which implies that the derived number of ionizing photons for any given region is approximately proportional to the apparent surface area to the power 1.3. This does not appear to be an artifact of the calculation, since that particular part allows only a linear proportion between the two quantities.

2.4.3 Star Formation

One of the most fundamental questions that can be addressed by observations of other galaxies is what defines the nature of the star formation process? The process itself is clearly very complicated and affected by many different physical parameters. However, to at least gain some feel for what the most important factors are, one can make some simplifying assumptions about any galactic environment and compare the resulting predictions with what is observed.

Star Formation Efficiency

The star formation efficiency (SFE) can be defined in several terms. For this study we shall use the more observationally oriented definition that the SFE is given by the ratio of the observed surface brightness of H α to the observed gas surface density. The flux from H α may be taken to be a good indicator of new star formation, since

the contribution to this line from massive stars such as OB stars will be dominant (Kennicutt and Kent 1983). The estimates of the amounts of neutral material available for star formation can be made through 21cm measurements (atomic hydrogen) and submillimeter CO radiation (molecular hydrogen, through a correlation between the two).

One note that should be added here is that the measurement of the star formation rate (SFR) by $H\alpha$ also has several disadvantages. This technique traces only the most massive stars, so an assumed IMF has to be used to gain an estimate of the SFR locally; the emission also suffers from extinction, making the estimate of the SFR a lower limit.

Kennicutt 1989 reintroduced the earlier model by Quirk 1972 that the observed distribution of star formation sites within a galaxy, especially late-type spirals, may be explained in terms of an instability criterion. This criterion is established by the relative value of the local gas density to a critical density, defined by a simple Toomre model of a thin gaseous disk embedded in a massive stellar disk (Toomre 1964).

$$\Sigma_c = \alpha \left(\frac{\kappa c}{3.36G} \right) \quad (2.9)$$

This critical density is a function of the local velocity dispersion of the gas c , the epicyclic frequency of the galaxy at that radius κ , and a stability index α . This latter quantity is an unknown, and is usually determined from the observable quantities: in this case the galactic rotation curve, and the gas velocity dispersion. Since:

$$\kappa = 1.41 \frac{V}{R} \left(1 + \frac{R}{V} \frac{dV}{dR} \right)^{\frac{1}{2}} \quad (2.10)$$

this quantity is easily calculable. For most systems a fairly constant velocity dispersion across the optical disk is a good assumption. Thus, the estimation of the stability index comes from assuming that the observed edge of the optical disk marks the radius where the gas surface density equals the critical density. Such estimates of the value of the stability index for M101 and other galaxies were made by Kennicutt 1989. He found that most of the late-type spirals had stellar disks whose edge was marked by a stability index of 0.67.

To analyze the dependence of the SFR on the local gas surface density, Kennicutt plotted the observed surface brightness of $H\alpha$ against the derived total surface density of neutral gas. On such a plot, three areas of interest become apparent. At a high surface density in neutral gas, there appears to be a well behaved relation between

the two quantities obeying a Schmidt Law (that is a function of the form $A \propto B^N$) of index $N=1.3$. At low surface densities, the SFR is very small and this area may be identified physically as the outer edge of the star forming disk. In between there is a transition region, where the functionality of the SFR appears much steeper with increasing surface density; where a much higher index would be appropriate.

To be rigorous, a study of the available mass surface density for star formation should also include the mass component from the stellar population, since this will contribute to the kinematic stability of any given area of the galactic disk. However, to make estimates of the stellar mass component several additional pieces of observational data are needed; information that we do not have available to us at this time.

Kennicutt hypothesized that this star formation law should be observed to move with radial position, and that point-by-point measurements of the SFR would reveal the applicability of this model, and define the limitations of the approach. To do just this, we endeavored to collect a set of data similar to Kennicutt's but with an emphasis on preserving the two-dimensional aspect of the analysis, to avoid the azimuthal averaging that has been implicit in most previous work on this subject.

Distribution of H I

Atomic hydrogen is best traced by the radio emission of the 21cm line. The problem with observing objects at this wavelength is that to get decent resolution very large telescopes (or complicated aperture synthesis techniques) have to be employed. However, the modern network of available radio telescopes allows for much better resolution than was available ten years ago.

The best available 21cm data taken for M101 comes from the short paper by van der Hulst and Sancisi 1988, where they publish their column density results in two forms: as a greyscale image and as a contour map. The greyscale image was reproduced and calibrated in units of number of particles per cm^2 using their published contour levels. The resolution of their study was defined by their beamwidth: $80'' \times 80''$.

Since we had no access to the original data, we scanned their Figure 1 using a flatbed scanner attached to a Macintosh, importing the resulting image into IRAF for further processing. The granularity in the printing process was removed by deconvolving the regular pattern out of the image to leave a good representation of

the original, with a little underlying false structure. To complete the reproduction, a gaussian transmission profile, emulating the beamwidth of the telescope used, was convolved with the image, effectively removing the false structure.

A commonly seen feature of spiral galaxy atomic hydrogen distributions is the central “hole” in the emission, surrounded by the intense ridges of gas that mark the most probable areas of star formation. This is well displayed by Figure 2.11, where the atomic hydrogen has been countoured on top of the $H\alpha$ emission to show the coincidence of the $H\text{ II}$ regions (marking new sites of star formation) and the ridges of neutral gas.

Distribution of H_2

The total CO luminosity received from a galaxy is directly proportional to the mass of molecular clouds in that galaxy (Young and Scoville 1991). The line most used for this tracing is the 2.6 mm line. CO is used to trace the amount of molecular hydrogen, H_2 , since a relation between the measured antenna temperature in CO and the total cloud mass (mostly H_2) may be derived (Young and Scoville 1991):

$$M_{cloud} = L_{CO} \sqrt{\frac{4\rho}{3\pi G T_{CO}}} \frac{1}{T_{CO}} \quad (2.11)$$

The ratio $\sqrt{\rho}/T_{CO}$ is not seen to vary very much at all from galaxy to galaxy, so this relation is taken to be a reliable measure of the molecular mass in any given system of interest. The technique of correlating CO emission to the amount of H_2 gas present has been studied extensively (Sanders et al. 1984, Young et al. 1986, Elmegreen 1989, Devereux and Young 1990).

The major problem with this approach is the empirical determination of the constant of proportionality between the two quantities. Various techniques exist to estimate the quantity (see the review by Young and Scoville 1991), but a typical number used in the literature is:

$$\frac{N(H_2)}{I_{CO}} = 3.0 \times 10^{20} \text{ cm}^{-2} \left[K(T_R^*) \text{ km sec}^{-1} \right]^{-1} \quad (2.12)$$

Absolute accuracy of the method is hard to test. One good method is to use the observations made by IRAS of the same galaxies, and use the warm dust masses derived from the IR emission. This reveals that estimates made using this technique are accurate to 30%.

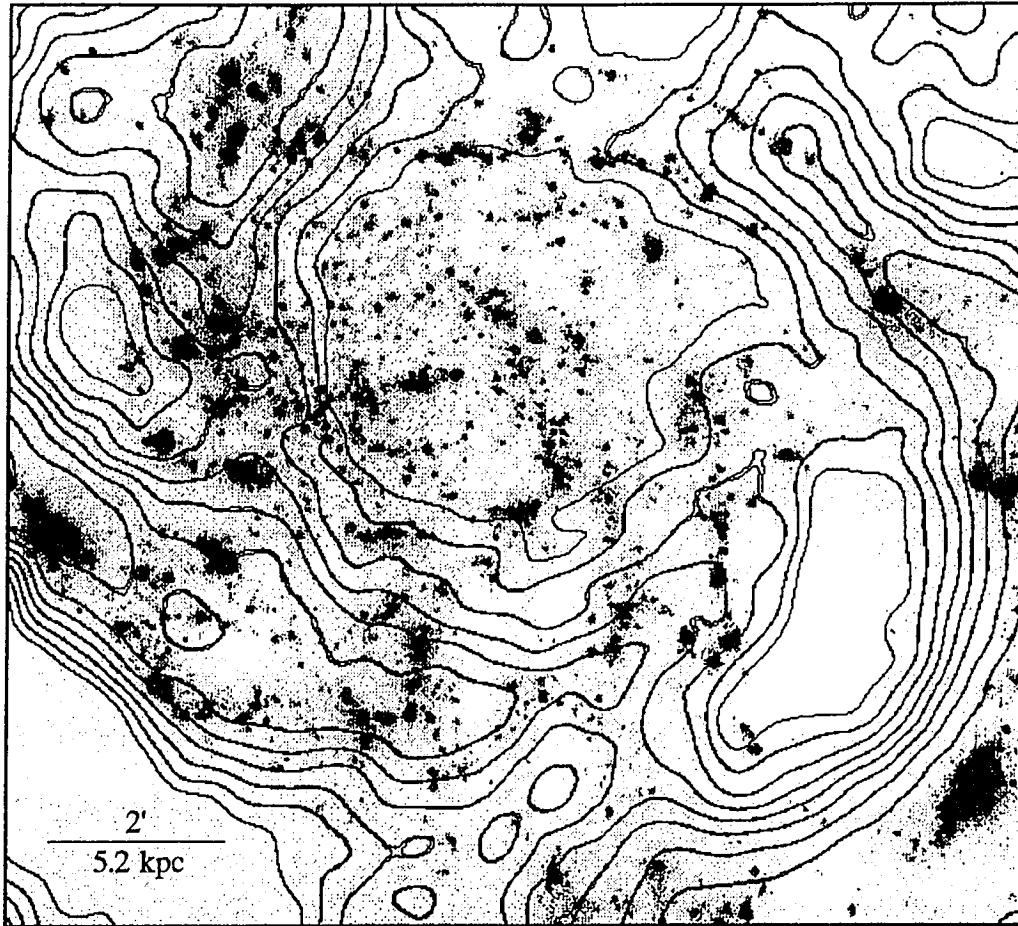


Figure 2.11 Contours of constant atomic hydrogen mass surface density overlaid onto our H α imagery. Note that the H I ridges coincide with those arms where areas of active star formation are visible, indicating that the two phenomena could have a common origin. The H α image is linear and displayed between 0 and 10^{-15} ergs cm $^{-2}$ sec $^{-1}$; the H I image is contoured at 10 equally spaced levels between 7 and 12 M $_{\odot}$ pc $^{-2}$.

Kenney et al 1991 published derived H_2 column density measurements for the inner 5 arcminutes of M101, calculated from the observed CO antenna temperatures. Unfortunately, they only published the result as a contour map and a table of positions, requiring us to reconstruct the image by hand. The reconstruction of the image was carried out by using the observed temperatures as a function of position from their Table 1. This process caused edge effects to be introduced, a result of the dataset being of finite extent, which had to be removed before proceeding. The resulting image was checked by reproducing an intensity contour map to allow direct comparison with the original published form. Again the original imagery was calibrated in units of numbers of particles per cm^2 , and we applied the same calibration to our reconstruction. The beamwidth of this study was $55''$.

Examination of the resultant image reveals the characteristic morphology of an H_2 distribution: that the emission rises to a central peak that contrasts the distribution seen at larger radii. This, of course, differs from the H I distribution, which is seen to exhibit a drop in surface brightness towards the center. The ratio of the two is seen to vary from 2.5 in the central regions to 0.3 in the outer disk (molecular to atomic).

Comparison of a contour map of the molecular emission to the $H\alpha$ surface brightness indicates that the molecular arm structures lag the new star formation. This fact was well established for M51 by Rand and Kulkarni 1990 with their much higher resolution of $7''$. This is indicative of the picture put forward by Young and Scoville 1991 that pre-existing giant molecular clouds enter the arm from behind, are compressed by some mechanism to produce a burst of OB star formation, which dissociate the molecular gas to produce the $H\alpha$ ridge downstream from the molecular arm. This should also produce a coincidence of the H I and $H\alpha$ emission, a phenomenon which is seen in Figure 2.11.

Distribution of Neutral Hydrogen

Since the 21cm study had the most coarse resolution the resulting H_2 image had to be convolved with a gaussian of the appropriate width to allow the two images to be combined. After calibration, the images were co-added to give a surface brightness map of the available mass of neutral Hydrogen in M101 as a function of position.

The paucity of emission from the atomic gas in the central regions is more than made up by the molecular emission, where the molecular gas bar structure reported by Kenney et al. 1991 dominates the neutral gas. Variations in the ratio of molecular

to atomic gas indicate changes in the efficiency of the of molecular cloud formation, or conversely of their destruction.

Distribution of Ionized and Neutral Hydrogen

As indicated earlier, $H\alpha$ emission may be used as a tracer of new star formation. The required imagery being already available, a gaussian of width $80''$ was convolved with the imagery to match the resolution of the gas data derived above. The apparent amount of star formation as a function of position within M101 may be estimated using this type of imagery. Comparison with the neutral hydrogen maps allows estimates of the efficiency of the star formation process and how, if at all, the efficiency varies as function of position. This is done explicitly by dividing the two to give Figure 2.12.

This method is the two-dimensional analog of Figure 8 of Kennicutt 1989, a very commonly referenced source for information concerning the variation of the star formation process with observed gas surface density. It is clear from a cursory glance at Figure 2.12 that the assumption of azimuthal symmetry would seem an oversimplification. Reconstruction of Kennicutt's figure from this image produces more detail about the functionality of the "efficiency" of the star formation with available gas mass. Further study of the plot, shown in Figure 2.13, in conjunction with the image that generated it, shows that certain distinct areas on the graph represent separate physical areas within the galaxy's structure.

Variations in the Observed Star Formation Law

Application of this imagery to the radial variation in the observed star formation law results in some interesting results. In accordance with Kennicutt's expectations there is an observed change in the mean local density of neutral gas with radius indicating a systematic increase in the critical density for local collapse.

The observed results are detailed in Figure 2.13. Here the star formation law (SFL) is shown after being calculated by averaging the data into 12 arcsecond square bins, and summed azimuthally into radial bins 5kpc wide. It may be seen that overall, if all annuli were coadded, the original shape identified by Kennicutt would be reproduced.

For radii further out (5-15 kpc) the population begins to slightly descend the gradient in $H\alpha$ emission (or transition region) indicating that in certain places the relation between the amount of star formation and the available gas is changing.



Figure 2.12 Logarithmic qualitative star formation efficiency image, displayed from -16.5 to -15.5. Radial markers at 5, 10 and 15 kpc have been added. The central region of the galaxy has a remarkably flat distribution of efficiencies, out to greater than 10 kpc to the west of the nucleus, and out to 5 kpc to the east.

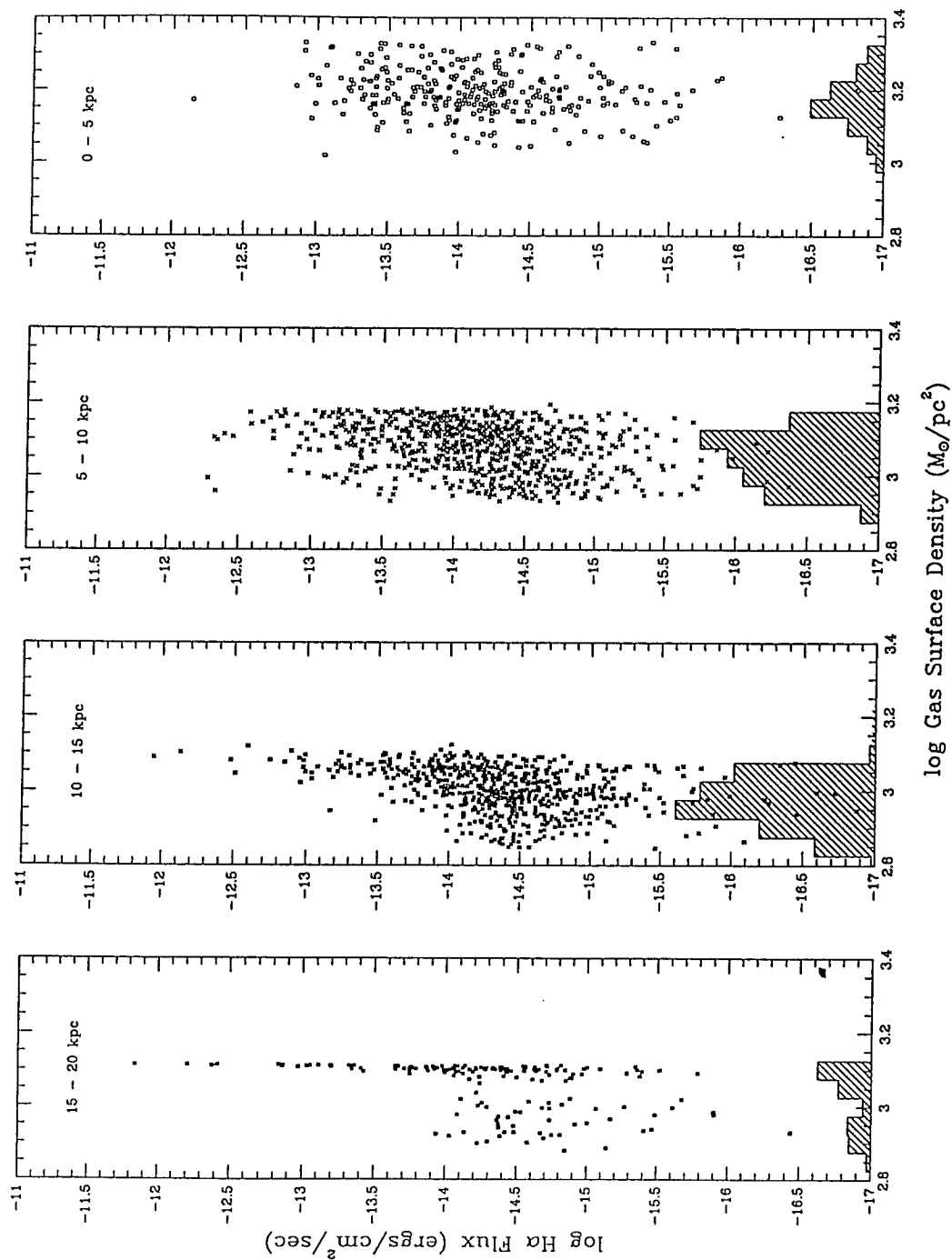


Figure 2.13 Variation in the effective star formation law as a function of radial position. This is observational confirmation that the effective collapse criterion changes as a function of radius.

Finally at the edge of our dataset, 20 kpc, a lower level becomes populated, as the regions that result from very inefficient star formation are included.

Since the near vertical distribution moves horizontally from radial bin to radial bin, more than one threshold is being described. This indicates that we are seeing a variation in the value of the kinematic Toomre critical density that is effective at different places in the galaxy.

Qualitative Star Formation History

Past studies of any changes in the SFE have been based on analysis of azimuthal averages of the three emission maps detailed above. In general the result for late-type spirals was that the ratio of molecular gas to the rate of current star formation ($\text{CO}/\text{H}\alpha$) appeared constant over the face of the galaxy. Indeed analysis of the two-dimensional maps reveals that this ratio may, on the whole, be represented by a single value over the whole disk with a spread of up to 50%.

Young and Scoville 1991 reported that the ratio of blue light to CO emission was also a constant in late-type spirals like M101. Thus if the blue/CO is taken to represent the long term star formation rate for intermediate mass stars, and if the ratio of $\text{CO}/\text{H}\alpha$ is taken to represent the current massive star formation rate, it may be concluded that the star formation efficiency is also a constant.

In performing the same calculations with our continuum imagery, and the newly assembled CO data, we found that the same degree of variation occurs, and that to first order the ratio of the blue/CO is a constant over the face of the galaxy. However, near the nucleus the bar identified by Kenney et al. 1991 causes an asymmetry in the ratio, indicating a local departure from the global value for the SFR.

2.5 Summary and Conclusions

Spectrophotometrically calibrated CCD imagery of two overlapping 16 arc min fields in the SAB(rs)cdI galaxy M101 in the emission of $H\alpha$, $[O\ III]\lambda 5007$, $H\beta$, & $[S\ II]\lambda 6723$ have been used to study various physical properties of the observed H II region population. Individual H II regions have been identified and mapped using an automated algorithm, thus eliminating any personal bias that might be included in the measurement process. Characteristics of the population studied include the H II region luminosity function and radial variations in extinction, $[O\ III]/H\beta$, O/H , $[S\ II]/H\alpha$, ionization parameter, and numbers of ionizing photons. In addition, radial *and* azimuthal variations in the H II surface density have been studied in comparison to that of H I and H_2 inferred from radio 21cm and CO observations.

Our work has identified several correlations, including:

(a) An apparent increase in the line-of-sight reddening towards the center of the galaxy has been implied by our measurements. The scatter in the results is appreciable, but a trend is apparent nonetheless. We estimate the central reddening level to be equivalent to a $C(H\beta)$ of 0.7, or an A_V of 1.8. The possibility of a change in the dust distribution with position above the disk of the galaxy is also implied as a result of detecting an anomalous amount of reddening associated with a set of H II regions arrayed along a ridge of recent star formation to the NW of the nucleus.

(b) A change in excitation with radius is exhibited by the H II region population of up to two orders of magnitude, with typical levels of 0.1 in the central regions to levels close to 10 at radii of 20 kpc.

(c) Using an empirical correlation between excitation and oxygen abundance (Edmunds & Pagel 1984), we derive the associated abundance gradients. For our upper threshold we derive an inner abundance gradient of 0.094 ± 0.005 dex/kpc, and an outer gradient of 0.038 ± 0.005 dex/kpc. A dependence between the limiting surface brightness of the H II region population and the derived gradients has been identified, casting doubts on the ability of any single set of observations to make any definitive estimate of such gradients.

(d) A very well defined correlation has been identified between the number of ionizing photons present within the volume of an H II region and the apparent size of the H II region, deriving a powerlaw relation of index 1.3.

(e) Reconstruction of measurements of the surface density distributions of neutral gas in the galaxy have allowed considerations of the star formation processes active

in M101. We have detected considerable variations in the effective star formation efficiency with position in the galaxy.

(f) Subsequent estimates of the star formation law at varying radial intervals has revealed the existence of more than one critical density for collapse at various positions throughout the framework of M101. This has implications for the application of simple kinematical models to late-type spiral systems such as M101.

Several properties have also been studied with an absence of correlation resulting. These studies include:

(g) There is no apparent relation between the size of an H II region and its position within the galaxy. The visual impression of the galaxy is counter to this, where the observer identifies several large regions in the outer sections of M101 without seeing the large number of much smaller regions also present.

(h) Integration of the observed line emission fluxes for each region yields no correlation with H II region position. This also appears contradictory to the observed appearance of M101 due to those very luminous superassociations at outer radii.

(i) After calculating the effective ionization parameters for each of the H II regions in our sample, we find no correlation between the observed value of U , the number of ionizing photons, or the mean region electron density with the position of the H II region within the galaxy.

Through the derivation of a differential luminosity function for the H II regions, it was possible to conduct a study of the completeness of our population sample. This has revealed that our population is complete to better than 80%. We find that the main source of incompleteness for the remaining part of the population is a lack of sufficient angular resolution, and not a result of any limiting luminosity problem.

The CCD imagery used provides the deepest study of M101 to date. The advantage of this study is that the entire volume of each H II region has been used to infer our results, whereas many previous spectrophotometric studies were purely based on measurements made of the bright “cores”. However, there are still many issues that need to be addressed in the aftermath of this paper. Future work will consider the specific environmental changes that are evident between H II regions in the central regions of the galaxy and those located at much larger radii. Continuing studies of other objects such as M51 and NGC 4449 are currently being assembled to study the effects of morphology and galactic environment on the results presented here.

Chapter 3

The H II Region Population of the Galaxy M51

3.1 Introduction

M51 is one of the nearest and largest “grand design” spiral galaxies. The galaxy is known to be undergoing an interaction with its companion NGC 5195, and shows an active system of star formation, largely confined to two spiral arms. An excellent review of the recent status of astronomical observations of this system may be found in Rand & Tilanus 1990.

The morphology of NGC 5194 has been classified by many people (van den Bergh 1960, Sandage 1961), but is listed by de Vaucouleurs 1976 as a SA(s)bc(pec)III galaxy. The companion has been determined to be an SB0 (Sandage & Tammann 1987), and as a I0(pec) by de Vaucouleurs, with other estimates varying the flavor of the classification only a little.

Physical parameters adopted in the analysis of this imagery include a distance of 9.6 Mpc (Sandage and Tammann 1975), a tilt angle of 20° and a positional angle of the major axis of 170° (Tully 1974b).

One of the earliest studies of the H II region population was published by Carranza et al 1969, and involved narrow band H α photographic imagery taken through a Fabry-Perot etalon and a H α interference filter of the galaxy. They catalogued 161 H II regions and presented the radial velocities for all of the regions. This survey has served as the standard for nomenclature in many subsequent studies of the H II region population in M51. These include studies by Smith 1975, Hodge 1982, Hodge & Kennicutt 1983, Rose & Cecil 1983, McCall et al 1985, Arsenault & Roy 1986, Roy et al 1986, van der Hulst et al 1988, Arsenault & Roy 1988, Kennicutt 1988, Kennicutt et al 1989, Peimbert et al 1989, Zaritsky et al 1990, Diaz et al 1991, and Rand 1992.

Due to the dramatic interaction evident in the system, the dynamics of the M51 system have proven a popular area for numerical modelling, but the difficulty of such a task has made it quite a challenging topic to study. The original numerical study was

performed by Toomre & Toomre 1972, and subsequently developed by Tully 1974c, Hernquist 1990, and Howard & Byrd 1990. The physical nature of the spiral arms in terms of the galactic dynamics have been studied by Elmegreen et al 1989, Howard & Byrd 1990, and Elmegreen et al 1992.

M51 has also been the subject of probably the most detailed star formation studies of spirals, due to very good radio and millimeter-wave observations of the galaxy in the past decade. As a direct result of this, the galaxy has served as a testbed for the newest ideas and theories concerning the role of star formation, and its causes, in spiral galaxies in general.

An initial HI survey of large galaxies by Rots 1980 included M51, and was continued by Bosma 1981, Bottinelli et al 1983, Israel & van der Hulst 1983, Scoville & Young 1983, Israel & Rowan-Robinson 1984, Rydbeck et al 1985, Lord et al 1985, Kimura & Tosa 1985, Young & Sanders 1986, Lo et al 1987, Tilanus et al 1988, Wakker et al 1989, Tilanus & Allen 1989, Rots et al 1990a & 1990b, Rand & Kulkarni 1990, Lord & Young 1990, and Young & Scoville 1991.

In this chapter, we will describe the reduction of the imagery in §2, derive the required emission characteristics of the H II region population in §3, and discuss the results and implications, as well as other aspects of the physical system, in §4. An Appendix containing the derived emission results for our full sample of H II regions has been added to allow the reader to assess for themselves the magnitude of the data involved with this method of analysis.

3.2 Data reduction and calibration

CCD imagery was taken using the Wide Field PFUEI device, developed by Jeff Hester, mounted on the Palomar 1.5m telescope. This is the same optical arrangement employed by Scowen, Dufour & Hester 1992 (hereafter SDH) to observe M101. Imagery were taken through narrow band interference filters with bandpasses covering H α , H β , [O III] λ 5007 and [S II] λ 6716+ λ 6731. Details of the observations made are included in Table 3.1. Additional wide band imagery, covering adjacent wavelengths, were taken to allow assessment of the continuum contribution to the measured line emission.

Flattening and registration of the imagery were performed using IRAF [†]. The images were aligned using a set of 86 reference stars, producing an agreement of 0.5 pixel between the images. The intensities of these reference stars were matched between the narrow-band and wide-band imagery to allow the successful subtraction of the continuum contribution to the line emission. This is performed by mathematically subtracting the appropriate wide-band image from the narrow-band image once it has been scaled correctly. An oversubtraction of the continuum emission was evident for the part of the imagery covering the companion object, indicating the presence an older stellar population in the companion when compared to the sample of foreground Galactic stars used as reference.

To calibrate the resulting narrow-band imagery, we attempted to use existing published spectrophotometry presented by Diaz et al 1991 (hereafter DTVPE). The spectra taken by DTVPE were obtained using a combination of an IPCS and a CCD for the blue and red parts of the spectrum, respectively. All of their observations were taken at a published position angle of 340° using a longslit about 1.5" wide. A reconstruction of their Figures 1a-c was attempted using this orientation, to no success. Several modified position angles were tried with variable success. The best match was achieved using a position angle of 345°. Having established the correct locations of the regions used by DTVPE, a rectangular aperture of the appropriate size was positioned across each region, and aperture photometry performed. The integrated emission yielded calibration coefficients for each of the interference filters that had variances between 25% and 40%.

[†]IRAF is distributed by the National Optical Astronomy Observatories, which is operated by the Association of Universities for Research in Astronomy, Inc., under cooperative agreement with the National Science Foundation.

Table 3.1 Details of Observations made of M51

Date (UT)	Filter Å (λ /FWHM)	Filter	Exposure (secs)	Field Center (1950.0)	
27 Feb 1987				$13^h 27^m 46.2^s$	$+ 47^\circ 27' 26.2''$
	6574/20	H α +500	100, 1500		
	6450/104	RC1	100, 500		
	6730/36	[S II]	150, 3000		
	5014/32	[O III]	150, 3000		
	5103/98	GC2	100, 500		
	4869/31	H β	100, 2000		
	4805/75	GC1	100, 500		

Attempts to simulate existing spectrophotometry (van der Hulst et al 1988, Smith 1975) using these images produced results that differed by more than an order of magnitude. Accordingly this avenue of calibration was abandoned. On the same night, as well as during the same observing run, imagery had been taken as part of the Galactic H II region survey by the authors, cf. Hester 1991a and Hester 1991b. As part of this survey a calibration database has been assembled for the interference filter set used, which consists of a set of coefficients for each filter normalised to unit exposure time and unit air mass. These coefficients were eventually used for the calibration of the M51 imagery, and proved rather successful. Comparisons with published line ratios (Smith 1975), and integrated fluxes (van der Hulst et al 1988, DVTPE), for various regions were made with generally good agreement being obtained (within 20%). The comparison with the Smith results was especially good, as may be seen by the reader if they compare the line strengths in Appendix B with the comparable entries in Table 2 of Smith.

3.2.1 Derivation of the H II Region population

SDH used a sophisticated algorithm to identify the H II regions in M101. This algorithm employed a detection threshold together with a random walk subroutine that explored the physical extent of each region, allowing for the many variations in morphology of each region. In this manner M101 is an easy example to study since the population of H II regions are observed to be spatially well separated, and set

against a uniformly dark background (after the continuum contributions have been removed; cf. SDH Figure 1).

The inset in Figure 3.1 reveals that M51 possesses an ambient, pervasive H α emission component that is not immediately associated with the local H II regions. This component defeats the mechanism used by SDH since the emission varies by more than a factor of 100 across the disk. The result is that adjacent sets of regions are either lost due to too high a threshold being employed, or are identified as one body of emission by too low a threshold. It was clear, therefore, that a modified approach was needed for imagery that contained such a large variation in the ambient H α emission.

Detailed inspection of Figure 3.1 reveals that most H II regions are identifiable by a bright core of emission. Using the appropriate combination of detection threshold and FWHM of the employed PSF, it is possible to use the IRAF task DAOFIND (Stetson 1987) to locate the centers of these local maxima in emission and derive a coordinate list of candidate H II regions. The final configuration employed a FWHM of 4 pixels, which served to eliminate any false identifications of local enhancements in the background noise, since these are typically no more than a pixel in size.

Using this list of coordinates, standard aperture photometry was performed using each emission line image with an aperture of radius 4 arcseconds. The results were combined with geometrical information of the galaxy such as tilt angle, position angle, and an accurate celestial coordinate reference file (derived from the Guidestar Catalogue) to produce composite data output files very similar to those originally generated for M101 by SDH. A list of the adopted and derived physical parameters for our imagery has been included as Table 3.2.

In a similar manner to the work performed by SDH, several detection thresholds were used to study any dependency in the observed optical emission quantities with emission intensity. The lowest threshold used was defined as being the level at which all apparent local concentrations of emission were successfully located by DAOFIND (1×10^{-16} ergs cm $^{-2}$ sec $^{-1}$), yielding some 465 candidate regions. Our preliminary results, Scowen & Dufour 1992, suggested that systematic radial variations in observed properties were only evident for the brightest H II regions. This earlier work was performed using the algorithm from SDH together with a very high threshold. When this same high value of 2×10^{-15} ergs cm $^{-2}$ sec $^{-1}$ was used with the DAOFIND method, only 75 H II regions were identified. It should be noted that many "regions" are actually the cores of larger complexes.

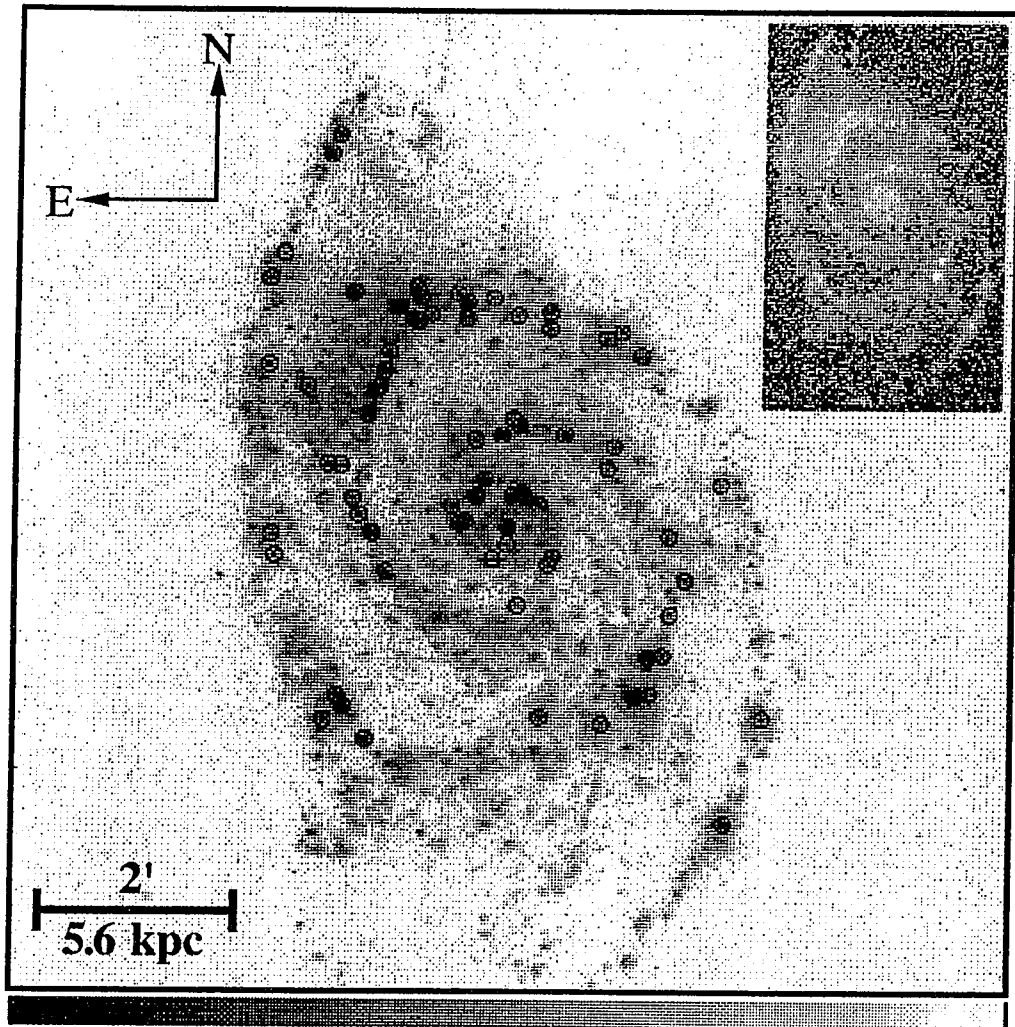


Figure 3.1 The disk of the galaxy M51 in the light of $H\alpha$. The continuum contribution to the emission has been subtracted. Indicated on the image are the bright regions that exhibit systematic variations in their emission properties. The inset illustrates the bright ambient $H\alpha$ emission component.

Table 3.2 Basic Physical and Geometric Information for M51

Distance used:	9.60x10 ⁶ parsecs
Tilt Angle:	20.0 degrees
Position Angle:	170.0 degrees
Galactic Center at:	13 27 46.7 RA, 47 27 11.0 Dec
Epoch of coords:	1950.0
Image Plate Scale:	1.190 arcsecs/pixel
Image Distance Scale:	55.4 parsecs/pixel
Field Rotation:	1.07 degrees
Error in RA:	0.05 sec
Error in Dec:	0.49 arcsec
Aperture Used:	4.0 arcsec

The standard for H II region nomenclature in the M51 system has been the system originally defined by Carranza et al 1969, who performed an extensive study of the population of H II regions yielding an excellent finding chart (their Figure 3) as well as a list of the region positions relative to the galactic nucleus (their Table 3). Other researchers (Smith 1975, McCall et al 1985, van der Hulst et al 1988, DVTPE) have published various emission properties for a subset of the complete ensemble, but it was thought appropriate that one of the results from this paper should be an extensive list of the derived emission properties for each of the Carranza regions that we could successfully identify. Using the original finding chart published by Carranza, we successfully located all but 15 of the H II regions. There were 15 H II regions for which we found no evidence for any H α emission at the locations assigned on the chart. These regions were numbers 15, 25, 29, 48A, 56A, 63A, 70, 75A, 76A, 76B, 87, 92, 96, 98 and 100A.

As part of this study we have assembled a new, more complete, sample of H II regions numbering 465. This detailed dataset is included as Appendix B, along with the Carranza designation for each region common to both sets for cross reference purposes.

3.3 Results

Initial analysis of the data was reported in the preliminary results presented by Scowen & Dufour 1992. In that paper, plots were made of derived emission line ratios $C(H\ \beta)$, $[O\ III]/H\ \beta$, and $[S\ II]/H\ \alpha$, as a function of galactocentric radius. This revealed a remarkable lack of any systematic variations in these observed quantities with radial ordinate for the full population of H II regions observed, with such variations only being exhibited by the very brightest regions.

With the automation of the identification technique, these plots were re-generated for a variety of thresholds for the H II regions in M51. One effect of changing the identification technique from that used by SDH is that we no longer have any estimate of the change in angular size between each H II region studied. Despite the increase in the numbers of regions identified from the earlier study to this one, less evidence for systematic trends was found due to an increased scatter in the various properties at a given galactocentric distance. At the lowest threshold, all derived quantities were evenly distributed with radius. Using the highest threshold (usually representative of emission from the “cores” of close proximity OB associations) some radial dependence was revealed, confirming the tentative result from the earlier work. A representative set of plots are included in Figures 3.2 and 3.3: where the upper panels have been derived using the high threshold, and the lower panels using the lowest threshold.

Using the identifications of the Carranza set of H II regions from within our largest dataset, we can plot the same emission properties for that limited subset. The results of this are shown in Figure 3.4(a) through (d). Similar global variations are evident with a much larger scatter at any given radius. The Carranza set was visually identified from a photographic image, and therefore introduces a limiting personal bias into the selection procedure. From Figure 3.5 (see §3.3.2) we can see that the Carranza set is a limited sample, incomplete at low luminosities, roughly equivalent to our intermediate threshold dataset. It should be emphasized that the Carranza set is an incomplete representation of the H II region population in M51, since many existing studies of the H II regions use this as their sample from which to select regions for analysis. The sample presented in Appendix B is presented as a far more complete sample, extending to much lower luminosities, and should serve to replace the Carranza set as the definitive sample of H II regions in the galaxy.

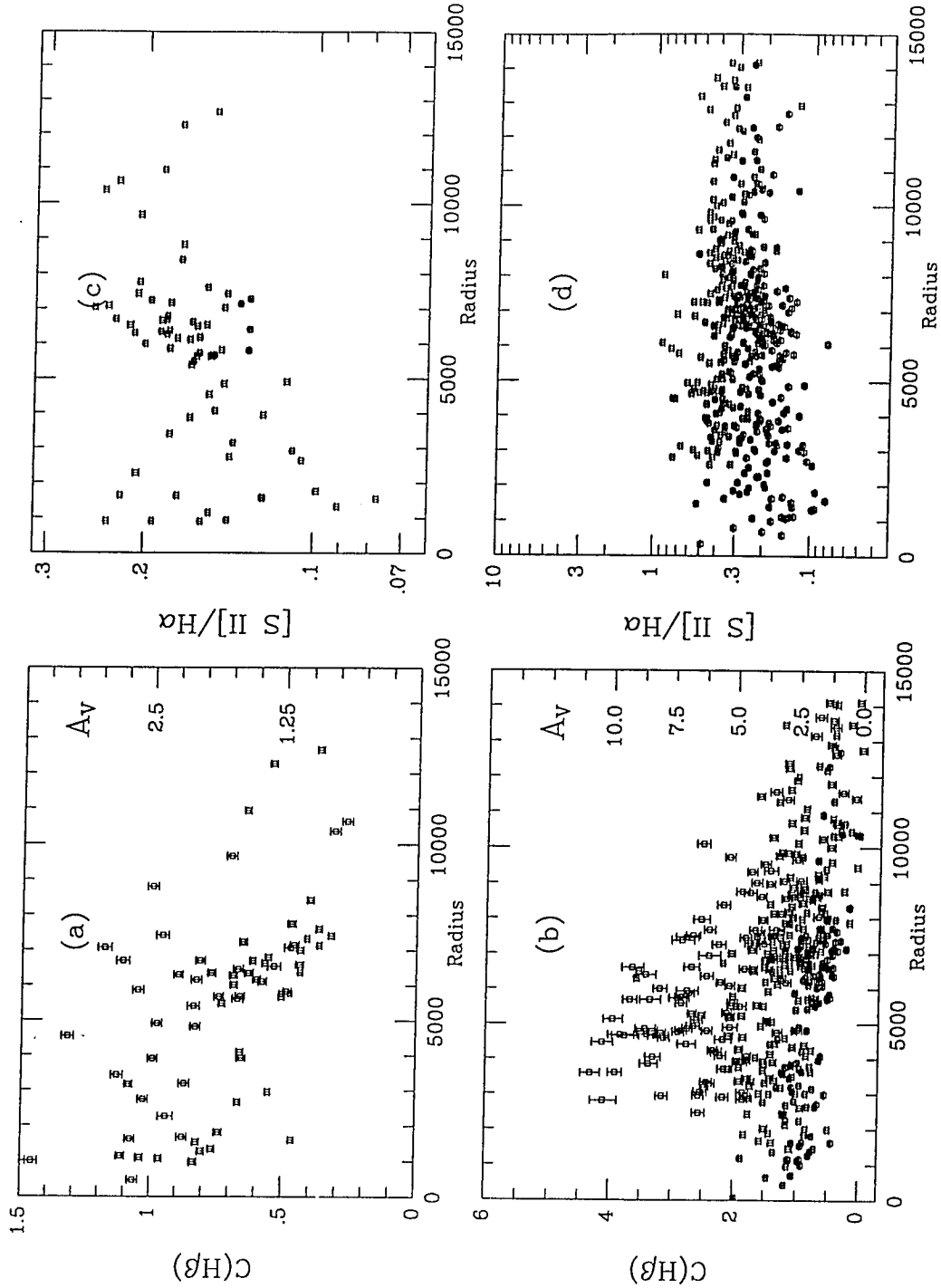


Figure 3.2 Derived emission properties of the H II region population of M51 as a function of galactocentric radius. Two thresholds are presented: the highest used for the upper panels, the lowest for the lower set. (a) and (b) depict the Balmer decrement. (c) and (d) depict the ratio of $[S II]/H\alpha$.

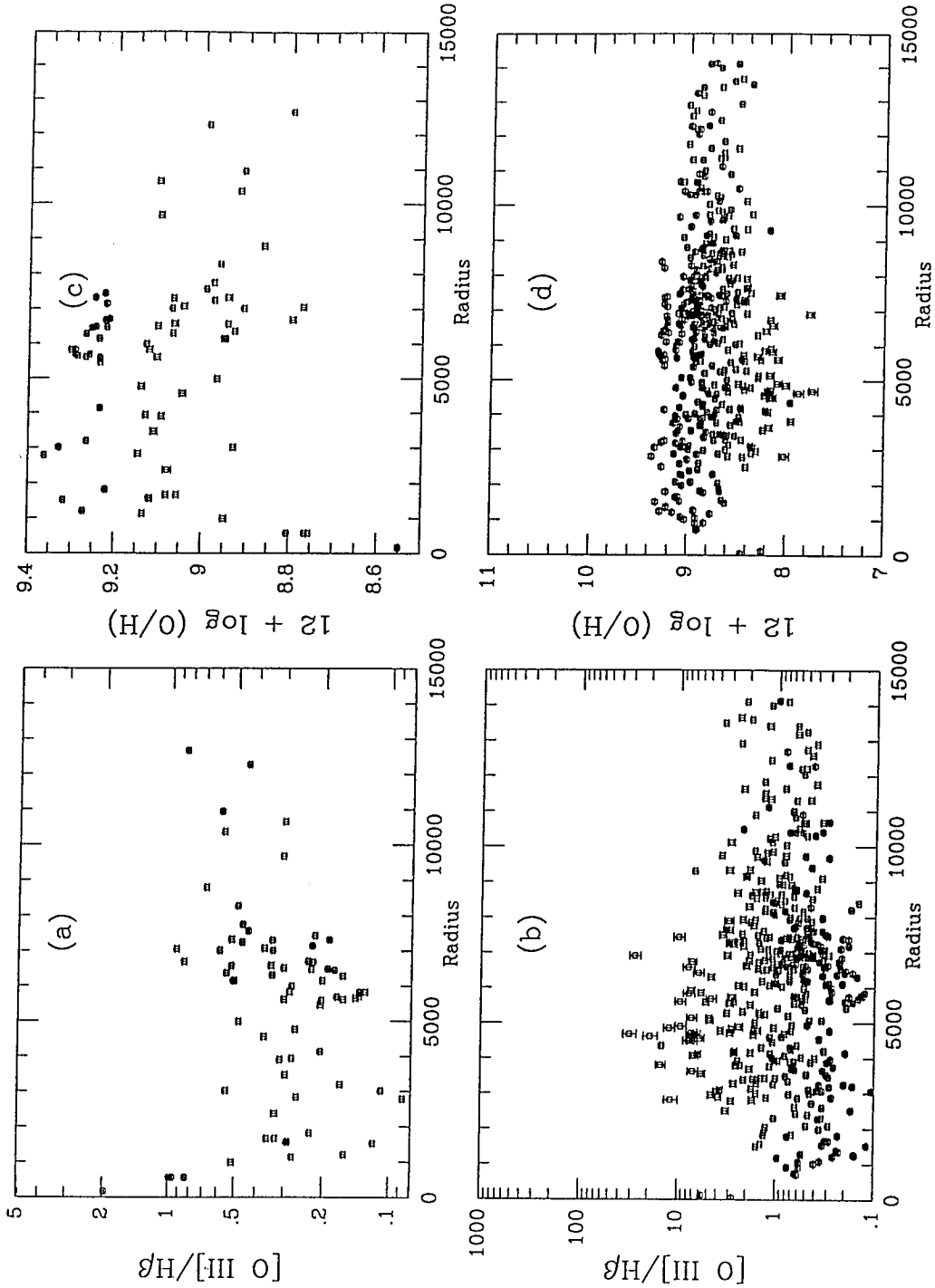


Figure 3.3 Derived emission properties of the H II region population of M51 as a function of galactocentric radius. Two thresholds are presented: the highest used for the upper panels, the lowest for the lower set. (a) and (b) show the region excitation as a function of radius. (c) and (d) depict the corresponding oxygen abundance, using a correlation between region excitation and oxygen abundance.

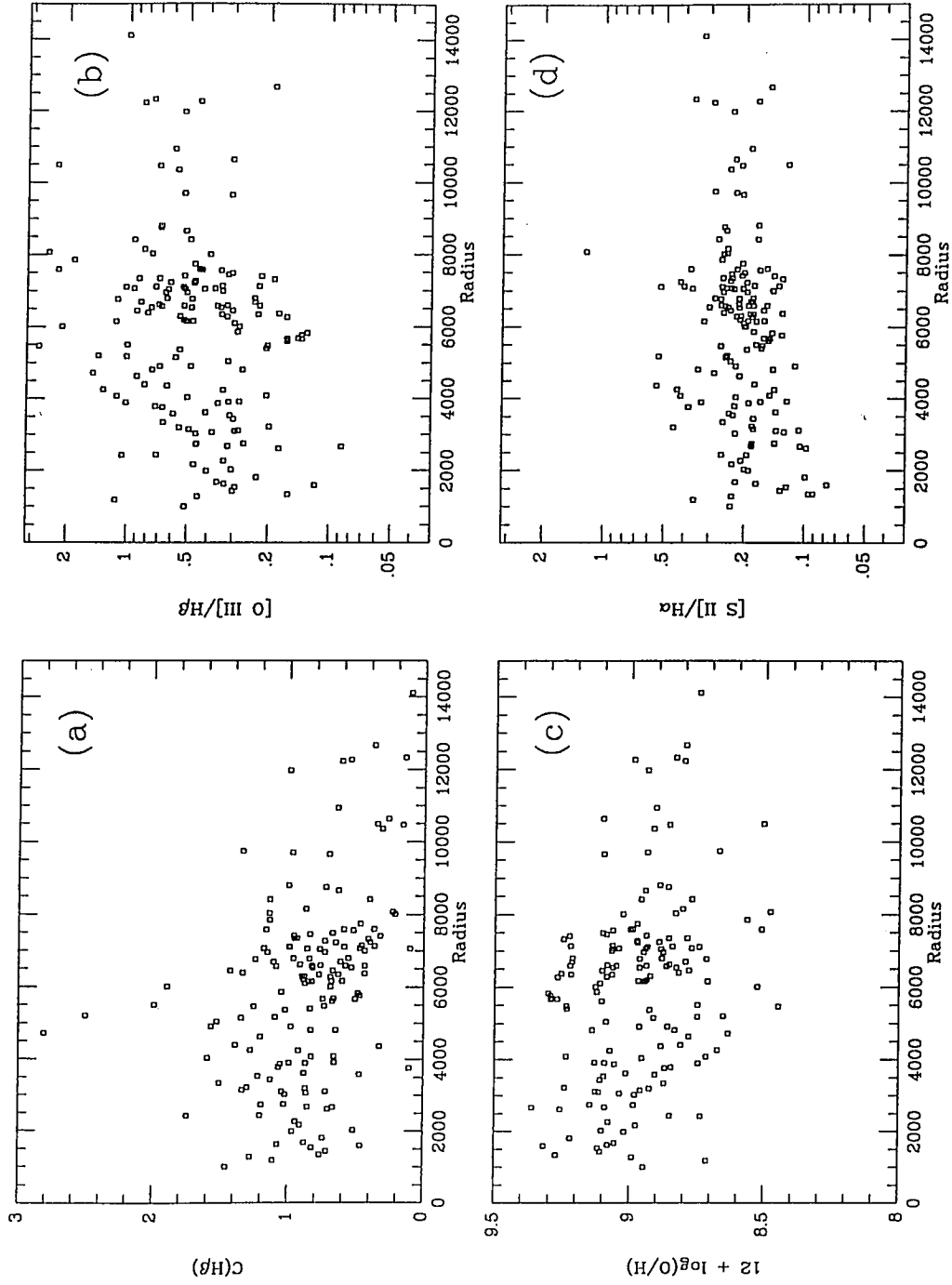


Figure 3.4 Derived emission properties of the Carranza set of H II regions as a function of radius. Numerical analysis of the linearity of the distributions in Figures 3.2 and 3.3 are presented in Table 3.3.

3.3.1 Emission Properties of the Brightest Regions

It appears from Figures 3.2 and 3.3 that systematic trends with radius only apply to the H II region sample with high surface brightness cores (identified with circles in Figure 3.1). For any threshold below the maximum used, an effective scatterplot is obtained. This may be quantitatively illustrated using a χ^2 analysis. The results of this approach are listed in Table 3.3. With reference to the appropriate panels in Figures 3.2 and 3.3, the data in the upper panels are more linear in their characterization than the lower panels. Not surprisingly, the data from the Carranza set falls in between the two extremes statistically. Although somewhat linear relations may be fit to the data, the success of this process is lowered by the inclusion of the faint end of the Carranza population.

Considering purely the lowest threshold data, we see that the properties of a scatterplot are well reproduced for the values for $[\text{O III}]/\text{H } \beta$ and O/H , since the derived gradient of a linear fit attempt is essentially zero, with low values of the linear correlation coefficient and large values of χ^2 . The corresponding intercept value reproduces the apparent vertical median of the distribution. However, when the data for $\text{C(H } \beta)$ are considered, the distribution does not appear to be completely random, with a mildly negative gradient resulting, in agreement with the trend evident at the higher threshold.

Table 3.3 Results of χ^2 Analysis of H II Region Emission Properties

Quantity	Figure panel	X_1^*	X_0^\dagger	χ^2	LCC
$\text{C(H } \beta)$	3.2(a)	-0.060	1.1	0.05	0.6
	3.4(a)	-0.051	1.2	0.34	0.2
	3.2(b)	-0.046	1.1	1.79	0.1
$\log [\text{S II}]/\text{H } \alpha$	3.2(c)	0.025	-0.9	0.01	0.6
	3.4(d)	0.016	-0.8	0.03	0.2
	3.2(d)	0.010	-0.4	0.07	0.2
$\log [\text{O III}]/\text{H } \beta$	3.3(a)	0.040	-0.8	0.04	0.4
	3.4(b)	0.031	-0.5	0.09	0.3
	3.3(b)	0.004	0.0	0.27	0.0
$12 + \log(\text{O}/\text{H})$	3.3(c)	-0.025	9.3	0.02	0.4
	3.4(c)	-0.020	9.1	0.03	0.3
	3.3(d)	-0.002	8.8	0.13	0.0

*Coefficient of radius in an attempted linear fit, in units of dex kpc^{-1} .

†Intercept value of emission property in an attempted linear fit, in units of dex.

When viewing the magnitudes of the gradients and the intercepts for the upper panels in Figures 3.2 and 3.3, and for the Carranza set in Figure 3.4, it should be remembered that these are results from incomplete samples, and are included here for their illustrative value concerning the properties of these smaller sets of H II regions. Such restricted groups of H II regions appears to exhibit radial variations in observable emission line ratios that are quite similar to the trends observed in M101 by SDH. There appears to be an increase in the line-of-sight reddening for these cores towards the center of the galaxy, as well as an observed increase in the excitation, a decrease in the oxygen abundance, and an increase in the $[S II]/H \alpha$ ratio, all with increasing radius.

It is interesting to compare the relative magnitudes of the variations observed in M51 with those previously determined for M101. The magnitude of the gradient in $C(H \beta)$ seen in M51 is of the order of $0.06 \text{ dex kpc}^{-1}$, which compares very well with the observed gradient in M101. This is illustrated in Figure 3a of SDH, although M101 exhibits this gradient over a much larger range in radius, extending out to 20-25 kpc.

There appears to be a radial increase in the ratio of $[O III]/H \beta$, which is in agreement with the general trend exhibited by M101. This gradient may be restated in terms of a radial decrease in the oxygen abundance using an empirical correlation between the two quantities (Edmunds & Pagel 1984). The basis for this anticorrelation is that a lower metallicity in an H II region will increase the radiative cooling of the region via the few metal lines still available, $[O III] \lambda 5007$ being one of the preferred mechanisms to do this. The rate of increase in the excitation of each region core with radius in M51 appears to be much lower than that observed in the inner 11 kpc of M101; the magnitude of the M51 gradient being about that of the observed inner gradient in M101 for the highest threshold. However, the M51 gradient is more comparable to the gradient observed at radii greater than 11 kpc in M101 (where two values of O/H gradients were found for the inner and outer parts of the disk).

The ratio of $[S II]/H \alpha$ does not vary by much, with a gradient again about half that of the high threshold gradient in the inner 10 kpc of M101. In that galaxy the ratio was seen to increase with radius, experiencing a peak in value at around 10 kpc, after which the ratio was seen to fall with increasing radius. No evidence of such a change in sign of the observed gradient appears in this dataset.

3.3.2 The H II Region Luminosity Function

A luminosity function has been assembled to describe the completeness of our survey sample. The results of this procedure are shown in Figure 3.5, for three representative thresholds including the high threshold discussed above. Not surprisingly, the population sample only appears complete for the lowest threshold used, indicated by the well described decrease in the lower luminosity population, which ultimately cuts off at around $10^{37.2}$ ergs sec⁻¹. This does indicate that the depth of our imagery is sufficient to sample all the resolvable regions present. We are also confident that all H II regions seen in emission in H α are representative of the entire population present since radio observations by Tilanus et al 1988 revealed no evidence for H II complexes being obscured in the optical by the sometimes considerable levels of intervening dust (see Figures 3.2(b) and 3.4(a)). However, the strict statement that all HII regions present are visible in the optical is called into question in §3.4.1.

An interesting benchmark for H II region luminosities is the estimated total luminosity of the prototypical Galactic H II region, the Orion Nebula. This luminosity is given as 10^{37} ergs sec⁻¹ by Kennicutt et al 1989, and is indicated on Figure 3.5. It is clear, then, that our sample extends nearly to luminosities this low, replicating a similar apparent relative distribution of H II regions with luminosity that was derived for M101 (SDH Figure 7). We have included the LF for the Carranza set, which appears to be very comparable to our intermediate set in number and distribution. However, the sample does not appear to be complete.

Rand 1992 assembled exactly the same kind of distribution function using comparable imagery, taken using the same filter. His resulting LF was presented along with an earlier version by Kennicutt et al 1989 (his Figure 3), to illustrate the improved completeness of his sample. This comparison has been made as an alternate check of the quality of our calibration, and to check that our aperture photometry compares well with that used by Rand to assemble his LF. Due to the visual rejection of certain candidate regions, our LF is terminated just above the luminosity of the Orion Nebula, and is seen to peak at a luminosity of $10^{37.4}$ ergs sec⁻¹. Although our LF disagrees slightly with that produced by Rand, the similarity is sufficient for the purpose of confirming that our sample is as extensive as his.

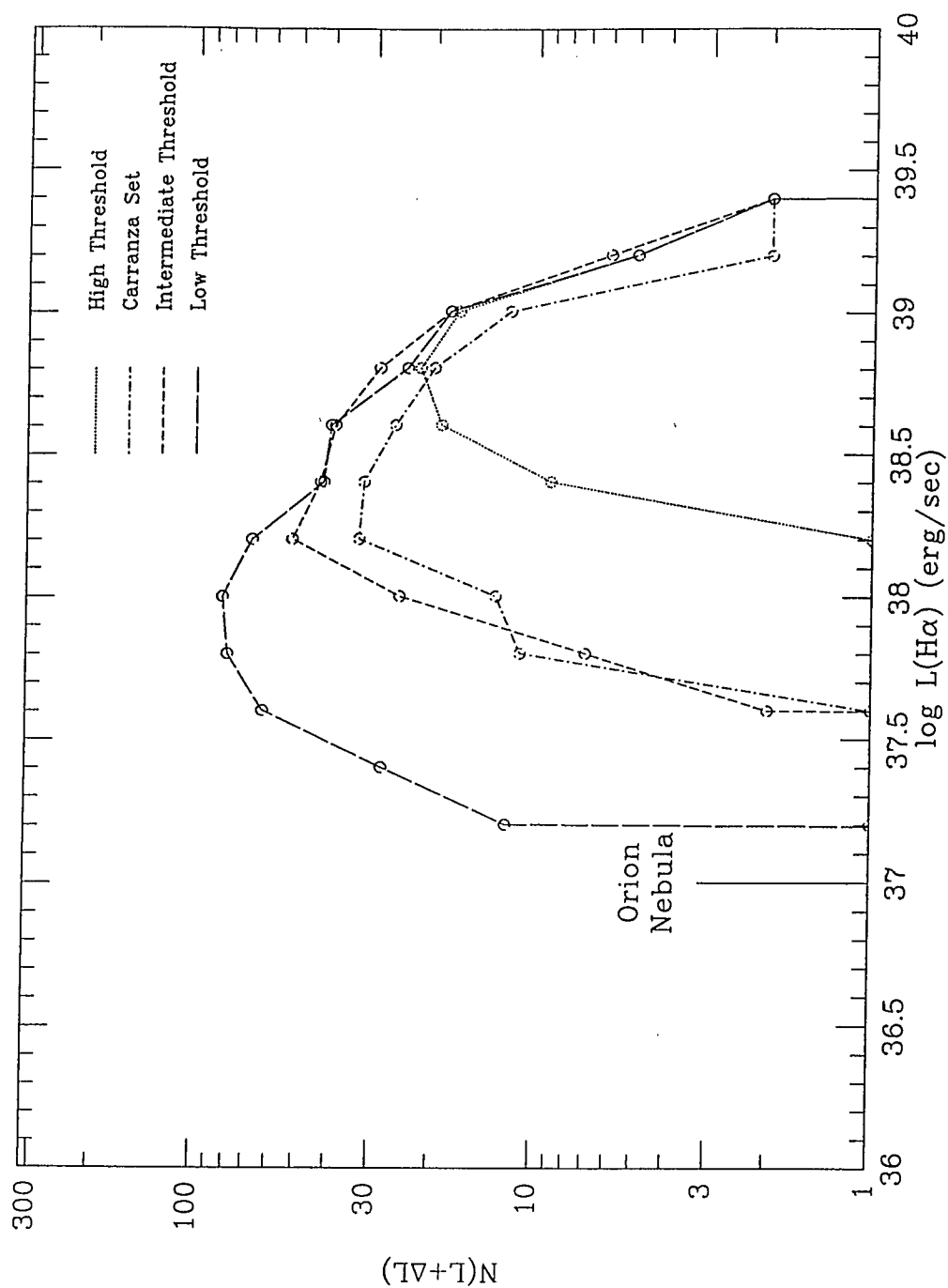


Figure 3.5 The H II region luminosity function, as derived from our imagery using an adopted distance of 9.6 Mpc, and a calibration coefficient calculated as part of the Galactic H II region survey mentioned in the text.

3.3.3 Velocity Dispersion

Arsenault & Roy 1986 performed a comprehensive study of many extragalactic H II regions to determine their velocity dispersions and radial velocities. They studied three regions in M51, as detailed in their Table II.

An attempt was made to identify their regions in our imagery, using the plate solution calculated for our imagery from the GSC database. Successful identification of their regions proved elusive. The coordinates used by Arsenault & Roy were originally provided by Kennicutt through a private communication, and our consultation with Kennicutt revealed that the regions have actually been mislabelled, with one of the sets of coordinates being rather unreliable. Using the new identifications provided to us by Kennicutt, the derived emission properties and positions for the three regions were calculated and assembled into Table 3.4.

In Table 3.4 we attempt to correlate the observed velocity dispersion with any of the observed properties we derive in this work. The trend reported by Arsenault & Roy 1988 that the velocity dispersion is correlated to the integrated H α emission is confirmed. The velocity dispersions for regions CCM 10 and 71 are essentially equal within the uncertainty stated by Arsenault & Roy 1986. However, other trends appear evident for the emission properties included, with the caveat that a sample of three regions can only hope to indicate a crude correlation at best. The reddening of each region appears anti-correlated with the dispersion, as does the region excitation. The region oxygen abundance and the ratio of [S II]/H α appear correlated to the velocity dispersion observed.

Our data are too crude to make any statement concerning the specific nature of any correlation, but are consistent with the results published by Arsenault & Roy. It would be interesting to assemble an enlarged dataset of velocity dispersions for an ensemble of H II regions within one system, instead of using a potpourri of a few of the brightest H II regions from several different galactic systems. This approach would sample the particular relation between derived quantities within an isolated system, as compared with any “universal” study that might omit such variations in a larger set of regions from different physical systems. Such observations would be best made using a Fabry-Perot etalon, similar to the original work of Carranza et al, and Tully, except that we would have the advantage of the newer technology available today in terms of both spatial and kinematical resolution.

Table 3.4 Comparison of Emission Properties with Velocity Data

A&R*	CCM [†]	α^{\ddagger}	δ^{\ddagger}	σ^{\S}	H α^{\P}	(1)	(2)	(3)	(4)
I	71	13 27 38.4	47 25 28.4	35.6	17.1	0.43	-0.77	9.26	-0.90
III	10	13 27 53.7	47 29 27.2	34.4	23.6	0.40	-0.72	9.25	-0.90
cm78	77	13 27 36.9	47 27 06.9	29.8	5.10	0.97	-0.32	8.97	-0.96

(1) C(H β)^{||}(2) $\log [\text{O III}]/\text{H } \beta^{\text{||}}$ (3) $12 + \log(\text{O}/\text{H})^{\text{||}}$ (4) $\log [\text{S II}]/\text{H } \alpha^{\text{||}}$

3.4 Discussion

3.4.1 The Brightest H II Regions

It is important to emphasize that using the highest threshold selects only H II regions with high surface brightness cores. The regions identified at this level are illustrated in Figure 3.1. The majority of the observed population appear centered on their host spiral arm just outside the corresponding dust lane, and are congregated into local groups, suggesting a common origin. The fact that systematic variations are seen only in the brightest H II regions, and that similar variations are seen for all region in another Sc galaxy, M101, suggests that there is a fundamental difference between the brighter and fainter regions.

The timescale associated with the interaction between the companion and the disk of M51 has been estimated to be of the order of 10^8 years by Tully 1974c, and 7×10^7 years by Howard & Byrd 1990 (extending the numerical studies of Toomre & Toomre 1972). The latter calculation used the kink depicted in Figure 3.7 (for a discussion of this figure, see section §3.4.2) to represent the radius where the time

*Region designation given in Arsenault & Roy 1986.

[†]Corrected region designation from the catalogue published by Carranza, Crillon & Monnet 1969.

[‡]Root mean square variances: RA = 0.696", Dec = 0.488". Total variance is 0.850". (Results derived from CTIO task COORDS.)

[§]Arsenault & Roy's velocity dispersions, in units of km sec^{-1} . Typical uncertainty is 1.8 km sec^{-1} .

[¶]In units of $10^{-14} \text{ ergs cm}^{-2} \text{ sec}^{-1}$.

^{||}In units of dex.

since perigalacticon equals one half the epicyclic period. Using this assumption, a time of perigalacticon of 70 million years is obtained. Their studies also attempted to match the apparent shape of the arms, as well as derive an approximate mass ratio between the companion and NGC 5194. They obtained a value of 1/10 for this ratio, whereas Hernquist 1990 finds a ratio of 1/2 is more promising based on his latest calculations.

The subject of the evolution of H II regions has been recently summarized by Yorke 1986. In this paper, Yorke discusses the current ideas concerning the dynamical evolution of H II regions, and the timescales applicable for certain critical phases of an H II region's development. All these timescales are a function of the spectral type of the ionizing star, with an O5 star evolving quicker from the main sequence to reduce the lifetime of an H II region.

We expect the brightest H II regions to be produced by stars with a high ionizing luminosity, O stars, and therefore a high mass. However, in assuming this we find that the expected timescale to cycle material through this phase is of the order of t_{ms} (the main sequence lifetime, from Mathews & O'Dell 1969), which is between 10^6 and 10^7 years for O stars (Mathews & O'Dell, Spitzer 1978), an order of magnitude less than the interaction timescale indicated above. The largest H II regions are typically created by O4 or O5 stars, whose lifetime is given as 5×10^6 years by Yorke.

This introduces a couple of apparently puzzling issues. We observed in M101 (SDH), an isolated late-type spiral, quite possibly very similar to the original galaxy that M51 once was, that appreciable radial variations in line-ratio quantities have been established and are exhibited by the entire H II region population. At the current time, M51 only exhibits such variations in the brightest H II regions, implying that there is a fundamental difference between the brighter and fainter H II regions in our sample. The existence of these variations cannot be explained by any model of material being recycled through the H II phase of the ISM due to the timescale arguments above.

3.4.2 Equivalent Widths at H β

What is it about the fainter population of HII regions that is different from the brighter regions? In Figure 3.6 we have plotted several of the derived emission properties against each other, in an attempt to study the nature of the fainter regions. From Figure 3.6(a) it is clear that the fainter HII regions are exhibiting a much

higher level of reddening, presumably from a more dusty local environment, although in stating this it should be noted that values of $C(H\beta)$ greater than two are probably suspect. The very brightest regions, with emission above -13.5 in the log of the $H\alpha$ emission, experience very little reddening in comparison.

Figure 3.6(b) reveals that the most reddened HII regions also have the highest level of excitation. This is a very unexpected and important result that has potential ramifications on the interpretation of the physical conditions in HII regions. The observed trend appears to be followed by essentially the entire population. Usually, the addition of dust to the ionized volume of a HII region has the effect of softening the radiation emitted by the region. Also, dust is usually seen to correlate with metallicity, and higher metallicity HII regions normally have lower excitation. In this case we are seeing the reverse trend, that higher levels of dust correlate with a harder spectrum. The final panel, Figure 3.6(c) indicates another unexpected result. By comparing Figure 3.6(b) with 3.6(c) it appears that those regions with higher excitation also have large values of the ratio of $[S\ II]/H\alpha$, but normally the reverse is seen with $[S\ II]/H\alpha$ usually decreasing with excitation. The major conclusions that can be drawn from results presented in Figure 3.6 are that (i) the fainter HII regions have higher levels of extinction, (ii) that these same HII regions have higher values of the ratio of $[O\ III]/H\beta$ than the brighter regions, (iii) these very (presumably) dusty regions are more highly ionized than the less reddened regions, and (iv) surprisingly $[S\ II]/H\alpha$ also increases with $C(H\beta)$.

These results are in general counterintuitive, when considering the expected physical response of each HII region. While the result in Figure 3.6(a) is plausible, the results in Figures 3.6(b) and (c) are quite puzzling and are contrary to photoionization theory. In general, large values of $C(H\beta)$ indicate the presence of larger amounts of dust. However, the addition of this dust should have the effect of softening the radiation field in the HII region, so reducing the ratio of $[O\ III]/H\beta$. Similarly, one does not expect $[S\ II]/H\alpha$ to correlate with $[O\ III]/H\beta$ unless some are explainable as supernova remnants.

van der Hulst et al 1988 reported that in the sample of 11 HII regions they studied optically, that most of the regions had an even 0.5 magnitude of A_V extinction in the optical when comparing the optical emission to the emission observed in the radio. The regions they selected were all quite bright and had optical reddening values that ranged up to 1.0 in $C(H\beta)$. Their conclusion about this result was that the observed extinction was due primarily to intervening dust, mostly extrinsic to the HII regions

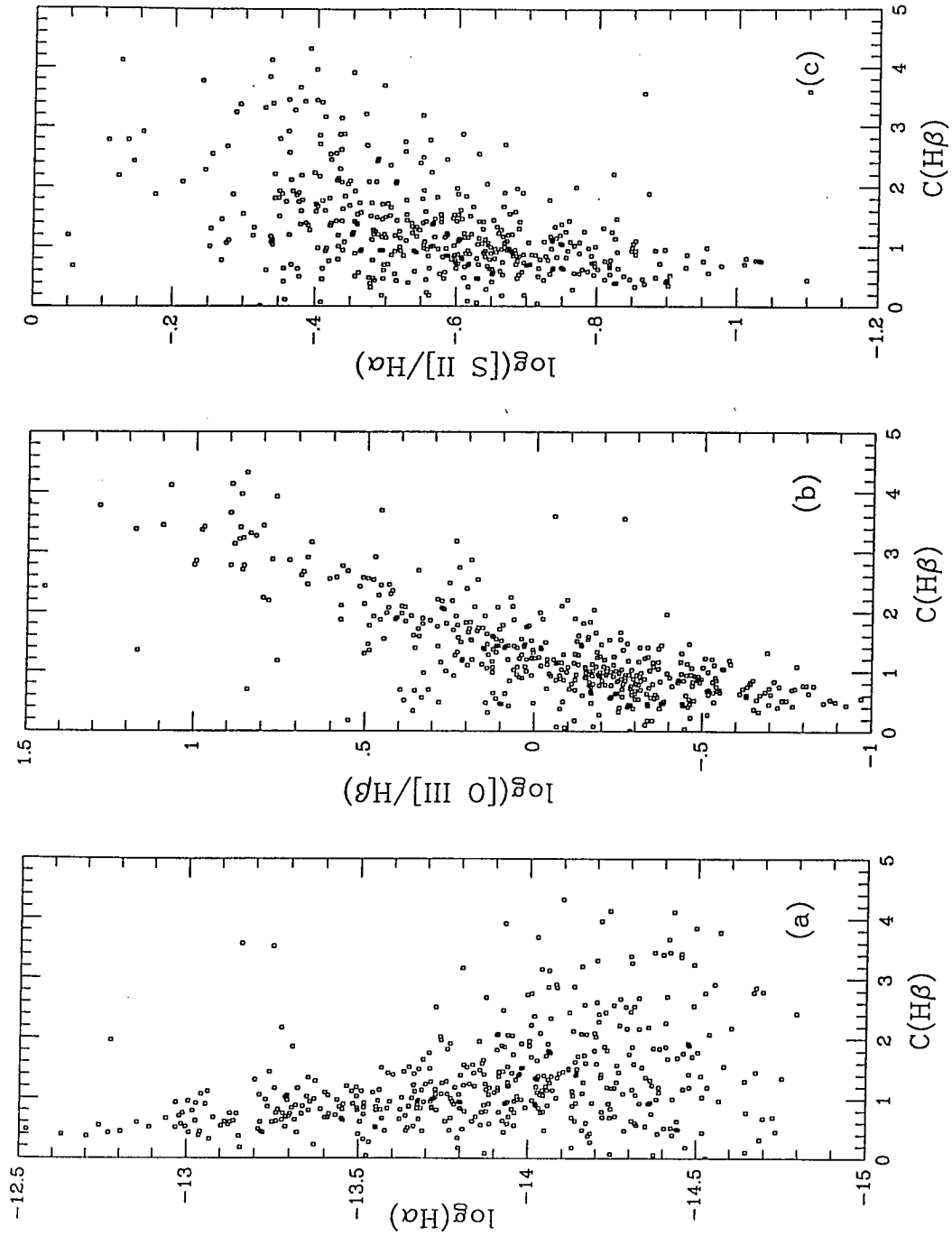


Figure 3.6 Emission properties of the full set of H II regions plotted as a function of line-of-sight reddening. (a) the integrated H α emission plotted against reddening. (b) the region excitation versus $C(H\beta)$. (c) the value of the ratio of [O III]/H β compared to the surface brightness of each H II region.

concerned. It was also reported that their results were consistent with the idea that the optical estimate was actually an underestimate of the total effective extinction.

van der Hulst et al commented on the fact that their sample was probably influenced by a selection effect derived from their choice of easily observable regions, since these would be the very brightest HII regions and would suffer the least extinction. We have seen that this is true through Figure 3.6(a), and the extrapolation may be made to imply that the fainter regions might have even higher levels of extrinsic dust than that measured by the radio observers.

The range in the values of the excitation presented in Figures 5(b) and (c) are in line with the idea suggested by van der Hulst et al that a temperature variation of several thousand degrees across the face of the galaxy would account for the observed increase of forbidden lines to $H\beta$ observed. We used the standard expressions for the temperature dependence of the ratio of $[O\ III]/H\beta$ from Aller 1987, and estimated the temperature dependence of the ratio of $H\alpha$ to $H\beta$ as an approximation to an reciprocal relation with temperature, using the appropriate normalization. Using these equations we derived the changes in the ratios that would be caused by a change in electron temperature of around 6000 K, assuming constant ionization fraction, and found the difference of 1.14 in the log to be in good agreement with the range of values seen in Figure 3.6. However, the calculation could only account for a change in the value of $C(H\beta)$ of at most 0.1.

It is possible that the faintest HII regions are being viewed through a dusty medium. The scale height of dust in our Galaxy is observed to be around 120 pc (Table 4-16, Mihalas & Binney 1981), while the scale height of O stars (and therefore HII regions), is observed to be 50 pc. Therefore it is not difficult to visualize that given a random distribution of HII regions throughout the dust layer in M51, that some regions would be located closest to the “edge” of the dust layer, so we only see them through a path length of order 60-70 pc, while others are seen much “deeper” in the layer through a much thicker layer of intervening dust. This scenario has problems, however, explaining the results in Figure 3.6(b) since this implies a preferential distribution of the hottest regions. If the most excited HII regions have very low surface brightnesses then this requires them to be behind a higher level of extinction, implying a location close to the far edge of the disk from our point of observation. This is clearly a distribution not typically observed in other galaxies and introduces an implausible inconsistency.

A suggestion was made by Manuel Peimbert that the peculiar trends we were seeing might be due to a problem with the underlying absorption at $H\beta$ from the stellar component in each HII region. Past corrections for this problem have involved using an equivalent width of $H\beta$ absorption equal to 2\AA , eg. McCall et al 1985 based on spectroscopy. A good example of this effect is illustrated in Figure 2a of Dufour et al 1980. To estimate this we studied the spectral library of stellar types published by Jacoby et al 1984, fitting equivalent width (EW) profiles to the absorption lines observed. The results of these fits are presented as Table 3.5 to illustrate the dependence of the underlying absorption contribution on the dominant spectral type in the HII region observed. If we assume that in most HII regions the dominant spectral type will be somewhere between an O7 and a B4 star, then an EW of underlying absorption of around 3\AA seems appropriate.

Table 3.5 Equivalent Width of $H\beta$ as a Function of Spectral Type

Name*	Type*	EW($H\beta$)†
HD 242908	O5	2.2
HD 215835	O5.5	2.9
HD 12993	O6.5	2.1
HD 35619	O7	2.4
HD 44811	O7.5	2.3
HD 242935	O8	3.2
HD 236894	O8	2.5
HD 17520	O9	2.3
HD 12323	O9	2.8
BD+62 249	O9.5	2.7
HD 158659	B0	2.0
HD 237007	B0	3.6
HD 35215	B1.5	3.9
HD 37767	B3	4.3
Feige 40	B4	8.5
HD 240344	B4	5.3
HD 30584	B6	7.4
O 1015	B8	8.7

*Designation from Jacoby et al 1984.

†In Angstroms, measured using IRAF task SPLOT. Typical RMS error is 0.1\AA .

In order to see how large this effect might be in affecting our estimates of quantities such as $C(H\beta)$ and $[O\ III]/H\beta$ we needed to estimate the EW of $H\beta$ emission from each HII region observed. Using the filter calibration obtained by Walter et al 1992 for the same instrument and filter set, we calibrated our GC2 continuum image to allow an estimate of the EW of each HII region. Having generated an image that represented the pixel-by-pixel variation in the EW of $H\beta$ emission, we corrected that emission using the global estimate of 3\AA of underlying absorption, to produce a new image of the galaxy. Using this image new datasets for each region were assembled and the line ratios calculated.

A recreation of Figure 3.6 yielded plots that were much improved in certain regards over the earlier versions. All regions appear isotropic with logarithmic surface brightness and derived $C(H\beta)$, as well as with the value of $\log [S\ II]/H\alpha$ and $C(H\beta)$. However, the most troubling plot, Figure 3.6(b), when rederived, yielded the same linear correlation, with less scatter. As a final test, the same plot was assembled using the logarithm of $[O\ III]/H\alpha$ instead, and this yielded an isotropic distribution. Another caveat with these latter plots was that as many as 50% of the regions now possessed values of $C(H\beta)$ that were negative, and therefore unphysical.

In conclusion, therefore, we find ourselves faced with a complex problem concerning the use of narrow-band CCD imagery to study HII region populations in metal-rich spirals with strong underlying stellar absorption. It is clear that for these purposes the variety of physical conditions represented by the full population of HII regions may not be well represented by a global estimate of the underlying absorption. As a result of this most previous efforts to account for this problem have probably been insufficient, and care should be taken assessing such results. To accurately estimate the absorption on a region-by-region basis will require the use of wide-band imagery and spectral synthesis calculations to better estimate the specific contribution to the observed EW of $H\beta$. Given the limited dataset we are using there is no simple solution to the problem.

3.4.3 Spiral Structure

The arms of a spiral galaxy may be mathematically characterized by either a logarithmic or a hyperbolic spiral. However, as has been pointed out by Kennicutt 1981, most spirals do not follow any single solution for the full length of a given arm. Kennicutt found that the exact mathematical description any single arm was “irrelevant for real

galaxies", but that their application could be used in interpolation to describe lengths of each arm. The most effective method, therefore, is to separately treat parts of each arm when fitting such mathematical solutions.

Spiral Density Wave theory predicts that a logarithmic description will best represent the shape of the arms (Roberts et al 1975). However, the creation of material arms by processes purely related to the local differential galactic rotation (through stochastic theory; Seiden & Gerola 1979) are more hyperbolic in form. General forms for both of these descriptions are studied below.

A solution was sought to the form of the spiral arms to allow analysis of any variations in the observed emission properties of each H II region as a function of the ordinate, L , along the length of the arm. Such a solution would also provide some indication of the possible origin of each section of each arm, with respect to the two possible theoretical models.

A standard logarithmic spiral may be generally characterised by the equation:

$$r = ae^{b\theta} \quad (3.1)$$

where r is the radial position of each region in the frame of the galaxy, and θ is the position angle of the region in the frame of the galaxy relative to the apparent major axis of the galaxy. The coefficient b may be re-expressed in terms of the pitch angle μ using:

$$\mu = \tan^{-1} \left(\frac{1}{b} \right) \quad (3.2)$$

A plot of $\ln(r)$ versus θ will be linear if this general form is applicable.

The other solution for a spiral arm is the hyperbolic solution, where the shape of the arm is dictated purely by the rotation curve of the galaxy. Thus:

$$r(\theta - \theta_0) \propto V_{rot}(r) \quad (3.3)$$

where $V_{rot}(r)$ is the tangential rotational velocity at radius r . A linear distribution is obtained in the $(r\theta, r)$ plane if this relation best characterises the data and the rotation curve is sufficiently flat over the range of radii studied.

Using the derived values from the detailed analysis by Tully 1974b (Table 7), of $i = 20^\circ$ and $\phi = 170^\circ$, the positions of each region were deprojected into the (r, θ) plane, and then studied with relation to the two general forms introduced above. The brightest regions were chosen to delineate the path of the arms, but further regions were added to increase the number of data points for certain key parts of each arm.

The resultant plots are shown in Figures 3.7(a) and (b). Figure 3.7(a) compares well with Figure 4 of Tully 1974c, and Figure 3F of Kennicutt 1981 (although he adopted very different values for i and ϕ that effectively hid some of the variations seen here). Figure 3.7(b) is equivalent to Figure 4F of Kennicutt 1981. Linear segments have been overlaid to detail the author's best fits to those sections of the data. The corresponding theoretical spirals were then calculated and reprojected into the frame of the sky, to produce Figure 3.8. Clearly certain fits are better than others, but no single solution does an adequate job of characterising the full extent of each arm, confirming Kennicutt's result.

In all the cases presented, each arm is best fit by two linear segments, with a discontinuity in the distribution at the radii between the segments, which occurs at roughly the same radius ($r = 6$ kpc) for both arms, and at the same position angles, which appear to be approximately 180° apart. It is interesting to compare Figure 3.7(a) with Figure 4 from Elmegreen et al 1989, where imagery itself was reprojected into the $(\ln(r), \theta)$ plane. This radius of approximately 6 kpc coincides almost exactly with the radius indicated by Elmegreen et al 1992, on their Figure 11 in the lower left panel, as the radius of corotation.

Elmegreen et al's earlier paper dealt with the relative amplitude of the spiral arms in relation to the apparent pattern speeds in a sample of three galaxies, M51 included. The same apparent discontinuities were seen for both arms, confirming our result. The interpretation of this feature by Elmegreen et al was that the inner and outer spirals result from differing pattern speeds, and that the misalignment observed is to be expected. The outer system appeared to fit to a model of corotation with the companion, and it was noted that no such discontinuity appears in the arms of M81 or M100, their other sample galaxies. A better depiction of the inner and outer pattern speeds is presented by Elmegreen et al 1992 in their Figure 21, where the stratification of the spiral patterns with $\ln(r)$ is clear. It appears that this change in pattern speeds occurs at the corotation radius in M51. Estimates for the values of the two pattern speeds were made by Tully 1974c, illustrated on his Figure 4, and are $70 \text{ km sec}^{-1} \text{ kpc}^{-1}$ for the inner spiral, and $90 \text{ km sec}^{-1} \text{ kpc}^{-1}$ for the outer spiral.

Taking the imagery in Figure 3.8 as the best gauge of the success of the fits, it is clear that the inner section of the galaxy is fit equally well by either the logarithmic or hyperbolic solutions. The inner radius of termination of the arms was identified as being evidence for the location of the inner Lindblad resonance by Tully 1974c, and occurs at an angular radius of $30''$, or a linear distance of 1.7 kpc at the distance we

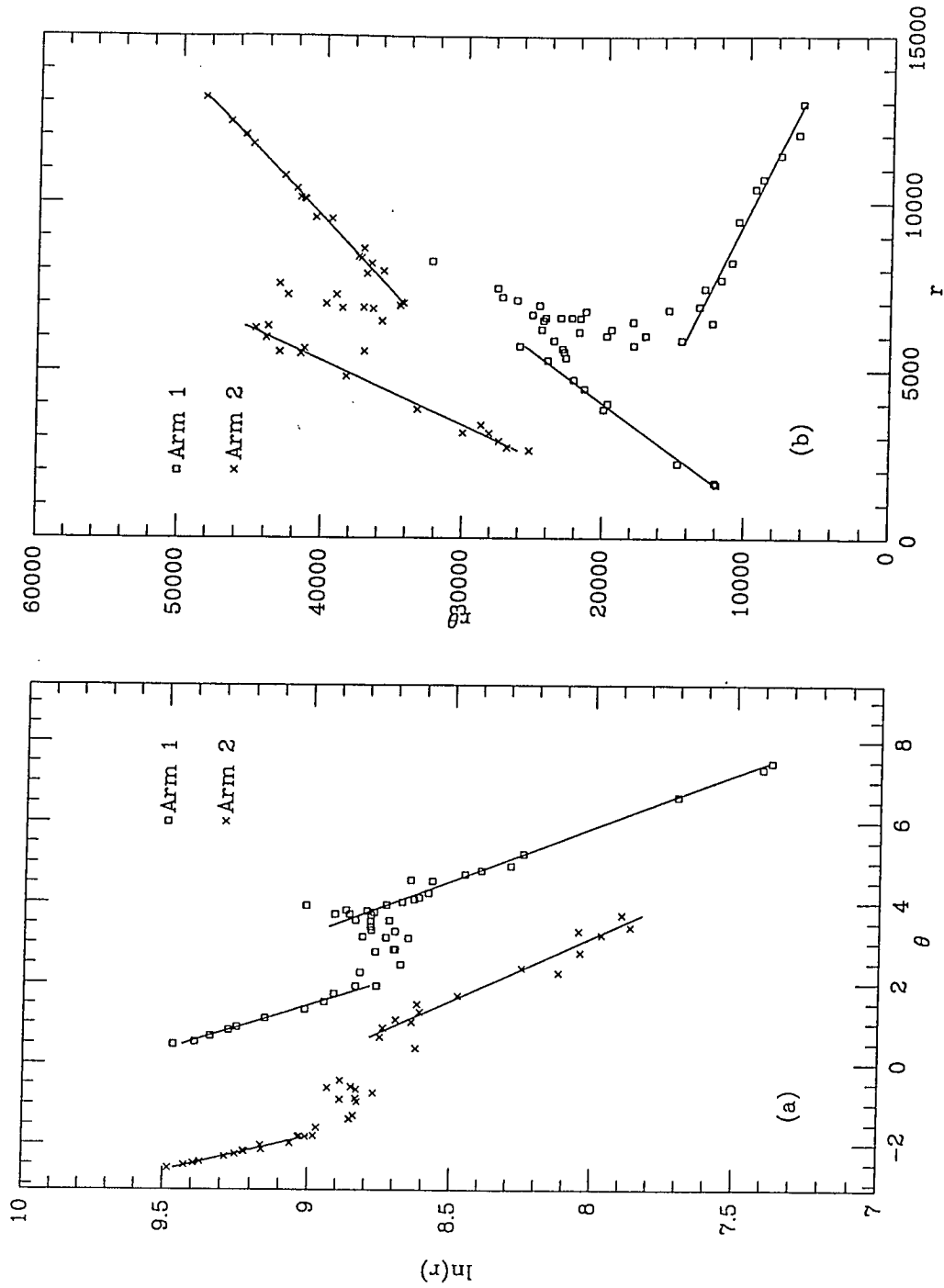


Figure 3.7 Results of the mathematical description of the spiral arms in M51. (a) assumes a logarithmic description, a break in the arms appears at a radius of around 6 kpc. (b) uses the material arm description to apply a hyperbolic solution, again exhibiting the break at 6 kpc.

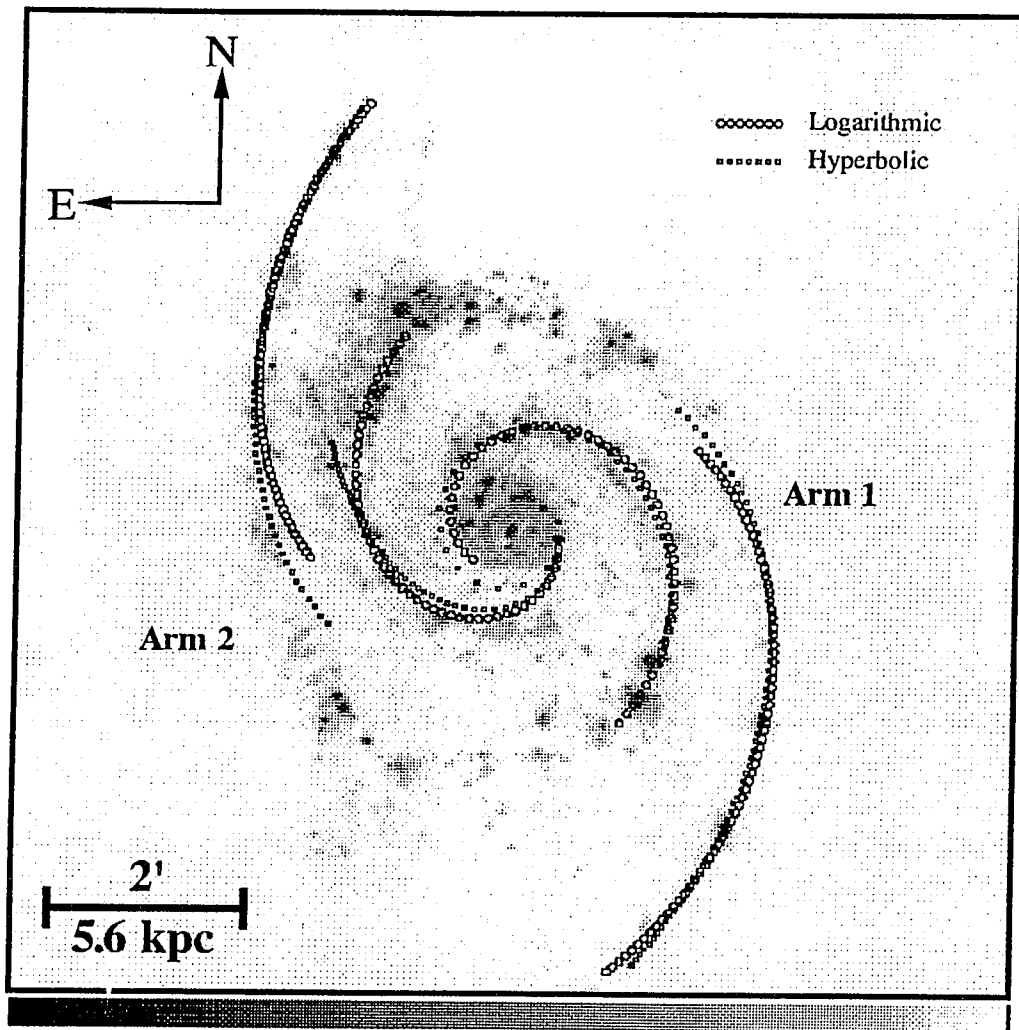


Figure 3.8 The mathematical solutions for each arm, as represented in Figure 3.7, reprojected onto the plane of the sky. The logarithmic description appears better in the inner disk, while the hyperbolic solution appears to more successfully model the shape of the arms in the outer disk.

assume. The better fit, if one is to be chosen, is made by the logarithmic solution that appears to exactly follow Arm 1 out to a radius of around 6.6 kpc, and Arm 2 to a radius of 6.1 kpc. The hyperbolic solution only appears to follow out to 4.6 kpc for Arm 1, and only from 2.5 kpc to 6.1 kpc for Arm 2. The results are listed in Table 3.6. Thus the inner spiral appear to be well modelled by a spiral that is driven by a density wave.

The outer segments of each arm are more open, with a larger value for the pitch angle as indicated by Table 3.6. Both sets of solutions appear similar again, but the hyperbolic solutions appear to fit better. This is consistent with the best fit model that Tully 1974c used for the outer disk, where he claimed that the outer spirals were material arms generated by the tidal interaction with the companion. This also agrees with the Elmegreen suggestion that the outer spiral is in corotation with the companion. It is apparent, then, that the inner disk is dominated by the underlying density wave, and that it is kinematically sheared from the outer disk, which is driven by the angular speed of the interaction with the companion, at the radius where the difference between the local rotation and the rotation of the density wave disappears. The relative position of the arms across this shear, in angular space, will vary as a function of time due to the effective difference in the applicable pattern speeds of the two disks.

Whatever solution is used, a clear departure from any theoretical path occurs at approximately the same location in (r, θ) space: at a radius of approximately 6 kpc, and a position angle (on the sky) of between -55° and $+15^\circ$ on Arm 1, and between $+105^\circ$ and $+205^\circ$ for Arm 2. In this area the distribution of H II regions, and correspondingly the spiral arm itself, does not appear to obey any simple mathematical description. An interesting point to make is that study of the upper panels in Figures 3.2 and 3.3 reveals an aggregation of H II regions at the corotation radius relative to any other radius. This is not surprising since the dynamical shear being experienced by the disk at that radius should affect the local collapse conditions for star formation in a beneficial manner, as the local ISM experiences local velocity perturbations in excess of the local criterion for the collapse of the gas phase under more static conditions.

To study the distribution of emission properties along the spiral arm, we need to derive a relation for the ordinate L , the length along the spiral arm. When the logarithmic spiral solution is used, the length L , may be given by:

$$L(r) = \sqrt{1 + b^2} r \quad (3.4)$$

Table 3.6 Results of Theoretical Fits to the
Apparent Spiral Structure in M51

Table 3.6(a): Logarithmic Description

Arm Number	a (kpc)	b	μ ($^{\circ}$)
1 inner	27.7 ± 2.2	-0.380 ± 0.017	290.8 ± 0.8
1 outer	15.6 ± 0.3	-0.449 ± 0.015	294.2 ± 0.7
2 inner	8.0 ± 0.4	-0.316 ± 0.019	287.5 ± 1.0
2 outer	2.9 ± 0.1	-0.571 ± 0.019	299.7 ± 0.8

Table 3.6(b): Hyperbolic Description

Arm Number	θ_0 ($^{\circ}$)	k $V_{rot}(r)$ (kpc)
1 inner	188.5 ± 5.0	6.9 ± 0.3
1 outer	294.2 ± 6.1	21.0 ± 1.0
2 inner	298.5 ± 10.7	12.5 ± 0.9
2 outer	129.1 ± 2.6	18.6 ± 0.4

which is linear with radius. Therefore any radial plot of an observable quantity, such as those presented in the previous section, will appear identical when the positional ordinate is changed to the length L along the host arm. No explicit gradient enhancements or reductions may be seen when considering plots versus L in relation to plots made versus r .

Using the general form for the hyperbolic spiral, we can derive the length L in the same manner, to give:

$$L(r) = \frac{1}{2a} \left[r\sqrt{r^2 + a^2} + a^2 \ln \left(r + \sqrt{r^2 + a^2} \right) - a^2 \ln(a) \right] \quad (3.5)$$

where $a = (1/kV_{rot})$, k is the constant of proportionality from Equation (4-3), and we have assumed that over the radii concerned the rotation curve is essentially flat ($\partial V_{rot}(r)/\partial r = 0$). Both Carranza et al 1969 (Figure 5) and Tully 1974b (Figure 3) found that the apparent rotation curve is flat from an inner radius equal to the Inner Lindblad Resonance out to a radius of around 11 kpc. Our range in radii slightly exceeds this, but we will assume that the flat curve holds out to our radial limit of 15 kpc.

The radial dependence of this function is such that at small radii ($r \ll a$) L is proportional to r , and at large radii ($r \gg a$) L is proportional to $(r^2 + a^2 \ln(2r))$. In the fits that were derived for M51, the values for a ranged from 5×10^{-5} to 1×10^{-4} pc, thus the only applicable condition in this case is the latter. This dependence is only weakly more dependent than quadratic, introducing a stretch in the relative positional displacement of points on a plot of, say, $\log[\text{O III}]/\text{H } \beta$ versus L . Such a change will serve to reduce any gradients that may be evident on the radial plots, since the result is also multiplied by the reciprocal of a , increasing the corresponding value of L by between 10^4 and 2×10^5 . Such a plot would appear essentially flat compared to similar plots versus radius.

The position of the dust lanes, evident in wide-band imagery, relative to the arms defined by the H II regions has an impact on the estimates for the time between the compression of the local ISM by the passage of the density wave and the peak in star formation represented by the H II region arm. When the dust arm is mathematically described by a logarithmic spiral (taking the density wave solution as the correct one for the inner disk) the dust lane is found to be separated from the H II region arm in a different manner for either arm.

For both arms the appropriate slopes on a plot in $(\ln(r), \theta)$ space, see Figure 3.9, are very close to parallel. This indicates an almost common scaling factor between

the arms; that at a common azimuthal angle (see Figure 3.10) the radial distance of one arm from the galactic center will be a constant multiple of the radial distance for the other arm. If the two arms are parallel in Figure 3.9, then at any given radius the value of $\Delta\theta$ is constant. Accordingly the time for the density wave to traverse the distance $r\Delta\theta$ will be a constant, since the velocity of the pattern is a linear function of radius. Arm 2 appears to exhibit a constant separation from its H II counterpart that represents an angular separation of 0.42 radians. Using the pattern speed quoted for the inner disk of $90 \text{ km sec}^{-1} \text{ kpc}^{-1}$ by Tully, these results may be expressed in terms of the relative timescales between the compression and star formation phases of the passage of a density wave, giving a value of 4.6 Myr for Arm 2.

Arm 1, however, exhibits an increase in the relative separation of the slopes with radius. The rate of this separation, in terms of the angular separation is 1.8 Myr ex^{-1} , or more explicitly the timescale at any given radius is given by,

$$t = 1.78 \ln(r) - 13.2 \text{ Myr} \quad (3.6)$$

The uncertainties associated with the positions of each H II region are sufficiently small that each point on the line would have negligible errorbars. For typical values of $\ln(r)$ of around 7-8 for the inner disk, this timescale is around 1.5 Myr, which is noticeably shorter than the timescale derived for the other arm, over the full range of radii in the inner disk.

The timescale for the main sequence lifetime of an O star has been seen to be around 5 Myr. The timescale for the collapse of a molecular cloud has been studied by Shu et al 1987 to be around 0.3 Myr for the collapse to form a $0.5 M_{\odot}$ star. After the evolution from the protostar to the main sequence has been allowed for, the collapse timescale for a molecular cloud to produce a 5-10 M_{\odot} O star will be around 2 Myr, assuming the parameters assumed by Shu et al in their review. The timescales we derive for the two arms in M51 are then quite comparable to the time needed to produce large O stars from the peak compression of the local ISM. The shorter timescale obtained for Arm 1 is somewhat problematic, but could indicate either a lower typical mass of O star, or that the peak compression occurs rather sooner than indicated by the location of the dust arm.

This issue is further studied by Rand & Tilanus 1990 as part of their review paper. An offset is seen between the ridges of CO emission (from the interferometric observations) and the peak in the H α emission. This offset is held to represent a 30 million year delay between the compression of the molecular gas and the peak in the

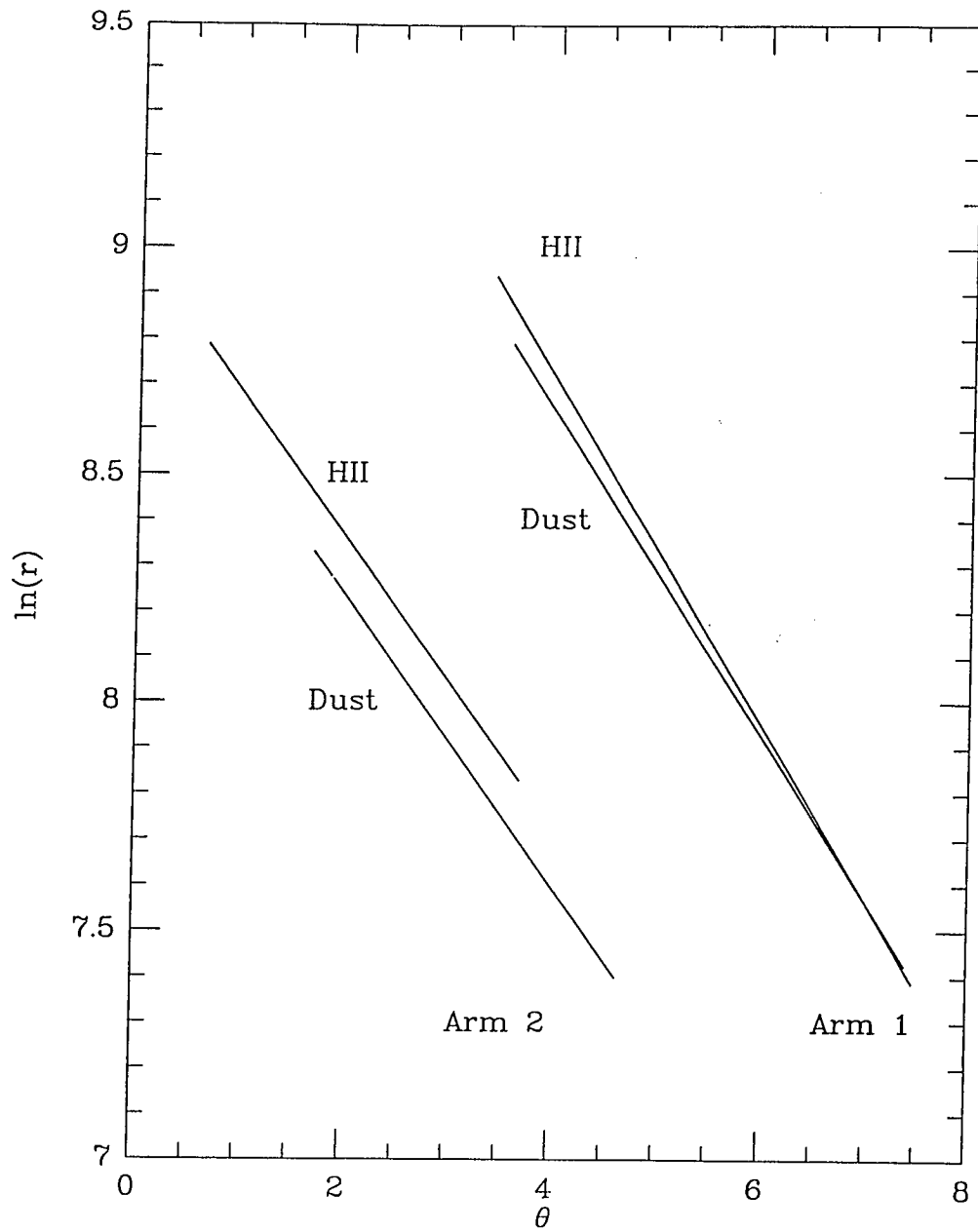


Figure 3.9 A plot of the logarithmic solution to the dust arms in M51 compared to the inner disk solutions represented on Figure 3.7(a). The two components of Arm 1 diverge with increasing radius, while the two components of Arm 2 appear parallel indicating a constant timescale with radius.

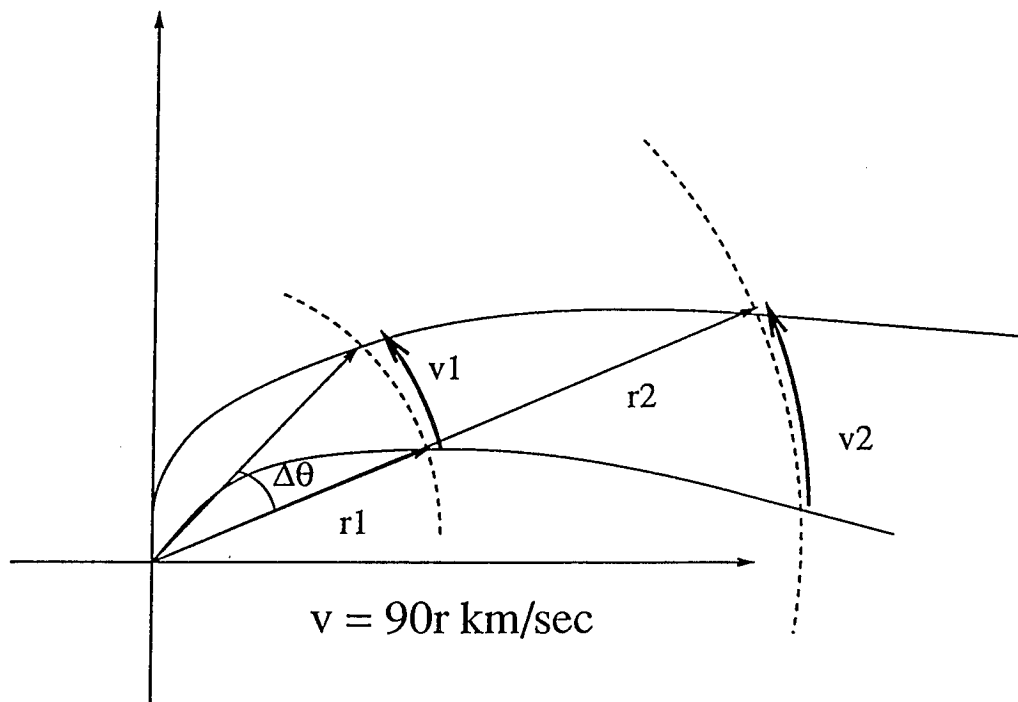


Figure 3.10 A cartoon representing the physical situation being used to calculate the timescale for the density wave to pass from the observed peak in local compression to the observed local peak in star formation.

star formation, rather more than the timescale we derive based on the location of the dust arms. This timescale appears rather long compared to the timescales considered here.

The range in radius that we have studied, the inner disk, it appears that the nature of Arm 1 is unusual when compared to Arm 2. Spatially, Arm 1 is the “Northern Arm” that other authors have referred to in previous work, and is the arm that passes closest to the interacting companion out of the two. The difference between the local angular velocity of material and the underlying pattern speed, $(\Omega - \Omega_p)$, is typically used to characterize the behavior of the spiral pattern. The value of this quantity is seen to decrease as the radius of the inner disk approaches the corotation radius, defined by the quantity being identically zero. In a normal spiral density wave, triggering star formation in a well-behaved galaxy, the angular distance between the dust and H II arms should stay constant. We observe in Arm 1 that this angular distance is increasing with radius, implying that the rate of change of the quantity $(\Omega - \Omega_p)$ is anomalous when compared to the ideal case. The suggestion is that the quantity is decreasing slower than would be expected, for such an increase in angular separation with radius. This can plausibly be interpreted as an immediate effect of the interaction of the northern side of the inner disk with the companion, since the southern arm (Arm 2) appears essentially undisturbed and well behaved.

3.4.4 Star Formation Efficiency

M51 has been the subject for intensive study by observers at radio and millimeter wavelengths, since the galaxy offers an excellent testbed for ideas concerning the processes involved with galaxy-wide star formation. The active interaction that the system is experiencing provides a wide range of star formation conditions from one part of the galactic disk to another. However, specific studies of this variation have only been forthcoming in the past few years.

Knapen et al 1992 presented azimuthal plots of the measured star formation efficiency (SFE) to highlight the contrast between conditions on- and off-arm. They reported considerable contrast between the two areas with a ratio as high as 10-15, as well as a lack of correlation between the peaks in H α and the molecular gas distribution. When calculating the SFE, the observer needs an estimate of both the current rate of star formation, and the amount of material available to that process, in order that any estimate of the efficiency may be made. The emission from the line H α

has been evaluated as a good measure of the recent star formation rate (Kennicutt & Kent 1983). A measure of the amount of material available to form stars may be obtained from the measured column density of atomic and molecular material, commonly measured at 21cm for neutral hydrogen, and at millimeter wavelengths for molecular CO. A correlation exists between the emission measured from CO and the column density of molecular H₂, although the actual determination of the correlation appears to change from paper to paper (cf. the review by Young & Scoville 1991).

For this purpose, we will take our H α imagery to be a good representation of the ongoing star formation in the M51 system. The best 21cm data were originally presented by Rots et al 1990a, and later in more detail by Rots et al 1990b, where observations taken using the VLA produced maps of the galaxy at resolutions ranging from 5" to 34" per pixel. This imagery was kindly made available to the authors, and is in appearance identical with Figure 2 of Rots et al 1990b. The best millimeter-wave data available for this application are the single dish observations that have recently been made by Nakai at the Nobeyama Observatory; interferometric data is inappropriate for this purpose since such observations undersample the important interarm emission. Unfortunately, these data are as yet unpublished, with all existing two-dimensionally complete observations that cover the entire galaxy being interferometric in origin (Lo et al 1987, Rand & Kulkarni 1990).

Single dish observations were made of select positions by Lord & Young 1990, which they used to assemble a thorough study of the SFE and star formation rates evident in the galaxy. Due to a lack of available, spatially complete, two-dimensional single-dish molecular imagery, we will use their Figure 2, and their Table 2, to approximate the CO distribution as a powerlaw function with the appropriate normalization. This has severe limitations as the local distribution of molecular material is almost certainly concentrated locally about the arms, from the results of the interferometric imagery. The data presented in columns 2 and 4 of their Table 2 may be fit using a powerlaw in r , with the best solution being,

$$N(H_2) = 10^5 r^{-1.4} \quad (3.7)$$

with N in units of $M_{\odot} \text{ pc}^{-2}$, and r in units of 2 arcseconds (the plate scale of the HI imagery produced by Rots et al). Using this relation, appropriately deprojected and rotated in the plane of the sky, we modelled the molecular hydrogen distribution to complete the estimate of the available gas density for star formation.

The peak number densities for the atomic gas are quoted by Rots et al as being around $5 \times 10^{21} \text{ cm}^{-2}$, or $40 \text{ M}_{\odot} \text{ pc}^{-2}$, although the typical value across the face of the galaxy is around half this. The typical number densities quoted for the molecular gas, from Lord & Young, varied between 2-3 and $30 \times 10^{21} \text{ cm}^{-2}$, or between 15 and $250 \text{ M}_{\odot} \text{ pc}^{-2}$. Over the majority of the inner disk ($r < 6 \text{ kpc}$) the molecular contribution to the local gas density is seen to dominate over the atomic gas contribution (Lord & Young, Figure 2b).

The resulting SFE map is included as Figure 3.11, and illustrates the rather high contrast in SFE from on-arm to off-arm that has been reported by Lord & Young and Knapen et al. Numerically we see very similar relative efficiencies between the arms and the interarm regions, of about 4-5 times. The broken appearance of the image is due to the inner paucity of HI emission reported by Rots et al, resulting in a complete calculation being impossible for those areas.

SDH performed a SFE analysis based on earlier work by Kennicutt, that plotted the available gas density versus the observed $\text{H} \alpha$ flux to make a measure of the effective local collapse density, and for comparison a similar calculation was made for the M51 data. The local collapse density is that space density of material above which the energy density of the cloud, based on thermal kinetic energy, exceeds the local energy density of the ISM that under pressure balance prevents the medium from collapsing. This type of plot was also assembled by Lord & Young (their Figure 3a) but they only used two radial bins. In this analysis we shall use 4 radial bins, each of width 3 kpc, to study the change in the apparent collapse criterion with radial ordinate. Figure 3.12 illustrates the results of the calculation. The horizontal clustering around a common mean value indicates the most likely value for the local density above which collapse to form stars is possible.

In direct comparison with Figure 11 of SDH, we again see the migration of the mean gas surface density from higher levels in the inner portion of the galaxy to lower levels in the outer parts of the disk. This is indicated by the population histograms at the base of each panel. There is an appreciable change in the local density from the inner 3 kpc to the outer 3 kpc of the inner disk (the inner disk will be defined as that portion of the disk interior to the break in pattern speed illustrated by Figure 6; ie. interior to $r = 6 \text{ kpc}$), with a much wider spread of densities being displayed in the inner disk.

Outside the pattern break, the distribution in surface densities is much tighter with no more than a 0.2-0.3 dex spread in value. Over the full range of radii used, the

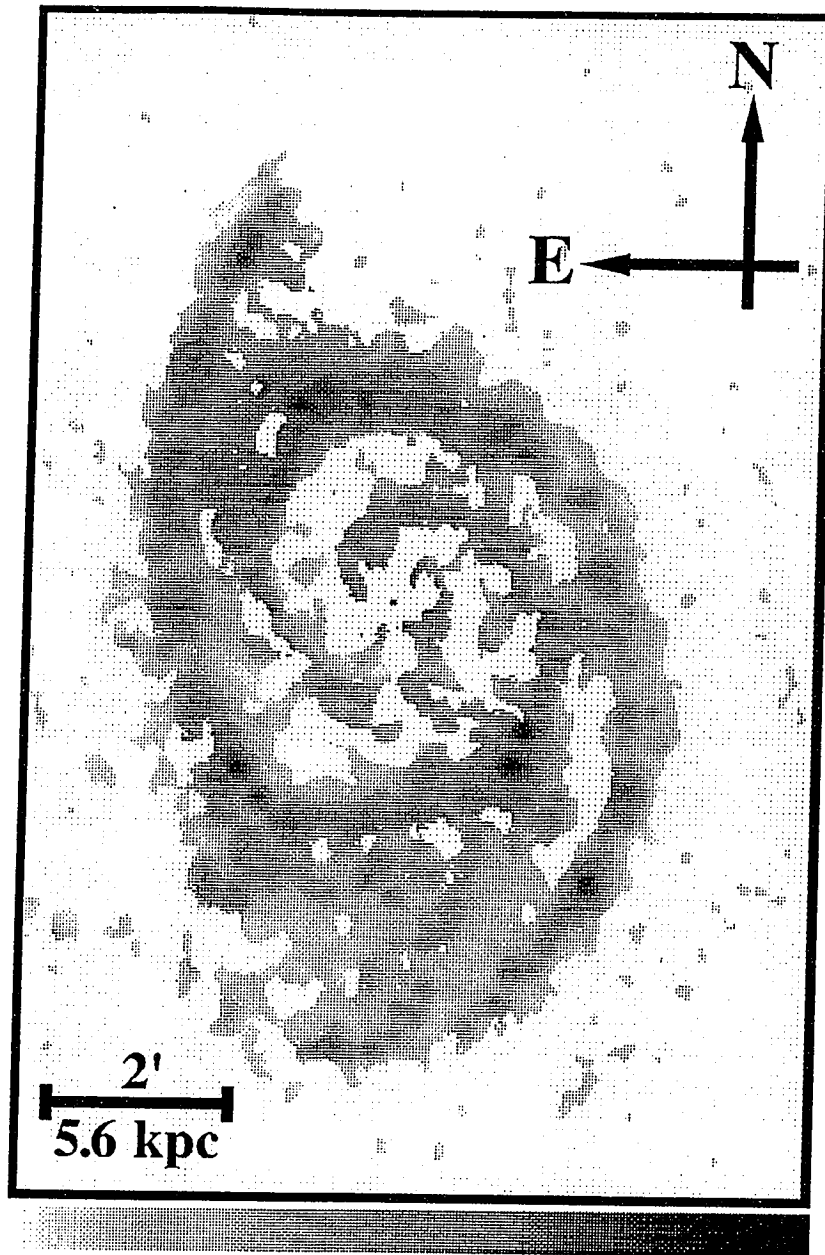


Figure 3.11 Spatial representation of the star formation efficiency (SFE) across the disk of M51. The contrast between the efficiency on-arm to that off-arm is very evident, in complete contrast to the much more uniform distribution seen in Figure 10 of SDH. The display range used is logarithmic from 10^{-19} to 10^{-16} $\text{ergs cm}^{-2} \text{sec}^{-1} M_{\odot}^{-1} \text{pc}^2$.

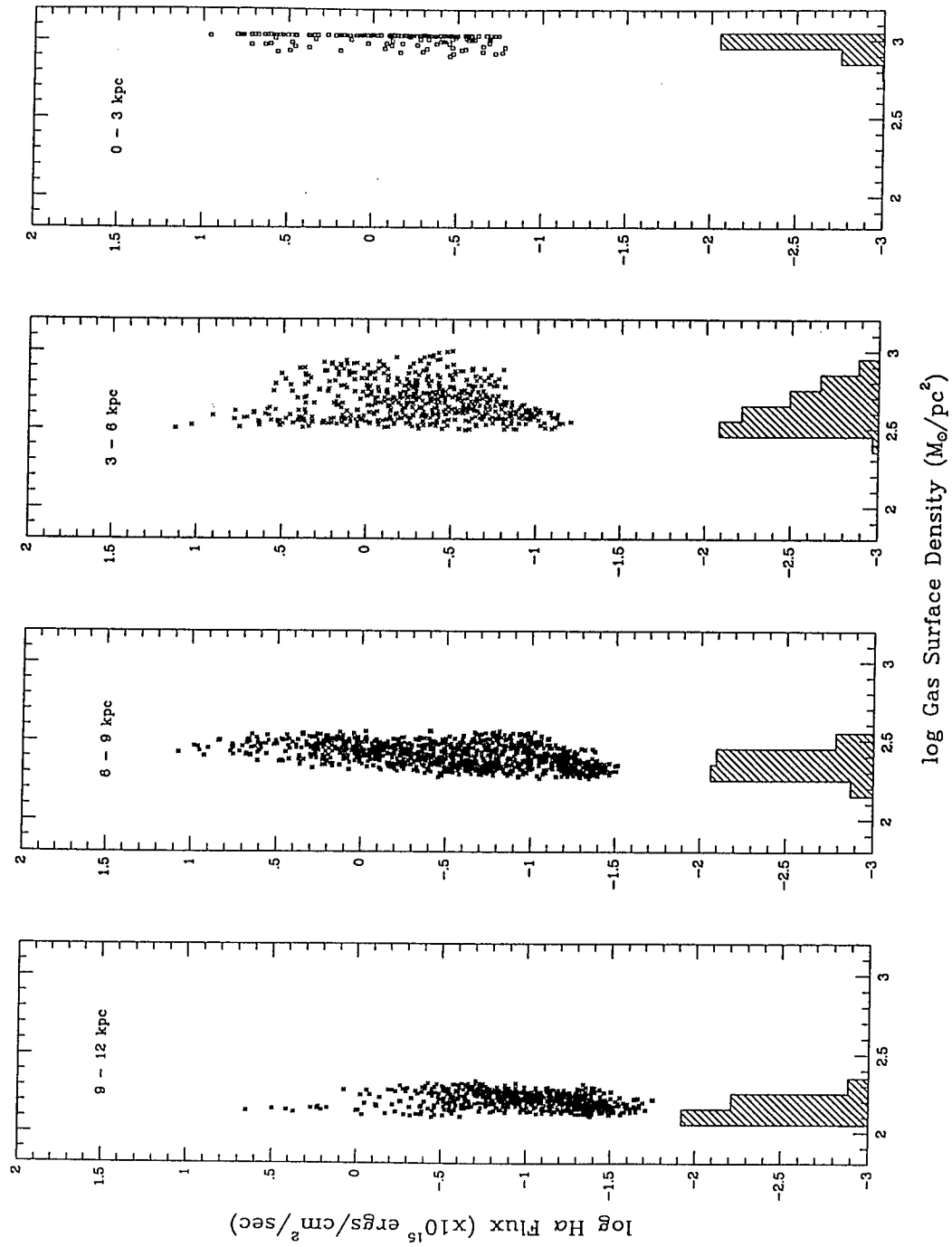


Figure 3.12 Analysis of the star formation law exhibited by the galactic disk of M51. A marked drop in the median gas surface density, a measure of the local collapse density for star formation, is seen with increasing radius.

faintest region emission detected in each distribution monotonically decreases with increasing radius. It would appear that these general trends are a common factor amongst late-type spirals.

Comparison of the actual derived values for the surface densities reveals that M51 possesses a much lower mean surface density of neutral gas than does M101. In the outer disk of M51 there is more than an order of magnitude difference between the derived surface density of gas and the corresponding value in M101. The mean level of the $H\alpha$ flux is also about an order of magnitude lower than seen in M101, even though the distances assumed to both objects are quite comparable (7.4 Mpc for M101, 9.6 Mpc for M51).

3.5 Summary and Conclusions

This chapter has dealt with several facets of the nature of the M51 system. To aid the reader, we will summarize the more salient points.

1. In this study we present the first complete set of optical emission line fluxes for a set of 465 H II regions complete down to a luminosity of $10^{37.5}$ ergs sec⁻¹. For these objects, we have derived accurate positions, fluxes, estimates of reddening, excitation, oxygen abundance and [S II]/H α ratios. We have identified all but 15 of the set of H II regions most used prior to this study, that of Carranza et al 1969.
2. Using several identification thresholds, we have found that systematic variations in these derived quantities are only exhibited by the brightest H II regions in the galaxy. Although it is tempting to invoke a recycling argument to remove all similar properties in fainter regions (when considering the results for M101 by SDH), basic theoretical considerations make this approach counterintuitive. We favor an explanation that involves an incomplete sample of faint regions (luminosity $< 10^{37.5}$ ergs sec⁻¹) obscured by considerable amounts of local dust, enough to impact the very emission characteristics of the regions.
3. Magnitudes of derived gradients in the emission properties exhibited by these bright regions have been compared to those values derived for M101. The reddening gradient appears about equal although the excitation, and accordingly the oxygen abundance, gradients do appear much lower than that seen in M101.
4. We compare our LF with that assembled by Rand 1992, and have indicated that our imagery is almost as deep but that some of the regions counted by Rand may be fictitious since our original LF was very similar to Rand's before a visual check was performed on the sample. We advocate that positive visual identification of each region is a vital check involved with any automated H II region selection procedure.
5. An attempt to mathematically describe the well-defined arms of the galaxy, using two different theoretical prescriptions, yielded results that agreed with existing ideas on the nature of the inner and outer disk of the galaxy. From Tully 1974c, we see that the inner disk ($r < 6$ kpc) appears to be a well behaved spiral with a pattern speed of $90 \text{ km sec}^{-1} \text{ kpc}^{-1}$, while the outer disk appears to be corotating with the companion at a pattern speed of about $70 \text{ km sec}^{-1} \text{ kpc}^{-1}$. This causes a break in the spiral pattern that is not immediately apparent to the unaided eye, with the two spiral patterns being misaligned at a radius of around 6 kpc, a distance that is estimated to be very close to the corotation radius. If the mathematical descriptions

are to be believed, the inner disk supports its arms through spiral density waves, while the arms of the outer disk are supported by the galactic rotation curve and are therefore material in origin.

6. Estimates of the timescale between local compression and the peak in star formation have been made based on the apparent separation of the arms delineated by the dust and H II regions respectively. This timescale is found to be a constant at 4.6 Myr for Arm 2, and an increasing function of radius for Arm 1 although the actual value for the timescale is less than that exhibited by Arm 2. The two timescales do not become equal until a radius far outside the corotation radius (13.3 kpc, compared to around 6 kpc) where the spiral density wave description used for this analysis becomes invalid.

7. An analysis of the star formation efficiency apparent in the system confirms earlier results concerning the high contrast between the arms and the interarm regions. A two-dimensional map of the efficiency has been assembled using the high resolution data previously published by Rots et al, and by modelling the CO emission with an exponential law derived from the single dish measurements of Lord & Young. A change in the local collapse density for star formation is observed with radius, complementing a similar trend seen in M101 by SDH. The magnitude of the available gas surface density is an order of magnitude lower in M51 than in M101.

In conclusion, the M51 system is a very complicated and dynamic system. Most of the unique properties exhibited by the system appear, not surprisingly, to be directly related to the interaction the disk is experiencing with the companion. This paper marks the most comprehensive study of the H II region population of the galaxy, and complements the other physical properties of the galaxy studied in the past decade. The dusty nature of the ISM in the galaxy appears to prevent the detection of any systematic variations in the emission from the fainter H II regions. The other emission properties imply that the very dusty ISM also has an intimate effect on the emission mechanisms of the H II region population itself.

Chapter 4

Line Emission from the Irregular Galaxy NGC 4449

4.1 Introduction

The galaxy NGC 4449 is commonly described as the archetypical giant Magellanic irregular galaxy. It displays a rich set of H II regions coupled with dramatic streamers of H α emission that permeate the entire structure of the object. It has been classified as an IB(Im) by de Vaucouleurs et al 1976, while the distance to the object is quoted as 5.0 Mpc (Sandage and Tammann 1975).

Due to its proximity and high surface brightness, this galaxy has been featured in many studies of the gaseous and stellar content of irregular galaxies and discussions of apparent star formation processes in such low mass and gas-dominated systems. Such studies include work by Shostak & Allen 1980, Gallagher et al 1984, Tacconi & Young 1985, Hunter & Gallagher 1986, Thronson et al 1987, Tacconi & Young 1987, and Sasaki et al 1992. Due to the low metal abundances in NGC 4449, the detection and analysis of the molecular gas is difficult and very incomplete.

The characteristics of the observed line emission, from both the H II regions and the observed streamers, have been studied by Lequeux et al 1979, Sabbadin and Bianchini 1979, Talent 1980, Blair et al 1983, Sabbadin et al 1984, Blair et al 1984, Bothun 1986, Malumuth et al 1986, Hartmann et al 1986, Kennicutt et al 1989, Skillman et al 1989, Hunter & Gallagher 1990 and Hunter & Gallagher 1992. Although the extensive spectroscopic study of the H II regions in H α has been made by several researchers, there is a lack of any narrow-band imagery in published form. Accordingly this paper will fill a need for two-dimensional evaluation of the ionization structure within the system as more than one emission line.

This chapter marks the third and finally part of work that comprises the Ph.D. thesis of one of the authors (P.A.S). Accordingly references will be made to two earlier papers: Scowen et al 1992a (Paper I), and Scowen et al 1992b (Paper II). We will discuss the data reduction and calibration in §2, present the results of the analysis

of the imagery in §3, and discuss these results in the context of the earlier work presented in Papers I and II in §4.

4.2 Data Reduction and Calibration

The CCD imagery was taken using the WFPFUEI device used in Papers I and II. The same optical configuration, and interference filters, were employed. Table 4.1 includes a log of the observations made. Narrow-band imagery was taken through interference filters with bandpasses covering H α , H β , [O III] λ 5007 and [S II] λ 6716+ λ 6731. Additional wide-band imagery covering adjacent portions of the continuum emission to these bandpasses was also taken to allow the continuum contributions to the line-emission to be subtracted.

Flattening and registration of the imagery were performed using IRAF[‡]. Using a set of 193 foreground reference stars the images were aligned to better than 0.1 pixel. Aperture photometry was performed on the same set of stars, so that the resulting stellar intensities could be used to match the relative intensities of each of the stars in each image, allowing the appropriate scaling of each line image to the corresponding continuum image. This allowed the continuum component of the emission imagery to be subtracted, leaving just the line emission.

Table 4.1 Details of Observations made of NGC 4449

Date (UT)	Filter Å (λ /FWHM)	Filter	Exposure (secs)	Field Center (1950.0)	
27 Feb 1987				12 ^h 25 ^m 48.6 ^s	+ 44°21'47.0''
	6574/20	H α +500	100, 1500		
	6450/104	RC1	100, 500		
	6730/36	[S II]	1200		
	5014/32	[O III]	100, 3000		
	5103/98	GC2	100, 500		
28 Feb 1987					
	4869/31	H β	2000		
	4805/75	GC1	500		
	6730/36	[S II]	100, 3000		

[‡]IRAF is distributed by the National Optical Astronomy Observatories, which is operated by the Association of Universities for Research in Astronomy, Inc., under cooperative agreement with the National Science Foundation.

Calibration of the imagery was performed using two independent methods, allowing cross-checking to prevent miscalibration. The successful calibration of CCD imagery is very difficult to achieve, as was experienced in Paper II. The first method employed the unpublished spectrophotometry of Talent 1980, performed as part of his Ph.D. thesis work – and to this day one of the best sources of spectrophotometry for the larger H II region complexes in NGC 4449. Simulating the apertures he used in his work, we developed calibration coefficients which scaled our line imagery to the correct flux levels.

The eventual solution employed in Paper II involved the use of the existing calibration database for a Galactic H II region survey, in preparation at this time, that used the same filter set. Since the NGC 4449 imagery was taken as part of the same observing run as the M51 imagery, we decided to use this database to check our calibration using Talent’s data. The comparison was very favorable, resulting in coefficients that agreed to within 40%. Since the datasets used by Paper II were so successful when compared to other existing spectrophotometry, it was decided to use the survey database again for this set of imagery.

4.2.1 Selection of the H II regions

Papers I and II used different methods to identify their H II region populations. In the first paper, an automatic algorithm was used that identified each region as a separate ionized volume, and allowed calculation of the emission and physical properties of each region. This method assumed a uniformly dark background against which the regions were set, allowing an easy separation of each region from its neighbor when employed with a detection threshold.

This technique was defeated in Paper II where the H II region population was set against an ambient H α component that varied in brightness by two orders of magnitude from the inner to the outer disk. Accordingly a different approach based on Stetson’s DAOFIND algorithm was employed. This was somewhat satisfactory but required a visual check of all H II regions before they were included in the final set of regions analyzed, Appendix B. The rejection level was around 17% (or 30 misidentifications).

In this galaxy, the H II region population is set against the same type of varying background emission encountered in Paper II with M51. However, the angular extent of the galaxy is substantially less than the extent of M51, as is the apparent space den-

sity of H II regions. Accordingly the more “traditional” approach of hand-identifying each region was taken, identifying some 160 H II regions within the structure of NGC 4449.

Having identified each region spatially, aperture photometry was performed using the list of coordinates on each emission line image to generate line emission data for each region. Using an accurate celestial coordinate list for the observed foreground stars (from the Guidestar Catalogue) and the assumed distance of 5.0 Mpc to the galaxy, accurate coordinates and radial positions for each region were also calculated. The center of the galaxy was taken to be represented by the kinematic center identified by Malumuth et al 1986, and used accordingly. A list of the adopted physical characteristics of the galaxy is included as Table 4.2.

Using the results of these measurements, derived line ratio quantities were calculated for each region, along with their physical positions, and these quantities have been assembled into Appendix C. Using the empirical correlation between the ratio of $[\text{O III}]/\text{H } \beta$ and the oxygen abundance O/H presented by Edmunds & Pagel 1984, the excitation values have been re-expressed in terms of the abundance exhibited by each region.

The original nomenclature standard was assembled by Crillon & Monnet 1969, and was used by numerous researchers until the late 1970’s. This work was superseded by Sabbadin & Bianchini 1979, who set the new standard. Accordingly, in Appendix C, we have included the corresponding SB notation used for the H II regions in their set.

4.2.2 Line ratio imagery

Having calibrated the imagery, we proceeded to produce line ratio images. Traditionally these kinds of images are very confusing in appearance due to the noisy characteristics of the sky regions. This results from the very low levels of emission at the sky level being included in a ratio where alternately large and small values result. To avert this troublesome phenomenon, and to ensure good visual representation of the results, we employed a masking technique similar to that used in Paper I.

In order that we might better evaluate the two-dimensional nature of the galaxy through the emission lines we observed, line ratio images were produced using a technique to maximize the evident structure. In each image a threshold was chosen at the 3σ level and all ratios below that set to zero. The line ratios were then calculated

Table 4.2 Basic Physical and Geometric Information for NGC 4449

Distance used:	5.00x10 ⁶ parsecs
Tilt Angle:	0.0 degrees
Position Angle:	0.0 degrees
Galactic Center at:	12 25 46.1 RA, 44 22 16.7 Dec
Epoch of coords:	1950.0
Image Plate Scale:	1.190 arcsecs/pixel
Image Distance Scale:	28.9 parsecs/pixel
Field Rotation:	0.97 degrees
Error in RA:	0.05 sec
Error in Dec:	0.30 arcsec
Aperture Used:	4.0 arcsec

using these images to produce the final noise-free products. This technique appeared to work very well.

Figure 4.1 illustrates the deep H α imagery, presenting the rich population of H II regions we have studied, and the “interstellar froth” described by Hunter & Gallagher 1990. Successively, Figures 4.2, 4.3 and 4.4 illustrate the ratio imagery described above. A discussion of the components evident in this imagery may be found in the next two sections.

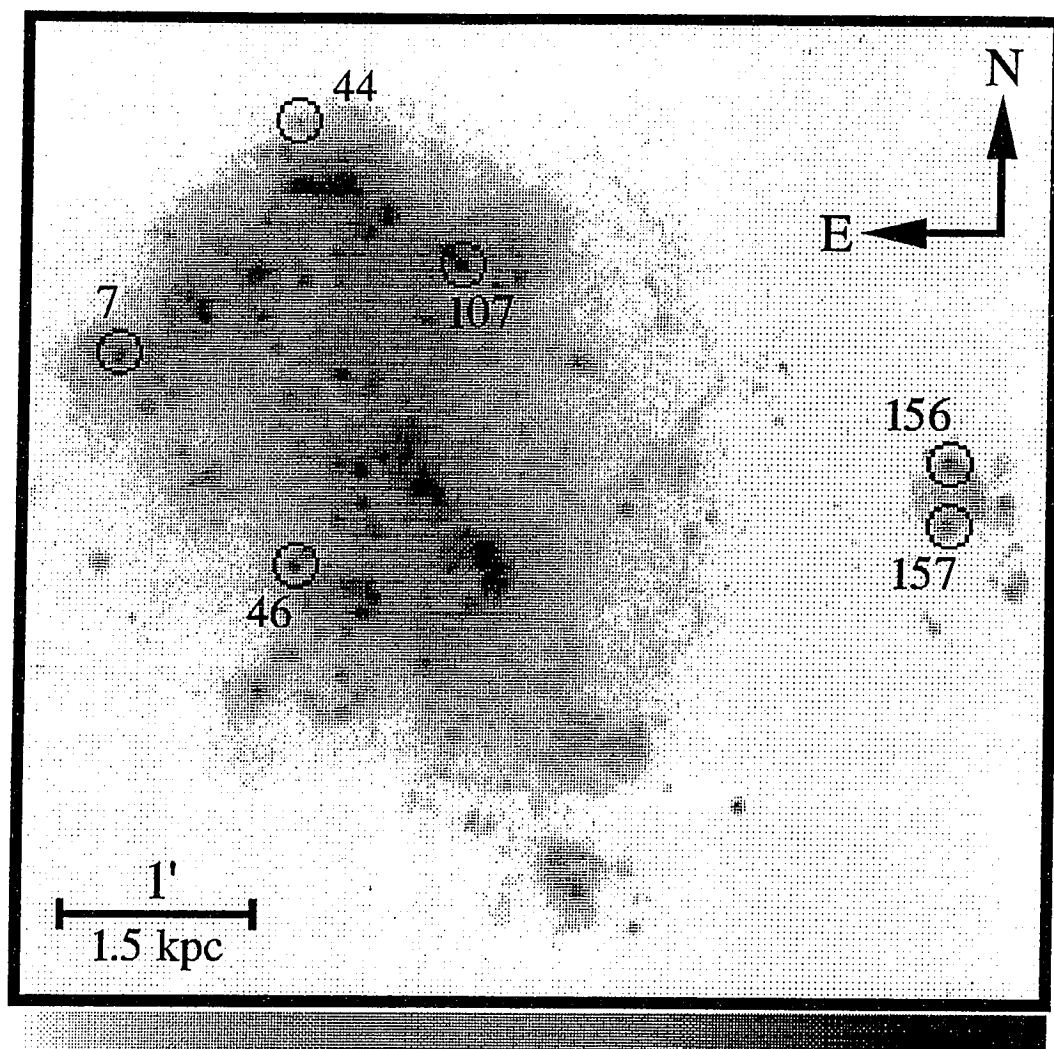


Figure 4.1 Continuum subtracted H α line emission image of NGC 4449 displayed logarithmically between the limits of 10^{-16} and 3×10^{-14} ergs cm $^{-2}$ sec $^{-1}$.

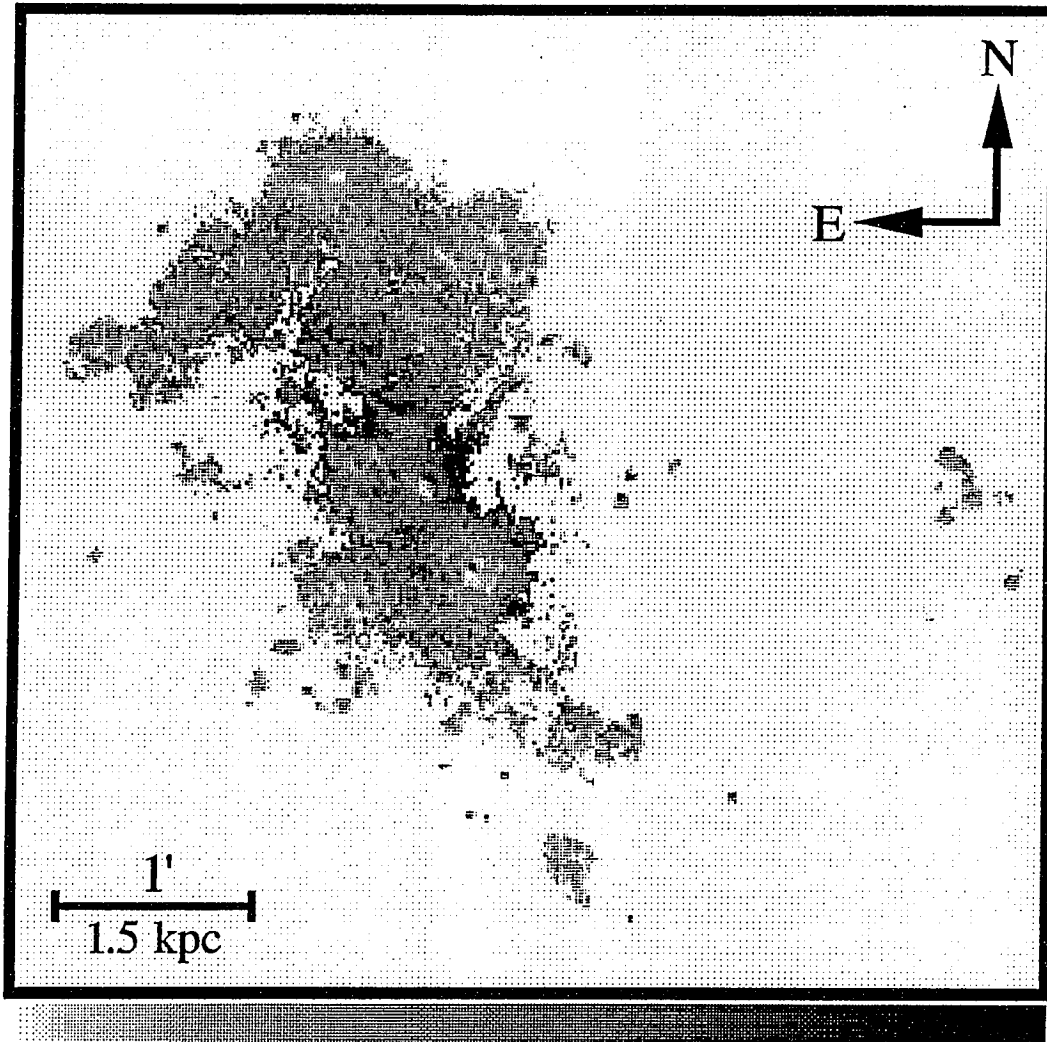


Figure 4.2 The line-of-sight reddening displayed two-dimensionally using the Balmer decrement, $C(H\beta)$. The image is displayed between the limits of 0.0 and 1.5.

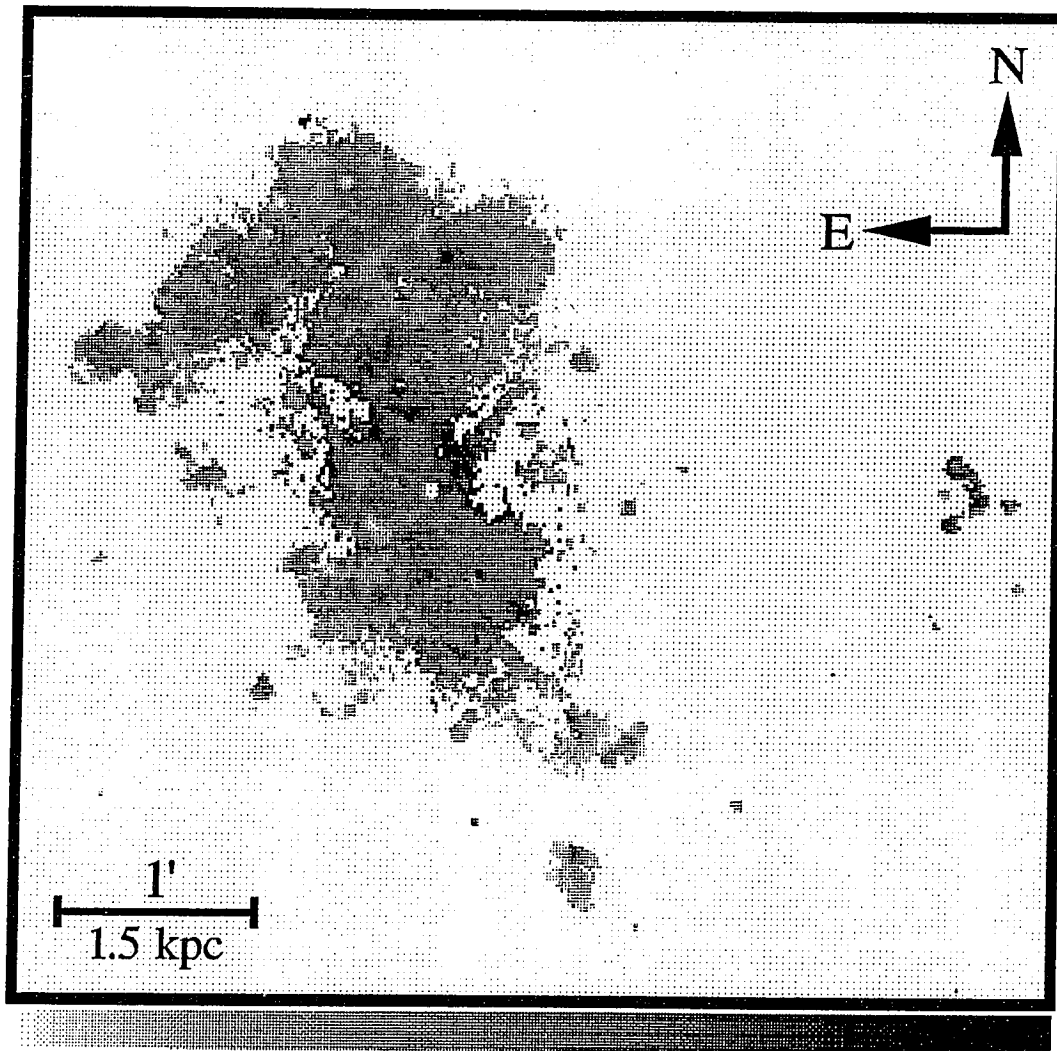


Figure 4.3 The excitation of the ionized gas, as measured using the ratio of $[\text{O III}]/\text{H } \beta$, displayed logarithmically from -0.2 to 0.8. Note the bright signature of the supernova remnant SB 187 in the north of the galaxy.

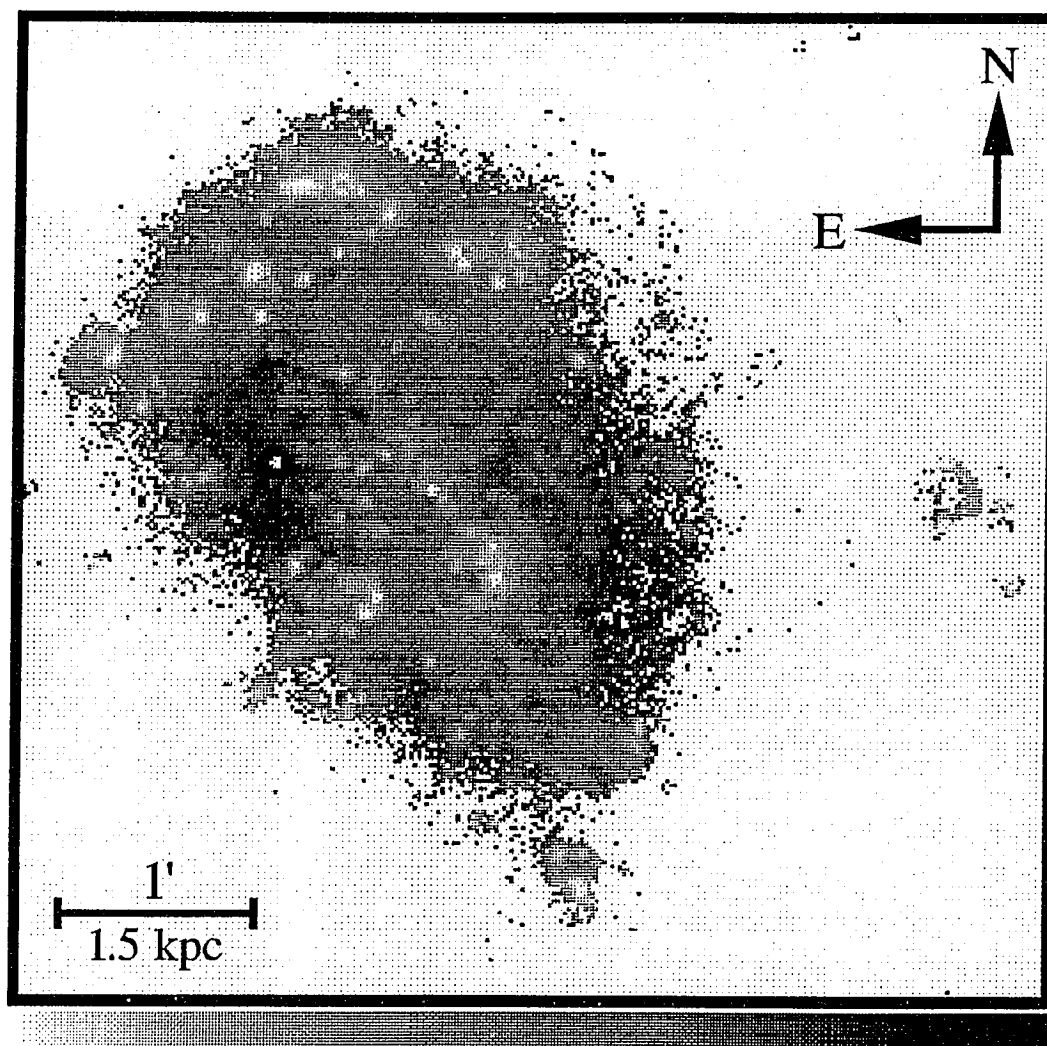


Figure 4.4 The value of the ratio of $[\text{S II}]/\text{H } \alpha$, displayed logarithmically between -1.0 and 0.0. Note the two filaments wrapped around the superassociation in the south of the galaxy.

4.3 Results

4.3.1 The H II Regions

An initial attempt at studying the H II regions in NGC 4449 was discussed by Scowen & Dufour 1992. In that paper, the original H II region identification technique from Paper I (based on threshold boundaries) had been used with little success other than to derive the median levels of the line ratios evident in the H II region population. The reason for this failure was the same (though more extreme) as that encountered in Paper II, that the ambient background emission from H α , not immediately associated with any H II regions, varied by a couple of orders of magnitude across the galaxy. Accordingly the use of a single threshold to identify the H II regions was futile. However, even with this data, a lack of radial variations in the line ratios derived was apparent.

Using the technique described in the previous section, a more successful attempt at defining and extracting the H II regions was made. The resulting datasets provided a much more extensive set of results for analysis than had been available previously. We produced new versions of the radial variations in the derived integrated emission properties of the H II regions, these are presented as Figure 4.5(a) - (d). With such an increase in the population of H II regions studied, any small radial variation, if present, should become apparent. As Figure 4.5 indicates, all derived emission properties are isotropic with radius.

Considering Figure 4.5(a), the distribution of the extinction derived from the Balmer decrement appears to be remarkably uniform, with variation being apparent only at the very periphery of the galaxy where a drop of about 1 magnitude of A_V is observed, at a radial distance of about 4 kpc. This is well outside the optical body of the galaxy, approaching the distance typically associated with the removed arc of emission directly to the west of the galaxy (see the next section). The radial distance quoted here is relative to the kinematic center identified by Malumuth et al 1986, which falls very close to the optical center of Sabbadin & Bianchini 1979. This bright core of emission, is identified in this study as region 93, in Appendix C.

Several H II regions are apparent at $R \sim 2.5$ kpc which have abnormally high values of $C(H\beta)$. Subsequent identification of these regions on the imagery reveals them to be low surface brightness regions at the very edge of the optical main body of the galaxy, rather isolated, and possibly rather dusty by comparison with their

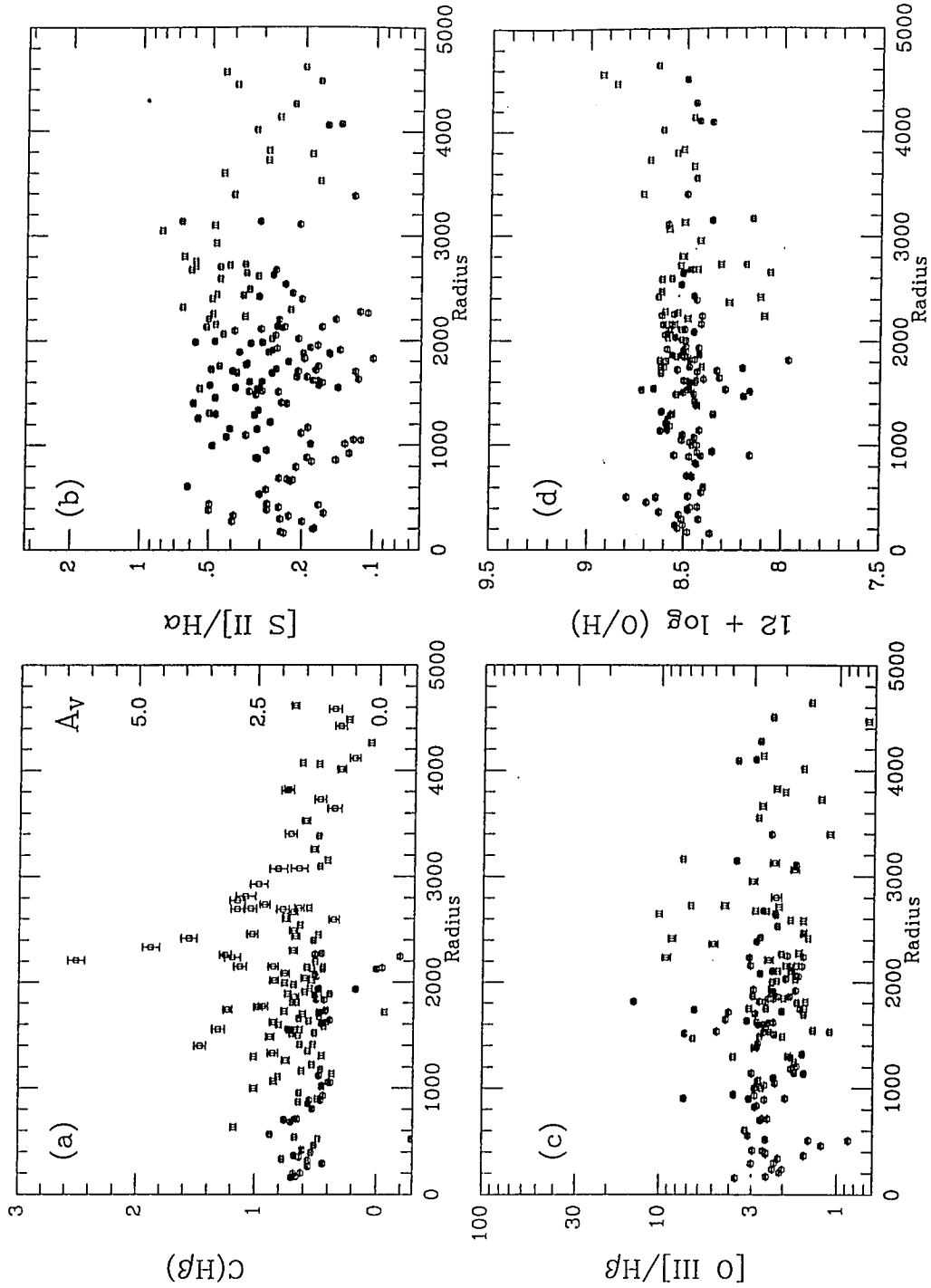


Figure 4.5 The derived emission properties of the H II region population, as a function of radial position (in parsecs). (a) The reddening as a function of radius. (b) The value of the ratio of $[S II]/H \alpha$, exhibiting a large scatter with essentially no systematic variations. (c) Excitation as a function of position, again no systematic variation. (d) Inferred oxygen abundance as a function of radial position.

counterparts closer in. Based purely on these gross properties, it is possible that these objects are older supernova remnants.

The distribution of integrated values of the ratio of $[\text{S II}]/\text{H } \alpha$, shown in Figure 4.5(b), appears to imply an essentially flat distribution of conditions within the set of H II regions. There appear to be no preferentially low or high values at any location within the galaxy, as well as there being no apparently anomalous H II regions as far as this ratio is concerned. This probably reflects another effect of the ubiquitously high star formation rate over the entire galaxy, where no specific part of the galaxy is preferentially active in star formation over another, in direct contrast to the mechanisms that drive star formation in spiral galaxies. The lack of any specifically interesting H II regions may seem odd, but this galaxy more than makes up for this paucity with other visually selected objects (see below).

The distribution of excitation values with position, indicated by Figure 4.5(c), also appears quite flat. There is some scatter, with some higher values being returned by objects in the radial range between 1 and 3 kpc, but these are more likely to be associated with the non-H II region objects studied in the next section, since many associations appear common. The very highest ratio value is given by region number 39 in our sample, which appears to be a large object with extraordinarily high levels of oxygen emission. The oxygen-rich supernova remnant SB 187 discussed later appears as a member of the high scatter regions, but does appear particularly extraordinary on this plot.

These levels of excitation may be transformed into abundances using the correlation between the $[\text{O III}]/\text{H } \beta$ ratio and the derived oxygen abundance identified by Edmunds & Pagel 1984. Using this relation we reproduce the same rather low levels of oxygen abundance reported by Skillman et al 1989. Caution needs to be employed when using this correlation, because for high values of the ratio $[\text{O III}]/\text{H } \beta$, or low values of the oxygen abundance, there is an ambiguity which may result in possible errors in the individual estimates of abundances. The levels of $[\text{O III}]/\text{H } \beta$ seen in NGC 4449 fall very close to this area of concern. Having taken this into account, our values are still very comparable to existing estimates, the median level of abundance across the face of the galaxy being about 8.5 for the value of $(12 + \log(\text{O}/\text{H}))$.

In Paper II an appreciable problem with the underlying absorption of emission from the H β line from H II regions was discovered, which led to counterintuitive correlations between the derived ratio of $[\text{O III}]/\text{H } \beta$ and the value of $C(\text{H } \beta)$. In retrospect, this problem was also detected on a smaller scale in the datasets from

Paper I. Accordingly similar plots were made for this sample of regions, and are presented in Figure 4.6. The lack of any appreciable correlation between the 3 sets of emission properties and the $C(H\beta)$ ratio indicates that there is no systematic underestimation of the $H\beta$ emission for each region, of the kind that was evident in the two earlier papers.

In Figure 4.6(b), several regions stand out as being curious, having either low $[O\text{ III}]/H\beta$ for a given $C(H\beta)$, or high $C(H\beta)$ for a given $[O\text{ III}]/H\beta$. Further study of the latter type of regions indicates that they are the same three regions discussed earlier that appear towards the edge of the optical galaxy. The two low excitation regions are again low surface brightness $H\text{ II}$ regions that are part of the arc system of regions that appear about 2 kpc to the west of the main galaxy. The derived reddening is generally lower at this distance, with the regions falling on the tail in Figure 4.5(a) mentioned earlier, where the resulting values of $C(H\beta)$ are falling off from the plateau exhibited across the optical component.

A differential luminosity function may be assembled from the tabulated surface brightness values we have measured for each of the $H\text{ II}$ regions. Using this it is possible to make some statement about the completeness of our sample. In Figure 4.7 we present the luminosity function scaled to absolute luminosity units using the assumed distance of 5.0 Mpc. Following the same comparison used in Papers I and II, we have compared the distribution of $H\text{ II}$ regions to the estimated integrated luminosity of the Orion Nebula as a standard comparison. We see that our sample is deep enough to reach regions of comparable luminosity, and since the distribution shows a marked turnover at lower luminosities, it appears that our sample is complete to those levels. The peak in the distribution is estimated to be at 10^{38} ergs sec $^{-1}$, with a low luminosity cut-off at $10^{36.8}$ ergs sec $^{-1}$.

4.3.2 Objects of interest within the galaxy

Comparisons between the various high resolution line emission images can yield some very interesting candidate objects. In this section we will identify and discuss several of the more notable ones. For easy acquisition the position of each of these objects within the various figures has been labelled on Figure 4.1.

1. Region 46. This is a relatively unremarkable object as far as the derived emission properties are concerned. The interest comes from the morphological information presented in an image of the ratio of $[O\text{ III}]/H\alpha$, Figure 4.8. This image was also

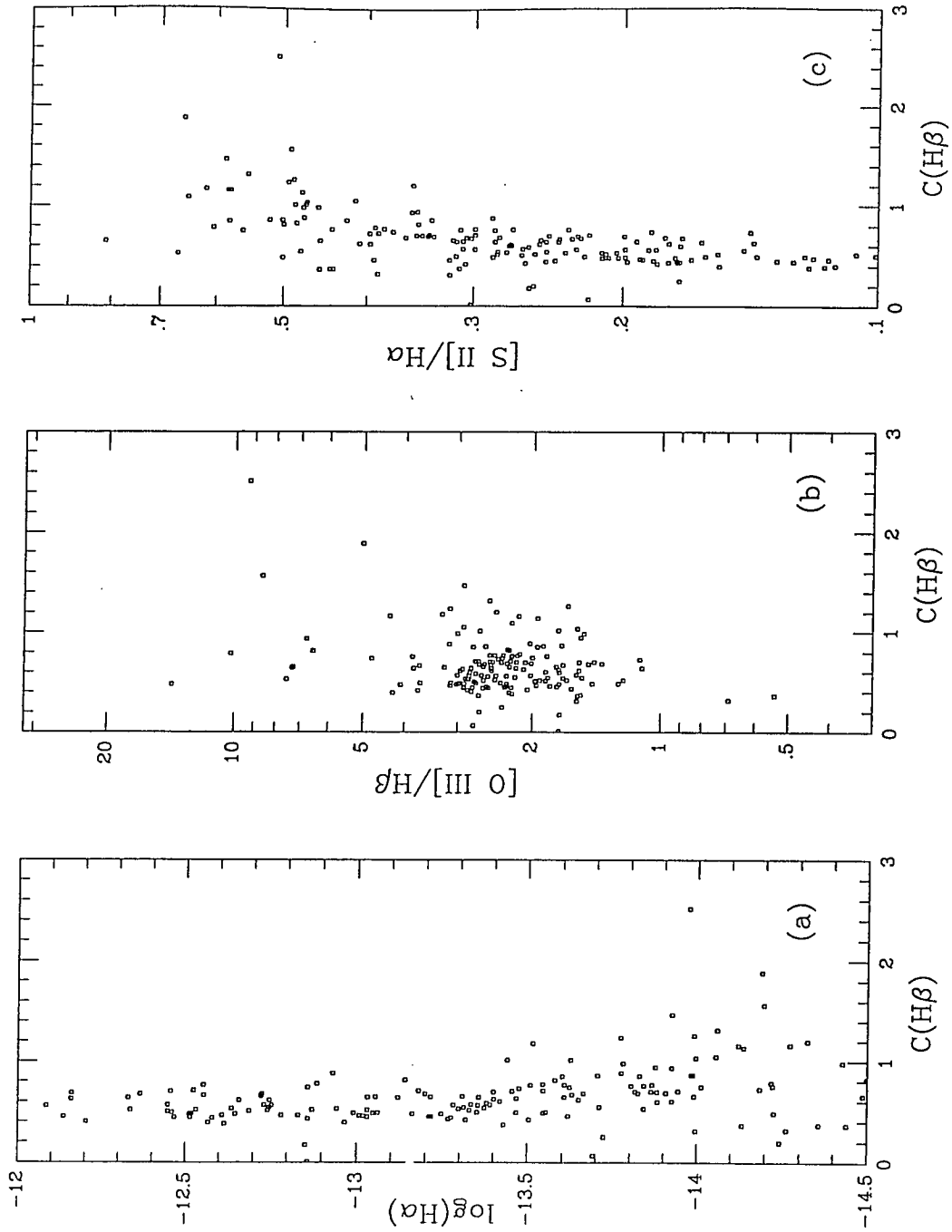


Figure 4.6 Plots of the derived emission properties of the H II regions as a function of their reddening values. No systematic variations are observed between the H II region reddening and (a) surface brightness, (b) the region excitation, and (c) the value of the ratio of $[S\ II]/H\alpha$.

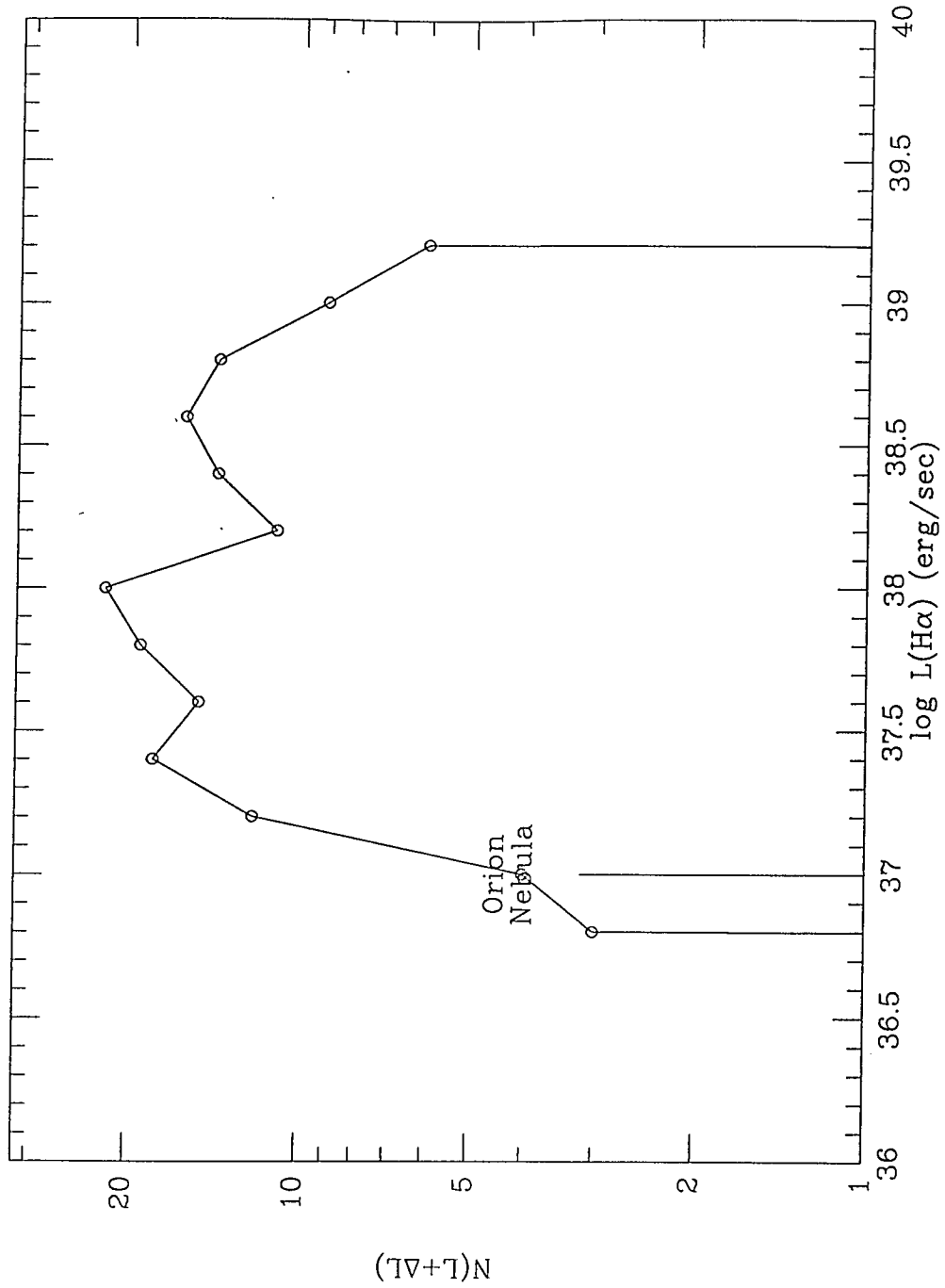


Figure 4.7 H II region luminosity function. The peak in the distribution occurs at 10^{38} ergs sec^{-1} , with a low luminosity cut-off at $10^{36.8}$ ergs sec^{-1} .

created since there are sections of the galaxy where we simply run out of $H\beta$ photons. In this image, a bright arc is seen to surround the object completely on the southern side. The tempting explanation for this structure is that it is a giant supernova remnant (the radius of the arc appears to be around 3 pixels, or about 90-100 parsecs) but the value of the ratio of $[S\ II]/H\ \alpha$ ratio seems rather low. However, the derived level of emission from the known supernova remnant SB 187, discussed in the next section, also appears low. Indeed in an image of the $[O\ III]/[S\ II]$ ratio, Figure 4.9, both SB 187 (our region 104,107) and region 46 appear very bright indicating highly shocked and ionized gas, or a predominance of oxygen over sulphur. The reason for these unexpectedly low values of the $[S\ II]$ emission may be directly attributable to the low metal abundances generally seen across this galaxy.

2. Region 107. This is the host giant $H\ II$ complex that contains the supernova remnant SB 187. This object is discussed in detail later, but it was included here for completeness. The remarkable thing about this object is the physical size of the ionized volume despite the rather ordinary levels of the emission properties we observe. This large region lights up as a bright, football shaped object in the image of $[O\ III]/H\ \alpha$, indicating the high levels of excitation, as well as relatively higher abundances of oxygen, throughout the volume.

3. Region 44. This is an inconspicuous $H\ II$ region at the very northern edge of the optical galaxy. It appears bright in the ratio images $[O\ III]/H\ \alpha$, $[O\ III]/H\ \beta$ and $[O\ III]/[S\ II]$. There are no morphological distinctions about this $H\ II$ region, but its location so close to the edge of the galaxy, coupled with its probably low metal abundances, makes this an interesting object to probe for conditions in the interstellar medium peripheral to the main body of the galaxy, allowing study of the extragalactic medium just exterior to this region of star formation. This will provide insight into the effect of such star formation on the properties of the gas immediately outside the system.

4. Region 7. This is a large $H\ II$ region complex, that comprises several cores listed separately by Sabbadin & Bianchini. The volume appears typical in terms of the levels of both the excitation from $[O\ III]/H\ \beta$ and $[O\ III]/H\ \alpha$, as well as the large “dark” area presented in an image of the $[S\ II]/H\ \alpha$ ratio. In the ratio image for $[O\ III]/[S\ II]$, however, there appear two distinct volumes of emission, one a much brighter and more symmetric volume directly centered on the core of emission evident at $H\ \alpha$, and a second more extended volume that spreads to the east from the first, effectively filling the area between region 7 and the filaments evident in Figure

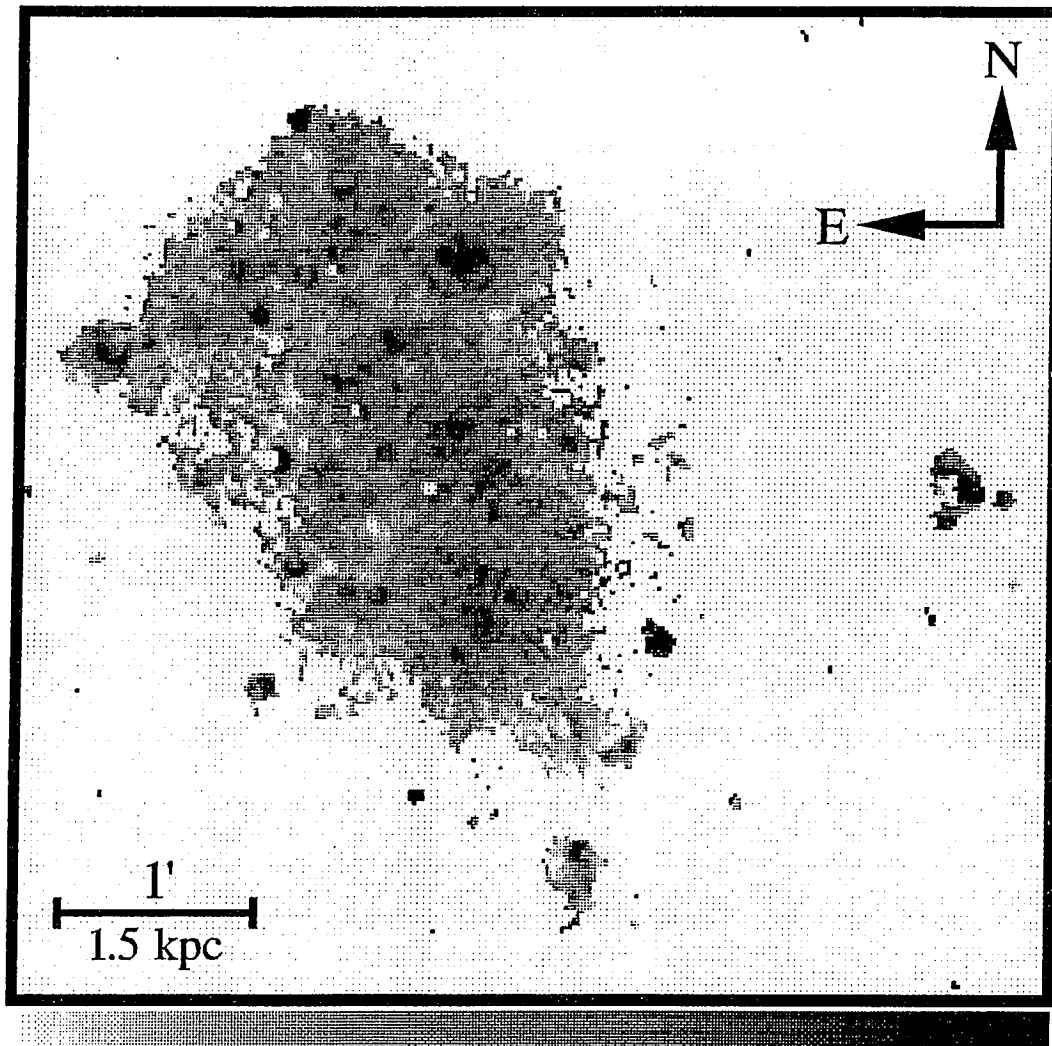


Figure 4.8 Line ratio image for $[\text{O III}]/\text{H } \alpha$. The image is displayed logarithmically between the limits of -0.7 and -0.1. Note the large volume of emission from the host H II region associated with the SNR SB 187, as well as numerous arcs of emission.

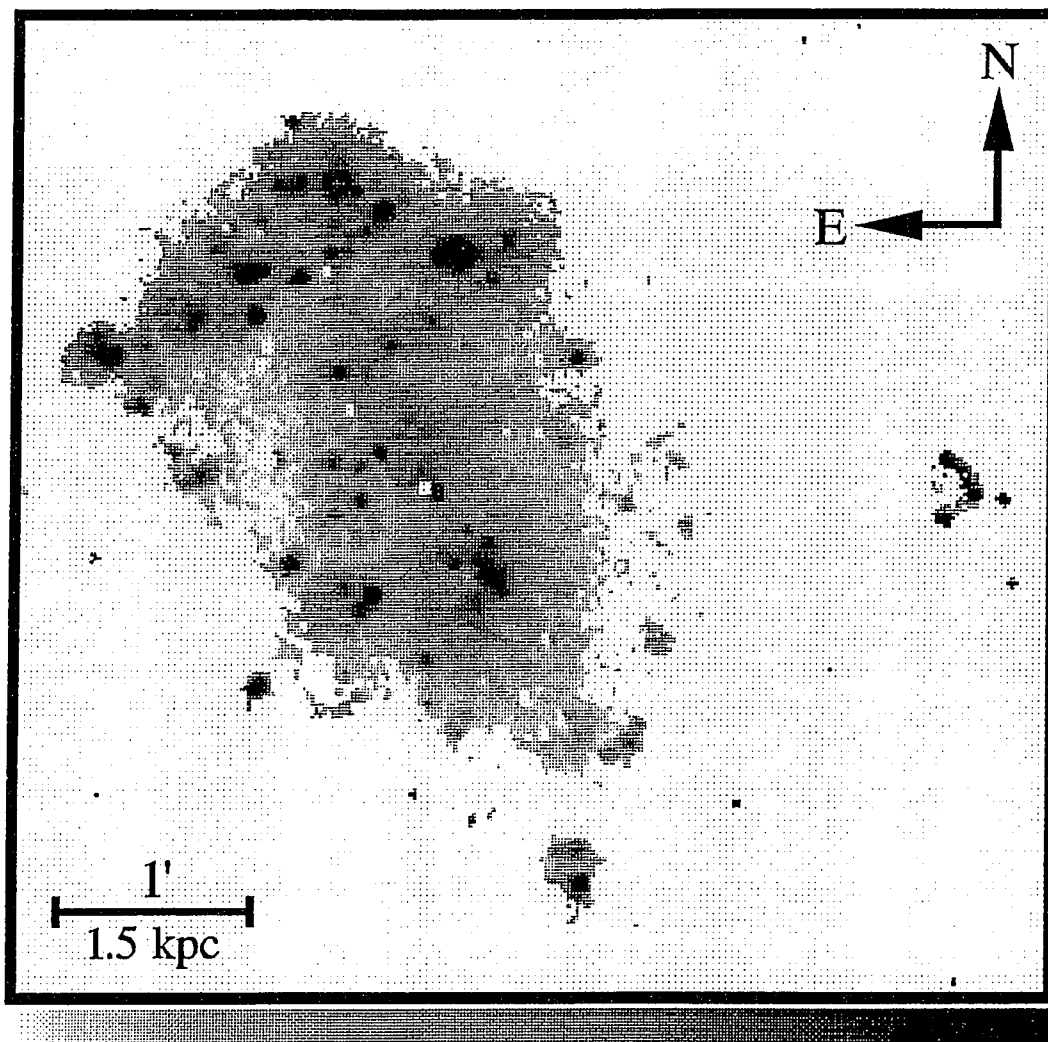


Figure 4.9 The ratio of $[\text{O III}]/[\text{S II}]$ displayed logarithmically between -0.5 and 0.7. Note again the large signature from the H II region 107 in the north.

4.10 (see the next section). It is possible that this object is a “leaky” H II region, unbounded to the east in terms of its radiative processes, and that this radiation is ionizing a larger volume that ultimately is bounded by the existence of a higher density filament of material that acts as a “wall”.

5. Regions 156 and 157. These two regions mark the northern and southern ends of a luminous arc of material, possibly a filament that is situated more than a kiloparsec to the west of the main body of the galaxy. This is a potentially important object that has effectively been ignored by most previous workers, in favor of its brighter and larger neighbor. The structure is made up of the arc and several satellite H II region that possess fairly typical properties, except for the two regions mentioned earlier that appear to have very low excitation. The arc of material appears centered on a much fainter region, number 155, and appears to have a radius approaching 250 pc. This is a huge structure that appears to have lasted some time, considering there has been time for the establishment of H II regions along its length. Possible explanations for its origin would be pure conjecture at this time, but further study of this object will be made by the authors.

There are many other interesting sites of emission across the face of the galaxy, too numerous to mention in any detail here. It is the intention of the authors to continue the high resolution study of these objects in the near future.

4.4 Discussion

The purpose of studying NGC 4449 at this time is to provide a comparison with earlier work carried out on two late-type spiral galaxies, M101 and M51, Papers I and II respectively. In this section we will discuss the various properties displayed by the irregular galaxy in the context of that earlier work.

4.4.1 Imagery of the Filaments

The $H\alpha$ imagery presented as part of this paper is the deepest line emission image taken of this galaxy. As a result it permits a high signal-to-noise study of the filamentary structures that pervade the galaxy as a whole. Recent work by Hunter & Gallagher 1990 and Hunter & Gallagher 1992 have revealed that the filaments extend out from the $H\ II$ regions into areas of lower HI column density, and exhibit lower ionization than the $H\ II$ regions. Specific results include higher values of $[S\ II]/H\ \alpha$ and lower values of $[O\ III]/H\ \beta$ relative to the observed $H\ II$ region population.

The matter of tracing the path of filaments is a challenging one, considering their somewhat chaotic apparent distribution. A good technique for examining the underlying structure of such objects was suggested for NGC 4449 by Sabbadin & Bianchini 1979, and used by Sabbadin et al 1984 in their Figure 12. The application of the unsharp mask process to their $H\alpha$ imagery was performed in the dark room, but an equivalent process can be performed on CCD imagery using a gaussian filter. The width of the filter has to be sufficiently large to effectively remove the gross surface brightness variations to allow the successful enhancement of the small scale variations in emission, thus revealing more structure within the galaxy.

Application of this technique to our $H\alpha$ imagery of NGC 4449 yielded Figure 4.10, revealing even more filamentary structure than presented by Sabbadin et al. All of the features indicated by Sabbadin & Bianchini on their Figure 3(b) are evident in Figure 4.11, as well as filaments that extend out further. Several notable additional features include super-filaments that appear to extend across an appreciable fraction of the galaxy. The size of Figure 4.11 has intentionally been made identical to Figures 4.1, 4.2, 4.3, 4.4, 4.8, 4.9 and 4.10 so that it may be photocopied onto a transparency and easily overlaid.

Having delineated the path taken by the filaments through the structure of the galaxy, it is then possible to make some statement about the ionization characteristics of them. From Figures 4.2, 4.3 and 4.4, using the overlay technique suggested above,

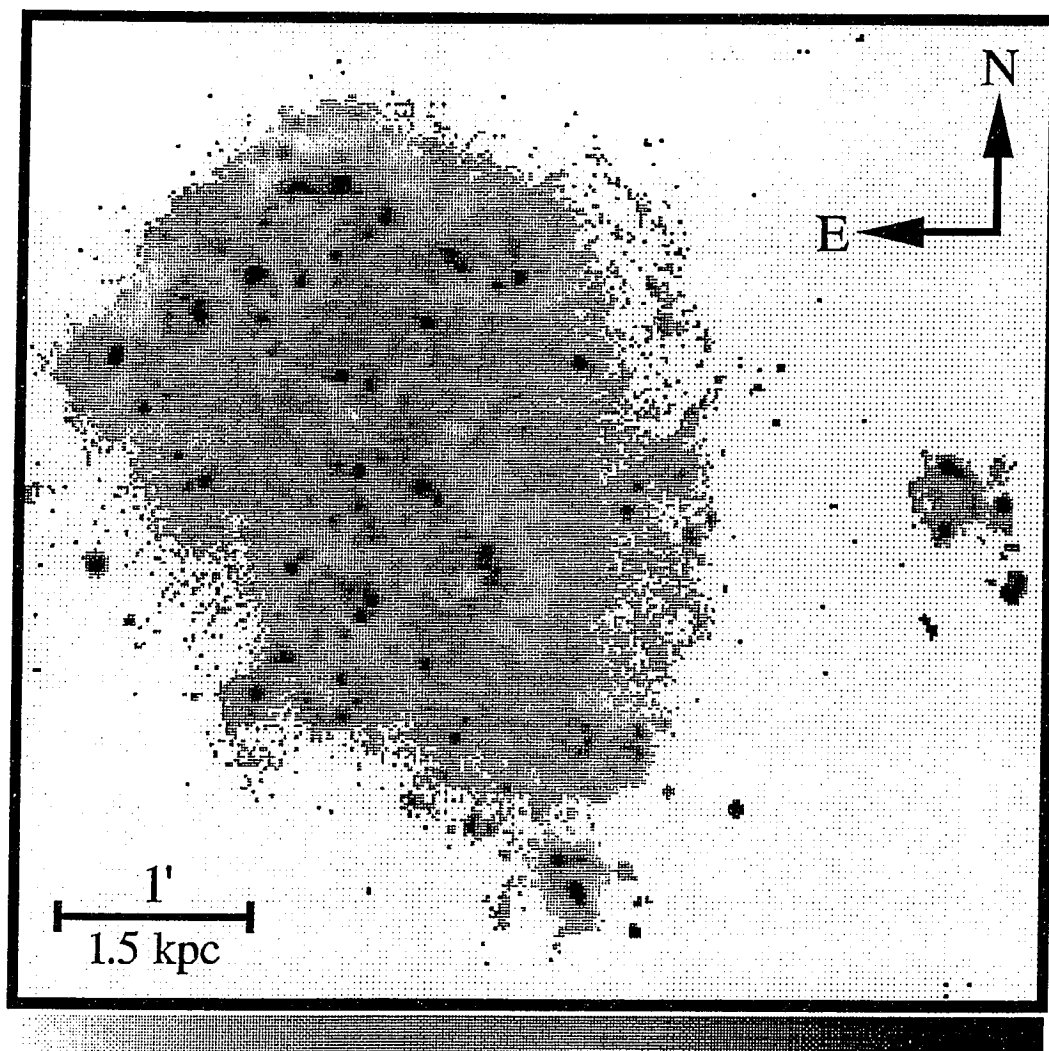


Figure 4.10 The result of applying an “unsharp mask” to the $H\alpha$ image to enhance the filamentary structure that runs throughout the galaxy.



Figure 4.11 Schematic of the main features in Figure 4.10. The size and scale of this figure has been purposely made identical to all the other images included in this paper to allow an overlay to be made for each cross-reference and comparison.

it is possible to make comparative estimates about the relative ionization level of the gas in the filaments compared to the surrounding medium.

When considering the $C(H\ \beta)$ image it is clear that very few filaments have any characteristic signature, indicating that the filaments are probably not associated with any local enhancements in the density of dust in the interstellar medium. There is one noticeable exception to this, however, a filament located just to the northeast of the bright edge in Figure 4.2, on the west of the galaxy. This filament is clearly associated with a bright ridge of emission in Figure 4.2 that runs the full length of the structure. This implies that this filament may contain appreciable amounts of dust. There are a couple of filaments directly to the east of this one that also appear to correlate with high levels of $C(H\ \beta)$, but these are at the edge of the galaxy when considering the numbers of $H\ \beta$ photons we detect, so the detection should be described as tentative. Another notable feature is that in both Figures 4.2 and 4.3 several of the filaments on the west side of the galaxy appear to mark the edge of the $H\ \beta$ surface brightness, and may be related to edges between the ambient ionized medium in the galaxy and the molecular cloud described by Sasaki et al 1992, supposedly located along the western edge of the optical galaxy.

Figure 4.3 has many features that appear to correlate with the filaments in Figure 4.11. In general though, there does not appear to be as noticeable an enhancement of the emission on-filament compared to off- as reported by Hunter & Gallagher 1990. The reason for this apparent disagreement may involve the fact that Hunter & Gallagher used longslits placed across the galaxy at various position angles, thereby cutting various filaments at angles sometimes approaching 90° and may have merely been measuring the local value for a small subsection of the whole filament. In our two-dimensional imaging mode we can better evaluate the variations of any single filament relative to its adjacent medium along its entire length, instead of sampling a chunk of one. The large filament observed in Figure 4.2, also has a bright component in Figure 4.3, indicating that it is also highly ionized compared to the surrounding interstellar medium. This may well be related to the fact that it is positioned rather close to the famous superassociation at the center of the galaxy.

To the north, close to the SNR mentioned in the next section, a filament runs east-west along the northern edge of the SNR and the $H\ II$ region complex that houses it. This filament also appears bright in Figure 4.3, and may acquire its high value of $[O\ III]/H\ \beta$ from a lower level of oxygen abundance compared to the local interstellar

medium, a good possibility when considering the high oxygen abundances reported for the SNR itself by Blair et al 1983.

Finally, upon comparing Figure 4.11 with Figure 4.4, we find that many of the filaments do appear as light streaks, indicating the lower values of the ratio $[S II]/H \alpha$ reported by Hunter & Gallagher, though not all appear this way. The most notable features in Figure 4.4 fall to the south around the base of the central superassociation, where two filaments are seen wrap themselves around this base from the north to the east, flaring apart to the south. This clearly is an intriguing structure and will prove very challenging to model. It appears low in the ratio of $[S II]/H \alpha$ indicating that it is not subject to intense radiation, but the lengths of both filaments suggest that the structures are fairly stable.

4.4.2 The Supernova Remnant SB 187

An oxygen-rich supernova remnant (SNR) was discovered in NGC 4449, in the north-western quadrant, by both Seaquist & Bignell 1978, and Balick & Heckman 1978. Since the early discovery, most research concerning this object has been performed by Blair (Kirshner & Blair 1980, Blair et al 1983, Blair et al 1984). The supernova is observed to be part of a large H II region, as noted in a previous section, and was given the identification 187 by Sabbadin & Bianchini 1979.

The object has been studied at various wavelengths, in the optical, X-ray and ultraviolet bands, to study the physical nature of the remnant. An X-ray source was associated with the object and reported by Blair et al 1983, but never explicitly published. This SNR has been calculated to be one of the most optically luminous examples of its type of object, considering its distance from us.

The optical spectra taken of the object have revealed two kinematic components: narrow emission lines that appear to originate from the host H II region, and much broader lines associated with the SNR itself. The velocity dispersion associated with the linewidths by Kirshner & Blair was estimated to be 3500 km sec^{-1} . Attempts to model the observed properties in terms of the derived plasma temperatures and observed expansion velocities produced a consistent scenario of a massive star ($>25 M_{\odot}$) exploding into a medium of density 25 cm^{-3} about 100 years ago.

For comparison, the derived emission line ratios published for the large H II region associated with the SNR by Blair et al 1983 are listed in Table 4.3.

Table 4.3 Comparison of Emission Properties of H II Region 107

Line Ratio	Blair et al	This paper
$\log [\text{O III}]/\text{H } \beta$	0.56	0.63
$\log \text{H } \alpha/\text{H } \beta$	0.56	0.46
$\log [\text{S II}]/\text{H } \alpha$	-0.51	-0.94

In our imagery we detect this strong [O III] source as part of a larger H II region, in much the same way as did Blair et al. We present the corresponding values from our emission line imagery from region number 107 in Appendix C, the core of the host H II region, which is some 7 arcseconds further west of the SNR. The only substantially different value appears for the ratio of [S II]/H α , since the published result is given separately for the doublet by Blair et al, and our filter covers both lines. An average of the two lines was made before taking the ratio, from Table 1A of Blair et al.

The remarkable size of the host H II region, some 16 by 12 arcseconds, or around 550 by 400 parsecs at the distance we assume, suggests an interesting origin. It may be possible that the supernova explosion could have had an enlarging effect on the ionized cavity, since the apparent source of ionization is not luminous enough to be able to produce such a large volume on its own. However, energetic considerations of this idea make it unlikely, as well as there not being enough time to have an appreciable effect if the models of the age of the SNR are accurate. This object appears to be a “superbubble”, since it is a very large volume of ionized gas with two confirmed sources of ionization.

4.4.3 Star Formation

Over the past 10 years there have been several studies made of the molecular gas content of NGC 4449. It has been noted by many observers that the relative abundance of the heavier elements in the galaxy is very low, less than 1/10th solar (Skillman et al 1989). In Papers I and II the study of the molecular content of each object was made using the published measurements in the millimeter wavelength bands of the emission from CO molecules through a rotational energy transition. A connection was then made between the measured antenna temperature at these wavelengths and the local column density of molecular material, ie. H₂. The constant of proportionality

used in this correlation varies from galaxy to galaxy, but not by more than an order of magnitude.

Since the relative abundances of the heavier elements are so low, there may be an immediate objection to using the correlation just described. If both the oxygen and carbon abundances are low relative to hydrogen, then the combined relative abundance of the CO molecule will undoubtedly also be lower. Therefore the expected emission levels from comparable densities of molecular hydrogen to the spirals, if associated with CO in the same physical manner, will also be reduced. Tacconi and Young 1985 reported CO emission levels a factor of 40-70 lower than those seen in nearby spiral galaxies. This fact, when compared to the relative levels of optical luminosity, reveals that irregular galaxies are more optically luminous than spirals for the same CO gas content. Not all carbon and oxygen will be tied up in the form of CO, and most reasonable estimates of the depletion of this molecule based on abundance arguments result in an expected factor of around 20. As a result of this Tacconi and Young stated that there must be an additional source of reduction of the CO emission other than a purely abundance related argument.

NGC 4449 is observed to be filled with a large ionized gas component. This implies the existence of an ambient ultraviolet radiation field that fills the volume of the galaxy unhindered. The presence of such a field would photodissociate any existing smaller concentrations of CO, since the energy to destroy the molecule is 11.1 eV (Stief et al 1972), and therefore quite easy to remove in the exposed environment of a warm ionized medium.

Later studies of more galaxies by Tacconi and Young 1987, including infrared observations, showed that the ratio of CO to HI evident within their sample of 15 galaxies was a factor of 10 lower than that seen in typical spirals, indicating that irregular galaxies have been unable to convert their large amounts of HI gas into molecular material. This might effectively reduce the possible star formation rate, by preventing the collapse of gas into star forming molecular clouds. However, in Paper I the regions of highest star formation rates were seen to be the superassociations in the outer disk, where the atomic gas dominates the molecular gas by an appreciable amount. It is therefore plausible that a similar phenomenon occurs in NGC 4449, where a lot of the existing star formation has been triggered by "star-forming" HI clouds. Another problem may result from a lack of molecular material since it becomes difficult to successfully collapse a cloud if the majority of the material present is atomic.

Similar work by Thronson et al 1987 compared the expected masses of gas and dust from infrared observations of NGC 4449 at $150\mu\text{m}$ to that predicted by the low levels of CO emission and found the two to be very different, implying that CO is an inadequate tracer for molecular hydrogen in NGC 4449. They also found concentrations of IR emission near the optical center of the galaxy, suggesting a warm dust component distributed throughout the galaxy, but only heated in the center by the diffuse radiation field evident in the optical at that location.

A rough estimate of the star formation efficiency in a galaxy may be made by taking the ratio of the observed blue luminosity to the available gas density, the latter being measured by the relative strengths of CO and HI emission. Such a calculation, made by Tacconi and Young, revealed that the blue luminosity of the irregulars they studied was proportional to the cube of the CO luminosity, whereas late-type spirals exhibit a more linear correlation. This implies that the star formation processes active in NGC 4449 are more efficient than those active in spirals.

The spatial variations in star formation efficiency identified in Papers I and II are not possible in this case since the required two-dimensional imagery of the galaxy at both radio and millimeter wavelengths have not been made. Indeed the CO emission levels are so low that the best single dish observations to date are single position integrations published as emission measures for two locations in the galaxy (Sasaki et al 1992). Although low-resolution measurements of the overall density of emission from HI have been made, the high-resolution observations necessary to make a statement about spatial variations have yet to be made, although the capability does exist.

As part of her original thesis work, Hunter 1982 published a comprehensive study of the properties of star forming regions in many irregular objects, including NGC 4449. She reported overall similarities between the star forming regions in spirals and those in irregulars with a few notable exceptions. There is evidence that many groups of H II regions in irregulars are coeval, in that their formation has been triggered as part of a chain reaction of collapse, formation and recompression of nearby material, being followed on the surface of a nearby large molecular cloud. Dust complexes appear to be more rare in irregulars, although they do appear correlated with H II regions when detected, and are usually optically thin. Her final statement remarked that the overall star formation process in irregular galaxies cannot be entirely random despite the lack of an organised triggering mechanism such as a spiral density wave, since there do appear to be concentrations of star formation sites close to the centers

of these galaxies, a fact that appears all too obvious when looking at imagery such as Figure 4.1.

Later work by the team of Hunter and Gallagher 1986, reported that a constant star formation rate was evident in many irregulars. The study, based on estimates of current star formation from $H\alpha$ surface brightness measurements, and recent star formation histories based on the ratio of $H\alpha$ to blue luminosities, stated that the star formation rates appear constant over the range of timescales valid for the assumption that the ratio just described does reliably estimate the recent star formation evolution, a few 10^6 years. If this is true then in irregular galaxies we see the effect of a constant star formation rate active within an environment that is not actively mixed by differential rotation, but instead left essentially static as the system tends to rotate as a solid body.

4.5 Summary and Conclusions

This paper has presented the initial results from high resolution narrow-band CCD imagery of the galaxy NGC 4449. The most interesting results are summarized below.

1. We have successfully calibrated four narrow-band CCD images of the irregular galaxy NGC 4449. Using these images we have extracted integrated emission properties for a set of 160 H II regions, as well as having identified the gross properties of the filaments, seen in emission, that thread the structure of the galaxy.

2. Plots of the line ratios exhibited by the population of H II regions as function of position within the galaxy have yielded remarkably flat distributions. This is in direct contrast with the considerable variations with position seen through earlier studies of spiral galaxies. These flat distributions are a result of the metal-poor nature of the interstellar medium, coupled with the fact that this medium evidently is well-mixed.

3. Several objects within this set of regions have been singled out as particularly interesting, based on their anomalous emission properties and their apparent morphologies. Some of these objects may be supernova remnant candidates, while others are examples of peculiar morphologies produced by other, as yet unknown, mechanisms. Many objects possess rather high values of the ratio $[\text{O III}]/[\text{S II}]$ indicating that most of the gas is highly ionized, and in some cases shock heated. The general levels of the oxygen abundances in NGC 4449 are about 0.1 solar.

4. The supernova remnant SB 187 has been successfully identified, and studied spatially in relation to the H II complex in which it resides. There appears to be some form of interaction occurring between the two objects, although the exact nature of this activity is unclear.

5. Another interesting object has been identified to the west of the main body of the galaxy. This arc-like structure contains two H II regions as well as having several others positioned close-by. It has been the subject of little study up to now, due to its distance from the main body of the galaxy, and should make an interesting subject of further observation. The arc appears to have a low-surface brightness object at its geometric center, and has an apparent radius of around 250 pc at the distance we assume.

6. A new finding chart has been produced that maps the locations of many filaments within the structure of the galaxy. This map was produced from an H α image of the galaxy, enhanced using the "unsharp mask" technique. The line ratio imagery of the filaments themselves appears consistent with current ideas that these

structures are of higher density than the ambient medium in which they are set, while possessing lower ionization levels across most of the galaxy. One particular set of filaments appears intimately associated with the southern base of one of the superassociations of H II regions that dominate the luminosity of the central part of the galaxy. Their lengths suggest stable configurations, while their emission properties indicate low levels of ionization.

7. A review of the current picture describing the star formation in NGC 4449 has been presented. Due to the low levels of metal abundances in the galaxy, the use of CO as a tracer for molecular hydrogen has been questioned. It appears that there may be an appreciable contribution to the star formation mechanism from star formation in HI clouds, rather than the more typical sites of dense molecular clouds in spiral galaxies. The dominant mechanism for star formation in this galaxy appears to be a chain-reaction process that produces whole sets of coeval H II regions.

This work has been performed to augment other material presented elsewhere (Papers I and II) as part of a larger project. In that capacity this has been an ideal galaxy to study since most of the derived properties we have observed contrast well with the marked variations observed in the earlier work.

Bibliography

- Allen, R.J., Goss, W.M. and van Woerden, H. 1973, A&A, 29, 447
- Allen, R.J., van der Hulst, J.M., Goss, W.M. and Huchtmeier, W. 1978, A&A, 64, 359
- Allen, R.J. and Goss, W.M. 1979, A&AS, 36, 135
- Aller, L.H. 1987, "Physics of Thermal Gaseous Nebulae", Dordrecht: D. Reidel, p.76
- Arsenault, R. and Roy, J.-R. 1986, AJ, 92, 567
- Arsenault, R. and Roy, J.-R. 1988, A&A, 210, 199
- Balick, B. and Heckman, T. 1978, ApJ, 226, L7
- Belley, J. and Roy, J.-R. 1992, ApJS, 78, 61
- Blair, W.P., Kirshner, R.P. and Winkler, P.F. 1983, ApJ, 272, 84
- Blair, W.P., Raymond, J.C., Fesen, R.A. and Gull, T.R. 1984, ApJ, 279, 708
- Blitz, L. and Glassgold, A.E. 1982, ApJ, 252, 481
- Bosma, A. 1981, AJ, 86, 1825
- Bosma, A., Goss, W.M. and Allen, R.J. 1981, A&A, 93, 106
- Bothun, G.D. 1986, AJ, 91, 507
- Bottinelli, L., Gougenheim, L., Paturel, G. and de Vaucouleurs, G. 1983, A&A, 118, 4
- Buta, R. and de Vaucouleurs, G. 1983, ApJS, 51, 149
- Campbell, A. 1988, ApJ, 335, 644

- Carranza, G., Crillon, R. and Monnet, G. 1969, A&A, 1, 479
- de Vaucouleurs, G., de Vaucouleurs, A. and Corwin, G.C. 1976, "Second Reference Catalogue of Bright Galaxies", Austin:University of Texas Press
- Crillon, R and Monnet, G. 1969, A&A, 1, 449
- Devereux, N.A. and Young, J.S. 1990, ApJ, 359, 42
- Diaz, A.I. 1989, in "Evolutionary Phenomena in Galaxies", ed. Beckman, J.E. and Pagel, B.E.J., Cambridge: Cambridge University Press, 377
- Diaz, A.I., Terlevich, E., Vilchez, J.M., Pagel, B.E.J. and Edmunds, M.G. 1991, MNRAS, 253, 245
- Dopita, M.A. and Evans, I.N. 1986, ApJ, 307, 431
- Dufour, R.J., Talbot, R.J., Jensen, E.B. and Shields, G.A. 1980, ApJ, 236, 119
- Edmunds, M.G. and Pagel, B.E.J. 1984. MNRAS, 211, 507
- Elmegreen, B.G. 1989, ApJ, 338, 178
- Elmegreen, B.G., Elmegreen, D.M. and Seiden, P.E. 1989, ApJ, 343, 602
- Elmegreen, B.G., Elmegreen, D.M. and Montenegro, L. 1992, ApJS, 79, 37
- Evans, I.N. 1986, ApJ, 309, 544
- Gallagher, III J.S., Hunter, D.A. and Tutukov, A.V. 1984, ApJ, 284, 544
- Garnett, D.R. and Shields, G.A. 1987, ApJ, 317, 82
- Grevesse, N., Sauval, A.J. and van Dishoeck, E.F. 1984, A&A, 141, 10
- Hartmann, L.W., Geller, M.J. and Huchra, J.P. 1986, AJ, 92, 1278
- Hernquist, L. 1990, "Dynamics and Interactions of Galaxies", Ed. Weilen, R., Berlin:Springer-Verlag, p.108
- Hester, J.J. 1991a, PASP. 103, 853
- Hester, J.J. 1991b, BAAS, 23, 1364

- Hester, J.J. and Kulkarni, S.R. 1989, *ApJ*, 340, 367
- Hill, J.K., Bohlin, R.C. and Stecher, T.P. 1984, *ApJ*, 277, 542
- Hodge, P.W. 1969, *ApJS*, 18, 73
- Hodge, P.W. 1982, *AJ*, 87, 1341
- Hodge, P.W. and Kennicutt, R.C. 1983, *AJ*, 88, 296
- Hodge, P.W., Gurwell, M. and Goldader, J.D. 1990, *ApJS*, 73, 661
- Howard, S. and Byrd, G.G. 1990, *AJ*, 99, 1798
- Hunter, D.A. 1982, *ApJ*, 260, 81
- Hunter, D.A. and Gallagher, J.S. 1986, *PASP*, 98, 5
- Hunter, D.A. and Gallagher, III J.S. 1990, *ApJ*, 362, 480
- Hunter, D.A. and Gallagher, III J.S. 1992, *ApJ*, 391, L9
- Illingworth, V. 1979, "A Dictionary of Astronomy". London: Macmillan Press
- Israel, F.P., Goss, W.M. and Allen, R.J. 1975, *A&A*, 40, 421
- Israel, F.P. and Rowan-Robinson, M. 1984, *ApJ*, 283, 81
- Israel, F.P. and van der Hulst, J.M. 1983, *AJ*, 88, 1736
- Keel, W.C., Kennicutt, R.C., Hummel, E. and van der Hulst, J.M. 1985, *AJ*, 90, 708
- Kenney, J.D.P., Scoville, N.Z. and Wilson, C.D. 1991, *ApJ*, 366, 432
- Kennicutt, R.C. 1981, *AJ*, 86, 1847
- Kennicutt, R.C. 1988, *ApJ*, 334, 114
- Kennicutt, R.C. 1989, *ApJ*, 344, 685
- Kennicutt, R.C., Edgar, B.K. and Hodge, P.W. 1989, *ApJ*, 337, 761

- Kennicutt, R.C., Keel, W.C., van der Hulst, J.M., Hummel, E. and Roettiger, K.A. 1987, *AJ*, 93, 1011
- Kennicutt, R.C. and Kent, S.M. 1983, *AJ*, 88, 1094
- Kimura, T. and Tosa, M. 1985, *PASJ*, 37, 669
- Kirshner, R.P. and Blair, W.P. 1980, *ApJ*, 236, 135
- Knapen, J.H., Beckman, J.E., Cepa, J., van der Hulst, T. and Rand, R. 1992, *ApJ*, 385, L37
- Lequeux, J., Peimbert, M., Rayo, J.F., Serrano, A. and Torres-Peimbert, S. 1979, *A&A*, 80, 155
- Lo, K.Y., Ball, R., Masson, C.R., Phillips, T.G., Scott, S. and Woody, D.P. 1987, *ApJ*, 317, 63
- Lord, S., Young, J. and Strom, S. 1985, *BAAS*, 17, 613
- Lord, S.D. and Young, J.S. 1990, *ApJ*, 356, 135
- Malumuth, E.M., Williams, T.B. and Schommer, R.A. 1986, *AJ*, 91, 1295
- Mathews, W.G. and O'Dell, C.R. 1969, *ARA&A*, 7, 67
- McCall, M.L., Rybski, P.M. and Shields, G.A. 1985, *ApJS*, 57, 1
- McGaugh, S.S. 1991, *ApJ*, 380, 140
- Mendoza, C. 1983, "Planetary Nebulae" (IAU Symposium No. 103), ed. Flower, D.R., Dordrecht: Reidel
- Mihalas, D. and Binney, J. 1981, "Galactic Astronomy: Structure and Kinematics", W.H. Freeman
- Osterbrock, D.E. 1989, "Astrophysics of Gaseous Nebulae and Active Galactic Nuclei", University Science Books, AGN²
- Peimbert, M., Torres-Peimbert, S. and Fierro, J. 1989, *Rev. Mexicana Astron. Astrof.*, 18, 189

- Quirk, W.J. 1972, ApJ, 176, L9
- Rand, R.J. and Kulkarni, S.R. 1990, ApJ, 349, L43
- Rand, R.J. and Tilanus, R.P.J. 1990, "The Interstellar Medium in Galaxies", Eds. Thronson, H.A. and Shull, J.M., Kluwer Academic Publishers, p.525
- Rand R.J. 1992, AJ, 103, 815
- Rasure, J. and Williams, C. 1991, J Vis Lang Comput, 2, 217
- Roberts, W.W., Roberts, M.S. and Shu, F.H. 1975, ApJ, 195, 38
- Rose, J.A. and Cecil, G. 1983, ApJ, 266, 531
- Rots, A.H. 1980, A&AS, 41, 189
- Rots, A.H., Bosma, A., van der Hulst, J.M., Athanassoula, E. and Crane, P.C. 1990a, "Dynamics and Interactions of Galaxies", Ed. Weilen, R., Berlin:Springer-Verlag, p.122
- Rots, A.H., Bosma, A., van der Hulst, J.M., Athanassoula, E. and Crane, P.C. 1990b, AJ, 100, 387
- Roy, J.-R., Arsénault, R. and Jonas, G. 1986, ApJ, 300, 624
- Rydbeck, G., Hjalmarson, A. and Rydbeck, O.E.H. 1985, A&A, 144, 282
- Sabbadin, F. and Bianchini, A. 1979, PASP, 91, 280
- Sabbadin, F., Ortolani, S. and Bianchini, A. 1984, A&A, 131, 1
- Sandage, A.R. 1961, "Hubble Atlas of Galaxies", (Washington: Carnegie), p.26
- Sandage, A. and Bedke, J. 1988. "An Atlas of Galaxies useful for measuring the cosmological distance scale", NASA SP - 496
- Sandage, A. and Tammann, G.A. 1974, ApJ, 194, 223
- Sandage, A. and Tammann, G.A. 1975, ApJ, 196, 313
- Sandage, A. and Tammann, G.A. 1976, ApJ, 210, 7

- Sandage, A. and Tammann, G.A. 1987, "Revised Shapley-Ames Catalog of Bright Galaxies", (2nd Ed., Washington: Carnegie)
- Sanders, D.B., Solomon, P.M. and Scoville, N.Z. 1984, ApJ, 276, 182
- Sasaki, M., Ohta, K. and Saito, M. 1991, PASJ, 42, 361
- Scoville, N. and Young, J.S. 1983, ApJ, 265, 148
- Scowen, P.A. and Dufour, R.J. 1992, BAAS, 23, 1459
- Scowen, P.A., Dufour, R.J. and Hester, J.J. 1992a, AJ, 104, in press (Chapter 2)
- Scowen, P.A., Dufour, R.J. and Hester, J.J. 1992b, AJ, in preparation (Chapter 3)
- Scowen, P.A., Dufour, R.J. and Hester, J.J. 1992c, AJ, in preparation (Chapter 4)
- Seaquist, E.R. and Bignell, R.C. 1978, ApJ, 226, L5
- Searle, L. 1971, ApJ, 168, 327
- Seaton, M.J. 1979, MNRAS, 187, 73P
- Seiden, P.E. and Gerola, H. 1979, ApJ, 233, 56
- Shields, G.A. and Searle, L. 1978, ApJ, 222, 821
- Shields, G.A. 1990, ARA&A, 28, 525
- Shostak, G.S. and Allen, R.J. 1980, A&A, 81, 167
- Shu, F.H., Adams, F.C. and Lizano, S. 1987, ARA&A, 25, 23
- Skillman, E.D., Kennicutt, R.C. and Hodge, P.W. 1989, ApJ, 347, 875
- Smart, W.M. 1977, "Textbook on Spherical Astronomy", Cambridge: Cambridge University Press, pp. 297-300
- Smith, H. 1975, ApJ, 199, 591
- Spitzer, L. 1978, "Physical Processes in the Interstellar Medium", Wiley, p. 246
- Stetson, P.B. 1987, PASP, 99, 191

- Stief, L.J., Donn, B., Glicker, S., Gentieu, E.P. and Mentall, J.E. 1972, *ApJ*, 171, 21
- Tacconi, L.J. and Young, J.S. 1985, *ApJ*, 290, 602
- Tacconi, L.J. and Young, J.S. 1987, *ApJ*, 322, 681
- Talbot, R.J. and Arnett, W.D. 1975, *ApJ*, 197, 551
- Talent D.L. 1980, Ph.D. Thesis, Rice University
- Thronson, H.A. Jr., Hunter, D.A., Telesco, C.M. and Decher, R. 1987, *ApJ*, 317, 180
- Tilanus, R.P.J., Allen, R.J., van der Hulst, J.M., Crane, P.C. and Kennicutt, R.C. 1988, *ApJ*, 330, 667
- Tilanus, R.P.J. and Allen, R.J. 1989, *ApJ*, 339, L57
- Toomre, A. 1964, *ApJ*, 139, 1217
- Toomre, A. and Toomre, J. 1972, *ApJ*, 178, 623
- Torres-Peimbert, S., Peimbert, M. and Fierro, J. 1989, *ApJ*, 345, 186
- Tully, R.B. 1974a, *ApJS*, 27, 415
- Tully, R.B. 1974b, *ApJS*, 27, 437
- Tully, R.B. 1974c, *ApJS*, 27, 449
- van den Bergh, S. 1960, *Publ. David Dunlop Obs.*, II, 6
- van der Hulst, J.M., Kennicutt, R.C., Crane, P.C. and Rots, A.H. 1988, *A&A*, 195, 38
- van der Hulst, J.M. and Sancisi, 1988. *AJ*, 95, 1354
- Viallefond, F., Allen, R.J. and Goss, W.M. 1981. *A&A*, 104, 127
- Viallefond, F., Goss, W.M. and Allen, R.J. 1982, *A&A*, 115, 373
- Vilchez, J.M., Pagel, B.E.J., Diaz, A.I., Terlevich, E. and Edmunds, M.G. 1989, *MNRAS*, 235, 633

- Wakker, B.P., Broeils, A.H., Tilanus, R.P.J. and Sancisi, R. 1989, A&A, 226, 57
- Walter, D.K., Dufour, R.J. and Hester, J.J. 1992, ApJ, 397, in press
- Yorke, H.W. 1986, ARA&A, 24, 49
- Young, J.S., Kenney, J.D., Tacconi, L., Calussen, M.J., Huang, Y.-L., Tacconi-Garman, L., Shuding, X. and Schloerb, F.P. 1986, ApJ, 311, L17
- Young, J.S. and Sanders, D.B. 1986, ApJ, 302, 680
- Young, J.S. and Scoville, N.Z. 1991, ARA&A, 29, 581
- Zaritsky, D., Elston, R. and Hill, J.M. 1990, AJ, 99, 1108

Appendix A

The automatic registration of HII regions in CCD imagery

A.1 Introduction

In studying imagery of extragalactic objects, for example late-type spiral galaxies, the wealth of information available in a single high-resolution frame can be quite daunting. As detectors achieve higher and higher data quality in terms of dynamic range and resolution, a need for automated procedures becomes indispensable, since the individual researcher becomes severely taxed when manually handling such enormous datasets.

The original problem that prompted this study was raised by Evans 1986, where it was pointed out that images of HII regions in other galaxies had different apparent sizes when viewed in the light of different emission lines. This is not an immediately troubling problem until one considers the issue of taking ratios of the emission line fluxes derived from those regions to perform typical nebular calculations. Since most emission line studies employ large slits to integrate all the available emission at each wavelength, this effect would cause erroneous estimates of the value of each line ratio, and the physical parameters derived therefrom, as a direct result of this difference in apparent surface area.

A solution to this problem may be found by developing a wavelength-independent method of identifying HII regions. This would allow consistent estimates of HII region emission line ratios by removing any observational bias from the process. Stated simply, the resulting program uses a CCD image taken through a narrow-band H α filter to define the template identifying each HII region. A significance threshold is applied to the image defined in terms of the intensity of the emission from each region.

A.2 Specification

To allow easy use, the algorithm needed to be simple while being robust enough to produce consistent results when applied to different sets of imagery. Certain quantities are of interest when studying a set of emission line images, including the physical size of each region, the position of that region (relative to some convenient coordinate frame), the integrated flux over the physical extent of the region, and the deprojected radial position of the region within the galaxy.

All these calculated values should be easily accessible after the process has been applied, to prevent any need for a re-application of the procedure. The most convenient form of output that satisfies this particular requirement is a table of data rendered in ASCII. This allows the data to be easily imported into other pieces of software at a later stage to calculate further quantities as well as representing the data graphically.

To simplify the programming, the IMFORT library (distributed as part of IRAF[§]) was used which, despite its age, is still one of the most easily applicable set of subroutines for the manipulation of imagery and the data contained therein available today.

A.3 Application

A typical set of imagery would consist of several narrow-band emission line CCD frames shot at several wavelengths, such as H α , H β , [O III] and [S II], and under similar observing conditions. The imagery used for the initial versions of the code were taken using a focal reducing camera at an effective F ratio of f/1.66. This assures high signal-to-noise imagery in reasonable exposure times. In one particular frame, the H α image, the HII regions are usually very apparent, and may easily be separated spatially as individual objects.

Among the optical emission lines, H α defines most clearly the physical extent of each HII region, out to the boundary where the ionization edge occurs. H α is advantageous for two more reasons, since wavelengths that are shortward of H α suffer more extinction, and since most CCD cameras have higher sensitivity in the red. The definition of the ionization edge is blurred when different emission lines, and

[§]IRAF is distributed by the National Optical Astronomy Observatories, which is operated by the Association of Universities for Research in Astronomy, Inc., under cooperative agreement with the National Science Foundation.

therefore different ionized species, are considered simply because the ions emitting at those energies originate from physically different parts of the structure of each nebula. Using the $H\ \alpha$ image as the starting point allows an easily accessible template that may be used to identify each HII region for all the emission line images.

Before the imagery can be used with the algorithm, several processing steps have to be applied including standard alignment and registration. After this, it is necessary for all continuum contributions to the observed emission to be removed. This is done by taking a broad-band image including a wavelength region adjacent to the emission line in question, and by appropriate scaling (applied by matching the intensity of the foreground stars in each image), the stellar continuum contribution to the galactic image can be almost totally removed.

After this, a phase of manual artifact removal has to be applied to remove stellar residuals and other sources of errant data, to allow only emission of direct interest to remain in the imagery. Of course, this meticulous approach only has to be applied to the $H\ \alpha$ image since that defines the original region template which is then blindly applied to the other images.

A.3.1 Initial Registration of the HII regions

The definition of a legitimate region, although easy to state verbally, is difficult to formulate into a piece of code. In a given CCD image, a subject pixel is determined to be part of a legitimate HII region when the emission in that pixel falls above a predefined threshold, and is a member of 4 or more contiguous pixels that are also above that threshold. The formulation of this criterion appears initially simple, but upon applying prototypical versions of the code to real data, it was apparent that a rather more robust algorithm was needed to allow the successful identification of real HII regions. The major source of difficulty arose from the many geometric forms each region could take, with many perimeters that doubled back on themselves.

The identification procedure is sequential in nature, methodically scanning the $H\ \alpha$ image starting at the coordinate origin and applying the identification criterion to each pixel. Upon the successful location of a candidate pixel, the process will identify all similar pixels that are part of that particular structure before proceeding with the search.

Once the physical extent of the region has been identified, all pixels in the region are labelled with a region identification number for later study. This allows those

parameters mentioned earlier to be calculated using the emission properties as derived from each region. The mathematical descriptions of the calculations made are detailed at the end of this Appendix.

A.3.2 Determining the physical extent of an HII region

Using Figures A.1, A.2 and A.3 as visual aids, a discussion of the technique used to identify each pixel as a unique member of a region will follow.

Upon encountering a pixel above the predefined threshold, the algorithm analyzes those pixels immediately surrounding that position, pixels 1 through 8 in Figure A.1, in that order. Following the flowchart in Figure A.2, any pixel encountered is checked to see if it has already been identified. If it has not, each of the eight pixels surrounding that original position are checked. Upon locating a pixel that satisfies the identification criteria, the 3x3 grid featured in Figure A.1 is recentered on that pixel and the same search applied around that position to locate more pixels that satisfy this criteria locally. This process continues to branch until no more pixels are found that have not been identified already.

Once the point is reached where no more local pixels are found, the routine backs up a step, relocating the grid at the location it occupied before the most recent branch. The next pixel in the sequence around this pixel is studied, and if necessary the process branches to follow more pixels until no more are found.

Ultimately the process will return to the original pixel encountered. When this happens, and when no more adjacent pixels exist that have not been identified, the algorithm will exit. At this point all pixels that have been identified as being part of that region are labelled with an identification code to uniquely associate them with that particular region, and prevent any subsequent re-identification. The scan of the image then continues looking for more pixels. A running record of detected pixels is continually maintained to prevent duplication of earlier work.

It should be explained how the algorithm handles regions that occur on the edge of the field. A check is built in to stop any attempt to access a pixel that lies outside the physical extent of the image. This prevents any floating point errors from occurring that might contaminate the calculations for that region.

Figure A.3 details a specific example of this process. A simple shape is shown, with each identification step included. The branching continues from step a to step

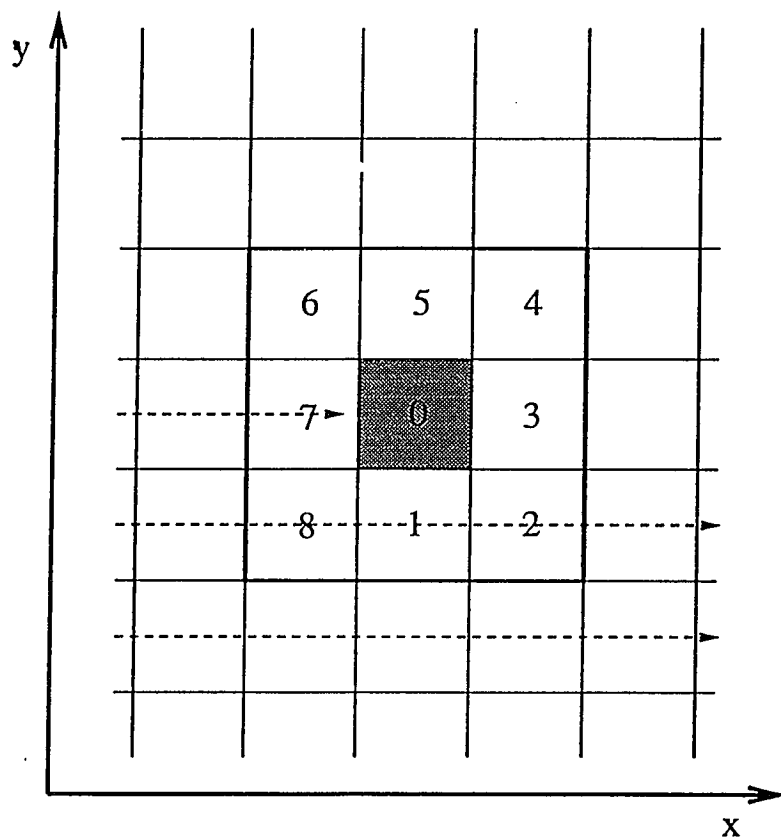


Figure A.1 Diagram showing hierarchy of the search protocol used by the algorithm upon encountering a candidate pixel. The coordinate scheme, together with its origin, is also included.

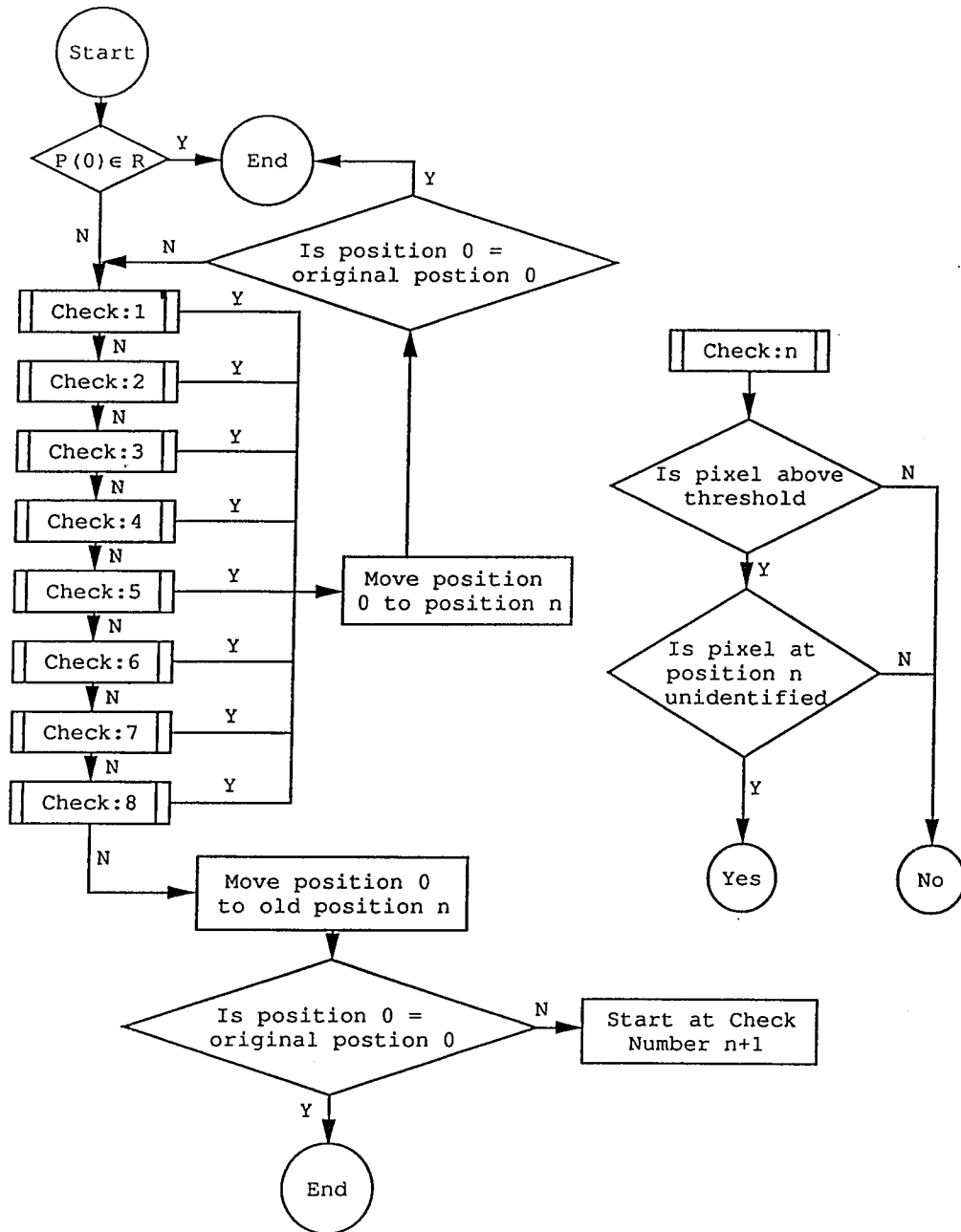


Figure A.2 Flow chart of the subroutine that explores and registers a previously unknown region upon encountering the first pixel in its structure. The eight level hierarchy represented in Figure 1 is explicitly detailed here.

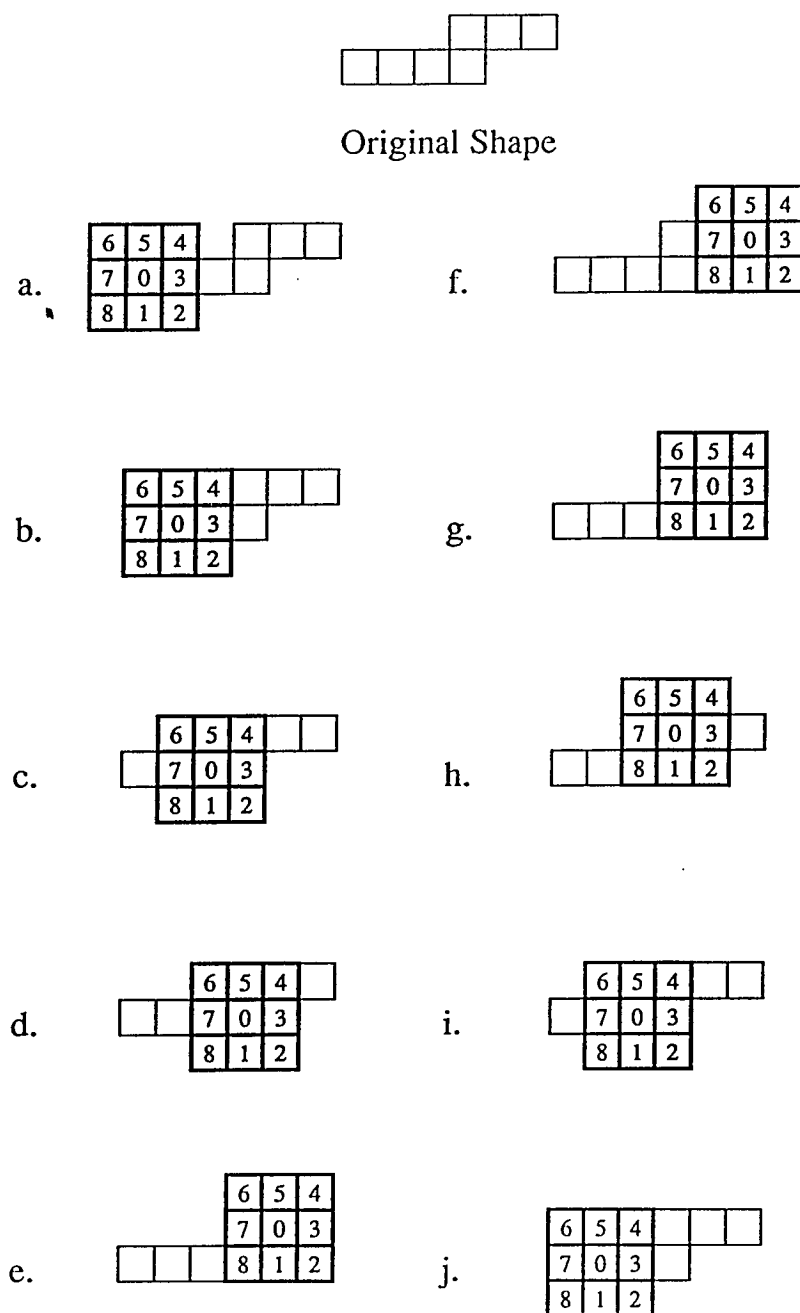


Figure A.3 An example of the passage of the identification algorithm across a simple geometric form. Step (a) indicates the first pixel encountered. At (d), the fourth pixel is identified. The top edge of the shape is followed back to the original pixel using positions 7 and 8 in the grid.

f. Then the grid is moved back a step, equivalent to step e, before continuing back to the original pixel, after step j.

The success of this technique is illustrated in Figure A.4, where several examples of real HII regions are overlaid with their representation after the code has completed its identification of the extent of the emission. Clearly, the more complicated structures are well represented by this approach.

A.3.3 Calculating the physical properties

Upon completing the scan of the entire frame, the process then re-examines the record of those pixels, and regions, identified. For each region the desired properties are calculated. The results are written to a file, along with all the input information used by the code, to allow complete reconstruction of the conditions under which the identification was applied. Examples of the input parameters, and the calculated results, are included in Tables A.1, A.2 and A.3.

Table A.1 Examples of Information Required at Initiation

Quantity	Typical Value
Name of image scanned	m101.ha.comb
Intensity threshold used	1×10^{-15} ergs cm^{-2} sec^{-1}
Distance assumed for object	7.4 Mpc
Galactic Plane tilt angle	17.0°
Galactic position angle	34.0°
Location of galactic center	$14^h 1^m 26.7^s$ right ascension $54^\circ 35' 16.4''$ declination
Location of galactic center	352 514 in image coordinates
Epoch of coordinates	1950.0

Table A.2 Examples of Information Produced

Quantity	Typical Value
Number of regions identified	248
Field rotation relative to α, δ	1.14°
Image plate scale	$1.192''$ pixel $^{-1}$
Image distance scale	42.8 pc pixel $^{-1}$
Error in α	0.08^s
Error in δ	$0.89''$

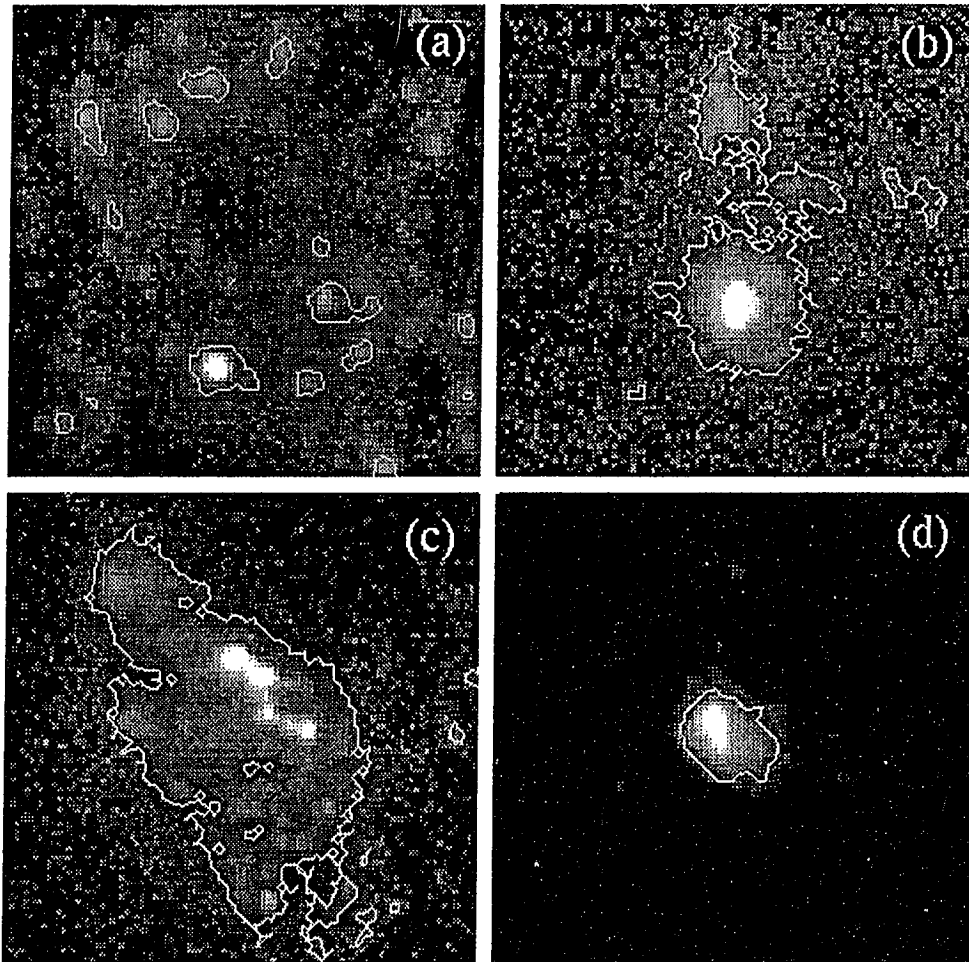


Figure A.4 A pictorial representation of four examples of typical morphological types of HII region encountered in real imagery: (a) well separated HII regions, (b) an extended structure with a single local maximum, (c) an extended source with many local maxima, and (d) a point like HII region (magnified $\times 2$ over the other images).

The accurate coordinate calculations are performed using an input file originally produced by the Space Telescope Guide Star Catalogue (STGSC) and subsequently edited. The heart of the coordinate calculation is based on the routine COORDS originally written by Don Terndrup for inclusion in the CTIO ¶ IRAF add-on package.

Calculation of the deprojected radial distance of each region uses the input tilt and position angles for the system in a simple geometric transform assuming the galactic disk is planar.

Two output images are also created: one a binary representation of the identification results - a mask image opaque at all locations except those identified as being part of a region; the second image is a literal representation of each pixel's identification flag identifying the particular region to which it belongs.

Table A.3 Example of Resulting Entries for Each Region

ID	x	y	α	δ	I_p *†	A †	I ††	ΔI †§	M ††	ΔM †§	R ††
2	678	145	14 0 41.2	54 28 04.5	4.33	21	48.3	2.62	2.30	2.28	21222
5	431	189	14 1 15.0	54 28 51.4	43.9	269	1700	15.5	6.33	5.09	14486
6	489	195	14 1 07.1	54 28 59.9	2.57	8	11.5	1.28	1.44	2.05	14976
7	521	200	14 1 02.7	54 29 06.5	5.11	16	40.7	2.40	2.54	2.99	15365
8	488	201	14 1 07.2	54 29 07.0	2.51	7	11.6	1.29	1.66	2.46	14721
9	535	205	14 1 00.8	54 29 12.8	8.58	42	115	4.04	2.74	2.96	15469
10	525	207	14 1 02.2	54 29 15.0	2.40	7	11.2	1.26	1.60	2.12	15181
15	428	226	14 1 15.5	54 29 35.3	2.72	40	64.9	3.03	1.62	0.85	12893
16	542	230	14 0 59.9	54 29 42.7	1.56	5	6.24	0.94	1.25	1.00	14716
17	486	233	14 1 07.6	54 29 45.0	7.80	22	66.6	3.08	3.03	4.22	13421
18	368	248	14 1 23.7	54 30 00.1	1.86	7	8.76	1.12	1.25	1.23	11615
20	674	284	14 0 42.1	54 30 49.9	42.2	770	3120	21.1	4.06	1.78	17139
22	458	265	14 1 11.5	54 30 22.5	2.25	9	13.0	1.36	1.44	1.45	11675
23	358	278	14 1 25.2	54 30 35.6	3.15	10	20.5	1.71	2.05	2.98	10304
26	357	287	14 1 25.4	54 30 46.3	3.59	14	28.5	2.01	2.04	2.34	9912
27	701	290	14 0 38.4	54 30 57.6	2.06	7	10.3	1.21	1.48	1.35	17991
28	542	301	14 1 00.1	54 31 07.2	1.36	9	10.0	1.19	1.11	0.38	12303
30	681	301	14 0 41.1	54 31 10.3	1.48	4	5.62	0.89	1.41	0.43	17000
31	697	302	14 0 39.0	54 31 11.8	3.22	11	19.8	1.68	1.80	2.09	17578
33	685	312	14 0 40.6	54 31 23.4	1.74	4	6.08	0.93	1.52	1.08	16911
35	332	318	14 1 28.9	54 31 22.6	11.5	52	157	4.72	3.01	3.36	8646
36	249	317	14 1 40.2	54 31 19.3	3.31	14	28.4	2.01	2.03	2.06	9914
37	318	318	14 1 30.8	54 31 22.2	6.39	31	75.7	3.28	2.44	2.45	8757
38	263	317	14 1 38.3	54 31 19.7	1.58	4	5.69	0.90	1.42	0.83	9620
39	344	319	14 1 27.2	54 31 24.0	4.01	28	52.8	2.74	1.88	1.60	8542

¶Cerro Tololo Interamerican Observatory, National Optical Astronomy Observatories, is operated by the Association of Universities for Research in Astronomy, Inc., under contract with the National Science Foundation.

*Intensity of brightest pixel, defining x, y, α , δ .

†See §A.7 for definition.

‡In units of 10^{-15} ergs cm^{-2} sec^{-1} .

§In units of 10^{-16} ergs cm^{-2} sec^{-1} .

A.4 Subsequent developments

Having identified all the regions in the dataset, the next step is to integrate each the emission from each region in the other line emission images. Using the region identification images, a secondary process, with most of the calculations reproduced from the first, is applied to the line emission images to calculate their emission properties. Any differences in apparent size of each region through the differing filters are ignored since the extent of each region is defined by the $H\alpha$ image for all further calculations.

The resulting calculated quantities are written into output files resembling the original in an attempt to preserve a formatting standard for later applications.

Subsequent smaller programs can then be written to access this large amount of information, as long as a specific sequence is followed, to perform multiple similar calculations for each and every region in the datasets. A typical number of identified regions range from a couple of hundred to nearly seven hundred for a particularly rich image, depending on the parameters set. Example values, used as part of a study of the galaxy M101, are detailed in Table A.1. The resulting calculated HII region properties are listed in Table A.2 for a representory subset of the total population identified.

There are many examples of the kind of subsequent calculations that can be performed at this point. Some involve simply taking the ratio of the integrated emission from one line relative to another for each region. More complicated examples involve taking ratios using region emission, followed by logarithmic calculations using that ratio, and then ultimately binning the results for each region according to their radial ordinate or some other distinguishing factor.

A later sophistication, that improved the visualization of the resulting datasets, involved the development of code that regenerated an image of the HII regions, except that for each region all the member pixels were replaced with a common data value. This technique allows, for example, the representation of spatially averaged physical quantities, allowing clear visual estimates of any positional dependences to be made without extensive study of the data using graphs or other methods.

A.5 Scientific Application

The derivation of important physical quantities from these datasets, for such a large population of regions, allows a major increase in the statistical completeness of such a study. Other researchers in the field have recently concentrated on the development

of multi-fiber optic spectrographs to measure the emission from many sources at once. This approach, of course, still suffers from the variation in apparent region size from emission line to emission line. The largest population sampled by this technique has been about 200-300 regions for M101 (Zaritsky et al. 1990), while recent work by the author (Scowen et al. 1992) has yielded a population of regions numbering 625 regions for the same object.

Another comparative statistic is the amount of investment made in telescope time by each study. The former study used a considerable amount of time, since their device observes 32 HII regions at a time, with a typical exposure time being of 45 minutes duration. The latter work took a series of CCD exposures all on one night, each lasting between 10 and 50 minutes. Not only does this approach allow access to many more HII regions, but it does so with a severe reduction in the observing overhead required.

The results from this latter work have allowed the study of changes in the physical conditions of many HII regions with relation to their environment and position within the galactic framework. Since the population derived is much larger than any previously used, certain trends in these properties are made clearer by this technique. As another comparison, attempts at this kind of study in the 1970's involved the use of region population samples numbering only several tens.

Currently this suite of routines is being applied to imagery of an interacting spiral system to study what effects this kind of active environment will have on the properties of the HII regions. This will be of special interest when comparing the local environmental conditions in such an object with the relatively stable conditions enjoyed by the region population in M101. Another class of object that will shortly be studied, in tandem with the interacting system, is an irregular galaxy to study how the chaotic distribution of material affects the formation and evolution of HII region populations.

A.6 Summary

This avenue of research and software development has resulted in a set of routines that allow the unbiased definition of a population of HII regions in any given set of narrow-band emission line CCD imagery of an external galaxy. The software itself is fairly simple with the majority of the complexity residing in the first application, and diminishing thereon.

Access to the results of this system is a trivial matter, requiring merely a knowledge of the format of the tabular datasets to allow extraction of the information needed for any specific calculation.

Future developments of this set of functions include the development of an X11 interface to the datasets and imagery allowing fast transfer between the two-dimensional representation of the data and a graphical output, that is of more use for publication purposes. Initial research has identified the KHOROS environment (Rasure & Williams 1991) as a suitable software library to use for this purpose.

Other goals include the compilation of the routines into an IRAF add-on package with online help pages to allow distribution to sites world-wide. Several groups, including people in Mexico and India, have expressed interest in using the code for applications other than that for which it was written.

A.7 Details of calculations used

Accurate celestial coordinates

For each region with coordinates (x_i, y_i) :

$$\alpha_i^{calc} = \alpha_m + \arctan \left[\frac{ax_i + by_i + c}{\cos \delta_m - \sin \delta_m (dx_i + ey_i + f)} \right] \quad (\text{A.1})$$

$$\delta_i^{calc} = \arctan \left[\frac{\cos \left[\arctan \left[\frac{ax_i + by_i + c}{\cos \delta_m - \sin \delta_m (dx_i + ey_i + f)} \right] \right] (\sin \delta_m + (dx_i + ey_i + f) \cos \delta_m)}{\cos \delta_m - (dx_i + ey_i + f) \sin \delta_m} \right] \quad (\text{A.2})$$

where (a,b,c,d,e,f) are the standard plate constants (Smart 1977) and α_m, δ_m are the Right Ascension and Declination of the field center. The uncertainty in each calculated coordinate is determined from the input file of known positions and calculated using:

$$\Delta \alpha = \sqrt{\frac{1}{N} \sum_{i=1}^N (\alpha_i - \alpha_i^{calc})^2 - \left(\frac{1}{N} \sum_{i=1}^N (\alpha_i - \alpha_i^{calc}) \right)^2} \quad (\text{A.3})$$

$$\Delta \delta = \sqrt{\frac{1}{N} \sum_{i=1}^N (\delta_i - \delta_i^{calc})^2 - \left(\frac{1}{N} \sum_{i=1}^N (\delta_i - \delta_i^{calc}) \right)^2} \quad (\text{A.4})$$

Derived physical properties

For each region the following directly calculable quantities are derived:

$$A = N_{pixels} \quad (A.5)$$

$$I = \sum_{i=1}^N I_i \quad (A.6)$$

$$\Delta I = \sqrt{N_{phot}} = \sqrt{\frac{\text{total energy deposited}}{h\nu}} \quad (A.7)$$

$$M = \frac{I}{A} \quad (A.8)$$

$$\Delta M = \frac{\Delta I}{I} M \quad (A.9)$$

Radial deprojection

Assuming the galactic disk is planar, and using the known tilt and position angles (θ_i and θ_p respectively), the galactocentric radius may be calculated for any region that has a position relative to the galactic center of $(\Delta x, \Delta y)$. The plate scale P is derived from the coordinate calculation above; D is the distance to the object under observation.

$$R = DP \sqrt{\Delta x^2 + \Delta y^2} \sqrt{\cos^2 \left(\theta_p - \arctan \left(\frac{-\Delta x}{\Delta y} \right) \right) + \frac{\sin^2 \left(\arctan \left(\frac{-\Delta x}{\Delta y} \right) \right)}{\cos^2 \theta_i}} \quad (A.10)$$

$$P = \arctan \left[\frac{N-1}{\sum_{i=1}^N \sqrt{\frac{(x_i - x_{i-1})^2 + (y_i - y_{i-1})^2}{(C_i^1 - C_{i-1}^1)^2 + (C_i^2 - C_{i-1}^2)^2}} \right] \quad \text{per pixel,} \quad (A.11)$$

where C^1 and C^2 are complicated functions of each set of right ascension and declination coordinates.

Appendix B

Emission Properties and Positional Information of the HII regions in M51

No.	α^*				δ^*			H α^\dagger	R ‡	(1)	(2)	(3)	(4)	CCM §
0	13	27	48.1	47	22	7.1	0.42	14103	0.055	-0.090	8.811	-0.629		
1	13	27	49.4	47	22	8.3	1.70	14081	0.473	0.003	8.748	-0.611	61A	
2	13	27	46.7	47	22	8.5	0.65	14035	0.422	0.075	8.699	-0.515		
3	13	27	50.4	47	22	9.0	0.48	14097	0.560	0.332	8.524	-0.461		
4	13	27	49.3	47	22	16.7	0.19	13691	0.692	0.396	8.480	-0.367		
5	13	27	49.0	47	22	22.7	0.18	13404	0.451	0.097	8.684	-0.410		
6	13	27	40.7	47	22	26.5	0.36	13598	0.481	0.280	8.559	-0.476		
7	13	27	44.0	47	22	36.2	0.52	12845	0.464	-0.384	9.012	-0.496		
8	13	27	39.9	47	22	38.4	0.22	13163	0.769	-0.193	8.881	-0.269		
9	13	27	43.7	47	22	38.9	0.30	12745	0.006	-0.286	8.945	-0.325		
10	13	27	45.1	47	22	39.8	0.30	12623	0.433	-0.338	8.980	-0.484		
11	13	27	38.6	47	22	42.2	1.18	13187	0.442	-0.282	8.942	-0.557		
12	13	27	57.2	47	22	41.0	0.34	13478	0.180	0.548	8.376	-0.562		
13	13	27	43.6	47	22	49.9	0.57	12244	1.178	-0.279	8.940	-0.512		
14	13	27	47.2	47	22	56.7	0.39	11791	0.503	-0.385	9.013	-0.457		
15	13	27	46.8	47	23	2.1	0.21	11543	0.313	0.137	8.657	-0.479		
16	13	27	58.4	47	23	0.7	0.38	12906	0.512	0.385	8.487	-0.904		
17	13	27	37.9	47	23	5.7	1.43	12297	0.705	-0.103	8.820	-0.603	67A	
18	13	27	47.3	47	23	5.6	0.23	11375	0.106	-0.330	8.975	-0.359		
19	13	27	37.6	47	23	9.4	1.15	12187	0.581	-0.229	8.906	-0.541	68A	
20	13	27	36.3	47	23	11.3	0.56	12370	1.188	0.079	8.696	-0.432		
21	13	27	43.7	47	23	24.2	0.37	10649	0.392	-0.253	8.923	-0.531		
22	13	27	42.8	47	23	24.7	0.41	10714	0.412	-0.278	8.940	-0.357		
23	13	27	35.7	47	23	26.3	0.74	11893	1.050	0.141	8.654	-0.645		
24	13	27	35.4	47	23	34.4	0.85	11629	1.145	-0.069	8.797	-0.616		
25	13	27	42.1	47	23	35.0	0.66	10313	0.380	-0.294	8.950	-0.478		
26	13	27	43.3	47	23	39.0	0.36	10008	0.494	-0.084	8.807	-0.378		
27	13	27	41.9	47	23	40.0	0.83	10118	1.019	0.061	8.708	-0.554		
28	13	27	34.7	47	23	44.0	0.73	11429	1.625	0.143	8.653	-0.438		
29	13	27	42.1	47	23	46.2	0.48	9813	1.070	0.051	8.715	-0.340		
30	13	27	41.6	47	23	47.2	0.35	9837	1.165	0.214	8.604	-0.339		

(1) C(H β) §

(2) $\log([O III]/H \beta)^\S$

(3) $12+\log(O/H)^\S$

(4) $\log([S II]/H \alpha)^\S$

*Epoch of coordinates is 1950.0. Root mean square variances: RA = 0.696", Dec = 0.488". Total variance is 0.850". (Results derived from CTIO task COORDS).

† Integrated flux through a 4" radius aperture, in units of 10^{-14} ergs cm $^{-2}$ sec $^{-1}$.

‡ Deprojected galactocentric radius, in units of pc.

§ In units of dex.

§ HII region nomenclature as defined in Carranza, Crillon and Monnet 1969.

No.	α		δ		H α		R	(1)	(2)	(3)	(4)	CCM	
31	13	27	57.5	47	23	46.6	0.90	10813	0.471	-0.169	8.865	-0.482	58A
32	13	27	55.9	47	23	46.9	1.60	10443	0.175	-0.120	8.832	-0.665	
33	13	27	34.0	47	23	53.1	0.94	11281	1.324	-0.185	8.876	-0.536	
34	13	27	56.2	47	23	50.2	1.34	10367	0.081	-0.176	8.870	-0.617	
35	13	27	58.4	47	23	52.0	0.47	10839	0.924	0.237	8.588	-0.616	
36	13	27	46.0	47	23	53.6	0.88	9162	1.142	-0.079	8.804	-0.612	57A
37	13	27	50.0	47	23	54.0	0.60	9242	0.698	0.842	8.176	-0.502	
38	13	27	33.2	47	23	58.3	2.05	11307	0.455	0.102	8.680	-0.631	
39	13	27	57.9	47	23	57.9	1.61	10458	0.340	0.357	8.507	-0.901	
40	13	27	51.3	47	23	59.0	0.57	9144	0.689	0.311	8.538	-0.631	
41	13	27	55.2	47	24	3.4	0.69	9594	0.474	0.143	8.653	-0.476	71A
42	13	27	47.4	47	24	5.7	1.10	8583	0.776	-0.163	8.861	-0.593	
43	13	27	43.5	47	24	7.4	0.41	8690	1.110	0.156	8.643	-0.341	
44	13	27	33.2	47	24	9.0	9.45	10911	0.629	-0.240	8.914	-0.737	
45	13	27	53.7	47	24	5.9	0.67	9192	0.598	-0.450	9.057	-0.496	
46	13	27	41.4	47	24	9.0	0.52	8892	1.091	-0.018	8.762	-0.528	59
47	13	27	58.4	47	24	6.7	0.36	10246	0.627	0.087	8.691	-0.357	
48	13	27	55.5	47	24	9.0	0.57	9439	0.069	-0.067	8.796	-0.409	
49	13	27	51.8	47	24	10.8	0.42	8677	1.000	0.261	8.572	-0.433	
50	13	27	44.7	47	24	13.4	0.49	8306	0.631	-0.169	8.865	-0.410	
51	13	27	54.2	47	24	13.5	0.54	8971	1.450	-0.137	8.843	-0.494	64A
52	13	27	46.7	47	24	14.9	1.30	8155	0.581	-0.260	8.928	-0.662	
53	13	27	55.7	47	24	18.3	0.75	9109	0.689	-0.119	8.831	-0.497	
54	13	27	46.5	47	24	18.2	1.10	8002	0.558	-0.225	8.904	-0.652	
55	13	27	41.1	47	24	20.7	0.58	8426	0.928	0.010	8.743	-0.520	
56	13	27	35.8	47	24	21.7	0.30	9662	1.029	-0.079	8.804	-0.341	59
57	13	27	46.9	47	24	20.8	0.74	7877	0.180	-0.350	8.989	-0.494	
58	13	27	32.7	47	24	25.8	0.65	10493	0.933	-0.212	8.894	-0.671	
59	13	27	32.2	47	24	25.5	0.74	10688	1.128	-0.454	9.059	-0.632	
60	13	27	55.0	47	24	23.4	0.44	8725	0.922	-0.171	8.867	-0.463	
61	13	27	55.7	47	24	25.1	0.95	8825	0.893	-0.401	9.023	-0.683	61
62	13	27	51.2	47	24	25.2	0.55	7954	1.565	0.226	8.596	-0.464	
63	13	27	49.5	47	24	27.5	0.62	7669	2.419	0.518	8.397	-0.486	
64	13	27	55.4	47	24	31.1	0.90	8521	0.787	-0.353	8.990	-0.608	
65	13	27	48.7	47	24	32.7	1.46	7371	0.624	-0.335	8.978	-0.647	
66	13	27	44.0	47	24	35.0	0.63	7367	1.586	0.342	8.517	-0.401	68B
67	13	27	56.0	47	24	33.9	0.41	8567	1.197	0.213	8.605	-0.452	
68	13	27	35.5	47	24	39.6	0.43	9057	1.232	-0.012	8.758	-0.453	
69	13	27	47.7	47	24	40.4	1.58	6974	0.839	-0.316	8.965	-0.586	
70	13	27	52.8	47	24	40.8	5.15	7533	0.534	-0.460	9.063	-0.774	
71	13	27	44.0	47	24	41.6	0.89	7071	1.208	0.010	8.743	-0.482	57
72	13	27	32.0	47	24	45.7	0.52	10091	2.534	0.480	8.423	-0.420	
73	13	27	49.9	47	24	44.1	1.22	6952	1.379	-0.369	9.001	-0.536	
74	13	27	36.1	47	24	46.7	0.55	8606	0.710	-0.036	8.774	-0.600	
75	13	27	57.7	47	24	45.6	0.91	8615	1.061	0.124	8.665	-0.276	
76	13	27	56.7	47	24	45.2	0.47	8311	-2.005	-0.825	9.281	-0.422	63
77	13	27	43.1	47	24	48.0	1.31	6897	1.074	-0.205	8.890	-0.555	
78	13	27	54.0	47	24	47.5	0.72	7516	1.401	-0.312	8.963	-0.578	
79	13	27	50.8	47	24	48.4	0.95	6869	1.202	-0.528	9.110	-0.488	
80	13	27	48.6	47	24	47.9	0.93	6665	0.853	-0.062	8.793	-0.507	
81	13	27	44.3	47	24	51.0	3.19	6611	0.814	-0.641	9.219	-0.742	57
82	13	27	35.7	47	24	51.8	0.57	8566	0.836	0.074	8.700	-0.560	
83	13	27	47.9	47	24	50.4	2.16	6515	1.121	-0.171	8.866	-0.604	
84	13	27	45.8	47	24	50.8	0.98	6506	1.704	0.104	8.679	-0.494	
85	13	27	30.8	47	24	53.8	0.61	10279	1.412	0.033	8.728	-0.557	
86	13	27	49.2	47	24	51.4	0.71	6549	1.713	0.193	8.618	-0.502	68B
87	13	27	44.6	47	24	51.7	3.20	6553	0.851	-0.648	9.221	-0.707	
88	13	27	39.0	47	24	54.8	1.69	7464	0.677	-0.513	9.100	-0.699	
89	13	27	41.7	47	24	55.2	0.76	6808	1.512	0.188	8.622	-0.505	
90	13	27	57.7	47	25	2.8	2.81	8012	0.517	-0.749	9.255	-0.689	
91	13	27	54.9	47	24	57.4	8.58	7355	0.323	-0.666	9.227	-0.854	57
92	13	27	40.9	47	25	1.3	2.56	6717	0.952	-0.188	8.878	-0.734	
93	13	27	31.2	47	25	2.6	0.87	9859	1.270	0.235	8.590	-0.548	
94	13	27	47.2	47	24	59.6	0.70	6075	2.089	0.395	8.481	-0.448	
95	13	27	37.9	47	25	3.0	1.15	7438	1.282	-0.085	8.808	-0.541	

No.		α		δ		H α	R	(1)	(2)	(3)	(4)	CCM	
96	13	27	35.4	47	25	5.9	0.49	8192	1.160	0.125	8.664	-0.493	55A
97	13	27	57.6	47	25	3.7	3.17	7960	0.407	-0.457	9.061	-0.650	
98	13	27	41.4	47	25	8.3	1.55	6308	1.231	0.009	8.744	-0.754	
99	13	27	48.6	47	25	8.2	0.28	5735	2.908	0.672	8.292	-0.156	
100	13	27	40.7	47	25	9.7	4.84	6418	0.655	-0.685	9.234	-0.797	68
101	13	27	57.5	47	25	9.2	6.07	7725	0.458	-0.337	8.980	-0.686	54
102	13	27	44.4	47	25	11.7	5.15	5653	0.712	-0.774	9.264	-0.792	64
103	13	27	31.0	47	25	14.7	3.97	9640	0.691	-0.519	9.104	-0.684	72B
104	13	27	56.0	47	25	12.0	4.27	7135	0.228	-0.465	9.067	-0.559	52E
105	13	27	41.7	47	25	16.0	1.19	5919	1.464	-0.275	8.938	-0.596	
106	13	27	37.6	47	25	20.6	3.21	6900	1.045	-0.368	9.001	-0.636	
107	13	27	59.0	47	25	16.6	0.20	8040	0.676	0.353	8.509	-0.058	
108	13	27	56.4	47	25	17.2	19.80	7077	0.369	-0.652	9.222	-0.869	55
109	13	27	31.1	47	25	22.2	1.38	9394	0.565	-0.345	8.986	-0.584	53
110	13	27	50.9	47	25	20.1	0.34	5500	1.923	0.477	8.425	-0.350	
111	13	27	42.0	47	25	22.1	0.63	5595	2.041	0.269	8.567	-0.445	
112	13	27	43.7	47	25	23.4	1.20	5218	1.888	-0.118	8.831	-0.668	
113	13	27	31.9	47	25	24.1	0.39	9016	1.673	0.171	8.634	-0.403	71
114	13	27	41.0	47	25	26.3	1.08	5673	0.989	-0.204	8.889	-0.519	
115	13	27	56.8	47	25	24.8	9.14	6962	0.448	-0.462	9.065	-0.847	
116	13	27	48.0	47	25	27.1	0.37	4828	0.999	0.025	8.733	-0.253	
117	13	27	38.4	47	25	28.4	17.10	6359	0.425	-0.767	9.262	-0.901	52B
118	13	27	47.3	47	25	27.2	0.35	4792	3.420	0.975	8.085	-0.383	
119	13	27	38.3	47	25	28.6	15.70	6389	0.449	-0.697	9.238	-0.865	
120	13	27	54.7	47	25	27.6	0.29	6174	1.194	0.025	8.733	-0.050	
121	13	27	30.6	47	25	33.0	0.21	9346	1.451	0.494	8.413	-0.269	52A
122	13	27	40.5	47	25	33.5	0.95	5523	1.647	-0.182	8.874	-0.506	
123	13	27	58.1	47	25	33.1	1.67	7208	0.955	-0.214	8.896	-0.574	
124	13	27	36.1	47	25	36.7	0.45	6919	1.365	0.123	8.666	-0.459	
125	13	27	35.2	47	25	38.1	0.26	7269	1.542	0.447	8.445	-0.299	52C
126	13	27	59.8	47	25	34.9	0.91	7837	1.147	0.276	8.562	-0.570	
127	13	27	42.8	47	25	40.3	0.50	4661	3.271	0.822	8.190	-0.370	
128	13	27	52.1	47	25	40.9	0.29	4901	2.078	0.385	8.488	-0.213	
129	13	27	46.4	47	25	42.6	0.64	4080	1.804	0.261	8.572	-0.419	65
130	13	27	57.0	47	25	41.0	1.86	6555	0.818	-0.491	9.085	-0.581	
131	13	27	47.6	47	25	42.5	1.02	4097	0.854	-0.085	8.808	-0.599	
132	13	27	31.3	47	25	46.1	0.32	8726	1.776	0.228	8.595	-0.381	
133	13	27	41.9	47	25	45.7	0.32	4661	3.237	0.859	8.164	-0.288	72
134	13	27	48.4	47	25	47.6	1.00	3923	1.968	0.394	8.481	-0.600	
135	13	27	51.8	47	25	48.1	0.25	4563	2.186	0.782	8.217	-0.121	
136	13	27	44.8	47	25	50.6	1.80	3843	1.079	-0.353	8.991	-0.735	
137	13	27	38.0	47	25	51.9	30.10	5739	0.475	-0.860	9.293	-0.884	59A
138	13	27	54.9	47	25	50.2	0.43	5509	0.753	-0.288	8.946	-0.420	
139	13	27	49.1	47	25	52.0	1.73	3812	1.080	-0.182	8.874	-0.671	
140	13	27	37.1	47	25	52.8	5.62	6085	0.608	-0.670	9.228	-0.778	
141	13	27	59.6	47	25	50.2	1.92	7390	0.842	-0.249	8.920	-0.588	51A
142	13	27	52.8	47	25	50.9	0.44	4757	1.313	0.228	8.595	-0.315	
143	13	27	30.8	47	25	55.4	0.33	8753	1.897	0.409	8.471	-0.376	
144	13	27	58.6	47	25	52.2	2.06	6942	1.147	-0.353	8.990	-0.584	
145	13	27	48.9	47	25	53.3	1.60	3728	0.955	-0.160	8.859	-0.655	69
146	13	27	43.4	47	25	54.9	0.86	3911	1.375	-0.019	8.763	-0.567	
147	13	27	50.7	47	25	55.5	0.88	3971	1.805	-0.143	8.847	-0.344	
148	13	27	45.5	47	25	57.1	0.72	3469	1.424	0.108	8.676	-0.429	
149	13	27	41.8	47	25	57.1	2.12	4224	0.916	-0.487	9.082	-0.849	74A
150	13	27	37.1	47	26	3.7	1.82	5783	2.036	-0.174	8.869	-0.642	
151	13	27	59.4	47	25	59.7	2.13	7120	0.842	-0.200	8.886	-0.524	
152	13	27	31.2	47	26	5.1	1.22	8392	1.451	0.030	8.730	-0.569	
153	13	27	29.7	47	26	7.7	0.27	9072	0.969	0.326	8.528	-0.416	51
154	13	27	58.8	47	26	3.9	2.11	6772	0.976	-0.194	8.883	-0.553	
155	13	27	38.5	47	26	7.3	0.76	5096	1.486	0.218	8.601	-0.498	
156	13	27	48.0	47	26	6.8	2.60	3002	1.434	-0.376	9.006	-0.652	
157	13	27	51.5	47	26	6.7	1.70	3761	1.925	0.365	8.501	-0.455	51
158	13	27	39.9	47	26	5.0	0.88	4592	3.140	0.884	8.147	-0.436	
159	13	27	38.2	47	26	10.9	0.61	5132	3.966	0.864	8.161	-0.399	
160	13	28	1.6	47	26	8.5	0.32	7956	2.550	0.494	8.413	-0.428	

No.		α			δ		H α	R	(1)	(2)	(3)	(4)	CCM
161	13	27	36.7	47	26	18.2	3.52	5612	0.646	-0.531	9.112	-0.818	
162	13	27	53.3	47	26	11.5	0.92	4248	0.773	-0.211	8.894	-0.481	
163	13	27	44.1	47	26	12.0	3.06	3020	0.854	-0.427	9.041	-0.928	66
164	13	27	40.6	47	26	12.4	0.54	4107	2.227	0.798	8.206	-0.398	
165	13	27	46.6	47	26	12.2	2.76	2697	1.154	-0.367	9.001	-0.733	60
166	13	27	59.9	47	26	11.5	1.07	7090	1.391	0.089	8.689	-0.552	50A
167	13	27	53.6	47	26	12.0	0.93	4347	1.072	-0.150	8.852	-0.441	52D
168	13	28	0.6	47	26	12.6	0.48	7400	0.598	-0.143	8.847	-0.333	
169	13	27	59.4	47	26	12.3	0.96	6868	0.917	-0.313	8.963	-0.512	
170	13	27	50.5	47	26	14.6	6.31	3190	1.318	-0.691	9.236	-0.739	56
171	13	27	42.3	47	26	16.1	0.82	3391	1.357	0.005	8.747	-0.566	
172	13	27	36.7	47	26	18.7	3.55	5601	0.676	-0.544	9.121	-0.818	73
173	13	27	49.2	47	26	16.3	2.72	2774	1.525	-0.222	8.901	-0.596	
174	13	27	52.0	47	26	16.7	1.18	3606	3.923	0.762	8.230	-0.452	
175	13	27	39.2	47	26	20.6	0.95	4436	1.352	1.168	7.954	-0.390	
176	13	27	44.3	47	26	20.2	2.38	2649	0.824	-0.471	9.071	-0.726	67
177	13	27	54.3	47	26	20.5	0.30	4432	2.772	0.856	8.166	-0.135	
178	13	27	46.0	47	26	22.8	2.12	2239	0.945	-0.464	9.067	-0.675	62
179	13	27	40.6	47	26	25.5	0.47	3719	2.171	0.275	8.563	-0.405	
180	13	27	38.4	47	26	27.6	0.27	4655	3.775	1.285	7.874	-0.240	
181	13	27	43.8	47	26	27.5	0.56	2479	2.565	0.508	8.404	-0.364	
182	13	27	39.3	47	26	29.0	0.62	4195	2.294	0.428	8.458	-0.434	
183	13	27	36.5	47	26	28.6	1.81	5488	1.981	-0.014	8.760	-0.769	74
184	13	28	1.5	47	26	26.9	0.36	7665	1.687	0.240	8.586	-0.448	
185	13	27	59.8	47	26	27.1	0.33	6821	1.414	0.285	8.556	-0.456	
186	13	27	52.1	47	26	28.4	2.10	3319	1.498	-0.125	8.835	-0.619	52
187	13	27	41.1	47	26	32.1	0.89	3353	1.723	0.155	8.644	-0.479	
188	13	27	51.6	47	26	30.7	1.37	3021	1.597	-0.130	8.839	-0.413	
189	13	27	36.8	47	26	33.8	1.34	5286	2.689	0.345	8.515	-0.668	
190	13	27	48.7	47	26	32.8	1.56	2000	0.489	-0.534	9.114	-0.716	58
191	13	27	38.0	47	26	36.0	0.32	4678	3.845	1.500	7.728	-0.335	
192	13	27	46.2	47	26	35.7	0.94	1628	1.384	0.152	8.646	-0.459	
193	13	27	55.3	47	26	35.1	1.64	4598	1.194	-0.055	8.788	-0.678	50
194	13	27	31.3	47	26	39.6	0.58	7863	1.197	-0.210	8.893	-0.497	
195	13	27	47.0	47	26	38.9	0.69	1459	1.099	0.198	8.615	-0.280	
196	13	27	44.5	47	26	38.4	1.73	1859	1.831	-0.164	8.861	-0.613	
197	13	27	35.8	47	26	40.0	5.24	5657	0.761	-0.830	9.283	-0.819	76
198	13	28	1.7	47	26	36.3	0.69	7636	1.276	0.137	8.656	-0.392	
199	13	27	34.4	47	26	41.4	0.50	6356	2.457	0.671	8.292	-0.488	
200	13	28	4.0	47	26	37.4	0.65	8774	0.273	-0.193	8.882	-0.765	
201	13	27	53.7	47	26	40.0	5.54	3759	1.181	-0.580	9.145	-0.747	
202	13	27	37.3	47	26	42.1	0.54	4937	2.669	0.683	8.285	-0.277	
203	13	27	40.3	47	26	43.9	1.24	3437	1.820	0.192	8.619	-0.572	
204	13	27	59.5	47	26	41.8	0.43	6557	1.851	0.309	8.539	-0.374	
205	13	27	54.0	47	26	42.4	5.88	3881	0.989	-0.517	9.102	-0.797	49
206	13	27	56.0	47	26	43.4	1.08	4804	1.049	-0.151	8.853	-0.668	48
207	13	27	52.7	47	26	44.0	1.11	3229	1.745	0.024	8.734	-0.377	
208	13	27	50.3	47	26	44.9	1.33	2132	1.162	-0.310	8.961	-0.543	
209	13	27	39.3	47	26	48.1	0.50	3861	3.382	1.177	7.948	-0.340	
210	13	28	0.5	47	26	45.5	1.54	6978	0.791	-0.110	8.825	-0.629	
211	13	27	51.1	47	26	46.8	1.44	2448	1.215	-0.328	8.974	-0.611	
212	13	27	44.2	47	26	48.0	4.82	1641	0.894	-0.538	9.117	-0.829	72A
213	13	27	38.5	47	26	49.2	0.86	4249	2.350	0.422	8.462	-0.505	
214	13	27	37.7	47	26	49.2	1.18	4615	1.866	0.063	8.707	-0.602	
215	13	27	45.9	47	26	51.2	3.31	966	1.134	-0.117	8.830	-0.520	
216	13	27	45.5	47	26	49.5	2.88	1147	1.107	-0.234	8.910	-0.641	67B
217	13	27	41.0	47	26	49.8	1.69	3015	1.014	-0.343	8.984	-0.645	75
218	13	27	31.9	47	26	51.4	0.47	7500	2.682	0.554	8.372	-0.472	
219	13	27	33.6	47	26	53.1	0.39	6616	2.704	0.860	8.164	-0.405	
220	13	27	43.9	47	26	53.1	6.11	1616	1.066	-0.501	9.092	-0.761	72C
221	13	28	0.7	47	26	51.2	2.65	7077	0.460	-0.440	9.050	-0.629	47
222	13	27	57.9	47	26	51.6	0.35	5682	3.369	0.981	8.081	-0.294	
223	13	27	53.3	47	26	54.1	0.88	3366	1.920	0.233	8.591	-0.369	
224	13	27	52.2	47	26	54.8	0.49	2861	1.867	0.458	8.438	-0.285	
225	13	27	46.1	47	26	56.2	5.09	719	1.058	-0.217	8.898	-0.702	

No.		α		δ		H α	R	(1)	(2)	(3)	(4)	CCM
226	13	27	37.9	47	26	57.8	0.58	4472	4.134	0.893	8.141	-0.337
227	13	27	31.9	47	27	0.3	0.41	7448	1.840	0.382	8.489	-0.441
228	13	27	59.2	47	26	58.2	0.61	6300	1.365	0.148	8.649	-0.380
229	13	27	32.6	47	27	1.8	0.68	7088	1.727	0.167	8.636	-0.462
230	13	27	46.7	47	27	0.6	4.76	444	1.178	0.755	8.235	-0.314
231	13	27	44.5	47	27	2.2	4.93	1189	1.876	-0.022	8.765	-0.873
232	13	27	40.1	47	27	4.1	0.59	3341	2.446	0.433	8.455	-0.421
233	13	27	35.6	47	27	3.1	0.83	5587	2.863	0.723	8.257	-0.607
234	13	27	41.5	47	27	4.0	0.72	2620	0.934	-0.193	8.881	-0.495
235	13	27	34.5	47	27	5.1	1.09	6134	1.318	0.004	8.747	-0.657
236	13	27	51.1	47	27	3.3	1.88	2247	1.157	-0.434	9.046	-0.666
237	13	27	52.8	47	27	4.2	0.49	3070	2.545	0.607	8.336	-0.255
238	13	27	36.9	47	27	6.9	5.10	4901	0.974	-0.316	8.966	-0.957
239	13	28	0.9	47	27	4.6	4.77	7127	0.431	-0.442	9.051	-0.724
240	13	27	54.8	47	27	6.3	7.71	4076	0.620	-0.702	9.239	-0.830
241	13	27	44.0	47	27	5.9	4.44	1368	1.359	-0.264	8.930	-0.748
242	13	28	2.0	47	27	7.6	2.10	7700	0.661	-0.168	8.864	-0.644
243	13	27	59.8	47	27	7.2	1.35	6585	0.898	0.045	8.719	-0.543
244	13	27	56.2	47	27	9.8	0.83	4767	2.912	0.474	8.427	-0.362
245	13	27	45.4	47	27	11.6	5.74	648	1.451	-0.198	8.885	-0.828
246	13	27	31.6	47	27	13.9	0.68	7588	1.598	0.358	8.506	-0.606
247	13	27	46.7	47	27	11.8	16.90	77	1.975	0.439	8.451	-2.561
248	13	27	52.6	47	27	12.6	0.58	2950	1.813	0.205	8.611	-0.349
249	13	27	49.7	47	27	13.3	9.41	1543	0.928	-0.474	9.073	-0.884
250	13	27	49.2	47	27	14.4	9.63	1271	0.798	-0.642	9.219	-1.013
251	13	27	38.8	47	27	16.4	1.40	3943	1.959	-0.391	9.017	-0.685
252	13	28	0.9	47	27	4.8	4.64	7116	0.750	-0.727	9.248	-0.811
253	13	27	40.9	47	27	17.9	0.51	2925	2.180	0.244	8.583	-0.380
254	13	27	55.7	47	27	16.9	4.24	4555	1.299	-0.436	9.047	-0.809
255	13	27	39.6	47	27	20.4	0.80	3599	4.325	0.850	8.171	-0.391
256	13	28	0.3	47	27	18.0	0.81	6851	1.423	0.085	8.692	-0.437
257	13	27	51.4	47	27	20.5	1.23	2431	1.186	-0.207	8.891	-0.587
258	13	27	32.2	47	27	24.0	0.35	7302	1.763	0.490	8.416	-0.410
259	13	27	38.7	47	27	24.0	2.04	4047	1.657	-0.255	8.924	-0.666
260	13	27	37.1	47	27	23.9	0.38	4854	3.445	1.096	8.003	-0.362
261	13	27	39.4	47	27	24.9	1.23	3713	2.088	0.066	8.705	-0.514
262	13	27	52.5	47	27	23.4	0.68	2972	2.574	0.587	8.350	-0.526
263	13	27	50.1	47	27	23.9	7.14	1820	0.749	-0.632	9.216	-1.034
264	13	27	58.0	47	27	24.7	1.14	5724	0.705	-0.260	8.928	-0.618
265	13	27	53.4	47	27	25.0	0.87	3435	1.792	0.332	8.523	-0.551
266	13	27	44.8	47	27	25.4	8.70	1160	1.122	-0.584	9.148	-0.826
267	13	27	48.6	47	27	30.8	10.30	1371	0.764	-0.808	9.276	-1.031
268	13	27	43.0	47	27	28.6	2.07	2018	0.845	-0.443	9.052	-0.712
269	13	27	40.9	47	27	30.3	0.39	3054	1.866	0.574	8.359	-0.175
270	13	27	33.5	47	27	30.6	0.61	6654	0.787	-0.264	8.930	-0.432
271	13	27	56.1	47	27	27.5	4.95	4808	0.851	-0.541	9.119	-0.855
272	13	27	32.7	47	27	31.8	1.19	7072	0.632	-0.247	8.919	-0.600
273	13	27	45.5	47	27	31.3	9.91	1128	0.965	-0.393	9.018	-0.850
274	13	27	57.9	47	27	29.1	1.12	5699	0.831	-0.246	8.918	-0.686
275	13	27	48.6	47	27	30.8	10.30	1371	0.764	-0.799	9.272	-1.027
276	13	27	46.5	47	27	31.6	8.82	1003	0.916	-0.235	8.910	-0.758
277	13	27	58.0	47	27	27.1	1.22	5744	0.779	-0.303	8.956	-0.647
278	13	27	45.9	47	27	33.6	10.80	1156	0.938	-0.452	9.058	-0.897
279	13	27	41.2	47	27	31.6	0.92	2941	3.163	0.662	8.299	-0.412
280	13	27	44.4	47	27	37.4	1.46	1684	1.577	0.122	8.667	-0.556
281	13	27	43.4	47	27	35.9	0.72	2023	1.505	0.099	8.682	-0.350
282	13	27	39.7	47	27	37.7	1.52	3683	1.533	-0.158	8.857	-0.529
283	13	27	37.6	47	27	38.4	0.40	4698	3.410	0.867	8.159	-0.407
284	13	27	33.8	47	27	40.0	2.26	6569	0.514	-0.474	9.073	-0.666
285	13	27	52.7	47	27	38.5	0.96	3303	2.385	0.202	8.612	-0.548
286	13	27	39.0	47	27	40.2	0.63	4050	3.314	0.837	8.179	-0.329
287	13	27	32.9	47	27	42.0	1.59	7057	0.852	-0.485	9.080	-0.695
288	13	27	47.2	47	27	41.0	5.04	1467	0.709	-0.620	9.211	-0.890
289	13	27	40.2	47	27	42.4	3.43	3568	1.214	-0.507	9.096	-0.660
290	13	28	2.4	47	27	39.3	1.26	8037	1.110	-0.130	8.839	-0.605

No.		α		δ		H α	R	(1)	(2)	(3)	(4)	CCM	
291	13	28	0.8	47	27	39.6	0.39	7247	2.272	0.464	8.434	-0.245	
292	13	27	55.6	47	27	40.6	1.57	4735	3.182	0.234	8.590	-0.550	39
293	13	27	50.5	47	27	42.2	1.96	2443	1.768	0.018	8.738	-0.731	28
294	13	27	48.0	47	27	41.6	9.86	1625	0.437	-0.925	9.315	-1.100	6A
295	13	27	41.9	47	27	43.2	0.37	2811	4.115	1.075	8.017	-0.124	
296	13	27	33.6	47	27	47.0	0.72	6768	-0.514	-0.473	9.072	-0.318	
297	13	27	58.5	47	27	45.1	0.98	6173	2.234	0.072	8.701	-0.564	
298	13	27	40.7	47	27	48.5	3.97	3449	1.108	-0.534	9.114	-0.734	83
299	13	27	55.3	47	27	45.5	0.93	4660	2.099	-0.078	8.803	-0.430	
300	13	27	56.8	47	27	48.1	3.53	5427	0.831	-0.713	9.243	-0.792	40
301	13	27	47.5	47	27	49.1	1.92	1864	0.860	-0.120	8.832	-0.602	
302	13	27	57.7	47	27	48.6	6.15	5835	0.493	-0.894	9.305	-0.839	41
303	13	27	46.1	47	27	50.5	1.45	1895	1.430	0.113	8.673	-0.515	
304	13	27	42.4	47	27	52.5	0.86	2880	1.770	0.096	8.685	-0.528	
305	13	27	41.6	47	27	52.4	1.19	3198	2.478	0.251	8.579	-0.552	
306	13	27	53.2	47	27	52.5	1.05	3855	1.515	0.011	8.743	-0.603	
307	13	27	38.8	47	27	55.1	2.17	4414	1.419	-0.139	8.845	-0.759	82
308	13	27	33.6	47	27	56.7	0.23	6859	1.296	0.504	8.407	-0.254	
309	13	28	0.9	47	27	54.3	2.70	7454	0.676	-0.300	8.955	-0.616	
310	13	27	58.3	47	27	54.4	1.79	6239	1.266	-0.130	8.839	-0.663	
311	13	27	55.2	47	27	55.0	0.88	4796	2.865	0.190	8.620	-0.433	
312	13	27	49.7	47	27	55.7	5.14	2639	0.697	-0.766	9.261	-1.011	17
313	13	28	1.1	47	27	55.9	3.13	7593	0.616	-0.360	8.995	-0.650	42
314	13	27	55.9	47	27	57.8	1.24	5177	2.076	0.111	8.674	-0.485	35
315	13	27	40.3	47	28	2.5	5.27	3966	0.646	-0.552	9.126	-0.927	84
316	13	27	55.4	47	28	2.6	2.33	5042	1.455	-0.459	9.063	-0.608	34
317	13	27	41.3	47	28	4.5	3.28	3646	0.917	-0.478	9.076	-0.855	85
318	13	27	33.8	47	28	6.2	0.16	6941	2.423	1.448	7.762	-0.143	
319	13	27	58.7	47	28	1.8	1.74	6554	1.290	-0.120	8.832	-0.688	
320	13	27	57.7	47	28	3.5	2.73	6099	0.824	-0.530	9.111	-0.689	36
321	13	27	48.7	47	28	5.7	5.15	2802	1.035	-0.563	9.134	-0.852	4
322	13	27	50.1	47	28	6.1	3.86	3150	0.749	-0.540	9.118	-0.952	12
323	13	27	39.6	47	28	7.5	0.74	4391	0.885	0.037	8.725	-0.456	
324	13	28	2.4	47	28	5.5	0.94	8337	1.111	-0.036	8.774	-0.479	
325	13	27	47.1	47	28	8.3	11.50	2718	0.672	-1.056	9.360	-0.978	107
326	13	27	43.4	47	28	9.6	9.09	3201	1.083	-0.779	9.266	-0.855	
327	13	27	32.3	47	28	11.2	0.18	7675	1.348	0.489	8.416	-0.421	
328	13	27	33.1	47	28	12.8	0.21	7375	2.852	0.998	8.070	-0.405	
329	13	28	1.6	47	28	9.5	1.87	8035	1.079	0.029	8.730	-0.603	
330	13	27	32.9	47	28	14.7	0.20	7460	2.787	1.002	8.067	-0.350	
331	13	27	46.1	47	28	14.3	18.20	2995	0.552	-0.970	9.331	-0.959	
332	13	27	45.1	47	28	14.5	3.88	3074	1.059	-0.467	9.068	-0.775	94
333	13	27	48.0	47	28	16.7	2.01	3182	1.242	-0.337	8.980	-0.781	2C
334	13	28	1.7	47	28	15.2	2.25	8163	0.870	-0.076	8.802	-0.618	39A
335	13	27	50.2	47	28	17.6	1.37	3633	0.776	-0.309	8.960	-0.718	10A
336	13	27	58.5	47	28	18.2	1.58	6796	0.943	-0.270	8.934	-0.558	38
337	13	27	46.6	47	28	19.8	4.39	3240	0.958	-0.437	9.048	-0.788	103
338	13	27	59.7	47	28	20.3	1.35	7340	1.413	0.114	8.672	-0.632	
339	13	27	55.4	47	28	20.0	10.50	5509	0.719	-0.697	9.238	-0.796	27
340	13	27	50.3	47	28	20.5	1.33	3776	0.792	-0.174	8.869	-0.654	
341	13	27	48.6	47	28	21.9	1.60	3499	1.072	-0.098	8.817	-0.724	
342	13	27	35.2	47	28	25.0	1.14	6672	1.219	-0.001	8.751	-0.537	
343	13	28	2.6	47	28	20.3	2.40	8673	0.659	-0.291	8.948	-0.612	37
344	13	27	57.4	47	28	22.1	1.94	6401	1.284	-0.128	8.837	-0.637	32
345	13	27	58.4	47	28	23.2	2.81	6861	0.874	-0.327	8.973	-0.613	
346	13	27	42.2	47	28	26.1	1.06	4139	1.419	0.061	8.708	-0.600	
347	13	27	59.8	47	28	23.9	1.36	7482	1.654	0.197	8.616	-0.623	
348	13	27	53.5	47	28	25.5	1.55	4934	1.575	-0.158	8.858	-0.682	22
349	13	27	34.7	47	28	28.7	2.30	6981	0.719	-0.285	8.944	-0.695	80A
350	13	27	45.5	47	28	27.1	2.18	3616	1.231	-0.187	8.877	-0.821	100
351	13	27	35.7	47	28	28.1	0.79	6549	1.453	0.141	8.654	-0.579	
352	13	28	1.8	47	28	25.9	1.17	8443	0.929	-0.074	8.801	-0.492	
353	13	27	43.8	47	28	29.0	0.59	3922	1.875	0.413	8.469	-0.354	
354	13	27	37.3	47	28	30.1	0.21	5933	2.776	0.893	8.141	-0.107	
355	13	27	42.4	47	28	30.8	1.05	4275	1.927	0.148	8.649	-0.553	89

No.	α			δ			Π	α	R	(1)	(2)	(3)	(4)	CCM
356	13	27	58.7	47	28	29.4	3.66	7140	0.983	-0.253	8.922	-0.648		
357	13	27	56.6	47	28	32.4	3.59	6324	0.872	-0.496	9.088	-0.649	26	
358	13	27	54.8	47	28	33.4	12.90	5692	0.526	-0.878	9.299	-0.818	24	
359	13	27	45.8	47	28	34.3	1.15	3935	1.539	0.040	8.723	-0.675		
360	13	27	37.7	47	28	37.7	1.00	6020	1.888	0.332	8.524	-0.693	84A	
361	13	27	59.0	47	28	36.7	3.05	7456	0.935	-0.303	8.957	-0.683	31	
362	13	27	54.6	47	28	38.1	10.80	5763	0.517	-0.736	9.251	-0.795		
363	13	27	52.8	47	28	39.6	0.67	5224	2.079	0.179	8.628	-0.475		
364	13	28	1.8	47	28	40.9	3.06	8751	0.744	-0.167	8.864	-0.599	33	
365	13	27	59.4	47	28	41.9	1.90	7746	1.003	-0.172	8.867	-0.567		
366	13	27	57.5	47	28	42.3	1.39	6991	1.485	-0.031	8.771	-0.486		
367	13	27	37.6	47	28	48.4	0.42	6396	3.441	0.799	8.205	-0.401		
368	13	27	56.9	47	28	46.3	1.92	6886	0.992	-0.227	8.905	-0.564		
369	13	27	42.3	47	28	48.9	1.58	5051	1.400	-0.336	8.979	-0.689		
370	13	27	57.8	47	28	47.0	1.49	7226	1.247	-0.236	8.911	-0.518		
371	13	27	54.4	47	28	47.6	8.36	6032	0.690	-0.550	9.125	-0.705	19	
372	13	27	37.2	47	28	50.9	0.39	6598	3.659	0.897	8.138	-0.377		
373	13	27	58.4	47	28	49.2	1.23	7525	1.141	-0.117	8.830	-0.499		
374	13	27	44.6	47	28	52.7	0.98	4861	2.764	0.570	8.362	-0.561		
375	13	28	1.4	47	28	49.8	4.28	8810	0.999	-0.165	8.862	-0.767	30	
376	13	27	55.9	47	28	50.9	2.78	6649	0.971	-0.153	8.854	-0.668	21	
377	13	27	41.4	47	28	54.9	2.25	5501	1.531	-0.254	8.923	-0.578	91A	
378	13	27	52.6	47	28	52.7	0.95	5676	3.695	0.458	8.438	-0.495		
379	13	27	46.8	47	28	53.3	0.76	4799	2.444	0.457	8.438	-0.586		
380	13	28	2.4	47	28	54.1	0.50	9314	1.749	0.287	8.554	-0.359		
381	13	27	43.5	47	28	58.0	1.88	5230	2.532	0.172	8.633	-0.631	95	
382	13	27	39.0	47	28	59.3	5.79	6318	0.870	-0.258	8.926	-0.680	86	
383	13	27	57.7	47	28	56.5	1.12	7480	1.432	0.079	8.696	-0.529		
384	13	27	45.6	47	28	59.4	0.63	5099	2.613	0.689	8.280	-0.435		
385	13	27	54.1	47	28	59.6	7.45	6382	0.760	-0.469	9.070	-0.729	14	
386	13	27	44.6	47	29	2.6	0.74	5313	2.133	0.505	8.406	-0.432		
387	13	27	53.1	47	29	2.2	1.95	6192	1.509	-0.126	8.836	-0.478		
388	13	27	42.2	47	28	59.5	1.15	5515	2.067	0.434	8.454	-0.436		
389	13	27	55.6	47	29	4.1	2.81	7014	0.815	-0.163	8.861	-0.606	18	
390	13	27	40.4	47	29	6.3	3.90	6209	0.687	-0.316	8.965	-0.702	88	
391	13	27	47.7	47	29	5.6	2.36	5407	1.021	-0.289	8.947	-0.750	109	
392	13	27	56.2	47	29	4.7	2.61	7219	0.842	-0.270	8.934	-0.596		
393	13	27	51.1	47	29	6.1	1.01	5877	2.738	0.224	8.597	-0.526		
394	13	28	2.6	47	29	5.8	0.64	9721	2.103	0.573	8.360	-0.366		
395	13	27	57.4	47	29	6.1	1.31	7710	0.920	-0.192	8.881	-0.540		
396	13	27	59.2	47	29	6.5	0.44	8374	2.201	0.288	8.554	-0.343		
397	13	27	43.5	47	29	10.0	0.73	5770	2.874	0.773	8.223	-0.440		
398	13	27	41.0	47	29	9.9	7.46	6204	0.608	-0.290	8.948	-0.801	91	
399	13	27	53.7	47	29	9.0	6.09	6613	0.613	-0.517	9.103	-0.751	11	
400	13	28	1.7	47	29	12.4	0.46	9525	1.534	0.115	8.672	-0.459		
401	13	27	49.7	47	29	20.7	6.95	6283	3.592	-0.054	8.787	-1.102		
402	13	27	40.1	47	29	14.4	5.98	6603	0.438	-0.287	8.946	-0.811	90	
403	13	28	2.4	47	29	11.1	0.88	9772	1.319	0.115	8.672	-0.543	29A	
404	13	28	0.2	47	29	11.5	0.58	8931	0.922	-0.047	8.782	-0.414		
405	13	27	56.9	47	29	12.2	1.75	7720	0.626	-0.299	8.954	-0.562		
406	13	27	44.4	47	29	14.6	4.48	5878	1.039	-0.559	9.131	-0.747	97	
407	13	27	43.4	47	29	14.8	0.70	5998	3.211	0.870	8.157	-0.469		
408	13	27	52.4	47	29	17.8	10.40	6652	0.576	-0.630	9.215	-0.787		
409	13	27	57.6	47	29	17.3	0.90	8130	1.390	0.053	8.714	-0.422		
410	13	27	57.1	47	29	17.5	1.15	7971	0.946	-0.123	8.834	-0.465		
411	13	27	51.6	47	29	23.6	5.30	6725	2.196	-0.094	8.814	-0.823		
412	13	27	58.7	47	29	19.6	0.49	8609	1.590	0.126	8.664	-0.380		
413	13	27	54.7	47	29	19.8	3.70	7311	0.728	-0.340	8.982	-0.665	16	
414	13	27	52.9	47	29	19.6	10.10	6833	0.530	-0.660	9.225	-0.732	8	
415	13	27	49.6	47	29	21.2	7.29	6301	0.634	-0.816	9.278	-0.749	2	
416	13	27	41.5	47	29	22.3	2.18	6615	0.538	-0.309	8.960	-0.577	93	
417	13	27	44.3	47	29	27.7	5.62	6487	3.552	-0.262	8.929	-0.866		
418	13	27	51.6	47	29	23.2	5.42	6718	0.820	-0.426	9.041	-0.641		
419	13	27	46.4	47	29	23.5	4.43	6204	0.805	-0.300	8.955	-0.755	102	
420	13	27	47.0	47	29	24.2	3.51	6244	0.909	-0.270	8.934	-0.677	105	

No.	α		δ		H α	R	(1)	(2)	(3)	(4)	CCM		
421	13	27	44.5	47	29	25.4	5.47	6363	0.627	-0.610	9.208	-0.717	99
422	13	27	46.3	47	29	24.0	4.61	6226	0.876	-0.294	8.951	-0.774	
423	13	28	1.2	47	29	26.1	2.03	9731	0.947	-0.281	8.942	-0.663	25A
424	13	27	53.7	47	29	27.2	23.60	7339	0.402	-0.724	9.247	-0.899	10
425	13	27	48.3	47	29	28.1	2.51	6486	1.403	-0.017	8.762	-0.638	109A
426	13	27	50.8	47	29	28.9	4.08	6810	0.831	-0.374	9.005	-0.680	3
427	13	27	49.5	47	29	31.1	14.00	6743	0.606	-0.630	9.215	-0.736	1
428	13	27	45.7	47	29	32.1	1.04	6610	1.525	0.189	8.621	-0.602	
429	13	27	52.4	47	29	32.6	7.55	7284	0.568	-0.365	8.999	-0.693	6
430	13	27	56.3	47	29	33.1	6.96	8300	0.179	-0.337	8.980	-0.696	
431	13	27	51.6	47	29	33.5	5.47	7152	0.768	-0.228	8.906	-0.598	
432	13	27	47.9	47	29	34.2	3.11	6743	1.131	-0.062	8.792	-0.741	108
433	13	27	54.9	47	29	34.0	2.83	7936	0.534	-0.300	8.954	-0.650	
434	13	27	46.8	47	29	36.5	1.15	6810	1.214	0.045	8.719	-0.586	104
435	13	27	50.1	47	29	37.3	3.22	7098	1.198	-0.036	8.775	-0.621	2B
436	13	27	45.5	47	29	38.2	1.05	6901	0.988	-0.094	8.814	-0.563	
437	13	27	44.6	47	29	37.8	1.10	6930	0.962	-0.251	8.921	-0.674	
438	13	27	56.3	47	29	33.1	6.96	8300	0.179	-0.337	8.980	-0.696	13
439	13	27	48.4	47	29	38.8	1.12	6993	2.059	0.274	8.563	-0.513	
440	13	27	49.3	47	29	40.3	2.20	7133	1.010	-0.242	8.915	-0.597	109B
441	13	27	52.6	47	29	39.6	9.21	7625	0.384	-0.372	9.004	-0.828	5
442	13	27	51.5	47	29	34.1	5.00	7166	0.751	-0.409	9.029	-0.686	
443	13	27	43.9	47	29	43.3	0.33	7229	1.708	0.344	8.515	-0.401	
444	13	27	50.0	47	29	44.5	1.94	7399	0.957	-0.042	8.779	-0.585	2A
445	13	28	1.5	47	29	43.0	3.06	10391	0.322	-0.251	8.921	-0.617	23
446	13	27	45.2	47	29	46.1	1.30	7278	1.187	0.185	8.624	-0.673	
447	13	27	45.9	47	29	48.8	1.65	7386	0.916	-0.195	8.883	-0.641	101
448	13	28	1.0	47	29	47.2	3.00	10337	0.038	-0.449	9.056	-0.715	
449	13	27	53.4	47	29	49.9	0.73	8215	0.631	0.122	8.667	-0.376	
450	13	27	47.9	47	29	50.6	2.25	7505	0.879	-0.489	9.084	-0.639	106
451	13	28	0.5	47	29	52.0	2.29	10325	0.464	-0.378	9.008	-0.582	
452	13	27	53.8	47	29	56.7	0.97	8604	0.976	0.125	8.665	-0.404	
453	13	28	0.7	47	29	59.3	2.95	10663	0.276	-0.515	9.101	-0.642	20
454	13	27	47.5	47	30	4.5	0.55	8135	1.275	0.038	8.724	-0.481	
455	13	27	49.9	47	30	7.2	0.43	8428	0.940	0.052	8.714	-0.439	
456	13	28	0.1	47	30	16.1	0.88	11083	0.895	-0.150	8.852	-0.656	
457	13	27	47.5	47	30	17.9	0.45	8755	0.541	0.113	8.673	-0.512	
458	13	28	0.1	47	30	16.1	0.88	11083	0.895	-0.154	8.855	-0.656	
459	13	27	59.4	47	30	29.2	0.33	11347	1.194	0.078	8.697	-0.364	
460	13	27	59.2	47	30	36.4	0.31	11572	1.386	0.353	8.510	-0.387	
461	13	27	58.6	47	30	51.0	1.88	11985	1.028	-0.259	8.926	-0.630	10B
462	13	27	58.0	47	31	1.7	7.90	12280	0.546	-0.356	8.993	-0.767	9
463	13	27	57.5	47	31	14.1	7.02	12691	0.373	-0.075	8.801	-0.825	7
464	13	27	56.3	47	31	38.0	1.34	13459	1.249	-0.193	8.882	-0.485	

Appendix C

Emission Properties and Positional Information of the HII regions in NGC 4449

No.	α^*		δ^*		H α [†]	R [‡]	(1)	(2)	(3)	(4)	SB [¶]		
0	12	26	0.6	44	22	37.1	0.97	3825	0.740	0.302	8.544	-0.732	
1	12	26	0.3	44	22	33.0	0.59	3725	0.483	0.099	8.682	-0.546	
2	12	25	56.7	44	22	9.3	0.53	2774	1.159	0.637	8.315	-0.235	
3	12	25	55.1	44	22	42.9	1.50	2435	0.677	0.170	8.634	-0.443	
4	12	25	54.9	44	22	52.1	3.41	2450	0.490	0.435	8.453	-0.653	3
5	12	25	54.5	44	21	48.0	1.37	2301	0.693	0.317	8.534	-0.645	
6	12	25	54.3	44	22	27.4	0.73	2148	1.134	0.290	8.552	-0.322	
7	12	25	54.1	44	22	52.2	14.70	2270	0.464	0.495	8.412	-0.942	5,6
8	12	25	53.6	44	21	31.3	0.48	2236	1.199	0.387	8.486	-0.451	
9	12	25	53.5	44	22	55.3	4.18	2138	0.583	0.435	8.453	-0.588	8
10	12	25	53.3	44	22	36.3	4.42	1939	0.559	0.362	8.503	-0.729	9
11	12	25	53.3	44	23	30.5	0.74	2594	0.361	0.196	8.617	-0.344	
12	12	25	52.9	44	22	44.1	3.81	1905	0.599	0.271	8.565	-0.568	12
13	12	25	52.8	44	23	29.2	1.32	2490	0.691	0.192	8.619	-0.469	
14	12	25	52.6	44	22	40.6	3.51	1806	0.698	0.339	8.519	-0.463	15
15	12	25	52.6	44	23	4.9	13.40	2074	0.517	0.222	8.599	-0.678	13
16	12	25	52.4	44	23	11.6	13.80	2124	0.010	0.240	8.587	-0.520	17
17	12	25	52.3	44	22	21.6	1.97	1617	0.854	0.411	8.470	-0.474	19
18	12	25	52.1	44	23	10.4	20.50	2049	0.506	0.295	8.549	-0.580	20
19	12	25	52.1	44	23	15.0	9.58	2123	0.454	0.245	8.583	-0.406	21
20	12	25	51.9	44	22	12.6	2.85	1533	0.705	0.435	8.453	-0.524	22
21	12	25	51.8	44	21	58.3	0.87	1553	1.312	0.404	8.475	-0.258	
22	12	25	51.8	44	23	7.7	30.40	1934	0.480	0.363	8.503	-0.760	23
24	12	25	51.5	44	22	14.5	5.04	1409	0.528	0.451	8.443	-0.631	26
25	12	25	51.2	44	22	0.5	1.19	1397	1.464	0.464	8.434	-0.232	
26	12	25	51.3	44	23	15.4	3.98	1973	0.692	0.375	8.495	-0.476	
27	12	25	51.2	44	23	25.7	6.15	2142	0.449	0.366	8.500	-0.619	28
28	12	25	50.6	44	22	58.0	3.35	1541	0.725	0.382	8.489	-0.411	
29	12	25	50.5	44	23	3.6	5.22	1627	0.564	0.388	8.486	-0.525	
30	12	25	50.3	44	23	7.2	8.82	1651	0.644	0.508	8.403	-0.715	
31	12	25	50.2	44	22	59.4	4.92	1490	0.651	0.861	8.163	-0.499	
32	12	25	50.2	44	23	17.9	35.70	1834	0.502	0.439	8.450	-0.998	37
33	12	25	50.0	44	21	3.8	1.19	2036	0.596	0.239	8.587	-0.565	
34	12	25	50.0	44	23	4.6	13.80	1552	0.736	0.679	8.287	-0.850	36
35	12	25	50.1	44	23	54.9	1.44	2602	0.756	0.268	8.567	-0.507	
36	12	25	49.8	44	21	9.3	2.85	1898	0.482	0.475	8.426	-0.701	44
37	12	25	50.0	44	23	33.9	4.87	2128	0.539	0.267	8.568	-0.608	40
38	12	25	49.7	44	23	38.3	4.69	2197	0.513	0.271	8.565	-0.596	
39	12	25	49.7	44	23	13.6	6.89	1669	0.477	1.148	7.967	-0.674	
40	12	25	49.6	44	22	54.6	3.63	1294	1.012	0.242	8.585	-0.327	47

(1) C(H β)[§]

(2) $\log([O III]/H \beta)$ [§]

(3) $12+\log(O/H)$ [§]

(4) $\log([S II]/H \alpha)$ [§]

*Epoch of coordinates is 1950.0. Root mean square variances: RA = 0.688", Dec = 0.297". Total variance is 0.749". (Results derived from CTIO task COORDS).

[†]Integrated flux through a 4" radius aperture, in units of 10^{-14} ergs cm⁻² sec⁻¹.

[‡]Deprojected galactocentric radius, in units of pc.

[§]In units of dex.

[¶]HII region nomenclature as defined in Sabbadin and Bianchini 1979.

No.	α	δ	H α	R	(1)	(2)	(3)	(4)	SB
41	12 25 49.4	44 23 55.0	4.40	25.40	0.640	0.340	8.518	-0.622	
42	12 25 49.2	44 21 33.2	1.04	1328	0.859	0.277	8.561	-0.299	
43	12 25 49.0	44 21 21.2	2.47	1544	0.639	0.044	8.720	-0.503	53
44	12 25 49.1	44 24 4.6	1.19	2734	0.932	0.829	8.185	-0.450	48
45	12 25 49.0	44 23 20.9	5.41	1734	0.424	0.313	8.537	-0.584	52
46	12 25 48.9	44 21 47.9	6.08	1012	0.451	0.463	8.434	-0.735	58
47	12 25 48.9	44 23 16.2	9.32	1615	0.445	0.443	8.448	-0.763	56,57
48	12 25 48.9	44 23 45.1	46.20	2264	0.517	0.285	8.556	-0.974	50,55,59
49	12 25 48.6	44 21 51.7	4.45	897	0.491	0.493	8.414	-0.502	63
50	12 25 48.5	44 21 37.4	3.72	1136	0.368	0.188	8.622	-0.506	64
51	12 25 48.3	44 21 7.8	1.33	1771	0.941	0.188	8.622	-0.456	
52	12 25 48.4	44 22 9.1	3.06	631	1.176	0.514	8.399	-0.209	
53	12 25 48.1	44 21 27.5	2.41	1305	0.454	0.262	8.572	-0.494	73
54	12 25 48.0	44 21 3.0	1.24	1858	0.682	0.305	8.542	-0.553	
55	12 25 47.9	44 21 46.6	6.09	868	0.643	0.863	8.162	-0.510	78
56	12 25 47.9	44 23 24.3	8.97	1710	0.483	0.462	8.435	-0.679	76
57	12 25 48.0	44 23 46.9	82.00	2243	-0.185	0.203	8.612	-0.838	75
58	12 25 47.7	44 22 3.3	6.32	536	0.673	0.399	8.478	-0.520	86
59	12 25 47.9	44 23 53.6	11.40	2395	0.529	0.454	8.440	-0.691	
60	12 25 47.8	44 23 16.0	6.62	1508	0.705	0.353	8.509	-0.471	80
61	12 25 47.6	44 22 20.0	17.90	417	0.612	0.397	8.479	-0.402	89
62	12 25 47.7	44 22 47.4	17.60	854	0.562	0.451	8.443	-0.738	81
63	12 25 47.6	44 22 59.2	7.23	1108	0.814	0.356	8.507	-0.458	
64	12 25 47.4	44 21 14.5	2.17	1548	0.679	0.139	8.655	-0.514	96
65	12 25 47.6	44 23 34.6	14.00	1931	0.174	0.238	8.588	-0.589	
66	12 25 47.3	44 21 3.4	2.35	1806	0.668	0.231	8.593	-0.639	100
67	12 25 47.5	44 24 7.0	1.02	2701	0.649	0.355	8.508	-0.344	
68	12 25 47.3	44 21 28.2	4.23	1220	0.536	0.230	8.593	-0.562	105
69	12 25 47.5	44 23 43.6	44.50	2137	-0.038	0.490	8.416	-0.779	
70	12 25 47.1	44 21 42.0	24.60	886	0.464	0.293	8.550	-0.719	99,116,125
71	12 25 47.0	44 21 57.8	10.20	519	0.483	0.161	8.640	-0.300	113
72	12 25 47.1	44 22 18.0	35.70	263	0.563	0.306	8.541	-0.701	108
73	12 25 47.0	44 21 7.5	2.24	1693	0.614	0.192	8.619	-0.567	118
74	12 25 47.0	44 22 8.1	18.50	317	0.565	0.479	8.424	-0.644	114
75	12 25 46.9	44 21 34.1	24.30	1055	0.381	0.349	8.512	-0.919	119,123
76	12 25 47.0	44 21 57.8	10.20	519	-0.289	-0.063	8.793	-0.303	
77	12 25 47.1	44 23 56.6	3.21	2437	-4.542	0.195	8.617	-0.510	
78	12 25 47.0	44 23 31.5	26.30	1830	0.440	0.406	8.473	-0.704	112
79	12 25 46.8	44 22 44.7	18.80	704	0.675	0.426	8.459	-0.649	
81	12 25 46.7	44 22 1.9	17.90	392	0.539	0.185	8.624	-0.551	128,129
82	12 25 46.6	44 21 38.8	34.10	929	0.441	0.463	8.434	-0.900	132
83	12 25 46.6	44 21 58.7	18.10	457	0.513	0.088	8.690	-0.551	131,137
84	12 25 46.4	44 22 22.6	27.90	171	0.662	0.567	8.363	-0.623	133
85	12 25 46.5	44 23 36.4	34.70	1936	0.491	0.472	8.428	-0.857	126,127
86	12 25 46.2	44 22 56.0	9.29	953	0.639	0.580	8.355	-0.548	139,140
87	12 25 45.9	44 22 28.6	30.60	291	0.442	0.351	8.511	-0.608	146
88	12 25 45.8	44 22 39.8	11.70	564	0.877	0.497	8.411	-0.544	152
89	12 25 45.8	44 22 22.7	35.00	162	0.698	0.395	8.481	-0.612	151
90	12 25 45.7	44 22 3.7	13.00	332	0.777	0.331	8.524	-0.407	161
91	12 25 45.6	44 22 33.1	22.00	411	0.612	0.471	8.429	-0.600	153
92	12 25 45.3	44 20 37.4	0.64	2417	1.562	0.934	8.113	-0.309	
93	12 25 45.3	44 22 13.9	69.10	200	0.623	0.321	8.531	-0.753	
94	12 25 45.4	44 23 4.5	16.50	1173	0.462	0.260	8.573	-0.722	165,169,174
95	12 25 45.3	44 22 14.0	68.90	198	0.683	0.362	8.503	-0.748	
96	12 25 45.2	44 23 18.6	9.32	1516	0.516	0.416	8.466	-0.595	168
97	12 25 45.0	44 21 19.7	7.58	1408	0.637	0.446	8.446	-0.608	181,182
98	12 25 45.1	44 23 39.1	1.95	2014	0.544	0.342	8.517	-0.321	
99	12 25 44.9	44 21 6.2	1.69	1737	1.234	0.496	8.412	-0.306	
100	12 25 44.8	44 22 10.8	46.80	351	0.635	0.398	8.479	-0.792	
102	12 25 44.4	44 21 54.4	28.00	699	0.763	0.390	8.484	-0.634	
103	12 25 44.5	44 21 13.0	2.64	1594	0.811	0.814	8.195	-0.301	
104	12 25 44.6	44 23 25.6	30.70	1710	0.475	0.611	8.334	-0.924	185,187
105	12 25 44.4	44 20 45.2	1.02	2261	1.257	0.220	8.600	-0.312	
106	12 25 44.4	44 21 48.9	23.10	806	0.531	0.459	8.437	-0.673	203
107	12 25 44.4	44 23 21.7	27.10	1635	0.392	0.629	8.321	-0.937	192
108	12 25 44.2	44 20 57.2	2.86	1990	0.765	0.370	8.498	-0.524	204
109	12 25 44.0	44 21 59.2	29.90	681	0.707	0.429	8.457	-0.659	208,209
110	12 25 43.8	44 21 2.6	2.39	1886	0.737	0.373	8.496	-0.429	211
111	12 25 43.8	44 21 37.5	22.60	1120	0.477	0.480	8.423	-0.693	212
112	12 25 43.6	44 20 30.0	1.14	2667	0.699	0.402	8.476	-0.456	
113	12 25 43.6	44 22 56.5	3.97	1162	0.619	0.241	8.586	-0.389	
114	12 25 43.4	44 21 53.8	82.10	886	0.555	0.407	8.473	-0.842	220
115	12 25 43.5	44 23 4.8	4.63	1347	0.569	0.198	8.615	-0.510	213
116	12 25 43.2	44 20 53.8	1.03	2146	0.860	0.234	8.591	-0.284	
117	12 25 43.2	44 21 45.6	62.40	1054	0.400	0.445	8.447	-0.950	221,222
118	12 25 43.1	44 20 30.0	0.88	2698	1.048	0.464	8.434	-0.384	
119	12 25 43.4	44 23 16.1	9.83	1603	0.461	0.361	8.504	-0.780	218,219
120	12 25 43.1	44 20 59.8	1.48	2016	0.850	0.291	8.552	-0.237	
121	12 25 43.1	44 21 48.6	72.80	1022	0.451	0.409	8.471	-0.881	
122	12 25 42.9	44 23 26.9	10.80	1885	0.393	0.355	8.508	-0.813	207
123	12 25 42.6	44 20 42.3	1.01	2456	1.031	0.196	8.616	-0.328	
124	12 25 42.7	44 22 42.3	2.51	1065	0.848	0.441	8.450	-0.374	
125	12 25 42.7	44 23 18.3	13.80	1723	0.432	0.211	8.606	-0.752	230,231
126	12 25 42.5	44 22 31.6	2.37	997	1.010	0.426	8.459	-0.314	235
127	12 25 42.3	44 23 14.6	2.39	1714	-0.060	0.807	8.200	-0.399	
128	12 25 42.7	44 23 18.3	13.80	1723	0.432	0.209	8.607	-0.763	
129	12 25 41.8	44 20 35.5	0.76	2693	1.156	0.334	8.522	-0.238	
130	12 25 41.8	44 22 56.8	1.68	1481	0.881	0.308	8.540	-0.325	

No.	α				δ		H α	R	(1)	(2)	(3)	(4)	SB
131	12	25	41.2	44	20	20.4	5.67	3096	0.477	0.240	8.586	-0.682	239,240
132	12	25	41.3	44	22	25.9	1.57	1258	0.751	0.584	8.352	-0.252	
133	12	25	41.0	44	22	52.5	5.31	1576	0.438	0.418	8.465	-0.766	237,238
134	12	25	40.6	44	20	10.1	8.69	3382	0.490	0.377	8.493	-0.914	245,247,248
135	12	25	40.6	44	20	20.9	3.13	3152	0.416	0.570	8.361	-0.513	244
136	12	25	40.8	44	22	51.7	4.80	1619	0.418	0.454	8.441	-0.739	
137	12	25	40.1	44	20	18.5	1.44	3258	0.528	0.875	8.153	-0.176	
138	12	25	39.5	44	22	7.7	2.47	1720	0.765	0.401	8.476	-0.418	249
139	12	25	39.3	44	20	16.4	0.66	3401	0.721	0.049	8.717	-0.401	
140	12	25	39.3	44	22	15.5	1.66	1763	0.980	0.181	8.626	-0.342	
141	12	25	39.3	44	24	0.4	0.32	3070	0.823	0.360	8.505	-0.316	
142	12	25	39.0	44	19	59.0	0.60	3813	0.751	0.350	8.511	-0.548	
143	12	25	39.1	44	20	54.5	4.08	2701	0.567	0.421	8.463	-0.581	250
144	12	25	39.0	44	20	59.3	3.10	2624	0.760	0.349	8.512	-0.570	251
145	12	25	38.9	44	20	7.8	0.36	3641	0.364	0.428	8.458	-0.356	
146	12	25	38.4	44	21	2.8	0.60	2690	0.785	1.008	8.063	-0.218	
147	12	25	38.2	44	20	42.4	0.33	3077	0.651	0.246	8.582	-0.090	
148	12	25	38.1	44	22	19.3	1.36	2081	0.761	0.336	8.521	-0.358	
149	12	25	37.7	44	22	0.6	1.06	2208	2.512	0.966	8.091	-0.293	
150	12	25	37.2	44	22	5.1	0.65	2333	1.884	0.700	8.272	-0.183	
151	12	25	36.2	44	20	37.1	1.31	3526	0.596	0.449	8.444	-0.767	
152	12	25	35.4	44	22	36.4	0.30	2814	1.090	0.350	8.511	-0.188	
153	12	25	35.3	44	22	52.5	0.37	2928	0.983	0.478	8.424	-0.324	
154	12	25	30.8	44	21	32.8	0.57	4115	0.197	0.426	8.459	-0.594	
155	12	25	30.6	44	22	13.8	1.01	4011	0.307	0.197	8.615	-0.495	
156	12	25	30.4	44	22	23.3	3.41	4071	0.629	0.466	8.432	-0.854	
157	12	25	30.5	44	22	3.9	2.80	4061	0.492	0.566	8.364	-0.797	
158	12	25	29.7	44	22	11.9	2.03	4263	0.065	0.440	8.450	-0.658	
159	12	25	29.1	44	22	24.4	0.55	4424	0.315	-0.162	8.860	-0.411	
160	12	25	28.8	44	22	11.3	1.89	4482	0.247	0.372	8.496	-0.766	
161	12	25	28.6	44	21	44.5	1.53	4614	0.695	0.157	8.643	-0.700	
162	12	25	28.5	44	21	58.7	0.44	4582	0.365	-0.269	8.934	-0.359	

Appendix D

Glossary

Many of the terms below have been paraphrased from “A Dictionary of Astronomy” (Illingworth 1979), and have been included for the benefit of the uninitiated.

- | | |
|-------------------|---|
| Case B Conditions | An assumption made when calculating the expected nebular characteristics of an ionized volume of gas such as an H II region. These conditions assume that the gas is optically thick to the ionizing Lyman continuum photons and that therefore the nebula itself is radiation bounded, ie. that the radiation does not escape the observed extent of the region. |
| C(H β) | See <i>Interstellar Extinction</i> , and Chapter 2. |
| Collapse Density | The critical local space density of neutral gas that will cause local unstable collapse of that material if exceeded. The numerical value of this density is thought to be affected by several factors including the local pattern speed, the velocity dispersion of the material at the location considered, and the local rate of pre-existing star formation. |
| H II Region | A region of predominantly ionized hydrogen, usually found as individual clouds. The dominant photoionization is by ultraviolet photons, resulting in a gas that emits thermally as well as with recombination line emission. Typical size are less than 200pc. |

Interstellar Extinction	The reduction in brightness of light emitted from stars, caused by the absorption and scattering of the radiation by interstellar dust. The result is largest when looking towards the center of our own Galaxy, where the effect is about 1 magnitude of extinction per kiloparsec of distance traversed. The extinction is a function of wavelength with blue light being more extinguished relative to the red. Radio wavelengths pass essentially unimpeded when compared to optical emission. The absolute level of the extinction can be expressed purely in astronomical magnitudes, A_V , or an equivalent measure $C(H\ \beta)$, where 1 magnitude of A_V equals 0.4 units of $C(H\ \beta)$. The mathematical description of $C(H\ \beta)$ is included in Chapter 2.
Ionization Parameter	A measure of the number of ionizing photons present in an ionized volume relative to the numbers of atoms available for ionization. A high value of this quantity indicates that the radiation field is strong and that most particles in the volume are in an ionized state. A low value of the parameter indicates that recombination is more common, returning many atoms to the neutral state. See Chapter 2.
Irregular Galaxy	A galaxy that possesses no discernable symmetry in shape or structure. The sizes of these objects are typically below average for all galaxies, and contain large amounts of matter for their size.
ISM	The interstellar medium. The material that fills the space between the stars in our own Galaxy, and constitutes about 10% of the Galactic mass. This material exists in a thin disk in the Galactic plane. Dust is found throughout this medium resulting in extinction.

Luminosity Function	In this thesis we refer to differential luminosity functions. This is the number of objects observed with a luminosity that falls within a given range. The luminosity function may be used to assess the completeness of the sample of objects considered. If the faint end of the distribution is well described, and not characterized by a sharp cut-off then the sample is said to appear complete.
OB stars	Main sequence O and B stars are typically very young stars with high ultraviolet luminosities, are very massive and therefore evolve more rapidly from the main sequence. Their presence indicates that the host cluster is less than 10^7 years old and that it may contain stars still in the process of forming.
Pattern Speed	The apparent angular velocity of the spiral pattern in a spiral galaxy. This angular velocity differs from the angular velocity of the constituent material at most radii, except the corotation radius where, by definition, the two velocities are equal. This means that at most radii material is seen to move through the spirals arms, and not reside within them for extended periods of time. Typical timescales to traverse arms are estimated to vary between 10^6 and 10^7 years.
Seeing	The quality of the observing conditions at the time the observations were made. The quality is dictated by the turbulence of the earth's atmosphere, which has the effect of distorting the incoming plane wavefront of the light from the object under observation resulting in a corrugated wavefront. Seeing is estimated by the apparent angular size of a point source of light. Poor seeing is typically characterized by a measure of 2 arcseconds or larger.

Spiral Galaxy Flattened disks of material dominated in their appearance by spiral arms of interstellar matter and young, bright stars. The most common type are two-arm spirals, although other examples with more do exist. Such galaxies are rich in gas and dust, which is usually distributed in clouds along the arms. The formation of the arms has been modelled using spiral density wave theory allowing the structure to be maintained over long periods of time. All spirals exhibit differential rotation, with the outer disk rotating slower than the inner.